UNIVERSITY OF NOTTINGHAM

PHD THESIS

Textile Reinforced Mortars for Masonry Structures

Ph.D Student:

Florentia A. KARIOU

Supervisor:

Dr. Savvas TRIANTAFYLLOU

Submitted in fulfilment of the requirements

for the degree of Doctor of Philosophy

in the

Centre for Structural Engineering and Informatics (CSEI)

Department of Civil Engineering

December 4, 2019



This Ph.D. thesis was financially supported by the University of Nottingham.

Copyright ©Florentia A. KARIOU, 2019.
All rights reserved.

UNIVERSITY OF NOTTINGHAM

Abstract

Faculty of Engineering

Department of Civil Engineering

Doctor of Philosophy

Textile Reinforced Mortars for Masonry Structures

by Florentia A. KARIOU

Unreinforced masonry (URM) is a common engineering practice in different types of construction, e.g., structural bearing walls and infill panels, bridge arches and cultural heritage buildings. Recent catastrophic events such as the earthquakes in L'Aquila (2009), Tohoku, Japan (2011), Christchurch (2011), Northern Italy (2012), and Central Italy (2016–2017) have tragically pointed out the need for restoration and strengthening of existing masonry structures. Masonry structures are also prone to ageing related structural deterioration, accelerated by the effect of adverse environmental actions, e.g.,high speed winds and heavy rainfalls.

Structural strengthening has emerged as a cost efficient solution for extending the life-span of critical infrastructure, as opposed to decommissioning and rebuilding. Furthermore, provided that the solution has a low footprint, structural strengthening has been proven vital for the preservation of cultural heritage.

Within this context, the Textile Reinforced Mortar (TRM) strengthening has been established over the last 15 years as a prominent, low footprint structural

strengthening technique. Despite the significant research endeavours involved, questions remain on the effect of various design parameters on the performance of TRM strengthened URM structures. These pertain to the uncertainties of the underlying materials, i..e, masonry, mortar and textile fibre composites that are overall non-standardized, depend on the variability of the pertinent manufacturing methods.

The overarching aim of this project was to experimentally and numerically investigate the performance of the TRM technique when used for the strengthening of URM structures and hence provide valuable data that can be used for towards the robust and reliable standardization of the method. To achieve this, an extensive experimental campaign was undertaken and corresponding numerical simulation tools were established.

In this project, uniaxial tensile tests on the fibre textiles used in this study (carbon, glass, basalt) were conducted to determine their mechanical properties. Following that, bond tests were performed to investigate the response between the TRM and masonry substrate. The investigated parameters were the bond length, the textile-fibre material and the epoxy-resin coating. Next, the out-of-plane performance of the TRM strengthened masonry walls was examined. The investigated parameters involved were the textile reinforcement ratio, the textile material, the coating of the textile reinforcement with epoxy resin, and the wall thickness. Following that, the TRM strengthened clay brick masonry arches response under monotonic loading at the quarter length of the span was studied. The experimental parameters comprised the number of TRM layers, the textile fibre material, and the strengthening layout.

The experimental results establish TRM as an effective strengthening solution which provides increased load and deformation capacity. Furthermore,

this work manifests the beneficial effect of epoxy-resin coating compared to the uncoated counterpart specimens; increase the tensile properties of the fibre textiles, improve the bonding conditions, and alter the failure mode of carbon and glass fibre-textile material. The amount of reinforcement utilised affects both the strength and deformation characteristics of the corresponding specimens, while it may alter the failure mode. The Finite Element (FE) investigation comprised a micro-modelling approach with the cohesive method to account for the non-linear response of the masonry components. Through an extensive numerical investigation, the employed models are proven to provide a satisfactory agreement to the experimental results and hence pave the way for further research to be conducted on the mechanics of TRM strengthened masonry, considering also the interface properties of the two materials.

Contents

iii

Abstract **v**

Acknowledgements **xxix**

1 Introduction **1**

1.1 Problem Statement 1

1.2 Research significance 4

1.3 Aim of the research 5

1.4 Original contribution 7

1.4.1 Bond tests 7

1.4.2 Masonry walls 7

1.4.3 Masonry arches 8

1.4.4 FE analysis 8

1.5 Publications 9

1.5.1 Publications in International Scientific Journals 9

1.5.2 Proceedings of International Conferences 9

1.5.3 Presentations 10

1.6 Thesis layout 10

2 Conventional strengthening techniques for masonry structures **11**

2.1 Introduction 11

2.2 External reinforcement 11
2.3 Post-tensioning 13
2.4 Near-surface mounted reinforcement 14
2.5 Confinement using Reinforced Concrete (RC) tie-columns and tie-beams 16
2.6 Grout and epoxy injection 17
2.7 Joint repointing 19
2.8 Rebuilding bulging spandrel wall 22
2.9 Surface treatment 22
2.10 Centre core technique 24
2.11 Saddling 25
2.12 Stitching longitudinal cracks 26
2.13 Replacing units 27
2.14 Sprayed concrete 28
2.15 Prefabricated liner 29
2.16 Archtec strengthening method 31
2.17 Case studies on strengthening of masonry arches 32
2.18 Concluding Remarks 37

3 Strengthening based-on high-strength composite materials 39
3.1 Introduction 39
3.2 FRP and TRM strengthening of masonry structures 40
3.3 Bond between TRM and masonry substrates 44
3.4 Out-of-plane strengthening of masonry walls with TRM 52
3.5 Strengthening of brick masonry arches with FRP and TRM 56
3.5.1 The effect of the strengthening configuration 70
3.6 Concluding Remarks 72

4 Materials **75**

4.1 Introduction . . . 75

4.2 Clay bricks . . . 75

4.3 Masonry joint mortar . . . 76

4.4 Compression tests on masonry walletes . . . 77

4.5 Strengthening mortar . . . 77

4.6 Textile-Fibre materials . . . 78

4.6.1 Textile fibre material characterization through tensile tests 79

4.6.2 Tensile tests on TRM specimens . . . 88

4.6.3 Discussion based on the experimental results of tensile tests 89

4.6.4 Comparisons with published test results . . . 93

4.7 Epoxy resin . . . 95

4.8 Conclusions . . . 96

5 Bond between TRM and masonry substrate **97**

5.1 Introduction . . . 97

5.2 Experimental Program . . . 97

5.2.1 Test specimens and investigated parameters . . . 97

5.2.2 Materials . . . 100

5.2.3 Strengthening procedure . . . 102

5.2.4 Experimental setup and procedure . . . 102

5.3 Experimental Results . . . 105

5.4 Discussion . . . 111

5.4.1 Effect of the bond length on different textile materials . . . 111

5.4.2 Effect of coating . . . 116

5.5 Conclusions . . . 117

6 Out-of-Plane TRM strengthening of masonry walls 119

6.1 Introduction . . . 119

6.2 Experimental Program . . . 120

6.2.1 Test specimens and investigated parameters . . . 120

6.2.2 Materials . . . 121

6.2.3 Strengthening procedure . . . 125

6.2.4 Experimental setup and procedure . . . 126

6.3 Experimental results . . . 127

6.3.1 Single-wythe walls . . . 127

6.3.2 Double-wythe walls . . . 134

6.4 Discussion . . . 140

6.4.1 Ductility of strengthened masonry walls . . . 140

6.4.2 Effect of the experimental setup . . . 140

6.4.3 The effect of wall thickness . . . 145

6.4.4 The effect of coating . . . 146

6.4.5 The effect of number of layers . . . 148

6.4.6 The effect of the textile material . . . 150

6.4.7 Comparison between bond and tensile tests results . . . 153

6.5 Conclusions . . . 159

7 Strengthening of masonry arches with TRM material 163

7.1 Introduction . . . 163

7.2 Experimental Program . . . 164

7.2.1 Test specimens and investigated parameters . . . 164

7.2.2 Materials . . . 167

7.2.3 Strengthening procedure . . . 167

7.2.4 Experimental setup and procedure . . . 169

7.3 Experimental Results 170
7.4 Discussion 178
7.4.1 Overview 178
7.4.2 The effect of the textile material 178
7.4.3 The effect of number of layers 186
7.4.4 The effect of the strengthening layout 188
7.5 Conclusions 191

8 Finite element analysis **195**
8.1 Introduction 195
8.2 Simulation approaches for masonry structures 196
8.3 Concrete damage plasticity model 203
8.4 Drucker-Prager 208
8.5 Cohesive surface-based element approach 211
8.5.1 Contact pairs 211
8.5.2 Traction-separation of the cohesive elements 211
8.5.3 Behaviour normal to the contact surface 213
8.5.4 Tangential behaviour - Coulomb friction model 214
8.5.5 Tie-constraint 215
8.5.6 Ductile damage 216
8.6 Modelling of single and double wall specimens 216
8.6.1 Description of the model 216
8.6.2 Modelling of the brick masonry units using the CDP . . . 218
8.6.3 Plasticity parameters of the CDP model 219
8.6.4 Application of the cohesive modelling approach on the mortar joints of the masonry wall specimens 220
8.6.5 Modelling of TRM and masonry substrate interface 221

8.6.6 Modelling of the TRM composite material 223
8.7 Finite element analysis results and discussion 224
8.7.1 Single-wythe walls: Numerical vs experimental results . . 227
8.7.2 Double-wythe walls: Numerical vs experimental results . 230
8.7.3 Effect of the dilation angle 246
8.7.4 Effect of the textile material of the numerical models compared to experimental results 256
8.7.5 Conclusions 257

9 Conclusions and Future Outlook **259**
9.1 Conclusions on the experimental work conducted 260
9.2 Conclusions on the finite element analysis results 264
9.3 Future work 265

Bibliography **269**

A Out-of-plane strength of single and double-wythe walls based on EC6291

List of Figures

1.1 (a) Maagden Tower, Belgium (Verstrynge et al. (2009)), (b) Upstream face of bridge RDG1 48 following the incident showing failed arch (RAIB, 2010) 3

2.1 Wall retrofit using steel strips (Taghdi et al., 2000) 12
2.2 Face to face connector in a double-wythe wall (Silva, 2007) 13
2.3 Application of tie-rods on a masonry arch (Santos, 2003) 13
2.4 Application of cross-bracing struts (Ma et al., 2012) 15
2.5 Application of the Near-Surface Reinforcement method on a bridge highway arch (a) Longitudinal section of the arch (b) Cross section of the arch (Garrity, 2001) 16
2.6 (a) Anchorage system (b) Anchorage plates (Apreutesei et al., 2006) 17
2.7 Application of the injection technique (Beuerman, 2009) 19
2.8 Grout injection (a) Injection of the internal core at the University of Padova (b) Crack injection (Giaretton et al., 2016) 20
2.9 Application of bed joint steel reinforcement technique at the church of St. Giustina (Padua, Italy) (Valluzzi et al., 2005) 21
2.10 Application of bed joint steel reinforcement technique at the church of St. Sofia (Padua, Italy) (Valluzzi et al., 2005) 21
2.11 Repointing of the joints (Apreutesei et al., 2006) 22
2.12 Strengthening of the arch A_1 (a) anchor scheme and (b) horizontal anchors (Apreutesei et al., 2006) 23

2.13 (a) Masonry wall strengthened with steel mesh (b) Spraying cement grout (Meireles and Bento, 2013) 24
2.14 Concrete saddles using varying cross section thickness (Beuerman, 2009) 26
2.15 Concrete saddle of uniform thickness (Beuerman, 2009) 26
2.16 CINTEC anchorage system (Apreutesei et al., 2006) 27
2.17 Application of sprayed concrete on masonry arches (Page, 1996) . 29
2.18 Abutment support for strengthening with sprayed concrete method (Beuerman, 2009) 29
2.19 Application of the prefabricated metal liner method (Beuerman, 2009) 30
2.20 (a) Clifton bridge (b) Ambersham bridge (Brookes and Tilly, 1999) 31
2.21 Boutaca bridge (Oliveira and Lourenco, 2004) 33
2.22 Corroded anchorage (Oliveira and Lourenco, 2004) 33
2.23 Masonry walls strengthening (a) View (b) Detail of the patress plate (Oliveira and Lourenco, 2004) 34
2.24 Donim Bridge (Oliveira and Lourenco, 2004) 34
2.25 Cracking of the arches (a) A_1 and (b) A_4 (Oliveira and Lourenco, 2004) 35
2.26 Strengthening of the arch A_1 with U profiles (a) in general and (b) close to the crown (Oliveira and Lourenco, 2004) 36
2.27 Strengthening of the arch A_4 (a) anchor scheme and (b) horizontal anchors (Oliveira and Lourenco, 2004) 36

3.1 (a) FRP application on masonry vault at the University of Padova (Giaretton et al., 2016) (b) GFRP application on masonry wall (Kalali and Kabir, 2012) 41

4.1 (a) Carbon (b) Glass (c) Coated Basalt 79
4.2 Configurations of uniaxial tensile tests of (a) 50 mm (b) 100 mm . 80
4.3 Experimental setup of uniaxial tensile tests 81
4.4 Failure modes of (a) glass, (b) coated glass and (c) coated carbon fibre-textile materials 82
4.5 Stress versus strain curves for (a) glass, (b) coated glass and (c) coated carbon fibre-textile materials 83
4.6 Stress versus strain curves for (a) carbon, (b) coated carbon (c) coated glass, (d) coated basalt and (e) glass fibre-textile materials 85
4.7 Failure modes of (a) carbon, (b) coated carbon, (c) glass (d) coated glass and (e) coated basalt based on ASTM D5034 87
4.8 Experimental setup and geometry of the TRM coupon (Raoof et al., 2017) 89
4.9 Comparison of the ultimate tensile stress between published and current study 93
4.10 Impregnation of the glass textile in epoxy resin 96

5.1 Experimental setup - all units are in mm (a) geometry and load configuration, (b) actual setup of G_co_150 specimen 98
5.2 (a) Application of the first layer of mortar, (b) impregnation of the carbon textile into the mortar and (c) application of the final layer of mortar 104
5.3 Experimental load cross-head displacement curves for (a) the glass fibre-textile, (b) the coated glass fibre-textile, (c) the carbon fibre-textile, (d) the coated carbon fibre-textile and (e) coated basalt fibre-textile 106

5.4 Experimental load-displacement curves for (a) the glass fibre-textile, (b) the coated glass fibre-textile, (c) the carbon fibre-textile, (d) the coated carbon fibre-textile and (e) coated basalt fibre-textile 107
5.5 Failure modes of specimens strengthened with (a)-(c) dry carbon textile, (d)-(f) coated carbon textile 110
5.6 Failure modes of specimens strengthened with (a)-(c) dry glass textile, (d)-(f) coated glass textile, (g)-(i) coated basalt textile . . . 112
5.7 Maximum load vs bond length curve 114
5.8 Bond stress of textile vs bond length curve 115

6.1 Experimental setup; (a) plan view and elevation (all dimensions in mm), (b) Double-wythe masonry wall, (c) actual setup 122
6.2 Textile material and corresponding mesh sizes considered in this study (a) Dampening of the wall, (b) application of glass textile layer into the mortar, (c) application of the final layer of mortar . 126
6.3 Experimental load-displacement response curves for (a) single-wythe walls, and (b) double-wythe walls 128
6.4 Experimental load-displacement response curves of single and double-wythe grouped in terms of (a)-(b) three vs seven textile layers, (c)-(d) three layers of textile 128
6.5 Experimental load-displacement response curves of single and double-wythe walls grouped in terms of (a)-(b) one layer of carbon fibre textile vs seven layers of glass and coated basalt textile, (c)-(d) one layer of carbon coated fibre textile vs seven layers of glass coated and coated basalt textile 129
6.6 Textile slippage of specimen S_C1; (a) side view (b) TRM surface after collapse 130

6.7 Failure of specimen S_C1_(Co); (a) side view (b) TRM surface after collapse 131
6.8 Failure of specimen S_G3; (a) side view (b) TRM surface after collapse 131
6.9 Failure of specimen S_G3_(Co); (a) side view (b) TRM surface after collapse 132
6.10 Failure of specimen S_G7; (a) side view (b) TRM surface after collapse 132
6.11 Failure of specimen S_G7_(Co); (a) side view (b) TRM surface after collapse 133
6.12 Failure of specimen S_B3; (a) side view (b) TRM surface after collapse 133
6.13 Failure of specimen S_B7; (a) side view (b) TRM surface after collapse 134
6.14 Failure of D_CON specimen 135
6.15 Failure of specimen D_C1; (a) side view (b) TRM surface after collapse 135
6.16 Failure of specimen D_C1_(Co); (a) side view (b) TRM surface after collapse 136
6.17 Failure of specimen D_G3; (a) side view (b) TRM surface after collapse 137
6.18 Failure of specimen D_G3_(Co); (a) side view (b) TRM surface after collapse 137
6.19 Failure of specimen D_G7; (a) side view (b) TRM surface after collapse 138
6.20 Failure of specimen D_G7_(Co) 138

6.21 Failure of specimen D_B3; (a) side view (b) TRM surface after collapse 139
6.22 Failure of specimen D_B7; (a) side view (b) TRM surface after collapse 140
6.23 Ratio of strengthened specimen maximum load to control specimen maximum load (a) single-wythe walls (b) double-wythe walls 144
6.24 The effect of coating on the out-of-plane bearing capacity 147
6.25 The effect of number of layers in the out-of-plane bearing capacity 150
6.26 The effect of textile material in the out-of-plane bearing capacity of single and double-wythe walls 152
6.27 Cross-section analysis in out-of-plane bending (a) geometry, (b) strain distribution and (c) internal force distribution 154
6.28 Cross-sectional analysis vs Experimental results 157

7.1 Experimental setup - all units are in mm (a) geometry and load configuration (b) plan view and position of displacement transducers (c) actual setup 166
7.2 (a) Application of basalt textile into the mortar (b) Extrados and (c) Intrados final strengthening configuration 169
7.3 Experimental load-displacement curves in terms of the number of layers, textile material, and the position of the strengthening . 171
7.4 Vertical Displacement profiles - Displacements are scaled by a factor of 5 and units are in m 179
7.5 Collapse mechanism of control specimen 180
7.6 Collapse mechanism of specimen G3_I 180
7.7 Collapse mechanism of specimen G7_I 181
7.8 Collapse mechanism of specimen B3_I 181

7.9 Collapse mechanism of specimen G3_E 182
7.10 Collapse mechanism of specimen B3_E 182
7.11 Collapse mechanism of specimen G7_E 183
7.12 Collapse mechanism of specimen B7_E 183
7.13 Ratio of the maximum strength effectiveness 184
7.14 The effect of textile material in terms of (a) the maximum load and (b) the corresponding displacement 185
7.15 The effect of number of layers in terms of (a) the maximum load and (b) the corresponding displacement 188
7.16 Ratio of the maximum strength effectiveness: Strengthening configuration 190
7.17 The effect of the strengthening configuration in terms of (a) the maximum load and (b) the corresponding displacement 191

8.1 Simplified micro-modelling (Lourenco and Rots, 1997) 198
8.2 (a) Tensile and (b) compressive behaviour described by the CDP model for concrete (SIMULIA, 2016) 202
8.3 Stress-fracture energy curve SIMULIA (2016) 204
8.4 Yield surfaces in the deviatoric plane for different K_c values (SIMULIA, 2016) 206
8.5 Yield surfaces in the deviatoric plane for plane stress condition (SIMULIA, 2016) 207
8.6 Yield surface of linear Drucker-Prager (SIMULIA, 2016) 208
8.7 Geometric representation of the dilation angle (SIMULIA, 2016) . 210
8.8 Typical traction-separation response (Bolhassani et al., 2015) . . . 212
8.9 Linear damage evolution (SIMULIA, 2016) 213
8.10 Contact Pressure-Overclosure relationship (SIMULIA, 2016) . . . 214

8.11 Shear stress versus total slip (SIMULIA, 2016) 215
8.12 Loading of (a) single walls, (b) Loading of double walls 217
8.13 Compressive response of brick masonry unit 219
8.14 Load-displacement curves of single-wythe wall specimens 225
8.15 Load-displacement curves of double-wythe wall specimens . . . 226
8.16 Deformed shape of FEM_S_CON 230
8.17 Strain contours of FEM_S_C1 including (a) equivalent plastic strain on the top and bottom of the wall, (b) maximum principal plastic strain and (c) longitudinal plastic strain in the x-axis (d) Failure mode of S_C1 specimen 231
8.18 Strain contours of FEM_S_C1_(Co) including (a) equivalent plastic strain on the top and bottom of the wall, (b) maximum principal plastic strain and (c) longitudinal plastic strain in the x-axis, (d) Failure mode of S_C1_(Co) specimen 232
8.19 Strain contours of FEM_S_G3 including (a) equivalent plastic strain on the top and bottom of the wall, (b) maximum principal plastic strain and (c) longitudinal plastic strain in the x-axis, (d) Failure mode of S_G3 specimen 233
8.20 Strain contours of FEM_S_G7 including (a) equivalent plastic strain on the top and bottom of the wall, (b) maximum principal plastic strain and (c) longitudinal plastic strain in the x-axis (d) Failure mode of S_G7 specimen 234
8.21 Strain contours of FEM_S_G3_(Co) including (a) equivalent plastic strain on the top and bottom of the wall, (b) maximum principal plastic strain and (c) longitudinal plastic strain in the x-axis, (d) Failure mode of S_G3_(Co) specimen 235

8.22 Strain contours of FEM15_S_G7_(Co) including (a) equivalent plastic strain on the top and bottom of the wall, (b) maximum principal plastic strain and (c) longitudinal plastic strain in the x-axis, (d) Failure mode of S_G7_(Co) specimen 236
8.23 Strain contours of FEM45_S_G7_(Co) including (a) equivalent plastic strain on the top and bottom of the wall, (b) maximum principal plastic strain and (c) longitudinal plastic strain in the x-axis, (d) Failure mode of S_G7_(Co) specimen 237
8.24 Strain contours of FEM_S_B3 including (a) equivalent plastic strain on the top and bottom of the wall, (b) maximum principal plastic strain and (c) longitudinal plastic strain in the x-axis, (d) Failure mode of S_B3 specimen 238
8.25 Strain contours of FEM15_S_B7 including (a) equivalent plastic strain on the top and bottom of the wall, (b) maximum principal plastic strain and (c) longitudinal plastic strain in the x-axis, (d) Failure mode of S_B7 specimen 239
8.26 Strain contours of FEM45_S_B7 including (a) equivalent plastic strain on the top and bottom of the wall, (b) maximum principal plastic strain and (c) longitudinal plastic strain in the x-axis, (d) Failure mode of S_B7 specimen 240
8.27 (a) Deformed shape of FEM_D_CON, (b) Failure mode of D_CON specimen 246
8.28 Strain contours of FEM_D_C1 including (a) equivalent plastic strain on the top and bottom of the wall, (b) maximum principal plastic strain and (c) longitudinal plastic strain in the x-axis, (d) Failure mode of D_C1 specimen 247

8.29 Strain Contours of FEM_D_C1_(Co) including (a) equivalent plastic strain on the top and bottom of the wall, (b) maximum principal plastic strain and (c) longitudinal plastic strain in the x-axis, (d) Failure mode of D_C1_(Co) specimen 248
8.30 Strain contours of FEM_D_G3 including (a) equivalent plastic strain on the top and bottom of the wall, (b) maximum principal plastic strain and (c) longitudinal plastic strain in the x-axis, (d) Failure mode of D_G3 specimen 249
8.31 Strain contours of FEM_D_G7 including (a) equivalent plastic strain on the top and bottom of the wall, (b) maximum principal plastic strain and (c) longitudinal plastic strain in the x-axis, (d) Failure mode of D_G7 specimen 250
8.32 Strain contours of FEM_D_G3_(Co) including (a) equivalent plastic strain on the top and bottom of the wall, (b) maximum principal plastic strain and (c) longitudinal plastic strain in the x-axis, (d) Failure mode of D_G3_(Co) specimen 251
8.33 Strain contours of FEM_D_G7_(Co) including (a) equivalent plastic strain on the top and bottom of the wall, (b) maximum principal plastic strain and (c) longitudinal plastic strain in the x-axis, (d) Failure mode of D_G7_(Co) specimen 252
8.34 Strain contours of FEM_D_B3 including (a) equivalent plastic strain on the top and bottom of the wall, (b) maximum principal plastic strain and (c) longitudinal plastic strain in the x-axis, (d) Failure mode of D_B3 specimen 253

8.35 Strain contours of FEM_D_B7 including (a) equivalent plastic strain on the top and bottom of the wall, (b) maximum principal plastic strain and (c) longitudinal plastic strain in the x-axis, (d) Failure mode of D_B7 specimen 254
8.36 Load-displacement curves of single-wythe wall specimens using 15° and 45° dilation angle 255

List of Tables

4.1 Casting and strengthening mortar of all the experimental campaigns . . . 77
4.2 Textile material properties . . . 79
4.3 Tensile properties of the fibre-textile materials . . . 81
4.4 Tensile properties of the fibre-textile materials based on ASTM D5034 . . . 86
4.5 Tensile properties of TRM coupons of the fibre textiles (Raoof et al., 2017) . . . 89
4.6 Axial stiffness ratio . . . 92

5.1 Specimens details . . . 99
5.2 Casting and strengthening mortar . . . 103
5.3 Summary of experimental results . . . 113
5.4 Exploitation of textile strength . . . 114

6.1 Wall Specimens . . . 121
6.2 Casting and strengthening mortar of masonry walls . . . 123
6.3 Summary of experimental results . . . 141
6.4 Ductility of masonry walls . . . 142
6.5 Horizontal vs vertical experimental setup . . . 143
6.6 Tensile tests vs cross-section analysis results . . . 157

7.1 Specimens and investigated parameters . . . 165

7.2 Casting and strengthening mortar of masonry arches specimens . 168
7.3 Summary of experimental results 172
7.4 Ductility of masonry arches 190

8.1 Brick properties for single and double-wythe walls 220
8.2 Cohesive surface element properties 222
8.3 Damage properties of the fibre-textile 224
8.4 Textile properties of the FE models 244
8.5 Experimental and simulated failure mode in single-wythe walls . 245
8.6 Experimental and simulated failure mode in double-wythe walls 245
8.7 Textile properties of the FE models of similar failure mode 257

Acknowledgements

This project was conducted at the University of Nottingham supervised by Dr. Savvas Triantafyllou. It has been financed by the Vice-Chancellor's Scholarship for Research Excellence (European Union). I would like to the thank University of Nottingham giving me this opportunity.

I would like to thank my supervisor Dr. Savvas Triantafyllou for his support through the whole project. His critical thinking, experience and engineering judgement helped me to improve my work and complete my PhD studies.

I would also like to thank the lab managers Tom Buss and Mike Langford, the chief technician Nigel Rook, and the technicians Balbir Loyla, Gary Davies, Sam Cook for their assistance in the experimental work.

In addition, I would like to thank my colleague Kuanysh Makashev for taking over and conducting a part of the experimental work on the textile coupon tests using the ASTM standards, under my guidance. His contribution is greatly appreciated.

I am deeply grateful for the incessant help and support of my friend Zoi. Her practical and psychological support in the lab at the beginning of this work was of great importance. In addition, I would like to thank all my colleagues and friends Andre, Manolis, Andreas, Aziz, Giulia, Alexis, Vagelis for contributing to the nice working environment.

In addition, I would like to thank my parents, and all my sisters for their help, love and support from the beginning until the end of this project. Finally, I deeply thank Francesco for all his encouragement, support and motivation that made me improve myself and achieve new challenging goals in my life.

Chapter 1

Introduction

1.1 Problem Statement

Unreinforced masonry (URM) in the form of structural bearing walls, arches and infill panels, is amongst the oldest construction systems worldwide. URM structures comprise a significant percentage of the existing building stock in the UK and abroad. There are nearly 450.000 listed buildings and 10.6 million pre-1944 buildings within the UK, making up the largest part of the built environment (Heritage, 2004). In many cases, these involve structures of significant cultural and historical importance.

URM walls are one of the most popular building components. URM of existing buildings were designed under gravity and wind loads without considering the seismic loads. In the event of an earthquake or high wind pressure in-plane and out-of-plane forces result in cracking, damage or collapse of these buildings. In addition to that, even low load levels result in out-plane phenomena as reported in Albert et al. (2001), Papanicolaou et al. (2008), and Valluzzi et al. (2014).

Masonry arches have been widely used in engineering practice as an effective structural system for spanning medium to large openings. Arches have

been utilised in historical structures of extreme cultural importance and also constitute a substantial part of rail and transport infrastructure worldwide. Unreinforced masonry arches are often imposed to asymmetric loading due to, e.g., seismic excitation and soil pressure applied to bridge abutments. Furthermore, they are susceptible to brittle failure modes often leading to structural degradation, and loss of human life.

In the event of catastrophic events such as earthquakes, a significant number of collapsed or damaged masonry structures has been reported in the literature. Coburn et al. (1992) reported that 1100 fatal earthquakes resulted in 1.53 million deaths in 1900-1992; 75% of deaths were caused by collapse of reinforced concrete, timber and masonry buildings, and 65% were deaths caused by masonry buildings collapse only. After the earthquake of L'Aquila (2009) several old URM buildings were damaged or collapsed. In particular, 18 000 damaged to a near collapse state buildings were recorded including Romanesque churches, historic buildings and monuments (Indirli et al., 2013). In the Wenchuan Earthquake (2008), for a sample of 1005 damaged buildings, masonry buildings demonstrated the worst performance. In addition, Galvis et al. (2017) reported that the Mexico earthquake (2017) resulted in 46 collapsed structures, where 33% corresponds to masonry structures. A significant issue is the cost required to repair unreinforced masonry structures, as reported in Sassun et al. (2016) and EEFIT (2009).

Within this setting, structural strengthening is required for those structures to withstand increased operational loads due to the heavy cargo movements and also avoid catastrophic collapse events. Structural strengthening interventions have been repeatedly documented as an effective method to not only preserve masonry structures but also to protect human lives, (see, e.g., (Dizhur et



FIGURE 1.1: (a) Maagden Tower, Belgium (Verstrynge et al. (2009)), (b) Upstream face of bridge RDG1 48 following the incident showing failed arch (RAIB, 2010)

al., 2011)). Masonry structures are also prone to ageing related structural deterioration, accelerated by the effect of adverse environmental actions, e.g., high speed winds and heavy rainfalls. Typical examples of partial collapse due to ageing include the Magdeen Tower Verstrynge et al. (2009) (Fig. 1.1a) and the Feltham bridge (RAIB, 2010) events (Fig. 1.1b). With the objective of mitigating such issues and also increase the durability and resilience of existing structures structural rehabilitation and strengthening techniques are employed. In addition, requirements for sustaining accidental events such as blast and impact, further necessitate upgrading of existing structures (Hamoush et al., 2001).

Various strengthening solutions have been implemented for strengthening

of masonry structures, including traditional methods (e.g., grout/ epoxy injection, external reinforcement) and composite materials such as FRP, NSM combined with epoxy-resin adhesives. Several drawbacks of these materials related with the epoxy-adhesion resulted to their replacement by the Textile reinforced mortar (TRM) composite. TRM has been extensively used the last decade, as a strengthening solution on masonry structures. They are composed by TRM layers of fibre textile materials, such as carbon, glass, basalt impregnated within inorganic matrices. The textiles typically consist of fibre rovings in at least two orthogonal directions, which create an open-mesh geometry.

1.2 Research significance

This research project deals with structures of high historical importance, including plane walls and masonry arches, which have not been designed under the current guidelines. In case of catastrophic events or ageing, these structures are prone to collapse or result in severe damages. Therefore, they need to be upgraded using strengthening solutions.

A significant number of experimental studies available in the literature is focused on strengthened masonry structures with the TRM material, using cementitious mortar as an adhesive material. In particular, uniaxial tensile tests, bond tests, in-plane and out-of-plane tests on masonry walls have been conducted, including several investigated parameters such as different materials, amount of the composite material and different strengthening configuration. However, future work needs to include further parameters, such as the effectiveness of these materials under high temperatures and the cost of various composite materials used. In addition, there are no design guidelines on the

performance of TRM strengthened masonry structures, therefore further research on this topic was necessary to be conducted to contribute to the performance of design guidelines. In particular, this work contributes to the quantification of the effectiveness of the TRM composite, in both out-of-plane walls and masonry arches, in terms of load and deformation capacity. This is also shown by the simulation of the strengthened masonry walls tests on the Finite Element (FE) software Abaqus, based on material characterisation tests, (bond tests and uniaxial tensile tests of the fibre-textile materials used), which resulted in a good agreement between the experimental and analytical results.

Also, the limited number of the available studies on strengthened masonry arches do not result in similar findings in terms of the failure mechanisms of the strengthened specimens. Therefore, this work initially investigated the bond behaviour, the tensile strength of the TRM material and then focused on larger scale specimens of masonry walls and masonry arches. The entire experimental work investigates a series of parameters, namely different composite materials and reinforcement ratio, including epoxy-resin coating on fibre-textile materials. The effect of the in house coating on the bare textiles of carbon and glass fibre-textiles proposed in this work, resulted in beneficial results, with significant increased maximum load and deformation capacity, compared to the uncoated specimens. By adopting this method, the effectiveness of the fibre textiles will be extremely increased and maximize the minimal masonry strength properties.

1.3 Aim of the research

The main aim of this research project is to assess the efficiency of the innovative TRM composite material for the strengthening of masonry arches/ structures.

To achieve this, the following measurable objectives were adopted:

- Examine the response of fibre-textiles materials used in this research project. Uniaxial tensile tests were conducted on fibre-textile materials to determine their tensile behaviour. The examined fibre-textile materials were the glass, coated glass, basalt, carbon and coated carbon.
- Examine the bond behaviour between the TRM composite material and brick masonry walls. The investigated parameters included:
  - The bond length (100 mm, 150 mm, 200 mm).
  - The textile-fibre materials, namely glass, coated basalt, carbon.
  - The epoxy-resin coating.
- Examine and quantify the effect of TRM in brick masonry wallets when subjected to out-of-plane bending. This provided significant insight on the load and deformation capacity of TRM at the time of failure. For this purpose, two sets of single and double-wythe walls were designed and tested under three point-bending. The investigated parameters were:
  - The number of the TRM layers.
  - The influence of masonry wall thickness on the effectiveness of masonry walls specimens (single and double-wythe).
  - The textile-fibre materials, namely glass, coated basalt and carbon.
  - The effect of epoxy-resin coating on bare textiles.
- Examine and quantify the effect of TRM solution on masonry arches. The investigated parameters included:
  - The number of the TRM layers.

- The textile-fibre materials, namely coated glass, and coated basalt.
- The strengthening configuration (intrados/ extrados).

1.4 Original contribution

1.4.1 Bond tests

This study comprises an extensive experimental work to study the bond behaviour between the TRM composite and masonry substrate, considering a series of parameters on a single-lap test setup. Three different fibre-textile materials are adopted, namely carbon, glass and coated basalt. In addition, the beneficial effect of coating on glass and carbon fibre textile in three different bond lengths (100, 150, 200 mm) is investigated. The experimental results obtained in this work were important to explain the response of the fibre-textile materials on masonry walls and masonry arches experimental studies.

1.4.2 Masonry walls

This project investigates for the first time in a systematic way the effect of a series of parameters on the out-of-plane response of masonry walls. In terms of textile reinforcement, both the textile material and the number of textile layers are considered as experimental parameters. Within this setting, a systematic study on the comparative effectiveness of glass, coated basalt and in addition carbon textile reinforcement is undertaken on the basis of utilizing textile layers of equivalent elastic stiffness. More specifically, the influence of 3 and 7 layers of glass and coated basalt TRM material is examined and their response is directly compared to the 1 layer of carbon fibre TRM case. Such a comparative

study has not been performed. Furthermore, the effect of the epoxy-resin coating on carbon and glass strengthened specimens is investigated. The behaviour of resin coated carbon textile has not been examined in the literature. Finally, both single and double-wythe walls are examined in this research project.

1.4.3 Masonry arches

This research work presents an extensive experimental study on the response of masonry arches strengthened with TRM composites. The investigated parameters comprise the strengthening material, i.e., coated basalt and coated glass, the amount of textile reinforcement used and the strengthening layout, i.e., intrados and extrados strengthening. Coated glass has been found to significantly enhance the out-of-plane response of masonry walls compared to bare glass textile reinforcement (see Chapters 6 and 7). This is the first time that a comparative study between all the aforementioned parameters is attempted within a single experimental campaign.

1.4.4 FE analysis

A detailed Finite Element (FE) analysis has been conducted on single- and double-wythe TRM strengthened masonry walls. For this purpose, a detailed FE model was built using the micro-modelling method and cohesive modelling approach to consider the joint mortar separation at the interface of the constituents. This study provides a numerical tool for modelling the TRM strengthened structures. Even though similar FE analysis have been reported in the literature an innovative procedure on the calibration of the model has been conducted in this work.

1.5 Publications

1.5.1 Publications in International Scientific Journals

This research has already contributed in two journal publications:

- **Kariou F.A.**, Triantafyllou S.P., Bournas D.A. (2019), "TRM strengthening of masonry arches: An experimental investigation on the effect of strengthening layout and textile fibre material", *Composites Part B: Engineering*, 173.
- **Kariou F.A.**, Triantafyllou S.P., Bournas D.A., Koutas L.N. (2018), "Out-of-plane response of masonry walls strengthened using textile-mortar system", *Construction and Building Materials*, 165, pp. 769-781.

1.5.2 Proceedings of International Conferences

In addition, parts of this project have been presented in the following international conferences:

- **Kariou F.A.**, Triantafyllou S.P., Bournas D.A "On the effectiveness of textile reinforced mortars for retrofitting of masonry arches", *8th International Conference on Advanced Composites in Construction*, 3 - 5 September 2017, Sheffield, United Kingdom.
- **Kariou F.A.**, Triantafyllou S.P., Bournas D.A, Koutas L.N. "Out-of-plane behaviour of TRM strengthened masonry wall.", *4th International Conference on Smart Monitoring, Assessment and Rehabilitation of Civil Structures*, 13 - 15 September 2017, Zurich, Switzerland.

1.5.3 Presentations

Kariou F.A. "Textile reinforced mortar strengthening of masonry arches", *2nd International Workshop in Seismic Loss, Rehabilitation and Post-Earthquake Crisis Management of Critical Infrastructure*, 20-24 November 2017, Istanbul, Turkey.

1.6 Thesis layout

This thesis is organised in eight chapters. Chapter 1 comprises an introduction on masonry structures. An overview of traditional strengthening techniques is presented in Chapter 2. An extensive literature review on the strengthening of masonry walls and arches with the TRM composite material is performed in Chapter 3. In Chapter 4 the materials used for the TRM strengthening solution are presented. Uniaxial tensile tests on bare textile are also included in this Chapter. Chapter 5 presents all the experimental work on the bond behaviour between masonry and TRM material. Chapter 6 includes the experimental work conducted on masonry walls. Chapter 7 includes the experimental work conducted on masonry arches. Chapter 8 comprises FE modelling on the single-wythe and double-wythe masonry walls using the Abaqus software. Conclusions and recommendations for future research are presented in Chapter 9.

Chapter 2

Conventional strengthening techniques for masonry structures

2.1 Introduction

Due to the generic brittle response of unreinforced masonry structures, a key objective of structural strengthening has been to increase both their strength and the ductility. The rational has been to improve the overall resilience of the structure by enhancing the existing defence mechanisms and also introduce additional ones if possible (Galati et al., 2006; EN, 1998b; Vintzeleou and Tassios, 1989). ElGawady et al. (2004) and Apreutesei et al. (2006) provided a thorough review of conventional strengthening techniques, i.e., techniques that have been used in practice over the past 50 years.

2.2 External reinforcement

The application of external reinforcement has been one of first strengthening techniques applied to masonry structures, either in the form of externally bonded steel plates, tubes, or strips, see, e.g., Fig. 2.1 or steel tying rods.



FIGURE 2.1: Wall retrofit using steel strips (Taghdi et al., 2000)

In the former case, bonding to the masonry surface is achieved using pin connectors. Primarily utilised in the form of vertical and diagonal bracing, externally bonded reinforcement successfully have been shown to increase the lateral resistance and overall energy dissipation of masonry structures, especially in the case of cycling loading. However, the increase in lateral resistance is bounded by the compressive strength of the masonry substrate, especially at the end toes, leading also to global buckling of the component (Rai and Goel, 1996). For the method to be efficient in the case of double-wythe walls, i.e., to ensure the collaboration of both masonry layers, transversal anchorage was required as shown in Fig. 2.2.

Iron and steel tie-rods have been used for centuries to reinforce masonry arches and vaults by providing a tension element to control, i.e., reduce, the

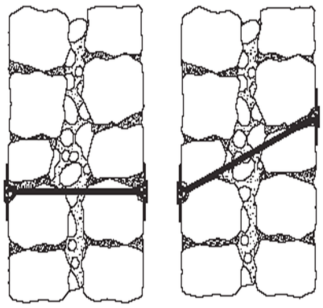


FIGURE 2.2: Face to face connector in a double-wythe wall (Silva, 2007)



FIGURE 2.3: Application of tie-rods on a masonry arch (Santos, 2003)

horizontal thrust to the arch supports (see Fig.2.3). The application of external reinforcement can effectively provide increase of the lateral resistance but is an invasive method since you need to drill holes to insert the pins.

2.3 Post-tensioning

Post-tensioning is a strengthening technique mainly used in historical monuments. The objective is to provide the necessary compressive stresses that will

counteract, hence reduce the tensile stresses arising from lateral loads (Karantoni and Fardis, 1992; ElGawady et al., 2004). The method is applied either internally, or externally with prestressing techniques. In particular, the internal method comprise application of the post-tensioning tendons into drilled cored cavities. The external method applies prestressing to the junctions and the main support regions of walls. An example of the external method is shown in Fig. 2.4. It was reported that guiding of the tendons can be a challenging task (Ma et al., 2012).

Post-tensioning is an efficient technique as it can reduce cracking and deflection under service loads and significantly increase strength and ductility. Furthermore, it is reversible and relatively easy to apply. On the other hand, the method cannot be applied in damaged masonry, where strength losses occur due to creep and shrinkage of masonry. In addition to that, drilling holes on masonry to anchorage the tendons comprises an invasive method.

2.4 Near-surface mounted reinforcement

The near-surface mounted reinforcement (NSM) technique involves the application of stainless steel reinforcing bars that are embedded into pre-drilled holes or grooves. Bonding is achieved using grout material. The rebars are applied at the positions where tensile stresses are expected to be developed due to external loads or settlements. It is important that each bar is completely encapsulated within the grout. Specifically to the case of masonry structures, it has been found that pitting corrosion of the reinforcement is possible close to the springings and also in cases where the bars are exposed due to voids or cracks. Therefore, a large number of smaller diameter steel rebars is suggested to be used.

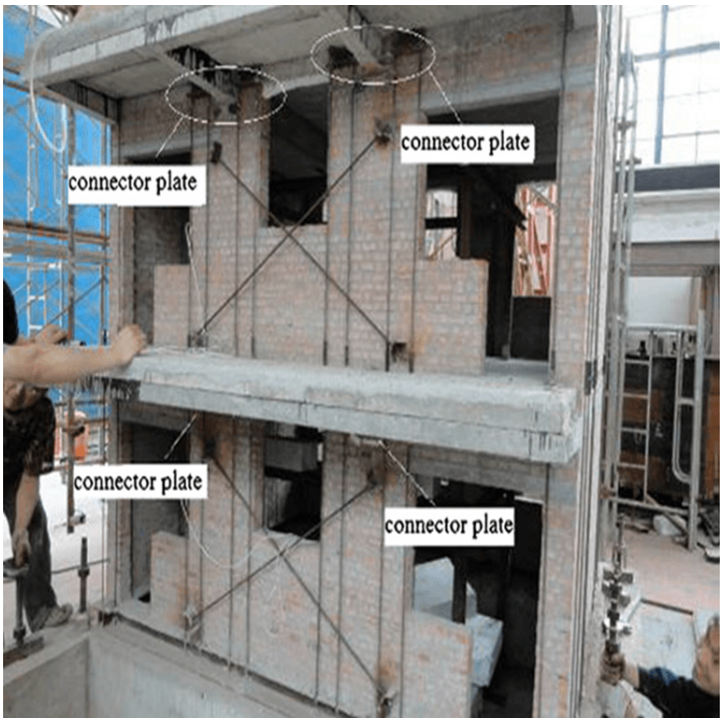
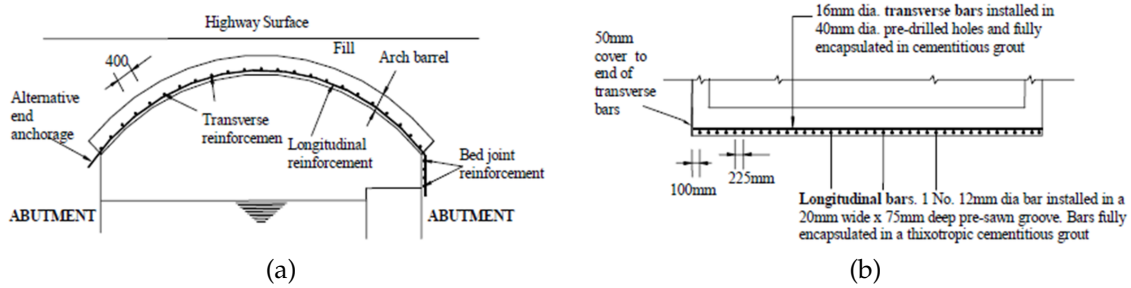


FIGURE 2.4: Application of cross-bracing struts (Ma et al., 2012)

The compatibility of the grout material with the masonry substrate is a critical factor for the efficiency of the method. The epoxy or polyester resin based grouts were typically required due to their increased bond strength. However, the different mechanical and physical properties compared to the masonry materials have been found to cause surface cracking (Garrity, 2001).

Furthermore, in the case of arches, the method necessitates the application of both transverse and longitudinal reinforcement. The transverse holes are drilled into the arch, the grout is pumped into the holes and the steel rebars are installed. The transverse reinforcement is used to improve the flexural capacity and the lateral load distribution (Fig. 2.5b). The longitudinal grooves are sawn at the intrados of the arch and the grout is injected into each groove. Additional grout is applied with the application of the longitudinal reinforcement (Fig. 2.5a). Also, the horizontal bed joint reinforcement is suggested to be used



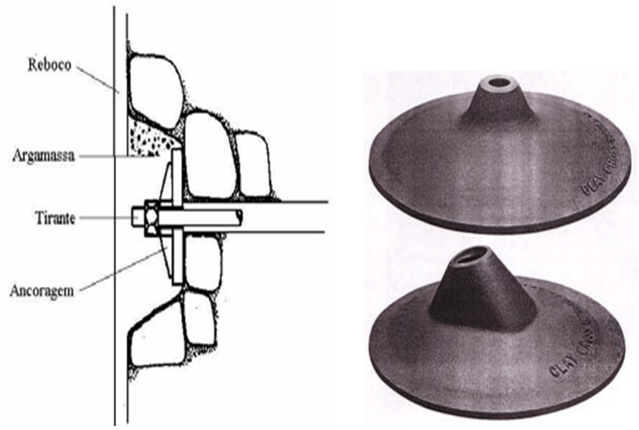
(a) (b)

FIGURE 2.5: Application of the Near-Surface Reinforcement method on a bridge highway arch (a) Longitudinal section of the arch (b) Cross section of the arch (Garrity, 2001)

at the abutments to provide additional support due to large live loads (see Fig. 2.5). This method can effectively increase the cracking resistance and improve the post-cracking behaviour of the structure. However, NSM is a highly invasive technique due to drilling of holes or grooves for the steel rebars application.

2.5 Confinement using Reinforced Concrete (RC) tie-columns and tie-beams

Confining of URM with tie-columns is a widely known method, which is performed using vertical reinforced concrete or reinforced masonry tie columns, to isolate the corners, wall intersections, vertical borders of doors and windows openings. Karantoni and Fardis (1992) reported that tie columns should be connected with a tie beam along the walls at floor levels to enhance the integrity and stability of the wall and improve the structure in terms of ductility and energy dissipation but without any increase of the load bearing capacity (Chuxian and Haibing, 1997). On the other hand, tie-beams should be connected to the floor or roof elements to increase their in-plane stiffness and transfer the horizontal loads to the walls. A combination of both tie-beams and tie-columns can



(a) (b)

FIGURE 2.6: (a) Anchorage system (b) Anchorage plates (Apreutesei et al., 2006)

be combined together to form a confined masonry panel.

In case of bridge arches, tie bars were applied to the structure to prevent further outward movement of the spandrel walls. In particular, a bar is passing through the width of the bridge to restrain the wall, which is fastened with the pattress plates at each end as shown in Fig. 2.6.

The benefit of this method is that can be applied without disruption of the traffic. However, the lack of scientific evidence and guidelines for the application of this method is possible to result in pattress plates fracture or spreader beams. In particular, it has been reported that after the tie bars installation, additional movement of spandrel wall occurred. In another case, corrosion of the exposed parts was observed, where stainless steel bars can be adopted to prevent this phenomenon.

2.6 Grout and epoxy injection

Grout injection is one of the most common technique to increase the in-plane strength of masonry. Epoxy resin injections are usually used for fine cracks less

than 2 mm wide, whereas cement-based grout for larger cracks, such as in multi-wythe masonry walls. Grout injection was used to fill the voids or cracks and restore the continuity and homogeneity of masonry stone walls. This method is effective only for non well-built stone walls. Experimental investigation on samples of stones and mortars, or site tests is required before the applications of the grout, to determine the effectiveness of the method in each particular case, due to the different mechanical properties of each masonry structure (Corradi et al., 2008). It was reported that cement-based grout injection resulted in 80-140% increase of compressive strength, in-plane stiffness, and lateral resistance (Schuller et al., 1994; Calvi and Magenes, 1994) (see Fig. 2.8).

The grouting repair technique was used to fill voids due to ring separation or cracks at the arch ring or spandrel walls. In particular, it improves the lateral resistance of the spandrel walls and can prevent further deterioration of the structure. Little traffic disruption and low cost of the material and the workers was reported among the advantages of the grouting method.

For a successful application of this method, the grout is designed according to the mechanical properties of the mortar and the existing masonry units, which defines the masonry arch properties, in terms of durability, compressive strength, flexural and tensile bond strength (Beuerman, 2009).

The injection technique can be applied on masonry arches above the arch, at the piers or the abutments to increase the load capacity, improve the load distribution, and prevent further deterioration of the structure. Before the application of the injection it is necessary to calculate the increased dead load due to the additional grout weight and ensure the resistance of the foundations to the additional load.

The application of this technique comprises drilling, cleaning of holes, and

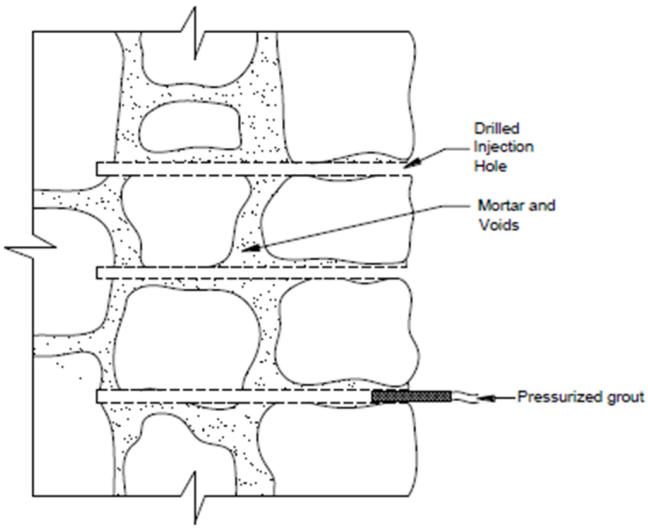


FIGURE 2.7: Application of the injection technique (Beuerman, 2009)

injection from the lowest to the highest drilled holes, by means of a pressure grouting machine (Fig. 2.7). The holes are covered with either a core, brick or stone of similar appearance to the existing material.

Grout and epoxy injection method can enhance the compressive strength, the in-plane stiffness of masonry walls, and the lateral resistance of the spandrel walls of an arch. However, disruption of the structure occurs due to drilling of holes for the injecting material application.

2.7 Joint repointing

Valluzzi et al. (2005) demonstrated a strengthening alternative of brick masonry structures, where steel reinforcement bars are embedded in the bed mortar joints. In particular, the strengthening material is applied in the mortar bed joints which were previously excavated and then refilled with a repointing material, such as the hydraulic lime or cement based mortar. This method is mainly used to control the formation of cracking and reduce the dilatancy of the wall.



(a) (b)

FIGURE 2.8: Grout injection (a) Injection of the internal core at the University of Padova (b) Crack injection (Giaretton et al., 2016)

It can be combined with transversal ties, which can prevent the out-of-plane detachment of the external wythes. The bed joint technique has been applied in two churches in Padua (Italy), namely St. Giustina's bell tower (Fig. 2.9) and Sofia's church (Fig. 2.10).

Repointing of masonry arches is a method used to refill the degraded mortar joints of masonry arch units, but cannot increase its load capacity (see Fig. 2.11). Additional damage can be occurred after the application of the repointing repair technique, such as spalling and cracking. Low cost and short-term traffic disruption, for the application of this method has been reported.

This repair technique can restore the deteriorate mortar joints to its initial condition, but cannot be beneficial in terms of load capacity. In addition, is an invasive method due to the excavation of the bed joints.



FIGURE 2.9: Application of bed joint steel reinforcement technique at the church of St. Giustina (Padua, Italy) (Valluzzi et al., 2005)



FIGURE 2.10: Application of bed joint steel reinforcement technique at the church of St. Sofia (Padua, Italy) (Valluzzi et al., 2005)



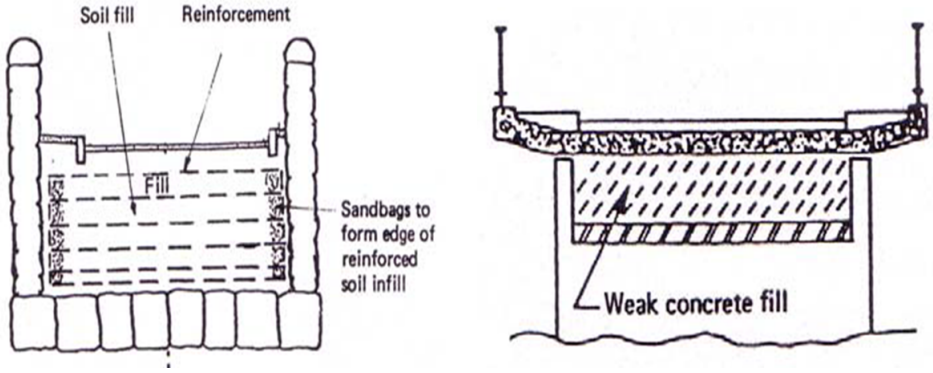
FIGURE 2.11: Repointing of the joints (Apreutesei et al., 2006)

2.8 Rebuilding bulging spandrel wall

The rebuilding bulging spandrel/wing walls technique requires excavation behind the wall and rebuilding it using concrete material. However, a reinforced earth system was adopted, to prevent inconsistent structural response and increased pressure at the spandrel wall (see Fig. 2.12). This method results in disruption of the structure due to the required excavation, but the compatible reinforced system adopted can restore the integrity of the structure without additional damage.

2.9 Surface treatment

Treatment of the surface can be performed using ferrocement, reinforced plaster and shotcrete (see Figs. 2.13). Ferrocement comprises layers of fine steel rebars embedded in a high strength cement mortar layer of 10-50 mm thickness. Typical mortar mix consists of one part cement, 1.5-3 parts sand and approximately



(a) (b)

FIGURE 2.12: Strengthening of the arch A_1 (a) anchor scheme and (b) horizontal anchors (Apreutesei et al., 2006)

0.4 water to cement ratio (Montes and Fernandez, 2001). Steel connectors are installed on the wall to enable new and existing elements work together. The mechanical properties of ferrocement mainly depend on the mesh properties. Ferrocement is applied at the most accessible areas e.g., inside or outside of the building, and at one or both faces of the wall to increase walls shear resistance, lateral stiffness and ductility for in- and out-of-plane applications (ElGawady et al., 2004; Corradi et al., 2008; Meireles and Bento, 2013). It can be used for low cost housing, due to their ease of application, and the no need of skilled workers.

Reinforced plaster is composed using a thin layer of cement plaster in combination with high strength steel reinforcement in diagonal, vertical and horizontal arrangement (Sheppard and Tercelj, 1980). The strengthening layer thickness can modify the strength of the plaster and the in-plane resistance can be increased by 1.25-3 times as reported in Sheppard and Tercelj (1980).

In addition, shotcrete is sprayed on a masonry wall over a mesh of reinforcing bars (ElGawady et al., 2004). The minimum thickness used is 60 mm and the chosen thickness depends on the seismic demand. Shear dowels are used



(a) (b)

FIGURE 2.13: (a) Masonry wall strengthened with steel mesh (b) Spraying cement grout (Meireles and Bento, 2013)

to transfer the shear stress across masonry-shotcrete interface (Karantoni and Fardis, 1992; Miha, 1999). This method can increase the load capacity of URM by 6 to 25 times (Kahn, 1984).

Surface treatment techniques can provide increased load capacity by 1.25-25 times according to the chosen strengthening, and a relatively low thickness of 60 mm is applied on the structure. On the other hand, the steel connectors used to keep the steel mesh in position, can be invasive for the masonry structure.

2.10 Centre core technique

The centre core method comprises a grouted core placed at the centre of the wall. For this purpose, a hole of 50-125 mm diameter is drilled from the top to bottom of the wall using the oil-well drilling technique. Then the reinforcement is applied in the centre of the hole and a filler material (epoxy, cement and polyester) is used to fill the core. This method provides a homogeneous structural element with the capacity to resist both in-plane and out-of-plane loading.

Experimental results of Plecnik et al. (1986) showed that cement grout resulted in 30% weaker specimens compared to sand/ epoxy or sand/ polyester grouts. However, due to the material price, sand to polyester volume ratio between 1:1 and 2:1, was suggested to be used. It was reported that the centre core technique can increase the resistance of masonry walls by two times (Abrams and Lynch, 2001). However, it comprises an intrusive method, since drilling of the wall is required.

2.11 Saddling

Saddling strengthening technique comprises fill excavation towards the springing level and casting of an in-situ concrete at the extrados of the arch. Application of concrete is performed either monolithically with various cross-section thickness (Fig. 2.14), or with a uniform thickness as shown in Fig. 2.15. A 150 mm -200 mm was reported as a typical concrete thickness dimension. Transverse brickwork or transverse debonding lamina can be combined with the concrete application if is required. Also, polypropylene and stainless steel fibers can be used to prevent surface cracking and provide increased strength, respectively. After the application of the strengthening material, the concrete saddle and the existing arch are designed to have a composite response, which results in improved distribution of loads and increased effective thickness.

Increase of the abutments capacity is necessary, with either piled foundations or spread footing behind the abutments. In addition, application of concrete can modify the nature of the bridge and can cause severe hazard on the original masonry arch (e.g falling of masonry blocks). Also, it requires major

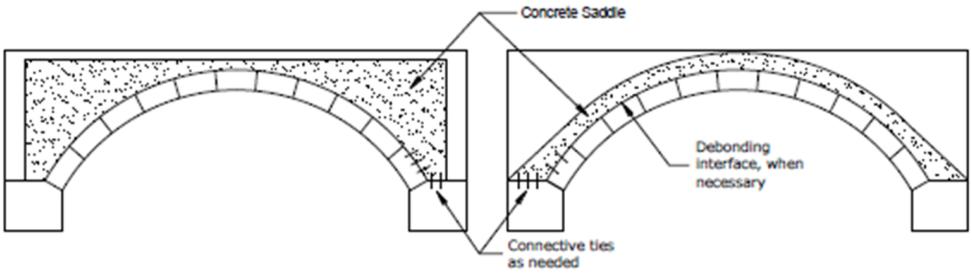


FIGURE 2.14: Concrete saddles using varying cross section thickness (Beuerman, 2009)

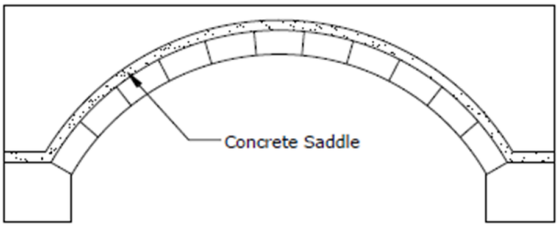


FIGURE 2.15: Concrete saddle of uniform thickness (Beuerman, 2009)

construction works resulting in disruption of the traffic for long period. However, increased effective thickness and improved distribution of loads are obtained after the application of this technique.

2.12 Stitching longitudinal cracks

Stitching longitudinal cracks is a strengthening method for bridge arches, used as an alternative of saddling method, when long-term traffic disruption cannot occur. The cores of alternate voussoirs are cored laterally in a diameter of 30 mm and kept to be used at the last step of the strengthening application. Then, a hole is drilled normal to the spandrel at mid-depth of the arch ring at a length of 750 mm. A maximum drilling length of 12 m was reported. Then a CINTEC-type hollow stainless steel bar, with an enclosing sock is installed and the grout

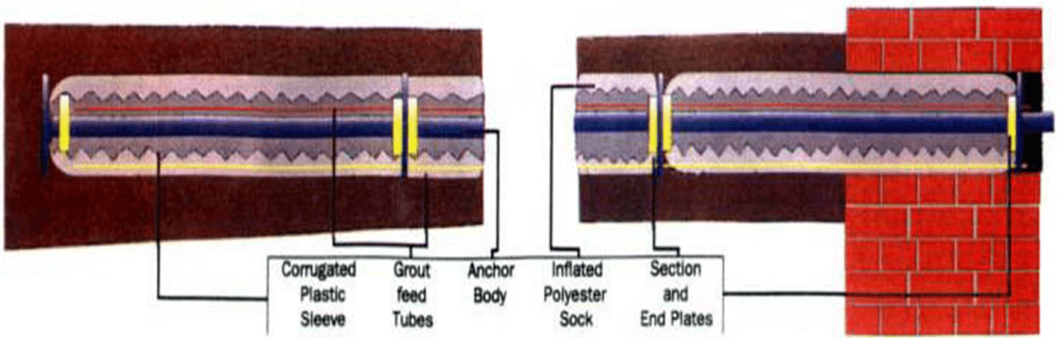


FIGURE 2.16: CINTEC anchorage system (Apreutesei et al., 2006)

is injected to fill the sock. Pressure is indicated at the position of the cracks and the cores of the stones are reinserted to cover the holes which have been drilled (see Fig. 2.16). It is an extremely invasive method due to that drilling of cores in voussoirs is required. However, it can be used without the need of long-term traffic disruption.

2.13 Replacing units

Masonry units can be damaged due to local stresses developed e.g at the edge of the masonry arch. Therefore, replacement of masonry units is required to prevent deterioration of the arch, by taking into account the mechanical properties, the colour, and the arch appearance. A temporary formwork is necessary to be installed to keep the structure stable without causing any movement. This method can be combined with repointing of the mortar joints and grouting (Beuerman, 2009). Replacing units can be performed at low cost without the need of a long-term traffic disruption. However, is an intrusive method and also requires to use compatible materials which is not always easy to find.

2.14 Sprayed concrete

Sprayed concrete strengthening technique is usually applied at the intrados of the arch with reinforcing mesh at a thickness of 150 mm and 300 mm. It can provide increased load capacity, stabilize and protect the masonry structure (see Fig. 2.17). Additional abutment support is required for the sprayed concrete arch as shown in Fig. 2.18.

It can be applied in three different ways, namely, dry, wet, and composite. Dry process uses batched cement and surface-dry aggregates of 10 mm maximum size at a low water to cement ratio of 3.4-4:1 without slump. The compressive strength attained in 28 days is 30-50 MPa.

The wet process is a pre-mixed concrete which is pumped at high air pressure with maximum aggregate size of 20 mm. A similar compressive strength value of the dry process (30-50 MPa) can be obtained after 28 days of the application.

The composite concrete is pre-mixed comprising concrete, aggregates, water and loaded into a placing machine as a wet mixture. This method results in better control of concrete quality and water to cement ratio compared to the wet process. In addition, lower water to cement ratio and higher velocity with the dry process can be achieved using the composite technique.

The sprayed concrete cannot be applied in a degraded area because can cause further damage of the structure. Therefore, the condition of the arch is required to be considered before the application of this method. In addition, the sprayed concrete is lower than the saddle method due to excavation is not needed. Application of the method require closure of the road until the concrete gain its strength (Beuerman, 2009).



(a) (b)

FIGURE 2.17: Application of sprayed concrete on masonry arches (Page, 1996)

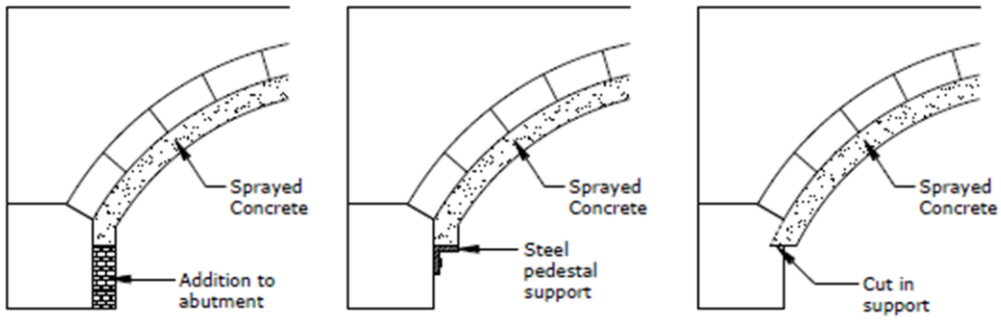


FIGURE 2.18: Abutment support for strengthening with sprayed concrete method (Beuerman, 2009)

The final thickness of the sprayed concrete is significant (150-300 mm) and can decrease the available space under the arch bridge or a masonry structure. However, it can effectively increase the load capacity and stability of the masonry structure.

2.15 Prefabricated liner

The prefabricated liners is a strengthening technique used at the intrados of masonry arches, which combines corrugated metal or glass with reinforced cement (see Fig. 2.19). Concrete or grout is used to fill the space created between the metal and the masonry but also the existing cracks, voids and missing mortar.

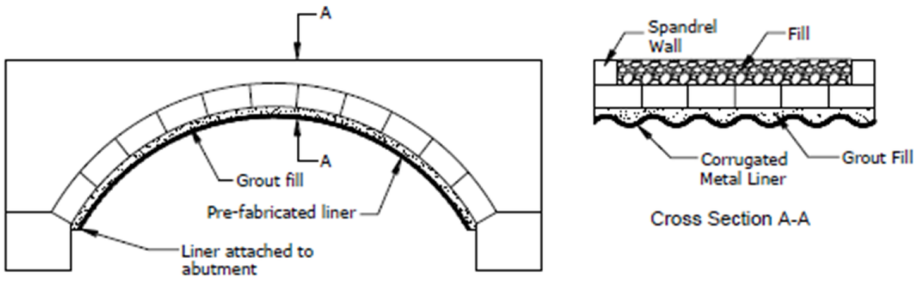


FIGURE 2.19: Application of the prefabricated metal liner method (Beuerman, 2009)

The following procedure is required to be performed for a successful application of this method.

- The arch shape is surveyed to ensure that there is the required space for the application of concrete.
- A unique shape of the prefabricated liner is manufactured for each arch.
- The prefabricated liner is supported on the structure at the springer level or by using anchor bolt system.
- The concrete is either injected or poured by means of chutes.
- For a successful strengthening application all the voids should be filled by concrete.

This strengthening method can increase effectively the load capacity of the arch and the traffic disruption will be short term. However, a reduced space under the arch will be obtained after the application of the strengthening material. In addition, corrosion of the corrugated metal can be occurred, which cannot be prevented even by using coating material.



(a) (b)

FIGURE 2.20: (a) Clifton bridge (b) Ambersham bridge (Brookes and Tilly, 1999)

2.16 Archtec strengthening method

Brookes and Tilly (1999) proposed an internal strengthening system for masonry arch bridges, namely Archtec, which was tested in a full scale laboratory model by the Transport Research Laboratory (TRL). Stainless steel reinforcing bars were inserted and grouted into the masonry. Both bars and grout were inserted into a 'sock' to ensure that the surrounding masonry will not be deformed or damaged by the grouting pressure. The steel rebars were positioned in the longitudinal direction and tangential to the curvature of the arch. Transversal reinforcement was applied according to the condition of the structure.

The Archtec method was implemented in 12 masonry arch bridges in the field of different materials and geometries. Assessment and strengthening of three bridges were reported, the Ducie Street Bridge (Manchester), the Ambersham bridge (West Sussex) (Fig. 2.20b) and the Clifton Bridge (Scottish Borders) (Fig. 2.20a), using the proposed method.

The difficulties reported during the application of the method, comprising damage of the drilled holes to insert the steel rebars and the position of the reinforcement. In particular, the position of the reinforcement was designed to avoid the gas, water, electricity and telecommunication services, which were located under the footways. In addition, this method was examined using numerical analysis on the tested specimens using the ELFEN nonlinear discrete element program, to provide an accurate analysis on the strength of masonry arch bridges.

It is an intrusive method due to drilling of holes on the masonry substrate, but enhanced durability and load capacity can be provided by this method.

2.17 Case studies on strengthening of masonry arches

Oliveira and Lourenco (2004) described the strengthening procedure proposed on two damaged stone masonry bridges in Portugal, according to the inspection performed to asses their damage condition. The first case study was on Boutaca bridge, built in 1860 in Batalha, and supported by six pointed masonry arches equally spanned (Fig. 2.21). The condition of this masonry arch was the following:

- Vegetation growth and humidity.
- Lost of plaster and painting in large areas of the bridge.
- Minor longitudinal cracking at the intrados and cracking in the buttresses, due to lateral forces developed through the fill by dead and live loads.
- Four metallic rods endowed with anchorages were detected only at one side of the bridge to bind the walls, which were significantly corroded and deformed (Fig. 2.22).



FIGURE 2.21: Boutaca bridge (Oliveira and Lourenco, 2004)

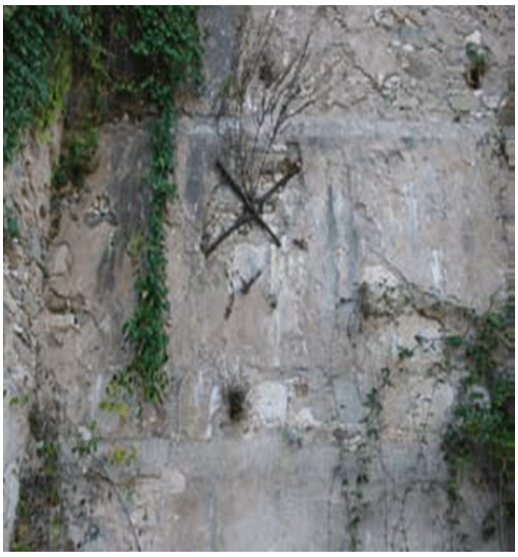
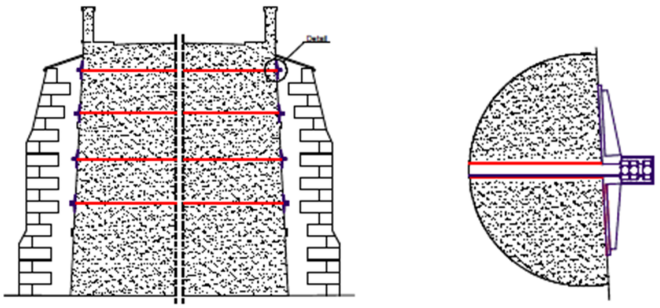


FIGURE 2.22: Corroded anchorage (Oliveira and Lourenco, 2004)

- Outward movement of masonry walls was detected by deformed anchorages and cracked buttresses.

The following strengthening procedure was recommended on the Boutaca bridge, taking into account the architectural heritage guide:

- Install a set of horizontal anchors across the width of the road, endowed with patress plates.
- Application of four vertical aligned tie rods between the two buttresses, where two cylindrical stainless steel patress plates are tightened up (Fig. 2.23), using a dynamometric wrench to apply a low force to the tie rods.
- Repair of the slight cracked masonry arches was not adopted, but a visual inspection proposed, periodically.



(a) (b)

FIGURE 2.23: Masonry walls strengthening (a) View (b) Detail of the patress plate (Oliveira and Lourenco, 2004)

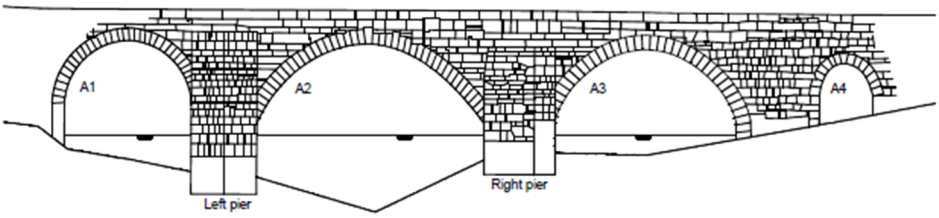


FIGURE 2.24: Donim Bridge (Oliveira and Lourenco, 2004)

The second bridge was the Donim bridge in Guimaraes, which was built in the 16th century with a flat roadway and supported by three semicircular stone masonry arches, of different spans (Fig. 2.24). The following damages were detected:

- Extensive longitudinal cracking at the intrados of the arches A_1 and A_4 (Fig. 2.25).
- A damaged right pier, with cracked stone blocks and a missing foundation stone.
- A severe damage on the right cutwater due to high vegetation developed all over the bridge.
- The spandrels walls were subjected to lateral movement, due to lack of maintenance and increased heavy loads.

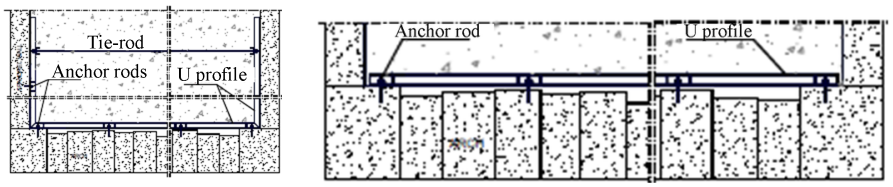


(a) (b)

FIGURE 2.25: Cracking of the arches (a) A_1 and (b) A_4 (Oliveira and Lourenco, 2004)

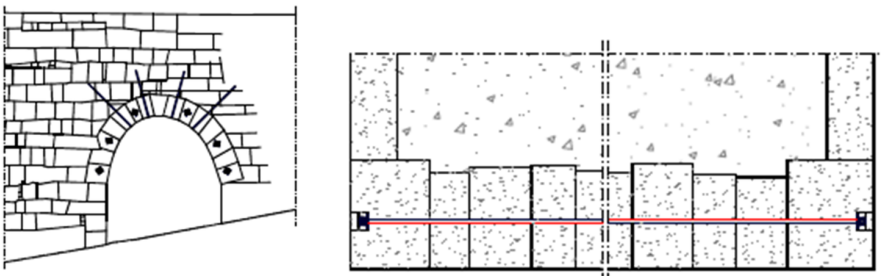
After numerical analysis, topographic survey, and visual inspection, strengthening of the bridge arches (A_1, A_4) and cutwater of the right pier was recommended to be performed. In particular, the application of rope-stretchers along the intrados of the arch can reduce the cracking observed on A_1 arch (Fig. 2.24). This method can be achieved after the application of props under the entire span before removing the infill. The strengthening system comprised six stainless steel U-shaped profiles at the extrados of the arch and at both spandrels walls using anchor rods (Fig. 2.26). The stainless steel tie-rods were suggested to be applied at the top of the vertical profile and tightened using dynamometric wrench to bind the spandrels walls together and reduce bending of the profile. The U-profile was clamped on the arch with anchor rods at the vicinity of the crown, due to the accessibility of the pavement. After completion of the strengthening procedure, the infill can be applied back in position and the props can be removed.

In the case of A_4 arch, the strengthening was proposed to prevent any further spreading of the arch and preserve its stability. Rehabilitation of the arch



(a) (b)

FIGURE 2.26: Strengthening of the arch A_1 with U profiles (a) in general and (b) close to the crown (Oliveira and Lourenco, 2004)



(a) (b)

FIGURE 2.27: Strengthening of the arch A_4 (a) anchor scheme and (b) horizontal anchors (Oliveira and Lourenco, 2004)

includes the application of six horizontal anchors at the full width of the bridge, endowed with cylindrical anchorage plates at each side of the arch (see Fig. 2.27). For each anchor, a stainless steel rod is placed in a drilled hole and grouted with a cement solution by injection under low pressure. To assure the connection between arch voussoirs and spandrel walls, four stitching anchors are applied at each side of the arch, as shown in Fig. 2.27a. The damaged cutwater, comprised cracked stones, out of their original places. It was recommended to rebuild it using similar stones from the region, and replace the missing foundation with a stone block. In addition, the de-gradated mortar joints should be cleaned and repointed using sand-lime mortar.

2.18 Concluding Remarks

It is evident that over the last 30 years several methods have been used in practice to repair, maintain and strengthen old existing masonry structures such as historical monuments and bridge arches. Main advantages are the documented increase in strength and deformability, to prevent further deterioration of the structure. Main drawbacks are that in practice all of the cases, they require extensive labour, craftsmanship and in several cases such as saddling, sprayed concrete, and prefabricated liner have a significant footprint in the final structure, which can significantly modify the nature of the structure. In particular, in the saddling method, major construction work is required including fill excavation and concrete casting. In addition, saddling, sprayed concrete and the prefabricated liner result in increased thickness of the strengthening material. Another drawback is the corrosion of the strengthening material used in several cases (prefabricated liner, tie-columns and tie beams).

A key requirement in structural strengthening, especially in the case of old structures is to impose minimum disruption in the structural form for both historical but also aesthetic reasons. Conventional methods comprise several invasive techniques, where drilling of masonry is required (NSM, injections, centre-core, joint repointing, saddling, stitching longitudinal cracks) or replacement of the masonry units. A second requirement is that the materials used have to be as much compatible as possible which is not the case when one is using, e.g., concrete or steel ties. An additional requirement for the conventional strengthening methods, is that several conventional methods namely joint repointing, sprayed concrete, tie columns/beams, post tensioning require good condition

of the structure before the application of the technique to prevent further damage of the structure.

Chapter 3

Strengthening based-on high-strength composite materials

3.1 Introduction

High strength composite materials provided the perfect means for achieving small footprint strengthening solutions with their high strength-to-weight ratios. Main advantages are the high stiffness, corrosion resistance, the quick site application, and their availability in long lengths which can prevent lapping of joints. In particular, the research is moving towards Fibre Reinforced Polymers (FRP), which comprise unidirectional, continuous fibres bonded with epoxy resin and the Textile Reinforced Mortar (TRM) or Fibre Reinforced Cementitious Matrix (FRCM), which combines textile fibres in two orthogonal directions with inorganic matrix (e.g. cement based mortar). The fibre textile materials used are the glass, carbon, basalt, aramid and kevlar.

3.2 FRP and TRM strengthening of masonry structures

FRP application was initially introduced to replace the application of the steel plates strengthening technique, due to the corrosion observed at the steel and substrate interface. FRPs are applied on the structure in the form of thin laminates, sheets or fabrics. They are made of unidirectional, continuous fibres such as glass, carbon, basalt, aramid and Kevlar, bonded together with an epoxy resin or polyester. The resin transfers the load between the fibres, and the fibres carry the load (Triantafillou, 1998a; Ehsani et al., 1999). The FRP composite is reported in several applications in the literature for strengthening masonry structures as externally bonded composites or Near Surface Mounted (NSM) FRP bars (see Fig. 3.1) (Sweidan, 1992; Schwegler, 1994; Triantafillou and Fardis, 1997; Triantafillou, 1998b; Galati et al., 2006; Hamoush et al., 2001; Valluzzi et al., 2003; Kuzik et al., 2003; Ehsani et al., 1993; Hamed and Rabinovitch, 2010; Turco et al., 2006).

Despite the effectiveness of the FRP composites, the inorganic matrix is more compatible with the mechanical properties of the masonry substrate compared to the polymeric resins, and provides durability in aggressive environments. In view of the aforementioned, an innovative mineral-based composite material, the textile-reinforced mortar (TRM), has been proposed for structural retrofitting, which comprises layers of textiles made of e.g. carbon, glass, basalt fibres, poliparafenilenbenzobisoxazole (PBO) or natural fibres impregnated with inorganic matrices, such as the cement-based mortars. The acronym 'FRCM' is also used in the literature for the same material (Carloni et al., 2016; Ascione et al., 2015; Lignola et al., 2017; Carozzi and Poggi, 2015). The fibre textiles used



(a)



(b)

FIGURE 3.1: (a) FRP application on masonry vault at the University of Padova (Giaretton et al., 2016) (b) GFRP application on masonry wall (Kalali and Kabir, 2012)

typically consist of fibre rovings in at least two orthogonal directions, thus creating an open-mesh geometry. Due to the use of mineral-based mortars TRM offers resistance at temperatures of up to 250 ^{0}C (Tetta and Bournas, 2016; Raoof and Bournas, 2017b) or even 400^{0}C (Raoof and Bournas, 2017a), compatibility with concrete and masonry substrates (Raoof et al., 2016), ability to be applied on wet surfaces and low temperatures, and air permeability.

Another group of composite materials, applied on existing masonry structures that uses ultra high strength steel filaments twisted to form cords are the Steel Reinforced Polymer (SRP) impregnated in epoxy resin and the Steel Reinforced Grout (SRG) impregnated in an inorganic matrix (Casadei et al., 2005; Huang et al., 2005; Cancelli et al., 2007; Borri et al., 2009; Carozzi et al., 2017a).

The main types of fibres utilised in civil engineering are the glass, aramid, carbon and basalt fibres. Glass fibres are classified in three categories according to their alkali resistance response (E-glass fibre, S-glass and AR-glass fibres). E-glass fibres have low alkali resistance, whereas AR-glass is an alkali resistance material. Aramid fibre is anisotropic, can provide higher strength and modulus of elasticity and the diameter of fibre is 12 μm. Carbon fibres are produced using pitch or PAN as raw material. For the pitch fibres refined petroleum or coal pitch is used whereas in case of PAN fibres polyacrylonitrile is carbonised through burning. The pitch-type carbon fibre have a 9-18 μm diameter, whereas the PAN-type 5-8 μm. The pitch-type carbon fibres are used in general purpose applications and can provide high strength and elasticity. In addition, PAN-type carbon fibres produce high strength and elasticity materials (Fib Bulletin, 2001). Additionally, fibre-textile materials have been used recently for TRM applications are the PBO (Alecci et al., 2016; Carozzi and Poggi, 2015; Donnini et al., 2016) and natural fibres namely flax and hemp (Olivito et al., 2016; Cevallos

et al., 2015; Valluzzi et al., 2014).

The TRM has been used as a strengthening and seismic retrofitting material for several applications on reinforced concrete and masonry structures. In particular, reinforced concrete applications were reported (Al-Salloum et al., 2011; Triantafillou et al., 2006; Bournas et al., 2007; Tetta and Bournas, 2016) and a number of experimental studies have been performed to investigate the in-plane response of TRM strengthened masonry walls, (Papanicolaou et al., 2011; Faella et al., 2004; Prota et al., 2006; Papanicolaou et al., 2007; Augenti et al., 2010; Bernat et al., 2013; Parisi et al., 2013; Cevallos et al., 2015; Noor-E-Khuda et al., 2016; Almeida et al., 2015). In particular, Prota et al. (2006) studied the in-plane response of tuff masonry panels strengthened with cementitious grid system. Papanicolaou et al. (2007) tested TRM strengthened hole clay-brick masonry walls under cyclic in-plane loading and Bernat et al. (2013) examined the in-plane compressive eccentric load of solid clay brick masonry walls. It was concluded that increase of strength and deformability was achieved after applying the composite material in each strengthening configuration. In addition, the bond behaviour between the TRM material and masonry was investigated by Faella et al. (2009), DAmbrisi et al. (2013) and De Felice et al. (2014). Furthermore, the effectiveness of TRM, was also investigated in few experimental studies reported for strengthened masonry arches at the extrados of the arch with the TRM composite material (Garmendia et al., 2011; Alecci et al., 2016; Garmendia et al., 2015). Analytical models have also been developed to further highlight the mechanical response of TRM strengthened systems (Koutas et al., 2014; Wang et al., 2017).

3.3 Bond between TRM and masonry substrates

The bond behaviour of the TRM composites on the masonry substrate has been investigated in several research studies using single- or double- lap test setup. The single-lap test setup was implemented in (De Felice et al., 2014; DAmbrisi et al., 2013; Ascione et al., 2015; DAntino et al., 2015; De Santis and Felice, 2015; DAntino et al., 2016; Maroudas and Papanicolaou, 2017; Carozzi et al., 2017b; Caggegi et al., 2017; Lignola et al., 2017; De Santis et al., 2017; Leone et al., 2017; Ombres et al., 2018; De Felice et al., 2018) and the double-lap setup in (Sneed et al., 2015; Raoof et al., 2016; DAmbrisi et al., 2013; Malena and Felice, 2014; Carozzi and Poggi, 2015; Alecci et al., 2015; Askouni and Papanicolaou, 2017; Askouni and Papanicolaou, 2019; Olivito et al., 2016; Carozzi and Poggi, 2015; De Felice et al., 2014).

In particular, Sneed et al. (2015) studied both single- and double-lap shear tests on reinforced concrete specimens strengthened with polyparaphenylene PBO-FRCM. They reported that in single-lap shear test setup the load is applied directly to the fibre-textile and not through strain or displacement measurements, which provides an unmistakable identification of the load. However, a crucial aspect is the alignment of the specimen in such position to develop pure stresses on the reinforcement without any normal stresses on the substrate-mortar interface. Also, the misalignment of the textile results in eccentricity of the applied load with respect to the support and in out-of-plane force components resulting in friction and peeling-off of the composite (DAntino et al., 2016). On the other hand, in double-lab configuration debonding did not occur at the same time in both sides, which resulted in slightly decreased values of the maximum load, compared to the corresponding values of the single-lap

test setup, when the bond length was larger than the effective bond length. In addition, cracking was observed after the maximum load was attained, which resulted in out-of-plane phenomena as described in Askouni and Papanicolaou (2017).

Maroudas and Papanicolaou (2017) investigated the response of the alkali resistant (AR) glass fibre textile TRM composite on a single-lap experimental setup for different bond lengths between 50-250 mm. A common failure mode was observed in all the specimens, namely slippage of the fibres at the textile-matrix interface. In particular, in case of 250 mm bond length a combined failure mode of slippage and fibre rupture was reported. The maximum load was increased by increasing the anchorage length from 50 mm to 200 mm, and then remained constant. Therefore, the effective bond length was determined equal to 200 mm.

Ascione et al. (2015) used a single-lap test setup to investigate the bond behaviour of basalt-steel, carbon, glass-aramid, and steel textiles using cement or lime mortars. The bond length used was 200 mm in all specimens. Different failure modes observed in each fibre textile. In particular, the specimen with basalt textile failed due to textile rupture within the bonded length, the specimen with carbon fibre textile due to sliding of the textile within the matrix, whereas glass-aramid due to textile rupture in the un-bonded region. In addition, debonding between masonry substrate and strengthening material was observed in case of using cement-based mortar with steel mesh, whereas in case of using lime mortar debonding at the mortar-substrate interface occurred.

DAmbrisi et al. (2013) performed bond tests using the double-lap test setup with carbon FRCM material on different bond lengths of 110 mm, 230 mm and

350 mm. The failure mode observed was cracking followed by fibre-matrix slippage. The effective bond length was defined equal to 110 mm, since the maximum recorded load was not increased when the bond length was increased from 110 mm to 350 mm.

Carozzi et al. (2014) investigated the behaviour of a push-pull double-lap test setup using glass fibre-textile with cementitious or lime mortar on three different bond lengths, namely 50 mm, 100 mm, and 150 mm. When cementitious mortar was used with glass fibre-textile, slippage was observed on the short bond lengths, whereas for longer bond lengths tensile rupture occurred. By increasing the bond length the maximum load was increased, therefore the effective bond length defined as 150 mm. In addition, in case of using lime mortar with glass fibre-textile, debonding occurred for the 100 mm bond length and textile rupture for 150 mm bond length.

De Felice et al. (2014) studied the behaviour of carbon TRM (CTRM), steel reinforced grout (SRG), and basalt TRM (BTRM) using single and double-lap experimental setup. The BTRM composite resulted in debonding at the substrate-mortar interface for the shortest bond length, whereas the longest bond length resulted in slipping of the textile within the mortar. A minimal increase on the maximum recorded load was observed when different bond lengths were adopted, therefore a reliable effective bond length was not derived in this case. The CTRM specimens failed due to sliding of the fibres within the matrix, in case of the shortest bond lengths (55 mm, 110 mm), whereas the longest bond length of 220 mm resulted in debonding at the fibre-matrix interface. When the intermediate bond length used, namely 165 mm, a combined failure mode occurred including debonding and sliding of the fibres within the matrix. Therefore, the effective bond length defined as slightly higher than 165 mm. The

specimens strengthened with the SRG composite material exhibited debonding at the substrate-matrix interface and the effective bond length in this case determined equal to 220 mm, which was higher compared to the CTRM effective bond length.

Carozzi et al. (2017b) investigated the bond behaviour of carbon fibre textile of different geometry, mass, density, yarn treatment and mechanical properties using a single-lap test setup and a bond length equal to 260 mm. Coating was only applied in the external part of the yarns without impregnation of the internal filaments. The dominated failure modes observed was slippage of the textile within the matrix and rupture of the textile. The failure modes observed among specimens of similar group were different in some cases (e.g., C_FRCM_1, C_FRCM_2, C_FRCM_3).

Lignola et al. (2017) examined the bond behaviour between the coated basalt FRCM composite (of different geometries and densities) and the masonry substrate using a single-lap test setup. Lime and cement-based mortar was used for comparison. The bonded length was equal to 260 mm and the bond width varied between 50 mm and 125 mm. The failure modes observed were (i) partial debonding and textile rupture, (ii) slippage within the mortar matrix and textile rupture, (iii) cracking of mortar and (iv) textile rupture.

Leone et al. (2017) examined the bond behaviour between the glass TRM and the masonry substrate using the single-lap and double-lap test setup. Different types of glass textile were used of different geometry, density, grid spacing and mechanical properties. In addition, cement/lime-based mortars and bond enhancing agents were used. The bond length was mainly 260 mm and in few cases was modified to 120 mm, 180 mm and 240 mm.

The failure modes observed were the following:

- slippage/ textile rupture
- debonding with cohesive surface of the substrate/slippage
- debonding at the textile to matrix interface/slippage
- textile rupture/slippage
- slippage
- slippage with cracking
- textile rupture

The data obtained in this study contribute significantly in better understanding of the properties and the bond behaviour of the glass FRCM materials with masonry structures. However, different failure modes occurred among specimens of the same group in some cases (e.g., group A, E, H), and different results among single and double-lap test setup were obtained due to different accuracy in the misalignment of all the rovings with respect to the loading direction. This demonstrates the need for further experimental work to establish standard procedures to investigate the bond behaviour between glass FRCM and masonry substrate.

Ombres et al. (2018) used the single-lap test setup to examine the bond behaviour between the carbon FRCM composite material and the masonry substrate using different bond lengths (150 mm, 200 mm, 250 mm, 300 mm). The failure mode observed was slippage between the fiber yarns and the matrix. The effective bond length obtained was 100 mm.

Alecci et al. (2015) studied the effectiveness of the double-test setup on three different materials, namely carbon, PBO and glass FRCM using different bond lengths of (150-250 mm). They concluded that carbon and PBO bond behaviour

was not influenced by the different bond length, therefore the effective bond length defined less than 150 mm. On the other hand, glass FRCM demonstrated a higher effective bond length between 150-200 mm. In addition, in terms of the maximum load attained, carbon resulted in the highest maximum load, whereas glass material resulted in the lowest. The failure mode observed in all cases was debonding of the composite at the fibre-matrix interface after cracking and also fiber-matrix slip occurred.

Carozzi and Poggi (2015) investigated the response of different fibre-textile materials, namely glass FRCM, carbon FRCM, PBO, and glass PBO (PBO-G) on a push-pull double-lap test setup. In case of the specimen strengthened with Glass FRCM the maximum load was increased by increasing the bond length resulting in an effective bond length equal to 150 mm. The failure mode observed was slippage in case of short bond lengths (50 mm, 100 mm) and textile rupture when the bond length was increased to 150 mm. On the other hand, the carbon FRCM response was not influenced by the different bond length and the failure mode observed was slippage between mesh-matrix interface. In addition, the maximum load obtained in PBO composite was not influenced by the bond length and a progressive failure of the rovings was observed. When glass textile was used with PBO, PBO-G composite demonstrated lower maximum load compared to PBO and also the maximum load remained constant for different bond lengths. In addition, the failure mode reported was rupture of the glass fibres followed by partial rupture of PBO fibres.

Askouni and Papanicolaou (2017) studied the bond behaviour of AR-glass fibre textile TRM composite on a double-lap test setup using various bond lengths of 50-250 mm. The dominated failure mode observed was textile slippage within

the mortar and the effective bond length determined equal to 125 mm. A similar value of effective bond length equal to 150 mm was reported in Carozzi and Poggi (2015), but with different failure mode, namely textile rupture. On the other hand, Maroudas and Papanicolaou (2017) which used a single-lap setup reported a higher effective bond length equal to 200 mm, and textile slippage failure mode. Alecci et al. (2015) also concluded to an effective bond length between 150-200 mm, where slippage of the textile occurred. In addition, Leone et al. (2017) concluded that in some groups where similar specimens were tested different failure modes were observed. Different effective bond length and failure modes observed for the glass FRCM composite, which shows that further research should be conducted due to the high variability of the experimental results.

Donnini et al. (2016) investigated the response of carbon fibre textile on a double-lap/single prism test setup using different epoxy-resin textile impregnation and a constant bond length of 150 mm. The failure modes observed were textile rupture and slippage of the textile within the mortar according to the epoxy resin impregnation level. In particular, textile rupture occurred when high level of epoxy resin was used, whereas slippage of the textile was observed, for low resin impregnation.

Olivito et al. (2016) investigated the behaviour of Natural Fibers Reinforced Cementitious Matrix (NFRCM) and synthetic Fabric Reinforced Cementitious Matrix FRCM composites using two different bond lengths of 50 mm and 100 mm on a double-lap test setup. Two different materials were used, namely flax and PBO-FRCM. They concluded that PBO-FRCM of 100 mm resulted in a slightly higher bond stress, compared to the corresponding specimens with flax-FRCM. In addition, it was found that both composite materials failed due to progressive

textile rupture, where the exploitation of Flax-FRCM defined as 60%, compared to the lower value of PBO-FRCM composite which was 20%.

Several experimental studies included carbon fibre textile (Ascione et al., 2015; DAmbrisi et al., 2013; Alecci et al., 2015; Donnini et al., 2016; De Santis et al., 2018a; Ombres et al., 2018), where the most common failure mode was slippage of the textile within the mortar. In Carozzi et al. (2017b) the dominated failure modes observed were slippage and textile rupture. In some cases, different failure modes observed among specimens of similar groups. It is clear that further studies should be conducted with additional coating materials to improve the performance of carbon textile. Addition of different types of coating on carbon fibre textile has been reported in Donnini et al. (2016) but only a single bond length of 150 mm was used. A failure mode of slippage of the textile within the mortar combined with textile rupture was observed. Therefore, further research on the coating materials of the carbon textile need to be conducted, to prevent and modify the slippage failure mode.

The bond behaviour between the basalt TRM and masonry substrate has been investigated in Lignola et al. (2017) and De Felice et al. (2014). De Felice et al. (2014) used 2 layers of BTRM and the maximum load attained was not increased by increasing the bond length, therefore an effective bond length was not derived. Lignola et al. (2017) performed an extensive work on different types of basalt textiles using a bond length equal to 260 mm. Therefore, additional study on the basalt composite can be conducted using different bond lengths to provide further results in terms of failure mode and effective bond length.

3.4 Out-of-plane strengthening of masonry walls with TRM

Previous experimental studies on the out-of-plane behaviour of masonry walls highlighted the substantial gain in strength and deformability due to TRM reinforcement. In particular, Kolsch (1998) examined the performance of masonry walls strengthened with three layers of a unidirectional Carbon Fiber Cement Matrix (CFCM) combined with a polymer modified mortar, and tested under cyclic loading. The author demonstrated that such an approach prevents the partial or complete collapse of the strengthened structure.

Papanicolaou et al. (2008) investigated the influence of the number of carbon fibre textile TRM layers, namely 1 and 2 on medium scale clay brick masonry walls tested under out-of-plane cyclic loading. It was observed that such a configuration resulted in a shear-flexure failure mode followed by debonding at the brick-bed joint interface. Increasing the number of layers has been found to result in a 25% increase of the maximum load. They concluded that TRM strengthening system is a promising solution in terms of strength and deformation capacity.

Papanicolaou et al. (2011) studied the out-of-plane cyclic response of medium scale clay and stone brick masonry walls strengthened with one layer of bitumen coated glass, basalt, carbon and coated basalt TRM composite. The authors demonstrated the superior performance of coated glass textile TRM systems compared to the uncoated basalt, by avoiding textile slipping that was the predominant mode of failure in the non-coated basalt strengthened specimen. They also reported that the transition from 1 to 2 layers of carbon TRM layers resulted in a significant increase of the load bearing capacity.

Harajli et al. (2010) studied the out-of-plane response of masonry walls built with brick, hollow concrete block or sandstone masonry stones. Masonry walls were strengthened with a single layer of coated glass and coated/ uncoated basalt textile TRM, which were tested under both monotonic and cyclic loading.

The authors concluded the following:

- All the TRM strengthened specimens demonstrated improved load and deformation capacity in both static and cyclic loading.
- The coated glass textile TRM demonstrated improved performance in terms of load (35.5%) and deformation capacity (61.5%) compared to the uncoated basalt fibre textile, due to the resulting uniform strain distribution. Conversely, in the uncoated basalt fibre textile a single predominant crack was formed leading to the local fracture of the textile.

Babaeidarabad et al. (2013) examined the out-of-plane cyclic loading on clay brick masonry walls strengthened with one and four layers of carbon textile TRM. The authors demonstrated that for lower reinforcement ratios the dominant failure mode was textile rupture, whereas for high reinforcement ratios shear failure preceded flexural failure due to over-strengthening of the specimen. They also observed, increased deformation capacity for the lower reinforcement ratio, compared to 4 layers of TRM composite material. The failure modes observed contradict with Papanicolaou et al. (2008), where debonding of the textile occurred in the similar case of both 1 and 2 layers of carbon TRM. This shows that additional tests on carbon textile will provide more accurate results.

Papanicolaou et al. (2008) investigated the influence of the number of carbon fibre textile TRM layers, namely 1 and 2 on medium scale clay brick masonry

walls tested under out-of-plane cyclic loading. It was observed that such a configuration resulted in a shear-flexure failure mode followed by debonding at the brick-bed joint interface. Increasing the number of layers has been found to result in a 25% increase of the maximum load.

Valluzzi et al. (2014) studied the out-of-plane response of hollow masonry blocks strengthened with basalt and glass TRM and tested under monotonic load. They reported that the strengthening configuration utilizing basalt TRM composite resulted in shear failure mode of the examined masonry walls, and tensile fibre rupture was observed in the case of glass textile TRM strengthening. It is also mentioned that increase of the axial stiffness of the basalt TRM, compared to the glass TRM composite, resulted in shear failure of the corresponding specimen. However, glass TRM attained a comparable load capacity with the basalt TRM specimen.

Very recently, Martins et al. (2015) investigated an innovative textile configuration on brick masonry walls tested under monotonic and cyclic load in four-point loading configuration. The strengthening materials comprising either carbon or glass braided composited rods (BCR) and the corresponding commercial meshes of carbon and glass materials.

The authors demonstrated that such an approach resulted in pure flexure failure mode of the glass BCR and a combined shear-flexure failure mode for the carbon BCR composite material. Carbon material resulted in increased flexural capacity compared to the glass composite material. On the other hand, BCR materials performed better compared to the commercial meshes in terms of both load and deformation capacity. This was mainly manifested in glass BCR material.

Dambra et al. (2018) conducted an experimental work on two strengthened

masonry walls specimens using the basalt BFRCM composite material. One of the specimens was repaired after the damage occurred during the test, and the other one was strengthened without being damaged. Two different failure modes were observed, where the repaired specimen resulted in two diagonal cracks crossing the mortar joints and the strengthened specimen in one ascending diagonal crack along the mortar joints. In both specimens, detachment of the reinforcement was observed, localized on the diagonal crack.

Padalu et al. (2018) studied the response of basalt fibre mesh reinforced cement mortar (BFRCM) composite material of strengthened masonry walls under out-of-plane loading. The basalt fibre mesh size used was 25 mm and 50 mm of similar amount of reinforcement. Mechanical anchors were used to attach the textile on the wall. It was concluded that the URM walls resulted in brittle and sudden failure mode. The strengthened specimens failed due to fibre mesh rupture and their out-of-plane load and deformation capacity was increased by 4.1 and 29 times, respectively. It was also reported that good bond was observed between the masonry substrate and the strengthening material due to the presence of the mechanical anchors. The failure mode observed contradicts with Dambra et al. (2018), where diagonal cracks were formed. This shows that additional experimental work and further study of the basalt FRCM composite should be conducted to provide reliable conclusions on the failure modes observed.

In addition, different failure modes were reported on the uncoated basalt, namely, textile rupture, slippage of the textile, shear failure of masonry (Harajli et al., 2010; Papanicolaou et al., 2011; Valluzzi et al., 2014; Padalu et al., 2018), which also demonstrates that further investigation is necessary to be performed on the out-of-plane performance of basalt TRM strengthened masonry walls.

Overall, most of the experimental studies conducted, did not investigate a series of different parameters in a single study on similar masonry walls to provide reliable results. In particular, a comparative study including parameters such the different number of textile layers of various textile materials, epoxy resin coating on the bare fibre textiles of carbon and glass has not been conducted.

3.5 Strengthening of brick masonry arches with FRP and TRM

Royles and Hendry (1991) investigated the response of three types of unreinforced full-scale masonry arch bridge models built with concrete, stone or clay bricks, and loaded at the quarter-span of each arch. The bridges failed due to the formation of three or four hinges, namely four-hinge mechanism. The hinges were located under the loaded section, at the vicinity of the crown, and at the region close to one or both supports.

Melbourne et al. (2004) studied the static and cyclic response of unreinforced doubled- and three-layered brick masonry arch of different geometries loaded at one- and three-quarter span. The static-loaded arches failed in a four-hinge mechanism or due to ring separation in a lower maximum load. The cyclic-loaded masonry arches failed in a maximum load 60% lower with respect to the corresponding static load and the failure mode was modified to ring separation.

Sumon (2005) studied a strengthening system with steel rebar reinforcement on brick masonry arch bridges, loaded at the quarter length of the arch. The load was applied using an hydraulic jack in increments of 10 kN. Sumon (2005) concluded that:

- All the specimens failed due to the four-hinge mechanism, apart from the fully-bonded arch which failed due to local crushing of the arch ring under the loaded cross-section.
- This strengthening system delayed cracking and increased the stiffness and the load capacity compared to the un-strengthened arch.
- The two different strengthening systems developed higher strength than the fully bonded arch.
- The fully-bonded arch provided 21% higher strength compared to the un-strengthened arch.

Valluzzi et al. (2001) investigated the response of solid clay brick masonry arches strengthened either at the intrados or the extrados. These were tested under static monotonic load at the quarter-length of the arch. The strengthening materials used were carbon or glass FRP strips.

The failure mechanism reported for the intrados configuration was detachment of the adhesion system from the masonry substrate at the loaded cross-section. Given that Glass FRP failed in higher load capacity compared to carbon FRP, the authors concluded that the optimum result was obtained for low strength and wider width of the FRP strip. The extrados strengthened specimens failed in higher maximum load with respect to the intrados due to shear sliding at the springer mortar joint. The authors concluded that the failure mode can be modified by increasing the strengthening material and the distance between the strips.

Bati and Rovero (2008) studied the response of brick masonry arches strengthened with carbon FRP strips in three different layouts namely intrados, extrados and localised strengthening under static monotonic load at the crown of the arch.

The authors reported that the collapse mechanism of the arches strengthened at the extrados was sliding along the mortar joint of the abutment. In case of strengthening at the intrados the strip width controlled the failure mode. The arches with the narrowest strip collapsed due to detachment of the strengthening at the keystone without damage of masonry while the arches strengthened with the widest strip collapsed due to crushing of the keystone masonry blocks.

In addition, the authors concluded that the extrados strengthened specimens resulted in enlarged load capacity compared to the intrados. A ductile behaviour was reported for the extrados specimens, whereas brittle response for the intrados.

Foraboschi (2004) conducted more than 50 full-scale tests on brickwork arches, vaults, and domes, which were strengthened with different FRP configurations. An overview of the whole experimental program is presented in this study. Three different configurations were investigated with the load applied at the quarter-span. The first configuration comprised strengthening with FRP strips at the intrados (28°, 50 mm wide, 2050 mm spacing), the second at the extrados (180°, 50 mm wide, 2050 mm spacing) and the third at the intrados (180°, 600 mm wide, and 1538 mm spacing).

The extrados strengthened specimens failed due to sliding along the mortar joint at the springing level of the less loaded side of the arch, whereas intrados specimens due to 4-hinge mechanism or masonry crushing.

Reflecting on the entire experimental work Foraboschi (2004) concluded the following:

- Debonding failure mode affects only the reinforcement applied at the intrados of the vault and includes ripping of a brick layer, or detachment of a block from the brickwork.
- FRP rupture occurred for low amount of reinforcement.
- For a non-symmetric loading configuration shear sliding was observed at the springing level of the less loaded side of the arch.

Oliveira et al. (2010) studied the response of glass FRP strengthened half-scaled solid clay brick masonry arches tested under static load at the quarter-span of the arch. Three different strengthening configurations were utilised namely intrados, extrados and localised strengthening. Spike anchors were used in combination with the intrados configuration.

The authors concluded that the localised configuration increased the maximum load, modified the hinges positions, but did not prevent the 4-hinge mechanism of the un-strengthened specimen to occur. Intrados specimens failed due to detachment of the strip at the load position, whereas the extrados specimens due to sliding along a mortar joint at the less loaded support of the arch. Enlarged values of the maximum load were observed at the intrados specimens, whereas increased deformation capacity was observed at the extrados.

They concluded that only the continuous strengthening procedure can prevent the four-hinge mechanism. A minimal increase of the load capacity was observed when widest strips were utilised at the extrados of the arch. This implies that application of additional material did not provide substantial improvement on the specimen response. Application of spike anchors resulted in

increased ductility (45%-85%) but the maximum load was not improved significantly.

Borri et al. (2009) studied strengthening of concrete brick arches tested under monotonic load at the quarter length of the arch. Specimens were strengthened at the intrados, the extrados, or at both sides with steel composites of polymeric resin (SRP) or mortar matrix (SRG), or carbon fibres with polymeric resin. Steel anchors were used in both configurations to investigate their contribution to the effectiveness of the arch.

The specimen without any strengthening material failed due to the formation of four hinges. Extrados strengthened specimens failed due to shear sliding at the support of the arch. Conversely, intrados configuration resulted in laminate rupture or debonding under the load position for lower and higher reinforcement ratio, respectively. Specimens strengthened at both positions exhibited shear sliding followed by detachment of the composite material under the loaded cross section.

They concluded that:

- Strengthening at the intrados of the arch resulted in higher strength and lower deformation capacity compared to the extrados.
- Steel cords provided higher strength compared to carbon fibres, in both layouts.
- Strengthening with cementitious grout demonstrated improved behaviour with respect to polymeric resin.
- The use of steel anchors resulted in a better response at the extrados compared to the intrados.

Borri et al. (2011) examined the intrados strengthening of brick masonry arches using Glass Fibre (GF) polymer or Carbon Plate (CP), which were tested under monotonic vertical load at the keystone of the arch. Aramid anchors were also inserted in both configurations (22 for GF, up to 5 for CP). Cementitious grout was adopted to examine the bonding mechanism between the substrate and the strengthening material and a number of specimens were built with lower mechanical properties to simulate the imperfections of masonry substrate.

The 4-hinge failure mechanism of the control specimen modified after the application of the strengthening material. The specimens with glass fibres failed due to detachment of the reinforcement with masonry substrate. The application of 22 aramid anchors delayed premature peeling of the composite and the arch failed due to masonry crushing at the keystone. When a cementitious grout was embedded among the strengthening material and the substrate, debonding of the laminate was occurred. The specimens built with lower mechanical properties failed due to sliding between brick mortar joint at the region of the load, which was followed by detachment of the strengthening material. Strengthening with carbon plates resulted in sliding along the mortar joint and in masonry crushing when 2 and (3-5) anchors were used, respectively.

They concluded that:

- Carbon plates demonstrated increased load capacity compared to glass fibre polymer.
- Application of more than 4 or 5 spike anchors was not effective for the structure in terms of load capacity.
- Glass fibres can provide ductile behaviour to the structure whereas carbon plates brittle behaviour prior to failure.

- Lower maximum load was observed when cementitious grout or lower mechanical properties were adopted during the construction of the specimens.

Tao et al. (2011) examined the behaviour of a two-span semi-circular concrete brick masonry arch bridge strengthened at the intrados with pre-cured CFRP plates. Dry sand-fill was applied, which was contained in plastic sheeting, timber spandrel walls and abutments. Each masonry arch was loaded with a line load at the quarter-span.

They concluded that:

- The FRP plates increased the load capacity of both arches, compared to the un-strengthened specimens.
- The un-strengthened arches failed due to the 4-hinge mechanism. Two types of failure modes were observed on the strengthened specimens, namely shear and peeling debonding. Shear debonding of the FRP plate occurred with a layer of brick attached to the plates, whereas peeling debonding within the surface of the plate, where fibres remained attached to the arch.
- The final collapse of the arches occurred due to debonding of the plates from the substrate, which subsequently resulted to the four-hinge mechanism of the arch.

Cancelliere et al. (2010) studied the extrados strengthening of clay brick masonry arches with Carbon Fibre Reinforced Polymer (CFRP) strips, which were

tested under monotonic load near to the crown of the arch. The control specimen failed due to the 4-hinge mechanism. After the application of the strengthening material the failure mechanism modified and the arches failed due to vertical sliding of the loaded brick which was followed by masonry crushing.

Garmendia et al. (2011) examined the extrados strengthening of stone masonry arches with Basalt Textile Reinforced Mortar (BTRM), which were tested under displacement control at the quarter length of the span. The experimental results demonstrated that the un-strengthened specimens failed due to the four-hinge mechanism. Three different failure modes were observed for the strengthened specimens, namely rupture or debonding of the BTRM composite, and masonry crushing.

The authors concluded that:

- The load and deformation capacity was significantly increased, compared to the un-strengthened masonry arches. The insertion of anchors did not provide any improvement to the system.
- The application of identical strengthening configuration resulted in different failure mechanism, which demonstrates that further investigation is required to be conducted with additional investigated parameters.

Garmendia et al. (2015) examined the extrados strengthening of clay brick masonry vaults tested under displacement control at the quarter length of the span. The strengthening material used were the Basalt and Steel Reinforced Mortar and polymer BRM/BRP and SRM/SRP, respectively. Spike anchors were also inserted to improve the response of the composite materials.

The un-strengthened specimens failed due to the four-hinge mechanism. SRP exhibited shear sliding along the mortar joint under the point load which

was followed by rupture of the fibres. In SRM specimen four hinges were formed. The failure mode observed in BRM was fibres rupture or detachment of the composite with subsequent 4-hinge mechanism. BRP specimen failed due to the detachment of the strengthening material and the formation of 4 hinges.

The authors concluded that:

- The proposed strengthening system increased the load and displacement capacity of all the specimens.
- This was not the case for the BRM specimen, where the deformation capacity was not improved.
- Spike anchors prevent debonding at the area of application.
- The mortar-based composites (SRM, BRM) did not prevent the four-hinge failure mechanism. Subsequently, further investigation on the effectiveness of the basalt textile with additional specimens will provide more reliable results.

Rovero et al. (2012) studied the response of double-layered brick masonry arches with various length (25°, 35°, 45°) of Carbon Fibre Reinforced Polymer (CFRP) strips at the intrados and extrados. A vertical load was uniformly distributed and subsequently a horizontal force was applied up to the point of collapse. Specimens strengthened at the intrados failed due to masonry crushing and four-hinge mechanism. When the length of the strip was increased to 45°, 3 hinges formed and sliding along the mortar joint resulted in FRP delamination. The extrados specimen failed due to the four-hinge mechanism.

The authors concluded that:

- Increase of the FRP length resulted in increased maximum load.

- The intrados specimens demonstrated increased maximum load and decreased kinematic ductility compared to the un-strengthened arches (35%).
- The extrados specimens resulted in a minimal increase of the maximum load and the kinematic ductility.

Alecci et al. (2017b) investigated the extrados strengthened masonry brick arches with Basalt Fabric Reinforced Lime Mortar (Basalt-FRLM) composite material, tested under displacement control at the quarter length of the span. A natural hydraulic lime mortar was adopted for this experimental work. The results were compared with previous experimental results with carbon FRP Bati and Rovero (2008) and PBO Fibre Reinforced Cementitious Matrix (PBO-FRCM) composite material (Alecci et al., 2016).

The four-hinge mechanism was observed at the un-strengthened arches. The Basalt-FRLM specimen failed due to sliding of the mortar joint at the right support. Cracks were formed at the left support and the right haunch of the arch and one hinge under the loaded cross-section. A similar behaviour was observed in PBO-FRCM specimen. The CFRP specimen failed by a sudden shear sliding at the right support. A hinge formed under the loaded cross-section and cracks propagated at the right haunch. The CFRP specimen obtained a doubled maximum load compared to the basalt-FRLM and PBO-FRCM but in a significant decreased deformation capacity. In addition, the Basalt-FRLM exhibited enlarged load and deformation capacity with respect to PBO-FRCM specimen.

Alecci et al. (2017a) studied the response of half-scaled brick masonry arches strengthened at the intrados and tested at the quarter length of the span under displacement control. The strengthening materials used were the cement-based PBO-FRCM, carbon-FRCM, and the polymer-based Carbon FRP (CFRP). The un-strengthened specimens failed due to the formation of four-hinges in

alternate positions of intrados and extrados. Specimen C-FRCM demonstrated higher load capacity with respect to PBO-FRCM. The failure mechanism of both FRCM specimens was debonding of the composite and masonry crushing at the loaded cross-section. Cracks formed at the intrados due to slippage between fibers-matrix interface and a hinge formed at the right haunch of the arch. A brittle failure mode was observed in CFRP specimen, where a sudden debonding occurred combined with masonry crushing under the loaded cross-section of the arch.

PBO-FRCM attained increased load capacity with respect to the C-FRCM specimen. C-FRCM demonstrated a more brittle behaviour and decreased kinematic ductility compared to PBO-FRCM, which was observed through the slippage between fibers-matrix interface. This was more pronounced in PBO-FRCM specimen with respect to C-FRCM composite, which was further corroborated by the bond tests performed in this study. The load capacity attained by CFRP specimen was increased more than double times with respect to the FRCM specimens. On the other hand, the kinematic ductility of CFRP specimen was significantly decreased compared to the PBO-FRCM specimen.

Carozzi et al. (2017a) studied the behaviour of extrados strengthened clay brick masonry arches and vaults tested under monotonic load at the quarter length of the span. Load-unload cycles were applied before the collapse of the specimens, for equal distribution of the load. The strengthening materials applied were the Steel Reinforced Grout (SRG), the glass TRM, and the carbon FRP.

The un-strengthened masonry arch and vault failed due to the formation of four hinges. The sequence where the hinges formed was: (i) under the point

load, (ii) at the right abutment (iii) at the right haunch and (iv) at the left abutment. The SRG arch formed two hinges under the point load and the left abutment. The specimen collapsed when complete detachment of the abutment occurred from the lateral wall combined with masonry crushing at the loaded cross-section. Subsequently, a local debonding occurred at the right abutment of the arch. The carbon FRP specimen failed due to detachment of the vault from the right abutment and debonding of the FRP from the right part of the vault. Two hinges formed, under the point load and at the left abutment. The TRM vault formed two hinges, under the point load and at the right haunch. The hinges at both abutments formed when collapse of the vault occurred. Slippage phenomena and rupture of the textile occurred at the right haunch, when the second hinge formed.

The authors concluded that:

- All the strengthening systems of the arches and vaults effectively increased the load and deformation capacity.
- The SRG masonry arch increased the load capacity significantly compared to the un-strengthened specimen.
- TRM strengthened vault demonstrated an improved response with respect to the FRP vault, in terms of load and deformation capacity.

Tiberti et al. (2017) examined the extrados strengthening of masonry arches; built with fictile tubules and strengthened with Basalt FRCM strips. A static load was applied at the keystone using a manual hydraulic cell. Failure of the arch occurred due to collapse of the mortar and the basalt fibres. Increase maximum load and deformation capacity was observed with respect to the unreinforced arch.

Gattesco et al. (2017) studied the behaviour of strengthened brick masonry barrel vaults with Glass Fiber Reinforced Mortar (GFRM), tested under horizontal cyclic load. The composite material was applied in two different strengthening configurations, namely intrados and extrados. The Glass Fiber Reinforced Polymer (FRP) mesh was produced with coated twisted fibres within a thermohardening resin, formed into wires. L-shaped GFRP connectors were also inserted into the arch.

The un-strengthened specimen formed five cracks at both springers and haunches and close to the crown of the arch. The extrados strengthened arch formed cracks at both haunches and collapse occurred due to GFRP rupture at one haunch. A minimal increase of the load capacity and significant increase of the deformation capacity was observed. The intrados specimen formed cracks at both haunches and springers.

The load capacity of the extrados specimen was increased with respect to the intrados specimen. Both strengthening configurations resulted in a significant increase of the deformation capacity. In particular, enlarged displacement was observed at the intrados specimen compared to the extrados.

De Santis et al. (2018b) investigated the response of full-scale masonry vaults strengthened with Steel Reinforced Grout (SRG) and tested under cycling loading at 1/3 span, taking into account the contribution of buttresses and backfill. The strengthening material comprised SRG material at the intrados or the extrados using lime-based mortar and connectors placed either at the abutments (extrados) or along the arch (intrados). They found that the SRG strengthening system prevented the development of the four-hinge mechanism and increased the deflection and strength capacity significantly. The failure mode observed at the extrados strengthened vault with higher textile density (8 chord/inch)

was crushing and shear sliding of the brickwork under the point load, debonding of the reinforcement at the textile-to-matrix interface from the right buttress and cracking in the middle of the arch. On the other hand, in case of lower density textile (4 chord/inch) failure occurred due to shear sliding among the bricks at the loaded region of the vault and SRG detachment from the right buttress. In addition, alternate cracks were formed at the intrados and extrados in both extrados specimens (left haunch, crown, right haunch). The intrados SRG strengthened specimen failed due to debonding of the textile to matrix interface among the intermediate connectors.

De Santis et al. (2019) examined the response of full-scale TRM strengthened masonry vaults with coated basalt mesh at the extrados and intrados. The arches were built with buttresses and filling to reproduce the actual condition of brick vaults. The load was applied at 1/3 of the span and was increased cyclically up to failure. The tests demonstrated increased load and deformation capacity after the application of the strengthening material.

The intrados strengthened specimen formed cracks at alternate positions of intrados and extrados (left haunch, crown, right haunch). Large detachment at the textile-to-matrix interface with breaking of matrix occurred under the point load and at the left haunch. In addition, local rupture of basalt wires occurred under the point load and a crack opened at the arch-to-abutment joint of the right support.

The extrados strengthened specimen resulted in cracks at alternate positions of intrados and extrados (left haunch, crown, right haunch). In addition, crushing of the mortar matrix occurred at the extrados of the left haunch and local crushing of the mortar joint was observed at the right haunch. Failure of the arch occurred due to detachment of the basalt fabric followed by brittle textile

rupture at the crown of the arch.

3.5.1 The effect of the strengthening configuration

Based on the literature review, the strengthening configuration significantly affected the performance of the strengthened arch in terms of the maximum load, deformability, and failure mode. As has been reported, both configurations resulted in beneficial results in correspondence to the composite material used.

The most common failure mechanism observed in the extrados strengthened masonry arches with FRP or TRM materials, was sliding along a mortar joint at the supports (Valluzzi et al., 2001; Foraboschi, 2004; Bati and Rovero, 2008; Oliveira et al., 2010; Garmendia et al., 2015; Alecci et al., 2016; Alecci et al., 2017b; Carozzi et al., 2017a). In addition, in case of De Santis et al. (2018b) shear sliding occurred under the point load, instead of the supports. However, several not consistent failure modes were reported in the literature. In particular, Carozzi et al. (2017a) reported debonding of the SRG or FRP specimens and slippage among mortar-textile fibres followed by textile rupture for the TRM specimens. In addition, Garmendia et al. (2011) found that by strengthening similar specimens with basalt TRM composite the failure modes were different, namely rupture of the textile, debonding, and masonry crushing. Similarly, in Garmendia et al. (2015) FRP or TRM strengthened specimens did not result in a consistent failure mode. This highlights the requirement for further experimental work to identify identical failure mechanism among the specimens with similar strengthening layout.

The failure mode and the FRP strengthening effectiveness of masonry arches, further relied on the FRP strip dimensions. In particular, Bati and Rovero (2008) observed that by increasing the strip width, the load and deformation capacity

of the arch was increased. This contradicts with Oliveira et al. (2010), where similar failure mode and load capacity was observed when wider FRP strips were applied. On the other hand, Foraboschi (2004) reported that FRP rupture occurred when the reinforcement ratio was decreased. In addition, Valluzzi et al. (2001) reported that the failure mode of masonry arches can be modified by increasing the distance between the strips.

The most common failure mechanism reported for the specimens strengthened at the intrados with FRP or FRCM composite materials was debonding of the strengthening material from the masonry substrate at the loaded cross-section (Valluzzi et al., 2001; Foraboschi, 2004; Bati and Rovero, 2008; Oliveira et al., 2010; Borri et al., 2009; Tao et al., 2011; Alecci et al., 2017a; De Santis et al., 2019; De Santis et al., 2018b). It was concluded that the use of wide and low strength FRP strips resulted in improved response with respect to higher strength composites reported in Valluzzi et al. (2001). Bati and Rovero (2008) found that wide strips resulted in masonry crushing whereas narrow strips in detachment of the composite material. It is clear that in the most FRP studies the debonding failure mechanism dominated. However, there are not enough studies with the TRM material comprising a complete series of experiments with all the available textile materials in the market, which indicates that more extensive research is required to provide beneficial results on the application of the TRM materials.

Several studies investigated the effectiveness of the spike anchors in both strengthening layouts of masony arches. In particular, Garmendia et al. (2011) found that the addition of spike anchors at the extrados, did not provide additional strength to the strengthening system, whereas in Garmendia et al. (2015) spike anchors prevent debonding of the TRM at the abutments, where they were

applied. It was also shown, that the application of spike anchors at the intrados resulted in increased ductility, which delayed the detachment of the composite but the maximum load was not improved or even decreased (Oliveira et al., 2010; Borri et al., 2011). These inconsistent experimental results show that further experimental work is required to be conducted to provide accurate results on the effectiveness of the anchored system of the TRM strengthening on masonry arches.

In addition, a conflict was observed for the predominated strengthening configuration, in terms of load and deformation capacity. In particular,Valluzzi et al. (2001) and Bati and Rovero (2008) agreed that the extrados strengthening is more effective in terms of load capacity compared to the intrados, but this was not the case for (Borri et al., 2009) and Oliveira et al. (2010), where opposite results were observed. In terms of deformation capacity, (Bati and Rovero, 2008; Borri et al., 2009; Oliveira et al., 2010) reported a more ductile behaviour on the extrados configuration with respect to the intrados.

3.6 Concluding Remarks

Despite their well-documented advantages (i.e. high strength and stiffness to weight ratio, corrosion resistance, ease and speed of application), the FRP technique entails several drawbacks, i.e., poor behaviour at moderate to high temperatures, combustibility, high costs, and safety-hazards for the manual workers. These are related to the properties of the organic resins used to impregnate the fibres as for example these have been reported to deteriorate for temperatures below or close to their glass transition temperature (usually in the range of 50-120^{0}C), see, e.g., (Firmo et al., 2015; Correia, 2008). Epoxy-resins furthermore decompose thermally, releasing heat, smoke, soot and toxic combustible

volatiles for temperature between 300-400 ^{0}C. Compared to wet lay-up epoxy-resin applications, TRM strengthening costs are lower due to the low-cost cement mortars utilized. Another disadvantage of FRP is that they are usually manufactured and applied in strips. This effectively results in regions of increased strength and stiffness within the retrofitted structure. In the case of brittle URM structures, this results in stress concentrations in the unreinforced regions that accelerate damage rather than mitigating it (Foraboschi, 2004). Bati and Rovero (2008) demonstrated that when the distance between the FRP strips applied at the extrados is reduced, the resulting ultimate displacements increase, thus resulting in an overall increase of the pseudo-ductility of the virgin masonry wall. The advantages of global rather than stripped strengthening solutions for the case of masonry have been further examined and substantiated in the literature, see, e.g., (Fuggini et al., 2013; Mosallam, 2007).

Several comparative experimental studies have been conducted comprising FRP and TRM composites. In particular, Valluzzi et al. (2014) studied the out-of-plane response of masonry walls strengthened with different composite materials including Fibre Reinforced Polymers (FRP), Steel Reinforced Polymers (SRP), Natural FRPs and TRM. It was concluded that the FRP and TRM composites performed similarly in terms of load capacity, whereas FRPs resulted in higher deformation capacity. In addition, the lowest maximum load was recorded for the Natural FRPs. Papanicolaou et al. (2007) studied the in-plane response of several strengthening configurations on different types of masonry walls. They concluded that FRP strengthened specimens performed better than TRM in terms of strength, whereas TRM composite outperformed FRP in terms of deformation capacity. Furthermore, Papanicolaou et al. (2008) conducted further research on the out-of-plane response of masonry walls with different

strengthening configurations including FRP, TRM and NSM composites in two different types of walls. They reported that when the failure mode was controlled by damage in the masonry, TRM resulted in improved behaviour with respect to FRP in terms of both load and deformation capacity. Conversely, when specimens failed due to textile rupture, FRP effectiveness was minimally increased. The lowest peak load and highest displacement was recorded in case of the NSM composite. This work shows that the TRM composite showed that is promising material and under certain conditions can outperform the already used composite materials. Therefore, further research should be conducted to verify those experimental results.

Chapter 4

Materials

4.1 Introduction

In this work, three experimental campaigns were undertaken. The first, comprised bond tests on masonry walls to investigate the bond behaviour between the TRM composite material and brick masonry walls. The second involved three point bending tests in strengthened masonry walls with the objective of identifying their out-of-plane flexural strength. The third involved quasi-static tests in masonry arches to identify the maximum collapse load and the failure mechanism of the arch. In this Chapter, the mechanical properties of the materials used in all the experimental campaigns are presented, including the joint mortar, clay bricks, masonry walletes, strengthening mortar, and fibre-textiles materials as identified through coupon testing.

4.2 Clay bricks

All the masonry specimens tested in this work were built using solid clay bricks with UK typical nominal dimensions of 215 x 102.5 x 65 mm. The average value

of the compressive strength was $f_b = 21.2$ MPa. This was determined in a perpendicular direction to bed (215 x 102.5 mm) and stretcher faces (215 x 65 mm) according to BS EN (2011).

4.3 Masonry joint mortar

In all cases, the joint mortar was prepared with a 1:4 cement to sand mix for both the head and bed joints. The water to (cement + sand) ratio was determined after trial mixes to achieve the desired workability. This was equal to 0.25 in all cases.

The mechanical properties of the joint mortar were identified via flexure and compression tests conducted in prisms with nominal dimensions 40 x 40 x 160 mm according to EN (1993) specifications. In particular, three prisms were tested in three-point bending and the ruptured segments obtained were used to define the uniaxial compressive strength on a bear surface of 40 x 40 mm. These tests were conducted on the day of testing of the corresponding specimen. The prism results for the bond tests, masonry walls, and masonry arches tests are presented in Sections 5.2.2, 6.2.2 and 7.2.2, respectively. The mean values of the tensile and compressive strength of the joint and strengthening mortar for all the experimental studies are presented in Table 4.1. A slightly higher variability was observed in casting mortar compressive and tensile strength compared to the strengthening mortar. It is pointed out that such variability does not significantly affect the results in terms of the failure modes observed.

TABLE 4.1: Casting and strengthening mortar of all the experimental campaigns

Specimens	Casting mortar		Strengthening mortar	
	Compressive Strength f_m [MPa]	Tensile Strength f_{mt} [MPa]	Compressive Strength f_m [MPa]	Tensile Strength f_{mt} [MPa]
Mean value	8.2	2.3	37.5	8.8
Standard deviation	1.03	0.42	3.80	1.06
Coefficient of Variation	0.12	0.19	0.10	0.12

4.4 Compression tests on masonry walletes

To determine the mechanical properties of masonry, three masonry walletes of dimensions 450 x 450 x 65 mm (length x height x width) were tested under compression in a perpendicular direction to the bed joints per EN (1998a). The tests were conducted 28 days after the specimen preparation. The wall assemblage deformation was captured through two potentiometers, positioned halfway on both sides at a gauge length of 250 mm. The resulting mean value of the compressive strength was $f_m^{'} = 9.7$ MPa. The secant elastic modulus at 0 % to 30 % of the maximum stress was found equal to 2.5 GPa.

4.5 Strengthening mortar

The strengthening of the specimens considered in this study was performed with an inorganic dry binder consisting of cement and sand polymers at a ratio 8:1 by weight. The preparation of the mortar mixture was carried out using water to cementitious material ratio equal to 0.23 by weight.

Similar to the case of the joint mortar, coupon tests on the strengthening mortar were conducted according to EN (1993). The corresponding prism results are presented in Sections 5.2.2, 6.2.2 and 7.2.2, for the bond tests, masonry

walls, and masonry arches tests, respectively. The mean values of the tensile and compressive strength of the strengthening mortar for all the experimental studies are presented in Table 4.1.

4.6 Textile-Fibre materials

In this project, three different textile-fibre materials were used, i.e., carbon-fibre textile (either uncoated or coated with epoxy resin), glass-fibre textile (uncoated or coated with epoxy resin) and coated basalt-fibre textile. The textile meshes used are shown in Fig. 4.1. The notation considered is C for carbon, G for glass, B for coated basalt, G_co for coated glass, C_co for the coated carbon fibre textile.

The textile materials properties, as provided in the manufacturer datasheets, are presented in Table 4.2. In this, the ultimate tensile stress (f_{fu}) and the Young's modulus of elasticity (E_f) correspond to the fibres, whereas the weight and the nominal thickness to the textile. In particular, the nominal thickness was estimated based on the equivalent smeared distribution of fibres and is defined as the ratio of the textile weight (per unit area) to the density as shown in Eq. 4.1 where (w) is the weight of the textile, (t_f) is the nominal thickness of the textile, and (ρ) is the density of the fibre-textile. The cross-section area of the fibre textile (A_f) is calculated using Eq. 4.2, where (b_f) is the width of the fibre-textile, (n_f) is the number of rovings, and (ms_f) is the mesh size in the direction of loading. The coated basalt fibre-textile employed in this study is a commercial product fabricated with a bituminous binder of 10 % content. The coated carbon and coated glass fibre textiles were impregnated in a commercial

TABLE 4.2: Textile material properties

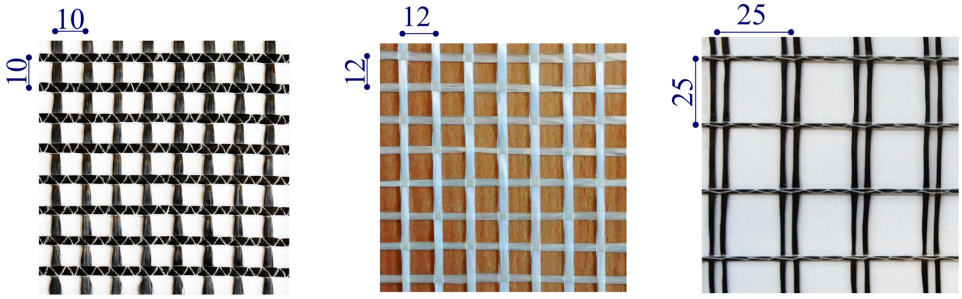
Material [/]	Weight [g/m^2]	Density [g/cm^3]	Thickness* [mm]	f_{fu} [MPa]	E_f [GPa]	Axial stiffness** [N/mm^2]
Carbon	348	1.8	0.097	3800	225	21.83
Glass	220	2.5	0.044	1400	74	3.26
Coated basalt**	220	2.67	0.037	1351	89	3.30

*Nominal thickness
**Calculated as the nominal thickness to Young's modulus product
***Commercial product fabricated with a bituminous binder of 10 % content

epoxy adhesive as further described in Section 4.7.

$$t_f = \frac{w}{\rho} \tag{4.1}$$

$$A_f = b_f t_f = n_f m s_f t_f \tag{4.2}$$



(a) (b) (c)

FIGURE 4.1: (a) Carbon (b) Glass (c) Coated Basalt

4.6.1 Textile fibre material characterization through tensile tests

Uniaxial tensile tests were conducted on fibre-textile materials to determine their tensile behaviour. Two different series of tests were conducted including tests of (i) 50 mm and (ii) 100 mm width and similar length (see Fig. 4.2).

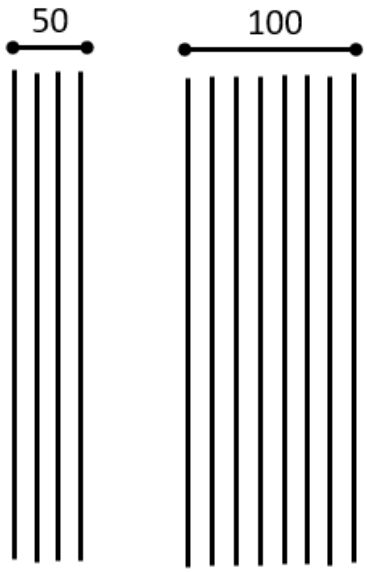


FIGURE 4.2: Configurations of uniaxial tensile tests of (a) 50 mm (b) 100 mm

For the width of 50 mm, the examined fibre-textile materials were the glass, coated glass, and coated carbon. Three samples of 50 mm width and 380 mm height were tested for each material. The tensile tests were carried out on a universal testing machine of 50 kN load capacity, under monotonic loading rate of 0.02 mm/sec. The textile was gripped to the universal testing machine via two aluminium plates. These were attached at the two ends of the textile using epoxy resin. The elongation of the gauge length (260 mm) was measured via an extensometer positioned as shown in Fig. 4.3. Tensile tests were not performed on the basalt textile due to the large mesh size geometry of 25 mm, which results in a decreased width of the textile comprising only two rovings. Therefore, accurate results wouldn't be obtained in this case.

The resulting stress versus strain curves for the 50 mm width specimens are presented in Fig. 4.5. The response is practically linear until failure in all cases. The failure modes observed were rupture of the coated carbon and coated glass

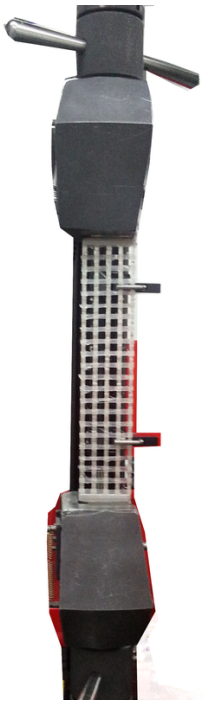
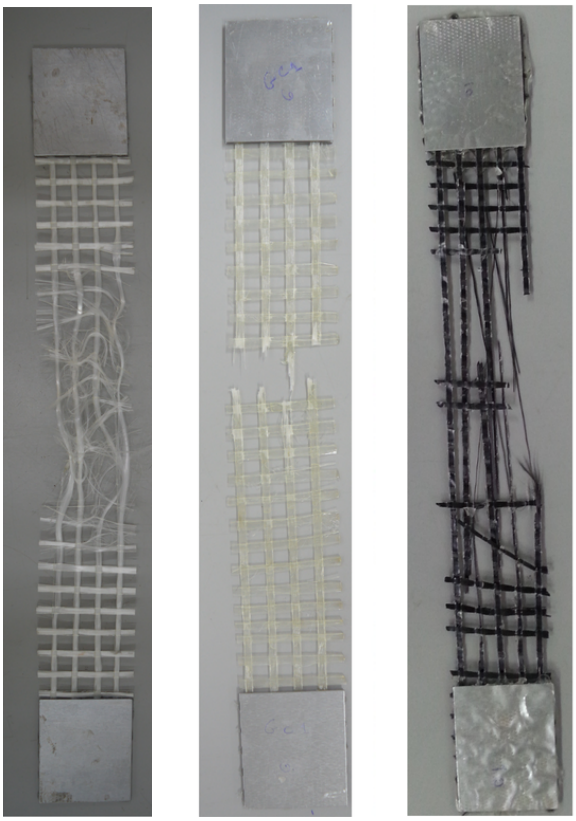


FIGURE 4.3: Experimental setup of uniaxial tensile tests

TABLE 4.3: Tensile properties of the fibre-textile materials

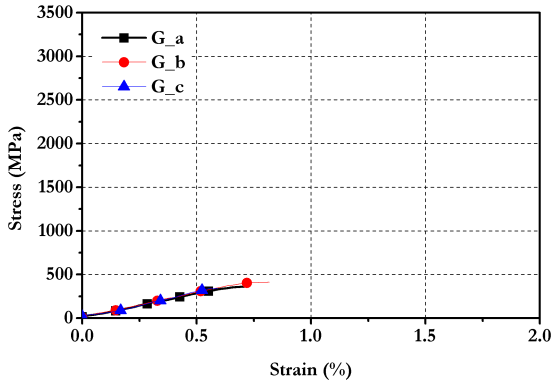
Glass			Glass coated			Carbon coated		
f_{fu} [MPa]	ϵ_{fu} [%]	E_f [GPa]	f_{fu} [MPa]	ϵ_{fu} [%]	E_f [GPa]	f_{fu} [MPa]	ϵ_{fu} [%]	E_f [GPa]
360	0.706	49.0	1142	1.757	60.9	3184	1.709	186.6
411	0.819	47.6	1040	1.590	61.1	2922	1.168	251.3
342	0.591	54.5	1140	1.526	66.3	3014	1.375	214.0
371*	0.760*	50.4*	1107*	1.624*	62.7*	3040*	1.417*	217.3*
35.6**	0.11**	3.65**	58.5**	0.1**	3.0**	133.1**	0.3**	32.5**
0.10***	0.16***	0.07***	0.05***	0.07***	0.04***	0.04***	0.19***	0.15***

*Mean value, **Standard deviation, ***Coefficient of Variation

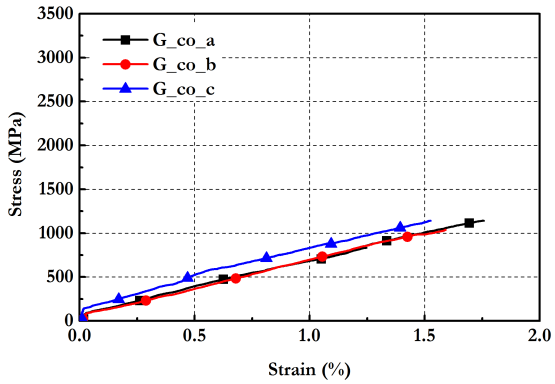


(a) (b) (c)

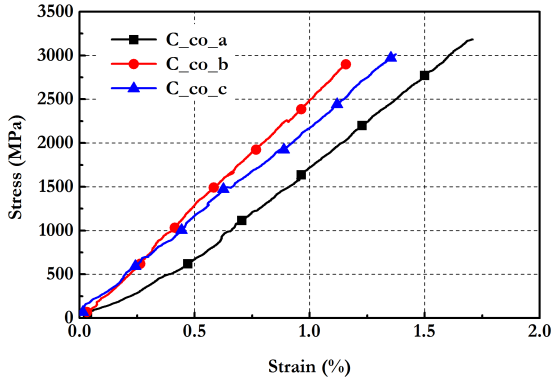
FIGURE 4.4: Failure modes of (a) glass, (b) coated glass and (c) coated carbon fibre-textile materials



(a)



(b)



(c)

FIGURE 4.5: Stress versus strain curves for (a) glass, (b) coated glass and (c) coated carbon fibre-textile materials

fibres, as shown in Fig. 4.4. It is highlighted that the abrupt failure mode of coated carbon textile resulted in a non-uniform textile rupture as presented in Fig. 4.4c. In case of the glass fibre textile slippage among the fibres and partial rupture of the fibres occurred. The ultimate tensile stress (f_{fu}), the ultimate strain (ϵ_{fu}) and the modulus of elasticity (E_f) are summarised in Table 4.3. The ultimate tensile stress (f_{fu}) is the ratio of the ultimate load to the cross-sectional area of the fibre textile in the direction of loading. The cross-sectional area of the textile is determined as the product of the textile width and the nominal thickness of the textile (see Table 4.2).

For the specimens of 100 mm width, the ASTM D5034 standard was adopted, where three samples of 370 mm height were tested for each material. The materials used were the glass, coated glass, coated basalt, carbon and coated carbon fibre-textiles. The tensile tests were conducted in a universal testing machine of 200 kN load-capacity, under monotonic displacement rate of 0.02 mm/s. The textile was gripped to the testing machine using two aluminium plates. Both ends of the textile were attached at the aluminium plates using epoxy resin. In addition, two LVDTs of 15 mm stroke and 0.01 mm sensitivity were positioned to measure the elongation of the gauge length.

The stress-strain curves are demonstrated in Fig. 4.6. A linear response was observed until the failure of the textiles. The failure modes observed were textile rupture in the coated basalt, coated glass, carbon and coated carbon textile specimens at the central region of the gauge length (see Fig. 4.7). An abrupt rupture of the coated carbon fibre textile was observed, as occurred in 50 mm width specimens (see Fig. 4.4c), resulting in a non-uniform failure as shown in Fig. 4.7b. In addition, the glass fibre textile demonstrated a similar failure mode as in case of 50 mm width specimens, where slippage among the fibres with

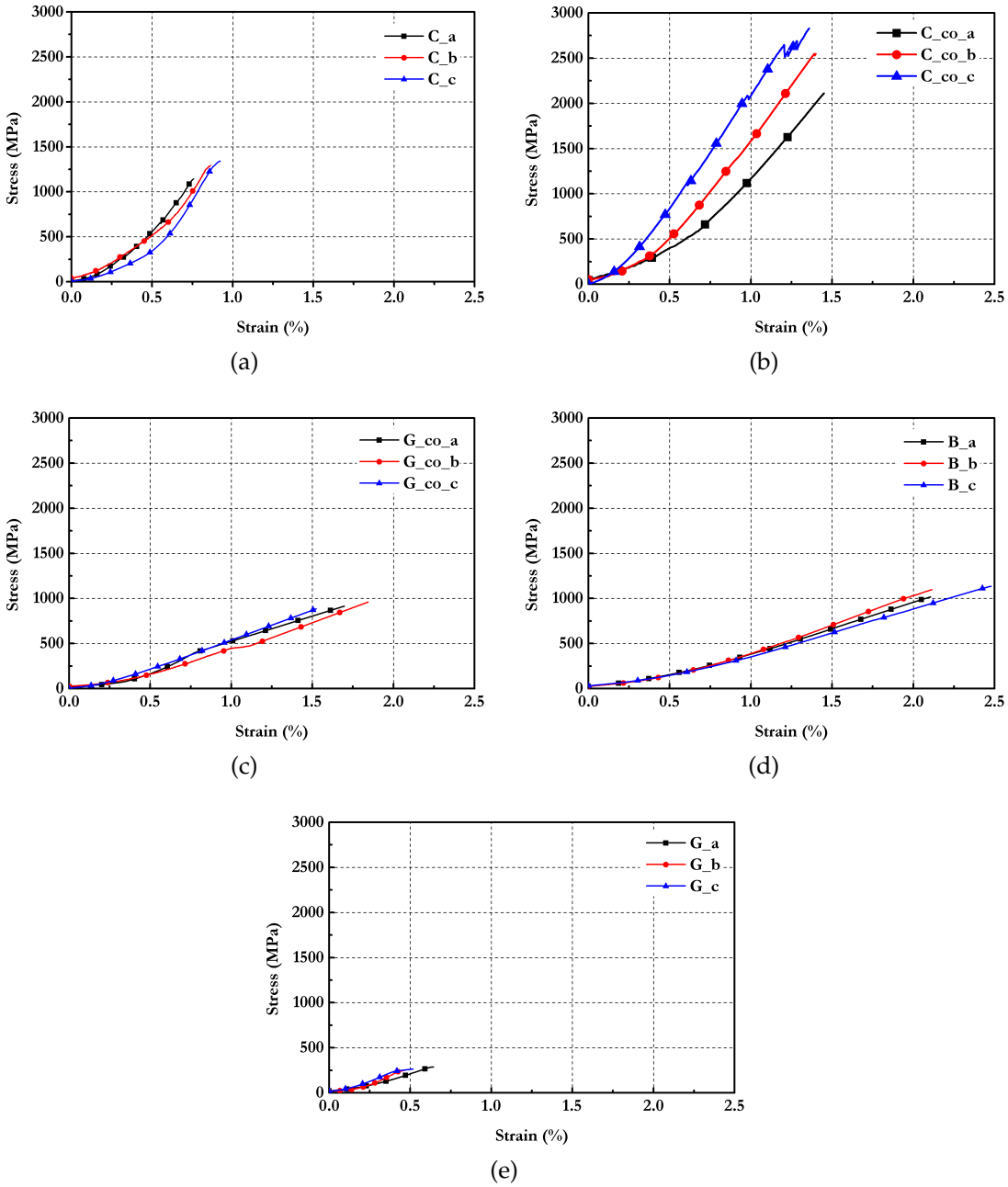


FIGURE 4.6: Stress versus strain curves for (a) carbon, (b) coated carbon (c) coated glass, (d) coated basalt and (e) glass fibre-textile materials based on ASTM D5034

TABLE 4.4: Tensile properties of the fibre-textile materials based on ASTM D5034

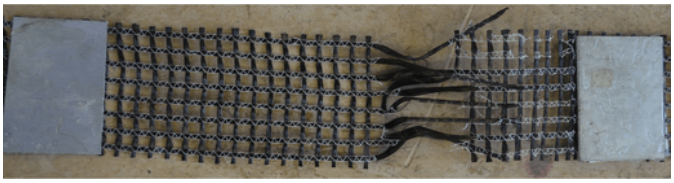
Glass			Carbon			Carbon coated		
f_{fu} [MPa]	ϵ_{fu} [%]	E_f [GPa]	f_{fu} [MPa]	ϵ_{fu} [%]	E_f [GPa]	f_{fu} [MPa]	ϵ_{fu} [%]	E_f [GPa]
286	0.644	44.5	1135	0.757	156.2	2111	1.451	164.2
252	0.468	53.8	1256	0.861	154.6	2547	1.399	201.6
264	0.518	50.9	1336	0.922	157.5	2829	1.358	220.1
267*	0.544*	49.7*	1242*	0.847*	156.1*	2496*	1.403*	195.3*
17.27**	0.09**	4.80**	101.17**	0.08**	1.43**	361.76**	0.05**	28.44**
0.06***	0.17***	0.10***	0.08***	0.10***	0.01***	0.14***	0.03***	0.15***

Glass coated			Coated basalt		
f_{fu} [MPa]	ϵ_{fu} [%]	E_f [GPa]	f_{fu} [MPa]	ϵ_{fu} [%]	E_f [GPa]
914	1.698	62.1	1017	2.107	52.6
959	1.844	58.6	1097	2.115	57.5
883	1.523	63.0	1133	2.479	49.0
919*	1.688*	61.2*	1083*	2.233*	53.0*
38.21**	0.16**	2.28**	59.34**	0.21**	4.27**
0.04***	0.10***	0.04***	0.05***	0.10***	0.08***

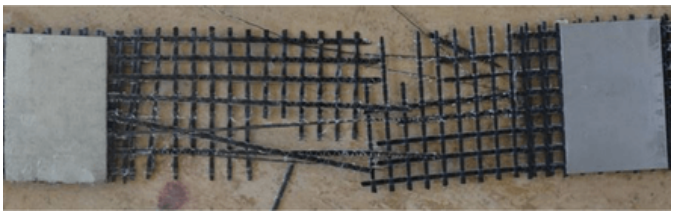
*Mean value, **Standard deviation, ***Coefficient of Variation

partial textile rupture occurred (see Fig. 4.7c). Table 4.4 presents the ultimate tensile stress (f_{fu}), the ultimate strain (ϵ_{fu}) and the modulus of elasticity (E_f) of the tested fibre-textile materials. Slightly higher variability was observed in the coated carbon in terms of (f_{fu}) and (E_f) compared to the rest fibre textiles in both series of testing (see Table 4.3 4.4). This is attributed to the non-uniform but also abrupt failure mode which in some cases results in inconsistent response of the textile under tension.

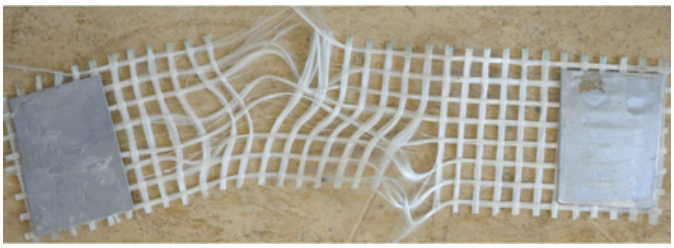
In both configurations of the glass fibre textile similar failure mode was observed, where slippage among the fibres with partial textile rupture occurred. When the number of rovings was increased from 4 to 8, alignment of the textile was more difficult to occur, which resulted in slightly decreased values of the ultimate tensile stress and the corresponding strain (see Tables 4.3 and 4.4). In



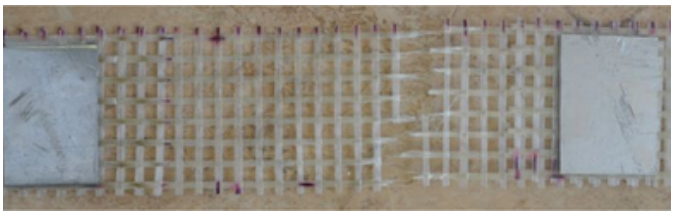
(a)



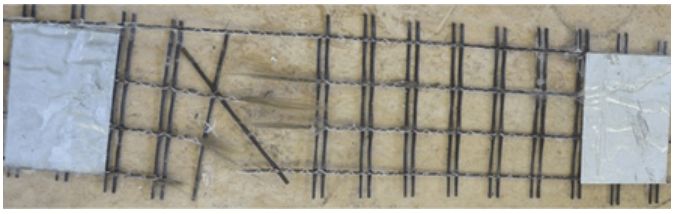
(b)



(c)



(d)



(e)

FIGURE 4.7: Failure modes of (a) carbon, (b) coated carbon, (c) glass (d) coated glass and (e) coated basalt based on ASTM D5034

the coated glass fibre textile, the higher number of rovings resulted in slightly decreased f_{fu}, due to that the rovings did not fail simultaneously as occurred in case of 4 rovings. In both layouts of coated carbon fibre textile, high variability was observed among the samples tested. This is attributed to the epoxy resin coating, which resulted in misalignment of the textile. In addition, the abrupt and not uniform rupture of the textile resulted in different f_{fu} values among the two tests (see Tables 4.3 and 4.4).

Also, in carbon fibre textile, the increased number of rovings, resulted in misalignment of the textile, and this can explain the response of the carbon fibre textile at early stage of loading (see Fig. 4.6a).

4.6.2 Tensile tests on TRM specimens

The mechanical properties of the fibre textile materials can be obtained either by direct tensile tests on the fibre-textiles, or by tensile tests on TRM coupons, which include the contribution of the mortar in the response of the TRM composite material.

Uniaxial tensile tests were also carried out on three TRM coupons of each textile material, namely carbon, coated carbon, coated basalt and glass by Raoof et al. (2017) and Tetta et al. (2018) using textiles of similar geometry with this study. The geometry and the experimental setup is presented in Fig. 4.8. A universal testing machine of 200 KN capacity was used for the load application at a displacement rate equal to 0.02 mm/s. Two LVDTs were positioned to monitor the elongation of the gauge length, one on each face of the coupon (Fig. 4.8). The failure mode observed was textile rupture at the central region of the gauge length. The response of the TRM coupon comprise three different stages: (i) a linear elastic behaviour where the TRM mortar remains uncracked, (ii) a

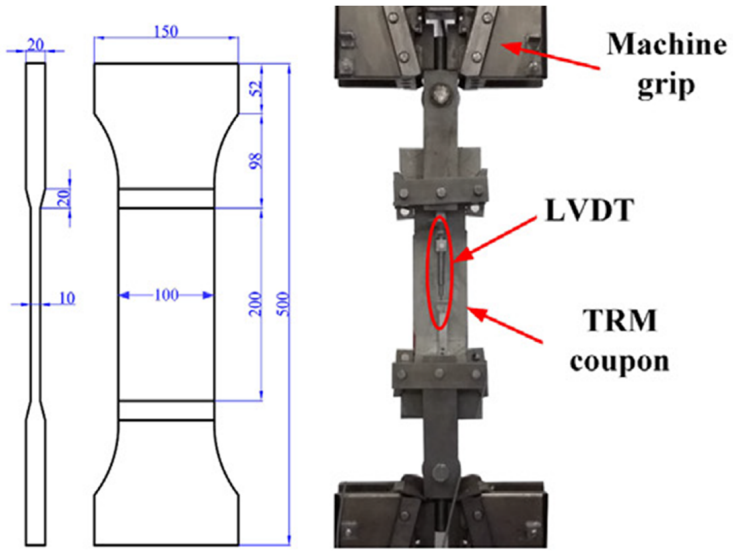


FIGURE 4.8: Experimental setup and geometry of the TRM coupon (Raoof et al., 2017)

TABLE 4.5: Tensile properties of TRM coupons of the fibre textiles (Raoof et al., 2017)

Textile materials	f_{fu} [MPa]	ϵ_{fu} [%]	E_f [GPa]
Carbon	1518(7.4)*	0.793(0.03)*	166.8(4.7)*
Coated carbon	2843(25.3)*	1.39(0.03)*	200.5(3.9)*
Coated basalt	1190(20.0)*	1.825(0.02)*	63.7(1.7)*
Glass	794(9.0)*	1.66(0.03)*	41.1(0.9)*

*Standard deviation

non-linear response where mortar cracking occurs and (iii) increase of the load until the maximum load is attained and fibres rupture occurs. The mechanical properties of the TRM coupons of Raoof et al. (2017) are presented in Table 4.5.

4.6.3 Discussion based on the experimental results of tensile tests

The uniaxial tensile tests on bare textiles demonstrated that the highest ultimate tensile stress and modulus of elasticity was observed in the coated carbon fibre

textile as shown in Tables 4.3 and 4.4. The coated glass and coated basalt fibre textiles resulted in similar response in terms of ultimate tensile stress and modulus of elasticity in both tests (see Tables 4.3 and 4.4). The epoxy resin coating was beneficial for the coated glass and coated carbon textile resulting in higher ultimate tensile stress and modulus of elasticity compared to the uncoated glass and carbon fibre-textile, respectively (see Tables 4.3 and 4.4).

The glass fibre textile demonstrated the lowest mechanical properties in both tests (Tables 4.3 and 4.4). The significantly low ultimate tensile stress obtained is attributed to the textile-knitting, which is such, resulting in a non-uniform stress distribution of the adjacent rovings in the weft and warp direction, visualised by slippage among the fibres and partial fibres rupture when the load was applied. In addition, the f_{fu} values obtained among the two experimental setups used were 40% different (Tables 4.3 and 4.4). Askouni and Papanicolaou (2019) used glass fibre textile of similar geometry and mechanical properties with this study and the f_{fu} obtained on the bare glass textile of 3 and 9 rovings width was 722 MPa and 822 MPa, respectively. These results show that different results obtained among different experimental setups and laboratories for the same material.

The ultimate tensile stress for basalt TRM and carbon TRM was 9% and 20% higher with respect to the textile tensile tests (Tables 4.3, 4.4 and 4.5). In addition, in case of coated basalt, coated glass and carbon bare textiles, slightly higher ϵ_{fu} was observed compared to the TRM coupons (Tables 4.3, 4.4 and 4.5). This is in agreement with Carozzi et al. (2017b) which reported that in some cases TRM tensile tests on dry textiles demonstrate better stress distribution which results in higher peak stress. This phenomenon is more pronounced in the dry textiles without any coating (De Santis et al., 2017). In addition, a

similar value of the ultimate tensile stress was observed for the coated basalt and coated carbon textile specimens (see Tables 4.3 and 4.4) with respect to the TRM coupons (see Table 4.5), which is in agreement with De Santis et al. (2017).

The ultimate tensile stress in glass TRM was (114%-197%) higher with respect to the bare textile tensile tests (Tables 4.3, 4.4 and 4.5). The glass textile resulted in reduced ultimate tensile stress due to the non-uniform stress distribution and slippage among the fibres with partial fibres rupture. This failure mode was prevented and textile rupture occurred when the mortar was applied on the glass TRM coupon, and the ultimate tensile stress was increased to 794 MPa (see Table 4.5). Hence, we consider the values derived from the TRM coupon tests as more reliable for the implicit characterisation of the textile fibre properties.

Leone et al. (2017) conducted tensile tests on glass TRM coupon of similar geometry and mechanical properties with this study in two different laboratories. Two different failure modes were observed, namely slippage of the textile within the mortar and textile rupture. When slippage of the textile occurred, a low tensile stress was reported equal to 369 MPa, whereas a higher value of 611 MPa was reported when textile rupture occurred. These experimental results demonstrate that different mechanical properties are obtained for the same textile between different laboratories.

A direct comparison of 1 layer of carbon-fibre textile (uncoated and coated), 3 and 7 layers of glass-fibre textile (uncoated and coated) and 3 and 7 layers of coated basalt-fibre textile, for both single and double walls, can be made. The number of 7 glass-fibre layers has been chosen on the basis of the axial stiffness similarity principle also utilised in Tetta et al., 2016.

The 7-layer glass and basalt fibre to single layer carbon axial stiffness ratio is

TABLE 4.6: Axial stiffness ratio

Manufacturer datasheets		Bare-textile	TRM coupon	
Glass	Coated basalt	Coated glass	Coated basalt	Glass
1.04	1.06	0.92	0.85	0.78

readily derived from the following expression using the manufacture datasheets values

$$\frac{n_{l,g}t_gE_{f,g}}{n_{l,c}\cdot t_cE_{f,c}} = \frac{7\cdot 0.044\cdot 74}{1\cdot 0.097\cdot 225} = 1.04$$

where $n_{l,g}$ is the number of glass fibre TRM layers, t_g is the nominal thickness of the glass textile, $E_{f,g}$ is the elastic modulus of the glass fibres, $n_{l,c}$ is the number of carbon fibre TRM layers, t_c is the carbon textile thickness and $E_{f,c}$ is the carbon modulus of elasticity. In case of coated basalt fibre textile the corresponding ratio is equal to 1.06. The aforementioned ratio using the textile coupon tests for coated glass/ coated carbon is equal to 0.92. The ratio for the coated basalt/ coated carbon TRM coupon is 0.85, and for the uncoated glass/ carbon is 0.78 (see Table 4.6). Thus, a direct comparison of the strengthening performance of the three materials utilised can be achieved as discussed in Section 6.4.

Clearly, the values of the ultimate stress and the modulus of elasticity obtained from the manufacturer datasheets were substantially larger compared to the coupon test results as the former were based on fibre rather than textile mesh tests. This is also shown by the equivalence of 1 layer of carbon (coated/ uncoated) with 7 layers of glass (coated/ uncoated) or coated basalt, in terms of axial stiffness which is different when the coupon tests results were used. Therefore, the coupon tests conducted in this study were mandatory.

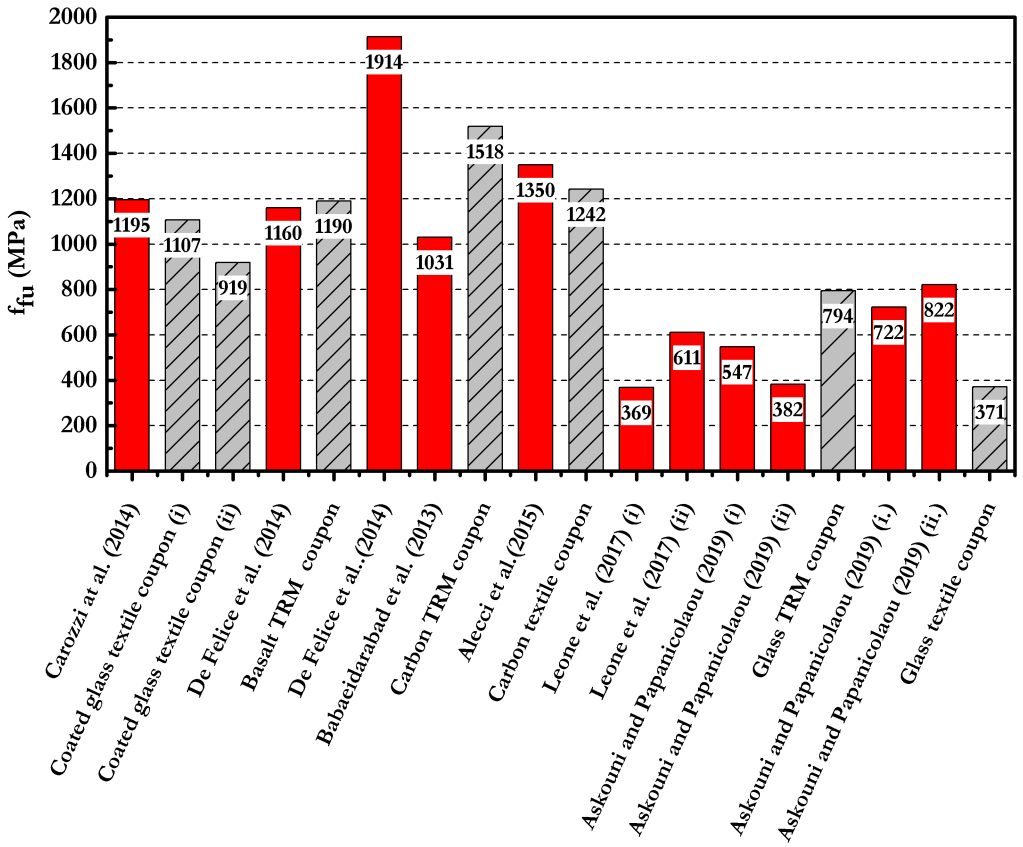


FIGURE 4.9: Comparison of the ultimate tensile stress between published and current study

4.6.4 Comparisons with published test results

Carozzi et al. (2014) used coated glass textile with Styrene Butadiene Rubber (SBR) of different mesh size in one direction (17 x 12 mm), compared to this study, to define the tensile properties of the bare textile. The ultimate tensile stress obtained was 1217 MPa and 1178 MPa in wrap and weft direction, respectively. The response is similar to that of the epoxy resin coated glass textile used in this study (see Fig. 4.9).

De Felice et al. (2014) used carbon of 10 mm mesh size, 0.047 mm thickness and bitumen coated basalt of 20 x 20 mm mesh size and 0.035 mm nominal

thickness to define the tensile properties of TRM coupons. The ultimate tensile stress and modulus of elasticity of carbon and coated basalt were (1914 MPa and 189.4 GPa), and (1160 MPa and 67 GPa), respectively. The geometry of the coated basalt textile was slightly different to this study, however resulted in similar f_{fu} as shown in Fig. 4.9. In addition, similar mesh size and different thickness of the carbon textile resulted in 26% higher f_{fu} with respect to this work (see Fig. 4.9).

In addition, Alecci et al. (2015) conducted tensile tests on bare textiles using a similar geometry mesh size (9 x 9 mm) and 0.047 mm nominal thickness of carbon textile, compared to this study. The ultimate tensile stress and modulus of elasticity were equal to 1350 MPa and 244 GPa, respectively. The similar mesh size and different thickness of the carbon textile demonstrated slightly different properties with respect to this study (see Fig. 4.9).

Babaeidarabad et al. (2013) carried out TRM tensile tests on carbon fibre-textile of similar mesh size (10 x 10 mm) but lower nominal thickness equal to 0.048 mm, compared to this study. This resulted in lower ultimate tensile stress and modulus of elasticity, equal to 1031 MPa and 80 GPa, respectively, with respect to the current work. This demonstrates that not only the mesh size but also the nominal thickness contributes to the mechanical properties of the fibre-textile.

Askouni and Papanicolaou (2019) executed tensile tests on bare textiles and TRM coupons, using glass fibre-textile of 12 x 12 mm mesh size but slightly higher thickness of 0.064 mm, compared to this work. The tensile stress and modulus of elasticity obtained when 1 layer of 3 and 9 rovings textile width of bare textiles were used was (722 MPa and 70 GPa) and (822 MPa and 71 GPa), respectively. In addition, the TRM coupon f_{fu} using a 9-roving textile width

was determined equal to 546.5 MPa and 381.6 MPa for 1 and 2 TRM layers, respectively. These results show that different tensile properties are obtained for the same textile.

Leone et al. (2017) carried out tensile tests on glass TRM coupon tests using 15 x 15 mm mesh size and equivalent thickness of 0.04 mm, which are slightly different compared to this work. The TRM tensile stress obtained was 369 MPa and 611 MPa, in two different laboratories.

Figure 4.9 demonstrates the ultimate tensile stress obtained in the aforementioned experimental studies. Different tensile properties were obtained among the carbon TRM coupon of Babaeidarabad et al. (2013) and De Felice et al. (2014) with respect to this study, where different nominal thickness of the carbon textile was used. In addition, a significant difference was observed among the bare glass tensile tests and the glass TRM coupon tests. This shows the significance of the material characterization tests together with the geometry and properties of the textile. Therefore is important to be reported in each experimental work.

4.7 Epoxy resin

Epoxy-resin coating was applied in-house in dry glass and carbon fibre-textiles. The coating procedure was performed by impregnating the fibre-textile materials in a commercial epoxy adhesive (two-part epoxy resin with a mixing ratio 2:1 by weight). The epoxy resin elastic modulus was 1.8 GPa and the tensile strength was 37 MPa, according to the manufacturer datasheets. The impregnation of fibre-textiles was performed using a plastic roll, and then left to cure for two days before the strengthening application (see Fig. 4.10). The textile mesh holes were not covered after the coating procedure. The average amount of the epoxy resin used for the impregnation was 180 g/m^2.

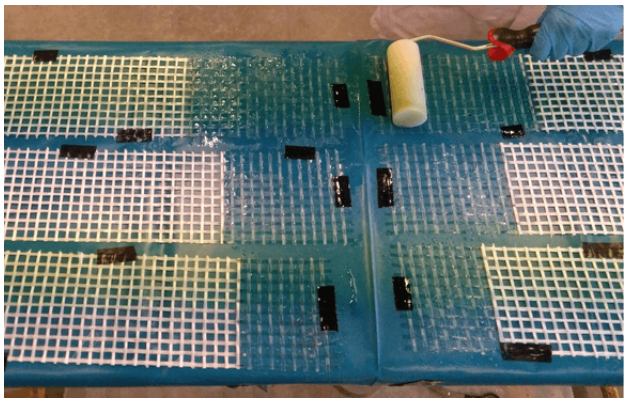


FIGURE 4.10: Impregnation of the glass textile in epoxy resin

4.8 Conclusions

In this Chapter, are presented all the pertinent mechanical properties for the materials used in this work, for conducting experimental work on masonry walls, and arches. The significance of conducting tensile tests on fibre-textiles and TRM coupon tests, has been clearly shown to explain the experimental results and conclude in accurate and reliable conclusions. In addition, the different ratio, in terms of axial stiffness, obtained by using coupon test results and manufacturer datasheets values also indicates the importance of the coupon tests. The high accuracy of the experimental results is shown by the low value of the Coefficient of Variation of f_{fu}, ϵ_{fu} and E_f values observed in the two series of the tensile tests, which were equal to (0.04-0.14), (0.03-0.17) and (0.01-0.15), respectively.

Chapter 5

Bond between TRM and masonry substrate

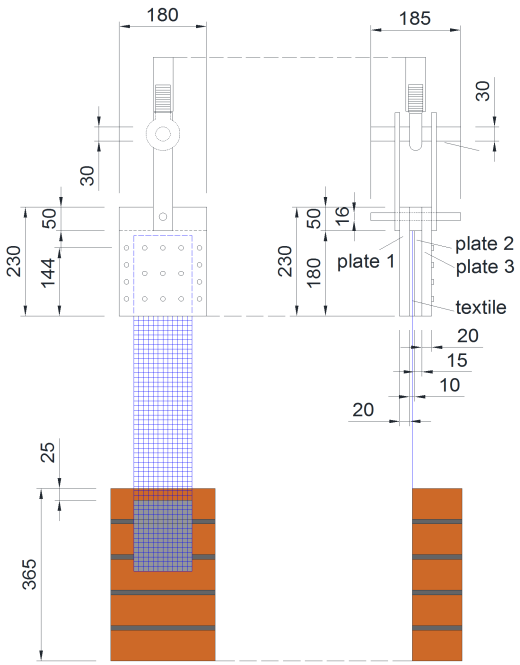
5.1 Introduction

In this Chapter, the experimental campaign undertaken to investigate the bond behaviour between the TRM material and the masonry substrate is presented, using different bond lengths and fibre-textile materials, and epoxy-resin coating. In the following, the experimental program is thoroughly described. Next, the experimental results are demonstrated. Following, the discussion is provided based on the experimental results obtained. Finally, the conclusions are drawn based on the discussion provided.

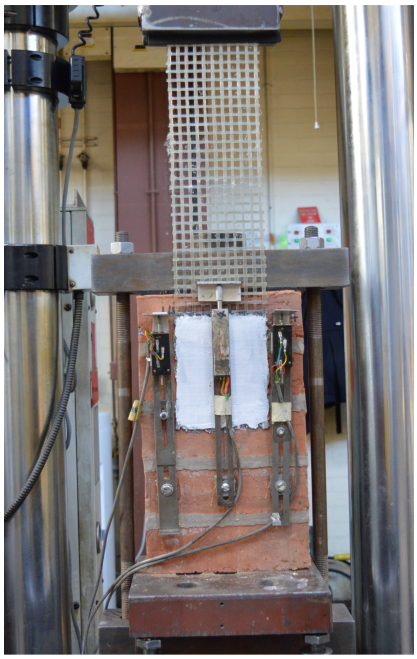
5.2 Experimental Program

5.2.1 Test specimens and investigated parameters

The main objective of this experimental study was to investigate the bond behaviour between the TRM composite material and brick masonry walls. Thirty



(a)



(b)

FIGURE 5.1: Experimental setup - all units are in mm (a) geometry and load configuration, (b) actual setup of G_co_150 specimen

TABLE 5.1: Specimens details

Specimen	**TRM material**	**TRM thickness [mm]**	**Coating**
C_100_a C_100_b C_150_a C_150_b C_200_a C_200_b	Carbon	3	No
C_co_100_a C_co_100_b C_co_150_a C_co_150_b C_co_200_a C_co_200_b	Coated carbon	5	Yes
G_100_a G_100_b G_150_a G_150_b G_200_a G_200_b	Glass	3	No
G_co_100_a G_co_100_b G_co_150_a G_co_150_b G_co_200_a G_co_200_b	Coated glass	5	Yes
B_100_a B_100_b B_150_a B_150_b B_200_a B_200_b	Coated basalt	5	No

masonry brick walls in total were built of 365 x 215 x 102.5 mm dimensions, in a running bond pattern. The mortar used for the construction of the walletes was a general purpose cement mortar of approximately 10 mm thickness for both bed and head joints.

The key investigated parameters of this study were: (a) the bond length, (b) the textile-fibre material, namely carbon, glass and coated basalt, and (c) the epoxy-resin coating. Specimens were strengthened in five groups of six specimens for each textile material (2 identical specimens for each bond length of 100 mm, 150 mm, 200 mm). All the specimens were strengthened with a single TRM layer of each fibre-textile material (see Table 5.1).

The wall specimens with their corresponding parameters are shown in Table 5.1. The strengthening configuration is shown in Fig. 5.1a while the actual test setup is shown in Fig. 5.1b. The notation considered for the specimens is X_BL_N, where X denotes the type of the textile (C for carbon, G for glass and B for coated basalt), BL denotes the bond length (100 mm, 150 mm, 200 mm) and N denotes the number of the twins specimens (a, b). The suffix co denotes textiles coating with epoxy resin (see also Table 5.1).

5.2.2 Materials

The specimens for the bond tests were constructed with solid clay bricks of UK typical nominal dimensions. The mechanical properties of the bricks and masonry walletes are described in Sections 4.2 and 4.4, respectively. For each specimen, the flexural and compressive strength of the joint and strengthening mortar were determined by conducting a series of three-point bending and compressive strength tests as shown in Sections 4.3 and 4.5, respectively. Table 5.2 demonstrates the mean values of the flexural and compressive strength of

joint and strengthening mortar, together with their standard deviation and the coefficient of Variation. Higher variability is presented in casting mortar compressive and tensile strength with respect to strengthening mortar. However, it is highlighted that the results and failure modes observed were not influenced by the variability observed.

The fibre-textile materials utilised were the carbon-fibre textile (either uncoated or coated with epoxy resin), the glass-fibre textile (uncoated or coated with epoxy resin) and the coated basalt-fibre textile. The different configurations and the mechanical properties of the textiles obtained from the manufacturer datasheets and from uniaxial tensile tests on bare textiles and TRM coupons are described in Section 4.6.

It is highlighted that the coated basalt fibre-textile is a commercial product fabricated with a bituminous binder of 10 % content. The coated carbon and coated glass fibre textiles were impregnated in a commercial epoxy adhesive as further described in Section 4.7.

The cement-based mortar used to bond the fibre-textile on the masonry substrate is described in Section 4.5. The mean values of flexural and compressive strength on the day of testing were 8.43 MPa and 37.48 MPa, respectively as shown in Table 5.2. The compatibility between the inorganic matrix and the fibre-textile has been investigated and the advantages of using compatible mortar mixes for each textile fibre material have been documented, see, e.g., (Leone et al., 2017; Lignola et al., 2017; Carozzi et al., 2017b; Bernat et al., 2013; Harajli et al., 2010). In this experimental study similar mortar was utilised for the application of the TRM composite for all the specimens with the objective to compare the experimental results with respect to the investigated parameters, namely the different bond length, the effect of the textile material, and the epoxy

resin coating of the textile.

5.2.3 Strengthening procedure

The application of the TRM material was performed with the following procedure:

1. The dust was removed from the specimen surface using air pressure.
2. After dampening the wallete a first layer of mortar was applied at the bond surface as presented in Fig. 5.2a.
3. The textile layer was impregnated into the previously applied mortar layer using hand pressure (Fig. 5.2b).
4. A final layer of mortar was applied to completely cover the textile. The procedure was completed while the mortar was fresh to achieve optimum adhesion of the TRM layers. The strengthened specimen is shown in Fig. 5.2c.

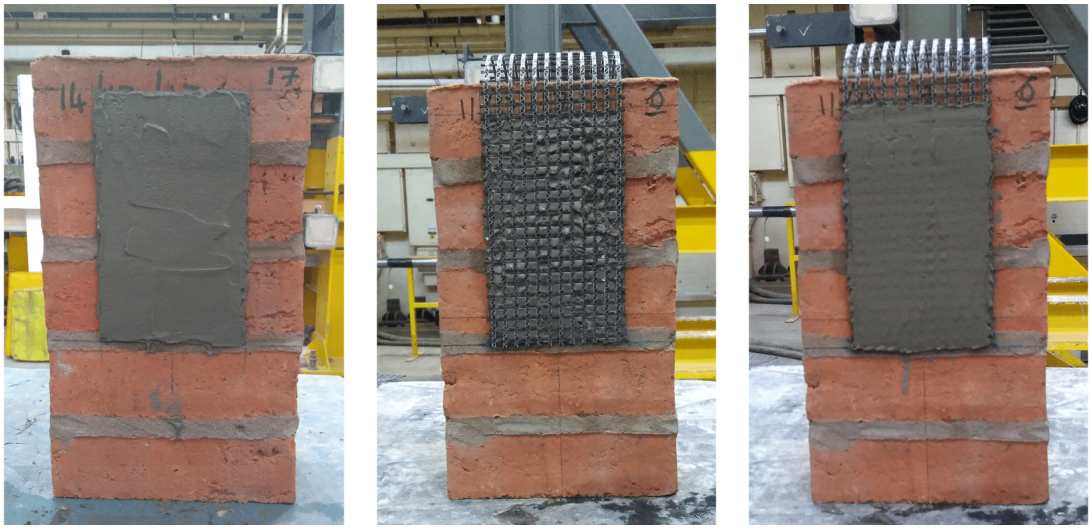
5.2.4 Experimental setup and procedure

The experimental setup comprised a single-lap shear bond setup of 5 bricks and 10 mm mortar thickness (Fig. 5.1). The single and the double-lap setup have been reported in the literature considering the setup preparation and the accuracy of the results of each method (see Section 3.3). For this experimental investigation the single-lap was adopted which is a simple setup to avoid technical difficulties and provides a valid post-peak response as reported in Sneed et al. (2015) and De Felice et al. (2018). It is highlighted that a particular attention

TABLE 5.2: Casting and strengthening mortar

Specimens	Casting mortar		Strengthening mortar	
	Compressive Strength [MPa]	Tensile Strength [MPa]	Compressive Strength [MPa]	Tensile Strength [MPa]
C_100_a C_100_b C_150_a C_150_b C_200_a C_200_b	7.25	2.01	40.75	8.45
C_co_100_a	8.91	1.87	34.89	7.57
C_co_100_b	8.89	1.92		
C_co_150_a	8.91	1.87		
C_co_150_b	8.89	1.92		
C_co_200_a	8.91	1.87		
C_co_200_b	8.91	1.87		
G_100_a	9.01	2.77	34.89	7.57
G_100_b	8.91	1.87		
G_150_a	8.91	1.87		
G_150_b	9.01	2.77		
G_200_a	9.01	2.77		
G_200_b	9.01	2.77		
G_co_100_a G_co_100_b G_co_150_a G_co_150_b G_co_200_a G_co_200_b	8.89	1.92	36.13	10.09
B_100_a	9.39	2.35	40.75	8.45
B_100_b	9.39	2.35		
B_150_a	7.25	2.01		
B_150_b	9.39	2.35		
B_200_a	7.25	2.01		
B_200_b	9.39	2.35		
Mean value	8.54 (0.81*/0.09**)	2.10 (0.31*/0.15**)	37.48 (2.75*/0.07**)	8.43 (0.94*/0.11**)

*Standard deviation/ **Coefficient of Variation



(a) (b) (c)

FIGURE 5.2: (a) Application of the first layer of mortar, (b) impregnation of the carbon textile into the mortar and (c) application of the final layer of mortar

is required during the preparation of the setup and during testing to avoid misalignment among the steel frame and the specimen and prevent out-of-plane phenomena and misalignment of the textile.

The specimen was positioned as shown in Fig. 5.1b and clamped using 2 metal plates and 2 threaded rods to keep it in position during testing. The bare textile was clamped between the metal plates shown in Fig. 5.1a, which were connected to a joint providing rotational capacity. The metal plates with the textile inside were pulled from above through the mechanism presented in Fig. 5.1a. The TRM material was un-bonded at a 25 mm long to prevent stress concentrations as reported in (De Felice et al., 2014). A universal testing machine of 1000 kN capacity was adopted for the load application at a displacement rate of 0.02 mm/s. Two potentiometers were applied close to the bond region at the masonry substrate and one at the textile to measure the displacement of the bonded material as shown in Fig. 5.1b. Data was collected at a frequency of

4 Hz, synchronised and recorded using a fully-computerized data acquisition system.

5.3 Experimental Results

The load versus crossed-head displacement curves for all the specimens including all the bond lengths and fibre-textile materials investigated is presented in Fig. 5.3. The potentiometers applied on the textile to measure the bond slip did not provide reliable results due to malfunction of the potentiometers. Therefore the displacement presented in Fig. 5.3 is the cross-head displacement of the Universal testing machine. However, in this experimental work it was important to define the maximum load obtained at the time of failure, to further explain the masonry walls tests response (see Chapter 6). In particular, the maximum load of the bond tests is used to calculate the bond axial stress developed at the textile (f_b) and compare it with the coupon tests ultimate tensile stress (f_{fu}) and masonry walls tests results.

In addition, the potentiometers applied at the masonry substrate close to the bond region resulted in zero displacement during the test, therefore the results are not presented.

To obtain more accurate results in terms of the displacement at the bonded region, in Fig. 5.4 the bond displacement was defined by deducting the elongation of the bare textile, which was not bonded, from the cross-head displacement. The elongation of the unbonded length of the textile was determined as the product of the ultimate strain ϵ_{fu} of the bare textiles coupon tests (see Chapter 4) times the unbonded textile length. The ultimate strain corresponds to rupture of the textile when the maximum load was attained at the bond tests.

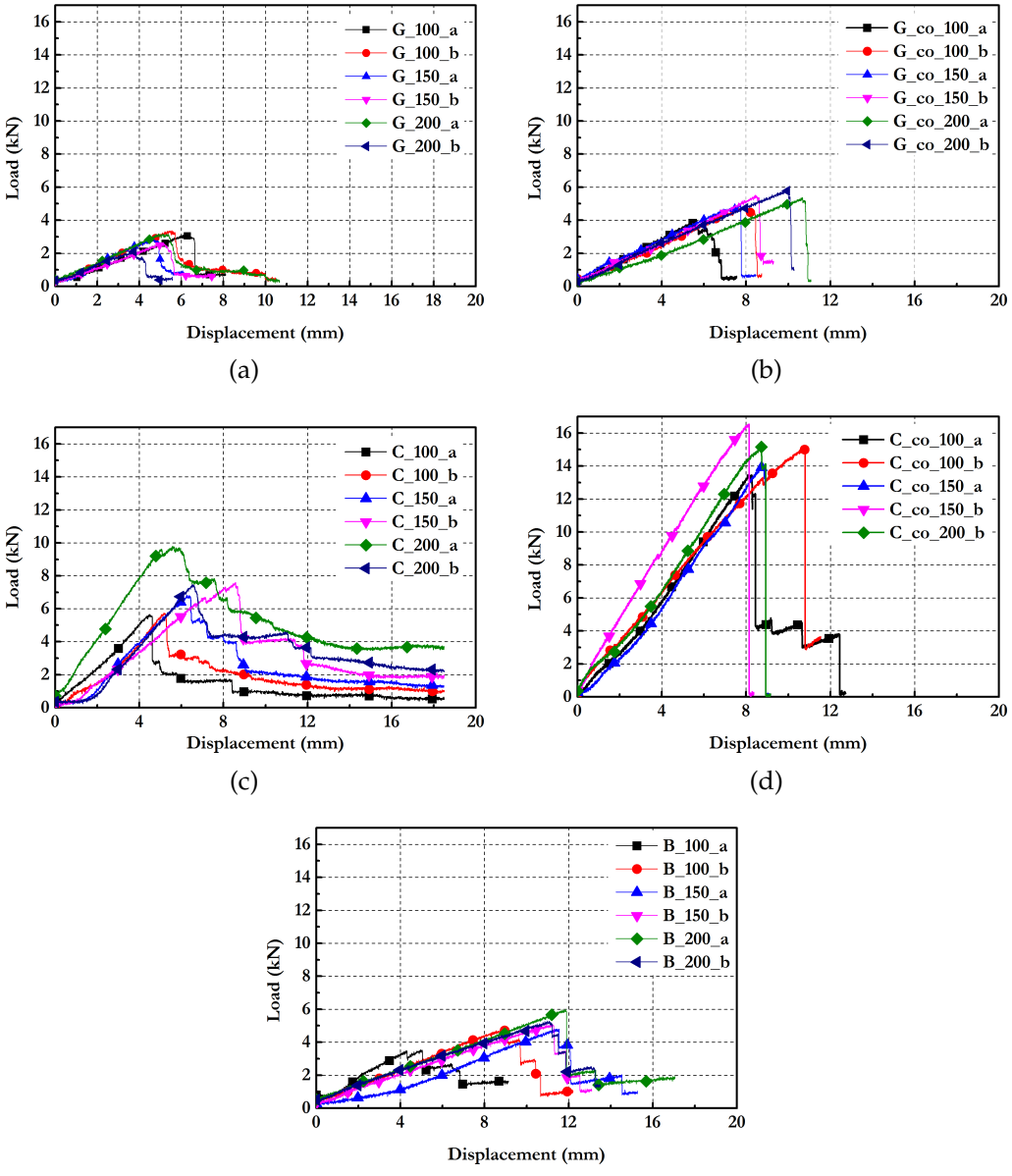


FIGURE 5.3: Experimental load cross-head displacement curves for (a) the glass fibre-textile, (b) the coated glass fibre-textile, (c) the carbon fibre-textile, (d) the coated carbon fibre-textile and (e) coated basalt fibre-textile

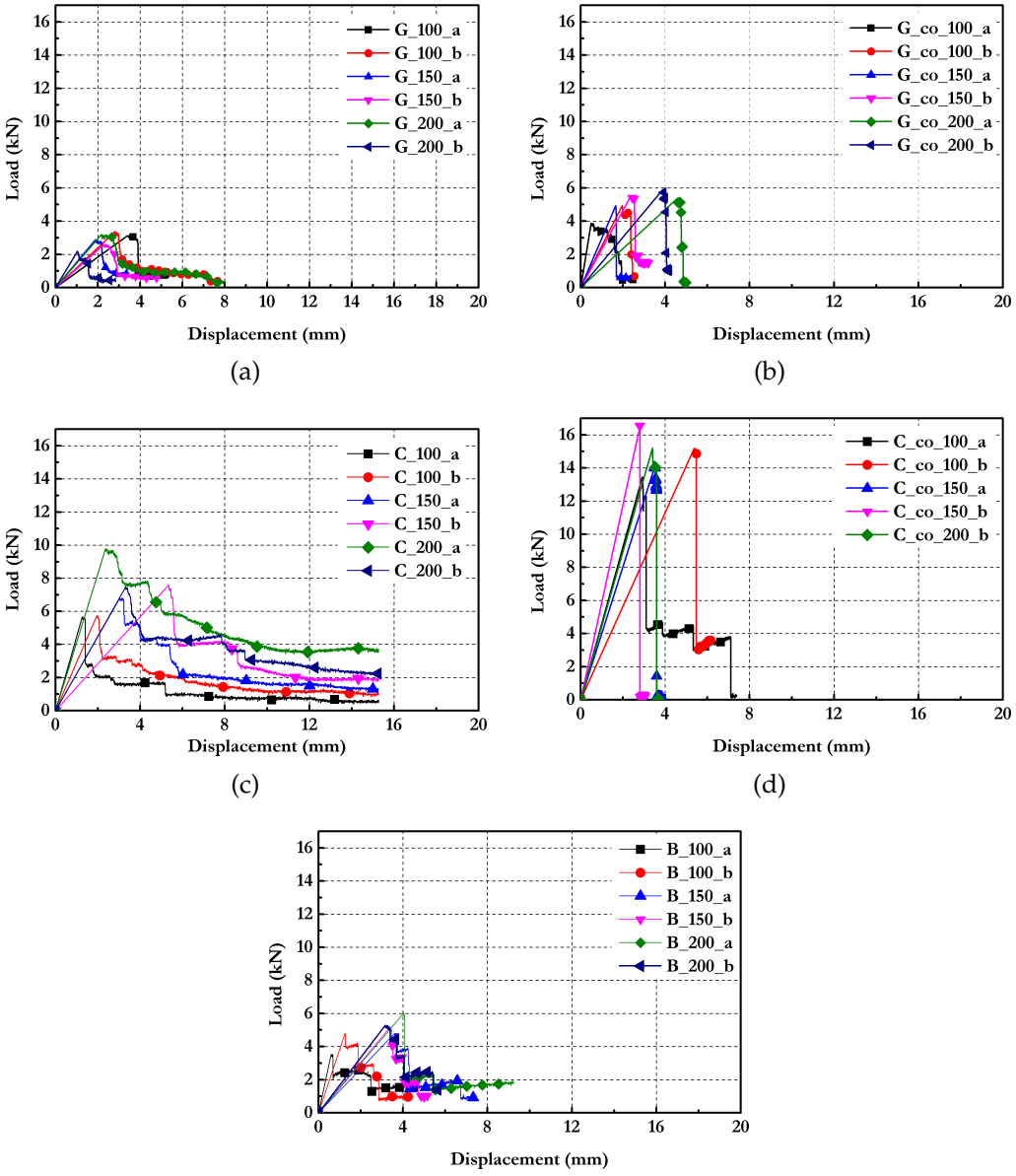


FIGURE 5.4: Experimental load-displacement curves for (a) the glass fibre-textile, (b) the coated glass fibre-textile, (c) the carbon fibre-textile, (d) the coated carbon fibre-textile and (e) coated basalt fibre-textile

The identified key parameters of the experimental results, i.e., the maximum load (P_{max}), the corresponding displacement at maximum load (D_{max}), the average maximum load (P_{av}) together with the standard deviation and the coefficient of Variation, the average displacement at maximum load (D_{av}) and the observed failure modes are summarised in Table 5.3. The corresponding failure modes are shown in Fig. 5.5 and Fig. 5.6 for all specimens. The experimental results are grouped for each fibre-textile utilised in ascending order of the bond length.

All the load-displacement curves demonstrated an ascending linear branch up to the maximum load (see Fig. 5.3). The post-peak behaviour was controlled by the different failure mode observed due to the different textile material utilised and the presence of coating or not. These were (a) slippage between textile-matrix interface (b) debonding at the fibre textile-matrix interface (tensile failure of the mortar layer) and (c) fibre-textile rupture close or out of the bonded area.

All the specimens strengthened with dry carbon fibre-textile material failed due to slippage of the carbon fibres at the textile-matrix interface. The average reported maximum load and the corresponding displacements were (5.7 kN, 4.8 mm), (7.2 kN, 7.4 mm) and (8.6 kN, 6.1 mm), for each bond length of 100 mm, 150 mm, and 200 mm, respectively (see also Table 5.3). A slightly higher variability of the maximum load was observed for the larger bond length of 200 mm compared to rest of the specimens (Table 5.3). At early stage of loading, hairline cracks initiated from the left towards to the right at the edge of the bonded region, which was followed by slippage of the textile through the mortar as presented in Figs. 5.5a-5.5c. As shown in Fig. 5.3c the post-peak response of the load displacement curve was characterised by a progressive load-drop to a

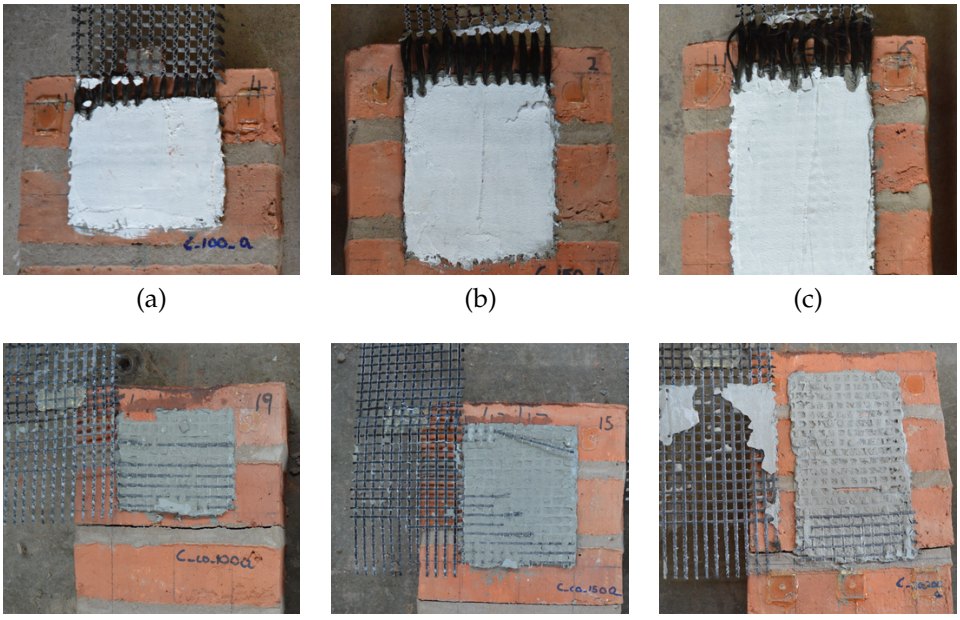
residual strength, which was more pronounced in the longest bond length of 200 mm with respect to the shortest bond lengths (100 mm, 150 mm).

The specimens strengthened with coated carbon fibre-textile material failed due to debonding at the textile-matrix interface with tensile failure of the matrix (see Figs. 5.5d-5.5f) coated carbon textile. The average reported maximum load and the corresponding displacements were (14.3 kN, 9.4 mm), (15.3 kN, 8.5 mm) and (15.2 kN, 8.5 mm), for each bond length of 100 mm, 150 mm, and 200 mm, respectively (see also Table 5.3). Due to high variability of the maximum load in case of 200 mm bond length, the maximum load of C_co_200_a was neglected when the average load was derived (Table 5.3). This occurred due to the low performance of C_co_200_a, which resulted in a lower maximum load with respect to the 100 mm length.

When the load was near the maximum load, hairline cracks were formed at the edge of the bonded region, in specimens with anchorage length of 150 mm and 200 mm. This was followed by a gradual tensile failure of the mortar layer which resulted in complete detachment of the textile from the cementitious matrix as shown in Figs. 5.5d-5.5f. In this case a sudden load-drop occurred as presented in Fig. 5.3d.

Specimens strengthened with dry glass TRM material failed due to slippage between the fibres of each roving combined with textile rupture when the maximum load was attained (Figs. 5.6a-5.6c). The average of the maximum load attained and the corresponding displacement were (3.3 kN, 5.9 mm), (2.7 kN, 4.8 mm) and (2.7 kN, 4.3 mm), for 100 mm, 150 mm, and 200 mm bond length, respectively (see also Fig. 5.3a and Table 5.3).

Specimens strengthened with coated glass fibre textile composite failed due to textile rupture when the maximum load was attained (Figs. 5.6d-5.6f). The



(a) (b) (c)

(d) (e) (f)

FIGURE 5.5: Failure modes of specimens strengthened with (a)-(c) dry carbon textile, (d)-(f) coated carbon textile

average peak load and the corresponding displacement were (4.4 kN, 6.7 mm), (5.2 kN, 8.1 mm) and (5.7 kN, 10.3 mm), for the anchorage length of 100 mm, 150 mm, and 200 mm, respectively (see also Fig. 5.3b and Table 5.3). In addition, slightly higher variability of the maximum load was observed for the shortest bond length (100 mm) compared to rest of the specimens.

When the bond length was 200 mm rupture of the textile occurred only at the bonded region. Before the failure of the textile, specimens with bond length of 150 mm formed hairline cracks when the maximum load was almost attained at the edge of the bonded area. Whereas for the longest reinforcement of 200 mm, hairline cracks initiated at early stage of loading at the edge of the TRM (Figs. 5.6d-5.6f).

Specimens strengthened with coated basalt fibre-textile material failed due

to textile rupture when the maximum load was attained as shown in Figs. 5.6g-5.6i. The average recorded values of the maximum load and the corresponding displacements were (4.2 kN, 7.0 mm), (5.0kN, 11.3 mm) and (5.7 kN, 11.4 mm) for the bond lengths of 100 mm, 150 mm, and 200 mm, respectively (see also Table 5.3). The highest coefficient of Variation of the maximum load for the coated basalt textile was observed in case of the bond length of 100 mm.

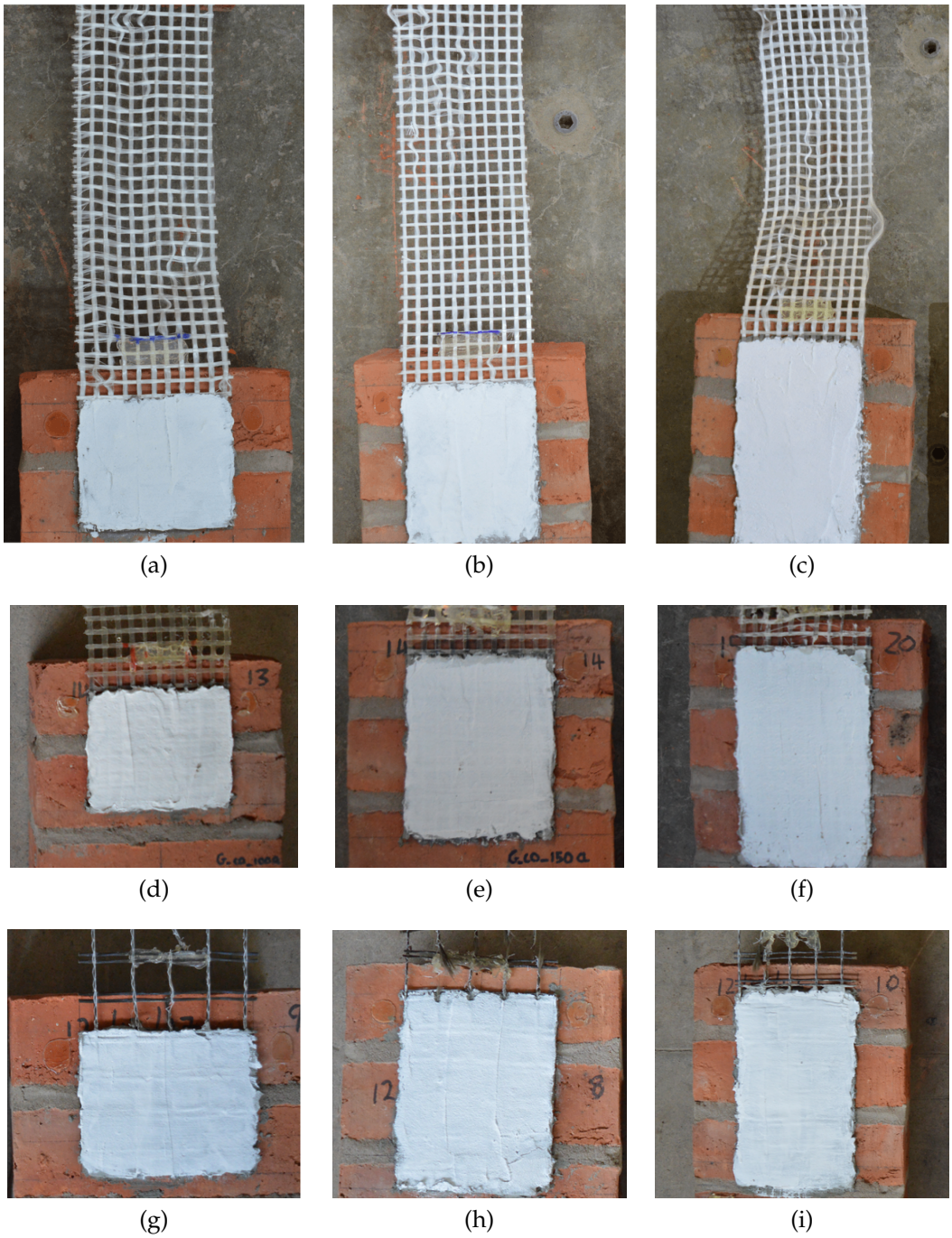
Hairline cracks were formed during the linear part of the load-displacement curve at the border of the TRM material (see Fig. 5.3e). In particular, for the bond length of 100 mm, rupture of the fibre-textile occurred out of the bonded region as shown in Fig. 5.6g. For the anchorage lengths of 150 mm and 200 mm, rupture of the textile was observed adjacent to the bonded area as presented in Fig. 5.6h and Fig. 5.6i, respectively.

5.4 Discussion

5.4.1 Effect of the bond length on different textile materials

The effect of the bond length on the average load capacity of each of the fibre-textiles utilised is presented in Fig. 5.7. All the different textiles demonstrated increase of the maximum load when the bond length was increased up to a certain bond length where tends to reach a constant value. This bond length is known as the effective bond length (L_{eff}) and for each fibre-textile was different.

The similar ascending trend of the load vs bond length curve in Fig. 5.7 of both coated glass and coated basalt fibre-textile demonstrated an effective length (L_{eff}) greater than or equal to 200 mm. A similar response of the carbon fibre textile resulted in an effective length greater than or equal to 200 mm.



(a) (b) (c)

(d) (e) (f)

(g) (h) (i)

FIGURE 5.6: Failure modes of specimens strengthened with (a)-(c) dry glass textile, (d)-(f) coated glass textile, (g)-(i) coated basalt textile

TABLE 5.3: Summary of experimental results

Specimen	P_{max} [kN]	D_{max} [mm]	P_{av} [kN]	D_{av} [mm]	Failure mode
C_100_a	5.66	4.48	5.7 (0.06*/0.01**)	4.8	Slippage***
C_100_b	5.74	5.18			
C_150_a	6.82	6.27	7.2 (0.55*/0.08**)	7.4	
C_150_b	7.60	8.57			
C_200_a	9.79	5.58	8.6 (1.63*/0.19**)	6.1	
C_200_b	7.48	6.53			
C_co_100_a	13.45	8.07	14.3 (1.22*/0.09**)	9.4	Debonding****
C_co_100_b	15.18	10.71			
C_co_150_a	14.04	8.83	15.3 (1.77*/0.12**)	8.5	
C_co_150_b	16.55	8.14			
C_co_200_a	10.16	8.21	15.2 (3.56*/0.28**)	8.5	
C_co_200_b	15.20	8.69			
G_100_a	3.13	6.15	3.3 (0.18*/0.05**)	5.9	Textile rupture
G_100_b	3.38	5.55			
G_150_a	2.88	4.61	2.7 (0.19*/0.07**)	4.8	
G_150_b	2.61	5.03			
G_200_a	3.19	4.90	2.7 (0.71*/0.26**)	4.3	
G_200_b	2.19	3.78			
G_co_100_a	3.88	5.38	4.4 (0.74*/0.17**)	6.7	Textile rupture
G_co_100_b	4.93	8.03			
G_co_150_a	4.93	7.73	5.2 (0.41*/0.08**)	8.1	
G_co_150_b	5.51	8.44			
G_co_200_a	5.38	10.66	5.7 (0.38*/0.07**)	10.3	
G_co_200_b	5.92	9.98			
B_100_a	3.55	4.96	4.2 (0.90*/0.21**)	7.0	Textile rupture
B_100_b	4.82	9.07			
B_150_a	4.80	11.32	5.0 (0.24*/0.05**)	11.3	
B_150_b	5.14	11.18			
B_200_a	6.02	11.85	5.7 (0.52*/0.09**)	11.4	
B_200_b	5.29	10.98			

*Standard deviation
**Coefficient of variation
***between textile and mortar substrate
****at textile to mortar interface (tensile rupture of mortar)

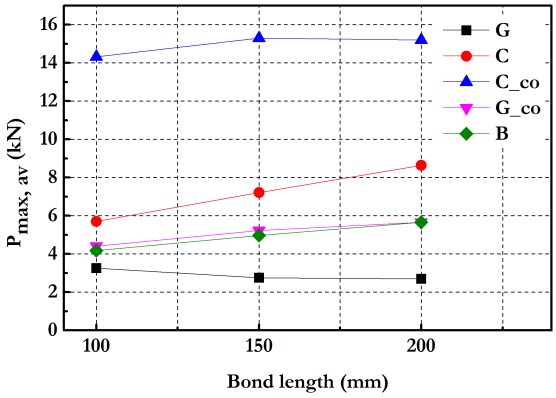


FIGURE 5.7: Maximum load vs bond length curve

TABLE 5.4: Exploitation of textile strength

Specimen	f_b [MPa]	f_{fu} [MPa]	Exploitation of textile strength [%]
C_100	490		32
C_150	619	1518	41
C_200	742		49
C_co_100	1230		43
C_co_150	1314	2843	46
C_co_200	1306		46
G_100	560		71
G_150	473	794	60
G_200	463		58
G_co_100	758		69
G_co_150	899	1107	81
G_co_200	973		88
B_100	905		77
B_150	1074	1190	92
B_200	1223		104

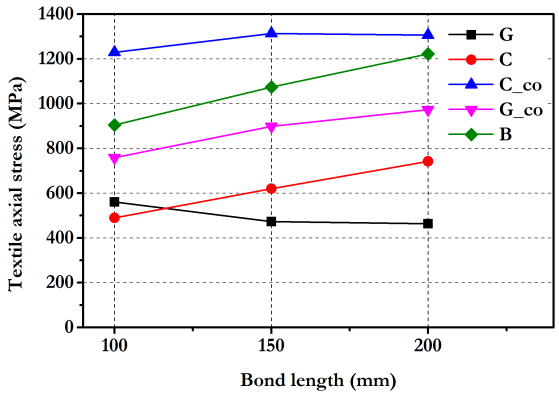


FIGURE 5.8: Bond stress of textile vs bond length curve

The maximum load of the coated carbon fibre textile material was increased from 100 mm up to the 150 mm and remained constant until the bond length of 200 mm, which means that (L_{eff}) was decreased compared to the dry carbon textile between 150 mm and 200 mm. This occurred due to the effect of epoxy resin coating which improved the bonding conditions as further discussed in Section 5.4.2 resulting in decreased anchorage length.

The glass fibre textile material resulted in similar values of the maximum load for different anchorage lengths (Fig. 5.7). The dry fibre-textile knitting is such resulting in a non-uniform stress distribution of the adjacent rovings in the weft and warp direction, which results in textile rupture out of the bond length region as shown in Figs. 5.6a-5.6c. Therefore an effective bond length could not be derived in this case (see Fig. 5.8 and Table 5.4).

The coated glass and coated basalt fibre textiles demonstrated an identical response in terms of the maximum load (Fig. 5.7). In terms of bond axial stress, coated basalt resulted in 20%, 20%, and 26% increased values, with respect to coated glass for 100 mm, 150 mm and 200 mm, bond lengths respectively (Fig. 5.8). The similar response observed in both materials is attributed to the textile rupture failure mode which occurred in both specimens. The higher bond

stress of 20%-26% observed in case of coated basalt textile, shows its superior behaviour compared to the coated glass textile material due to the actual roving surface of each fibre-textile.

The use of the mechanical properties of each textile was quantified through the ratio of the bond axial stress (f_b) to the ultimate tensile stress (f_{fu}) presented in Chapter 4. The exploitation of the textile strength in all the materials was increased when the bond length was increased as shown in Table 5.4. It is highlighted that the coated basalt fibre-textile material demonstrated the highest exploitation of the textile strength (77%-104%) due to the textile rupture failure mode and the geometry of the textile. Dry and coated carbon fibre-textile showed the minimum exploitation of the textile (32%-46%) due to the failure modes observed. In particular, slippage between the textile-mortar substrate and tensile failure of the mortar layer without evolving rupture of the textile resulted in decreased bond stress values. In addition, the exploitation of the coated glass fibre textile for the largest bond length (200 mm) was 88%, close to the unity value, due to the textile rupture failure mode. In case of the glass textile the exploitation of the textile strength was 58%-71% (see Table 5.4). It is lower than unity due to the bond test setup and the textile knitting, which underestimates the bond stress.

5.4.2 Effect of coating

In coated carbon the maximum load was increased by 151%, 112%, and 76% compared to dry carbon, for bond lengths equal to 100 mm, 150 mm and 200 mm, respectively (see Table 5.4). Higher values were observed due to the effect of coating which improved the interlocking conditions among the textile fibres and the cementitious mortar resulting in enhanced bonding strength. The load

increase was more pronounced at the shorter bond length where the bonding strength was not entirely developed as at the longer reinforcements (Fig. 5.7). Apart from the load increase, coating modified the slippage failure mode to debonding at the fibre textile-matrix interface combined with tensile failure of the mortar layer (see Figs. 5.5d-5.5f).

In coated glass specimen the maximum load attained was increased by 35%, 90%, and 110%, with respect to dry glass fibre textile for 100 mm, 150 mm, and 200 mm bond length, respectively. The effect of coating in coated glass TRM specimen in terms of bond axial stress was pronounced in the longer bond lengths of 150 mm and 200 mm where the coated glass textile developed further its bond axial stress and the exploitation of the textile was maximised (see also Fig. 5.8). The epoxy resin coating modified the weak dry glass textile to rigid, resulting in a uniform stress distribution. Therefore, the rupture of the coated textile occurred close to the bond length area (Figs. 5.6d-5.6f) mainly when the bond length was maximised to 200 mm and not closer to the steel plates where the textile was fitted as in dry glass textile (see also Figs. 5.6a-5.6c).

5.5 Conclusions

This experimental work investigated the bond behaviour between the TRM composite material and brick masonry walls. The main objective was to study: (a) the bond length (100 mm, 150 mm, 200 mm), (b) the textile-fibre material, namely carbon, glass and coated basalt, and (c) the epoxy-resin coating on glass and carbon fibre textile. According to the analysed and discussed experimental results in terms of the maximum load, the deformation capacity, and the different failure modes conclusions are summarised as follows:

- The epoxy-resin coating resulted in increased maximum load compared to their uncoated counterparts due to (i) the enhanced bonding between the fibre-textile and the cementitious mortar and the stiffening of the rovings, (ii) the improved friction among the fibres within a roving which resulted in increased bond stress f_b.

- The effect of the epoxy-resin coating was pronounced by the failure mode shift from slippage between the carbon textile-fibre and mortar to the debonding (at textile-matrix interface) failure mode in coated carbon fibre-textile material. Coating also modified the weak dry glass textile to a rigid textile, where rupture of the textile occurred close to the bond length area.

- The effective bond length of carbon, coated glass and coated basalt was greater than or equal to 200 mm, and for coated carbon was between 150-200 mm. The fibre textiles C, C_co, B and G_co resulted in ascending trend of the maximum load when the bond length was increased. Only the glass fibre textile demonstrated similar values among for the different bond lengths which shows that with this experimental setup an effective bond length could not be derived.

- The coated basalt demonstrated 20%-26% higher bond axial stress with respect to the coated glass which shows its superior behaviour due to the actual roving surface of each fibre-textile.

Chapter 6

Out-of-Plane TRM strengthening of masonry walls

6.1 Introduction

In this Chapter, an experimental work in the out-of-plane response of masonry walls strengthened with TRM is presented. The main aim of this study was to examine the effectiveness of the TRM composite material on the masonry wall specimens when subjected to out-of-plane bending including several investigating parameters (e.g., different composite materials, different amount composite materials, epoxy-resin coating, wall thickness). In the following, the experimental program is thoroughly described and then the experimental results are demonstrated. Following, the discussion is provided on the experimental results obtained. Finally, the conclusions are drawn based on the discussion provided.

6.2 Experimental Program

6.2.1 Test specimens and investigated parameters

The main aim of this experimental investigation was to examine the performance of brick masonry walletes strengthened with TRM composite material when subjected to out-of-plane bending. The investigation was carried out in two sets of single and double-wythe walls. Eighteen masonry brick walls in total were constructed (nine single and nine double-wythe) with dimensions of 1340 x 440 x 102.5 mm, in a running bond pattern. The double-wythe masonry wall thickness was 205 mm. Medium-scale specimens were built as these are more representative of real walls; this further adds confidence to the test outcomes (i.e. failure modes etc.), see also (Papanicolaou et al., 2011; Valluzzi et al., 2014; Martins et al., 2015). A general purpose masonry cement mortar of approximately 10 mm thickness was used for both the bed and head joints.

The key investigated parameters of this study were: (a) the number of TRM layers, (b) the textile-fibre material, namely carbon, glass and coated basalt (c) the epoxy-resin coating, and (d) the wall thickness (single and double-wythe). Two specimens built to serve as control specimens, one for single (S_CON) and one for double-wythe walls (D_CON), respectively. The remaining 16 specimens were strengthened at the tensile wall face with the objective of improving their out-of-plane flexural performance. A single TRM layer was considered for the case of carbon-fibre textiles, whereas 3 and 7 layers were examined for the case of both glass-fibre and coated basalt-fibre textiles.

The wall specimens with their corresponding parameters are shown in Table 6.1. The strengthening configuration is shown in Fig. 6.1a while the actual test setup is shown in Fig. 6.1c. The notation considered for the strengthened

TABLE 6.1: Wall Specimens

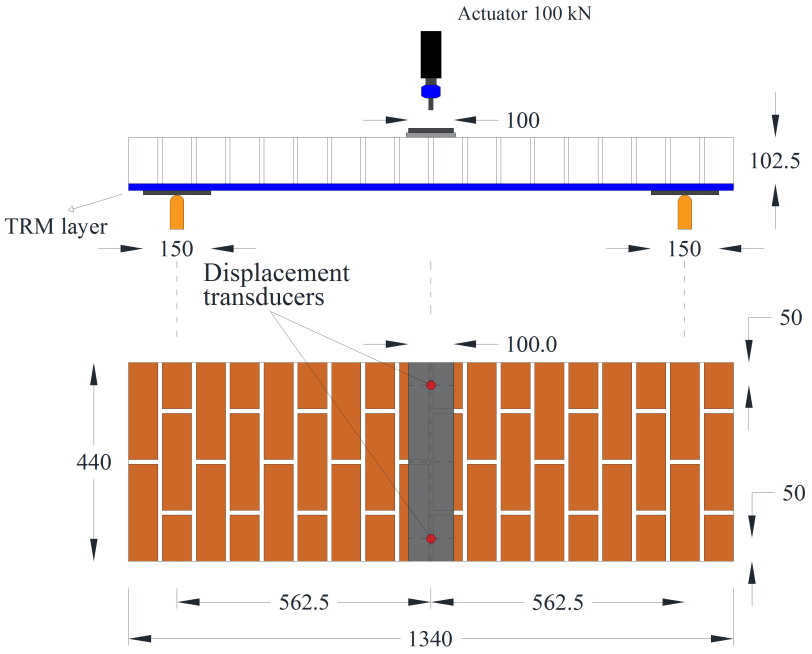
Specimen	Wythe	TRM material	Number of TRM layers	TRM thickness [mm]	In-house coating
S_CON	Single		Unstrengthened		
D_CON	Double		Unstrengthened		
S_C1	Single	Carbon	1	3	No
S_C1_(Co)	Single	Carbon	1	5	Yes
S_G3	Single	Glass	3	4	No
S_G3_(Co)	Single	Glass	3	7	Yes
S_G7	Single	Glass	7	8	No
S_G7_(Co)	Single	Glass	7	9	Yes
S_B3	Single	Coated basalt	3	9	No
S_B7	Single	Coated basalt	7	13	No
D_C1	Double	Carbon	1	3	No
D_C1_(Co)	Double	Carbon	1	5	Yes
D_G3	Double	Glass	3	4	No
D_G3_(Co)	Double	Glass	3	7	Yes
D_G7	Double	Glass	7	8	No
D_G7_(Co)	Double	Glass	7	9	Yes
D_B3	Double	Coated basalt	3	9	No
D_B7	Double	Coated basalt	7	13	No

specimens is W_XN, where W denotes the single or double-wythe walls (S for single and D for double-wythe wall), X denotes the type of the textile (C for carbon, G for glass and B for coated basalt) and N denotes the number of layers (1, 3 and 7). The suffix Co denotes textiles coating with epoxy resin.

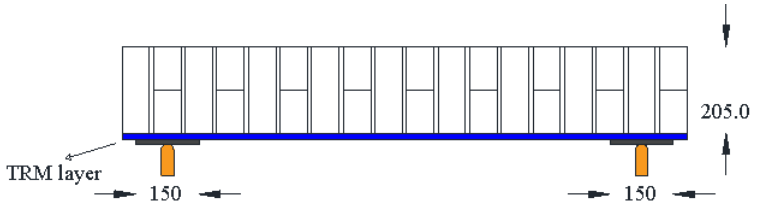
6.2.2 Materials

Masonry walls were built with solid clay bricks of UK typical nominal dimensions. The properties of the bricks and masonry walletes are described in detail in Sections 4.2 and 4.4, respectively.

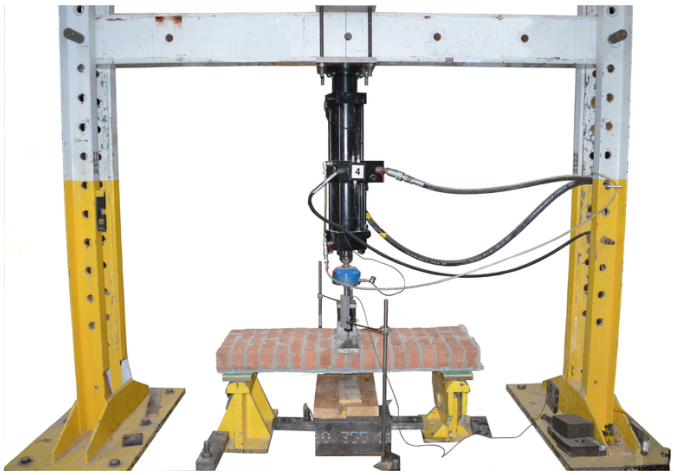
For each individual wall specimen, the flexural and compressive strength of both joint and strengthening mortar were identified by conducting a series of three-point bending and compressive strength experiments as described in



(a)



(b)



(c)

FIGURE 6.1: Experimental setup; (a) plan view and elevation (all dimensions in mm), (b) Double-wythe masonry wall, (c) actual setup

TABLE 6.2: Casting and strengthening mortar of masonry walls

	Specimens	Casting Mortar		Strengthening Mortar	
		Compressive Strength f_m [MPa]	Tensile Strength f_{mt} [MPa]	Compressive Strength f_m [MPa]	Tensile Strength f_{mt} [MPa]
Single Wythe	S_CON	8.09	2.06	-	-
	S_C1	6.54	1.99	38.36	10.19
	S_C1_(Co)	8.86	2.26	37.30	8.20
	S_G3	6.54	1.99	38.36	10.19
	S_G3_(Co)	8.86	2.26	37.28	7.98
	S_G7	7.73	1.99	37.39	8.70
	S_G7_(Co)	10.30	2.36	39.69	8.88
	S_B3	7.73	1.99	37.39	8.70
	S_B7	8.09	2.06	37.30	8.20
	Mean Value	7.4 (2.3* / 0.31**)	1.9 (0.5* / 0.26**1)	37.9 (0.9* / 0.02**)	8.9 (0.9* / 0.10**)
Double Wythe	D_CON	9.35	3.38		
	D_C1	6.59	1.95	37.39	8.70
	D_C1_(Co)	6.90	2.21	41.49	8.22
	D_G3	6.68	2.40	46.58	11.05
	D_G7	6.68	2.40	46.58	11.05
	D_G3_(Co)	9.35	3.38	41.49	8.22
	D_G7_(Co)	8.29	2.41	37.30	8.20
	D_B3	6.90	2.21	41.49	8.22
	D_B7	6.90	2.21	40.43	8.34
	Mean Value	7.5 (1.2* / 0.16**)	2.5 (0.5* / 0.20**)	41.6 (3.5* / 0.08**)	9.0 (1.3* / 0.14**)

*Standard Deviation, **Coefficient of Variation

Sections 4.3 and 4.5. The mean values of the corresponding quantities together with their standard deviation and the coefficient of Variation for the case of single and double-wythe walls are summarized in Table 6.2. The casting mortar demonstrates higher variability in its corresponding compressive and tensile strength than the strengthening mortar. It should be highlighted that such variability does not significantly affect the results in terms of the reported failure modes.

Three different materials were used, namely the carbon-fibre textile (either uncoated or coated with epoxy resin), the glass-fibre textile (uncoated or coated with epoxy resin) and the coated basalt-fibre textile. The different textile configurations and their properties, as provided in manufacturer datasheets and from tensile tests on bare textiles and TRM coupons are described in Section 4.6.

The coated carbon and coated glass fibre textiles employed in this study were impregnated in a commercial epoxy adhesive as presented in Section 4.7. In addition, the coated basalt fibre-textile is a commercial product fabricated with a bituminous binder of 10% content (see Section 4.6).

As shown in Table 6.1, five strengthening configurations were investigated in this experimental program, i.e., 1 layer of carbon-fibre textile (uncoated and coated), 3 and 7 layers of glass-fibre textile (uncoated and coated) and 3 and 7 layers of coated basalt-fibre textile, for both single and double walls. The number of 7 layers of glass/ coated basalt fibre-textiles has been chosen on the basis of the axial stiffness similarity principle described in Section 4.6.

The cement-based mortar used during the TRM composite system application, between the textile and the masonry substrate is presented in Section 4.5. The mean values of flexural and compressive strength on the day of testing were 8.9 MPa and 39.7 MPa, respectively (see Table 6.2).

Compatibility between the mortar matrix material and the textile fibre reinforcement has been investigated and the advantages of using appropriate mortar mixes for different textile fibre materials have been documented, see, e.g., (Bernat et al., 2013; Harajli et al., 2010). In this work, the same mortar was employed for all specimens with the objective of providing a comparable basis with respect to the investigated parameters of interest, i.e., the effect of the textile material, the number of TRM layers, the epoxy resin coating of the textile, and the wall thickness.

6.2.3 Strengthening procedure

The TRM application procedure involved the following steps:

- Air pressure was used to remove dust from the masonry wall surfaces to be strengthened with the TRM composite.
- The wall was slightly dampened and a first layer of mortar was applied at the whole surface of the wall (Fig. 6.2a).
- The first textile layer was applied and impregnated into the previously applied mortar layer using hand pressure (Fig. 6.2b). It is noted that in all specimens, the textile covered the entire brick wall surface to be subjected in tension.
- Application of a final layer of mortar to completely cover the textile. For multiple strengthening layers the procedure of alternate textile and mortar layer was repeated. The procedure was completed while the mortar was fresh to achieve optimum adhesion of the TRM layers. The final strengthened configuration is presented in Fig. 6.2c.



(a) (b) (c)

FIGURE 6.2: Textile material and corresponding mesh sizes considered in this study (a) Dampening of the wall, (b) application of glass textile layer into the mortar, (c) application of the final layer of mortar

In actual infill applications, it is recommended to leave some margins around the strengthened surface to prevent stress concentrations, see, e.g. (De Felice et al., 2014). In this experimental work, such a provision was not made as no stress concentrations were expected at the free boundaries of the specimen.

6.2.4 Experimental setup and procedure

A three-point-bending loading configuration was adopted for the out-of-plane tests of the masonry walls, resulting in an effective span of 1125 mm, as shown in Fig. 6.1a. The supports were spaced 107.5 mm from the ends of the masonry wall. The test setup consisted of a stiff steel reaction frame fastened with a vertically positioned actuator as shown in Fig. 6.1c. A 100 kN capacity servo-hydraulic actuator, used for the load application at a displacement rate equal to 0.017 mm/s (i.e., 1mm/ min). Two potentiometers were used to measure

the out-of-plane displacement at mid-span. The transducers were placed at a distance of 50 mm from each side of the wall, as shown in Fig. 6.1a. Data was collected at a frequency of 4 Hz, synchronised and recorded using a fully-computerized data acquisition system.

6.3 Experimental results

The load versus out-of-plane deflection curves for all tests are presented in Fig. 6.3a for the case of single-wythe walls and in Fig. 6.3b for the case of double-wythe walls respectively. The identified key parameters of the experimental results, i.e., the maximum load P_{max}, the midspan deflection at maximum load, the ultimate load, the midspan deflection at the ultimate load, the ratio of the maximum load to that of the control specimen, and the observed failure modes are summarised in Table 6.3. The corresponding failure modes are shown in Figs. 6.6-6.22 for single- and double-wythe specimens. The ultimate load defined as P_{ult} = max(0.8P_{max}, final load). Experimental results are further grouped in terms of investigated parameters in Figs. 6.4-6.5 to facilitate discussion in terms of the behaviour observed.

6.3.1 Single-wythe walls

The control specimen failed under the action of its own weight during placement on the test-setup. The nominal strength of the wall, as evaluated from EN (1996) is used herein for the sake of comparison (see Appendix A).

All strengthened specimens demonstrated significantly increased maximum and ultimate loads as compared to the control specimen. Different failure modes were observed in the strengthened specimens depending on the textile material used, the presence of coating or not and the number of applied layers. These

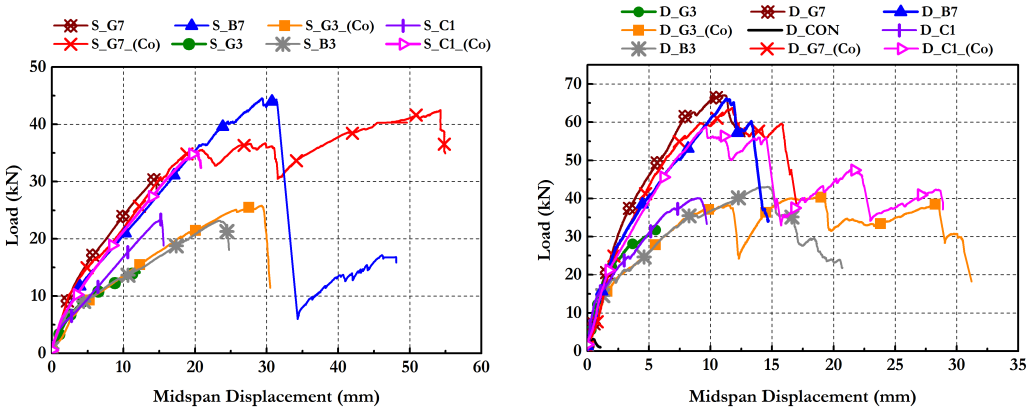


FIGURE 6.3: Experimental load-displacement response curves for (a) single-wythe walls, and (b) double-wythe walls

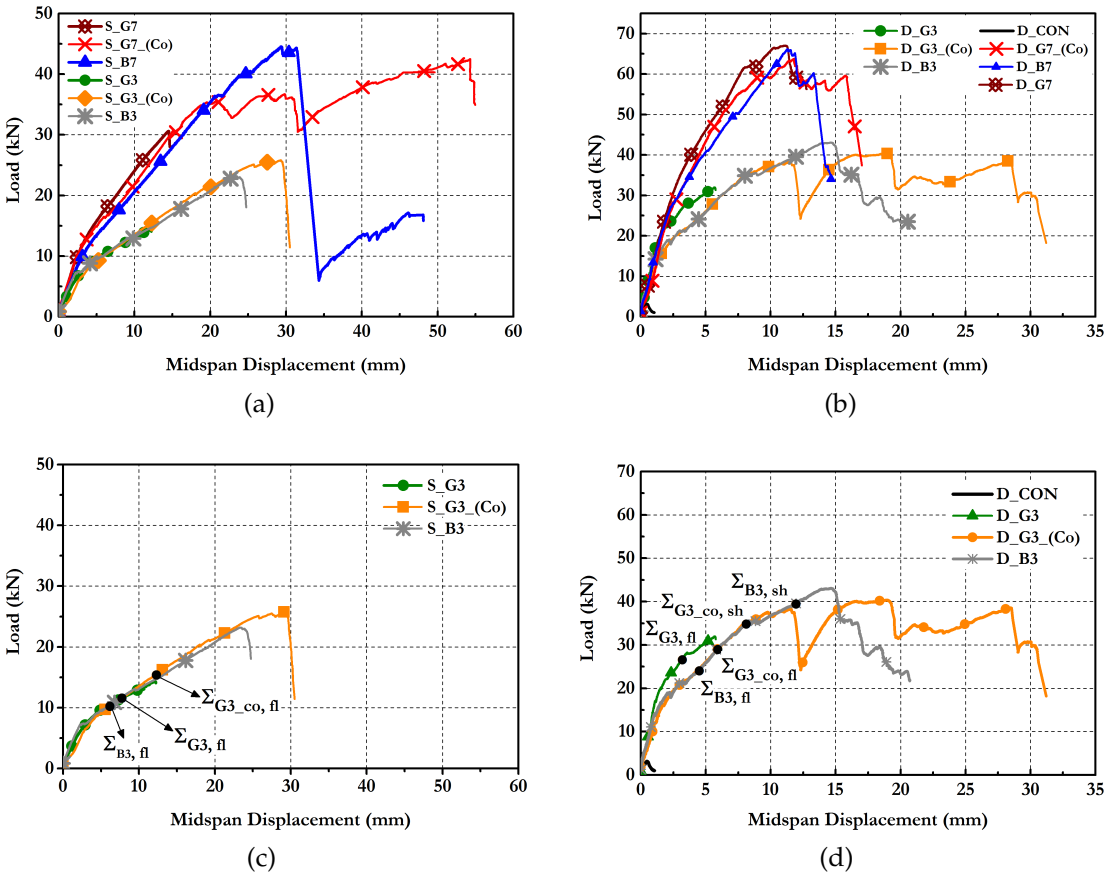


FIGURE 6.4: Experimental load-displacement response curves of single and double-wythe grouped in terms of (a)-(b) three vs seven textile layers, (c)-(d) three layers of textile

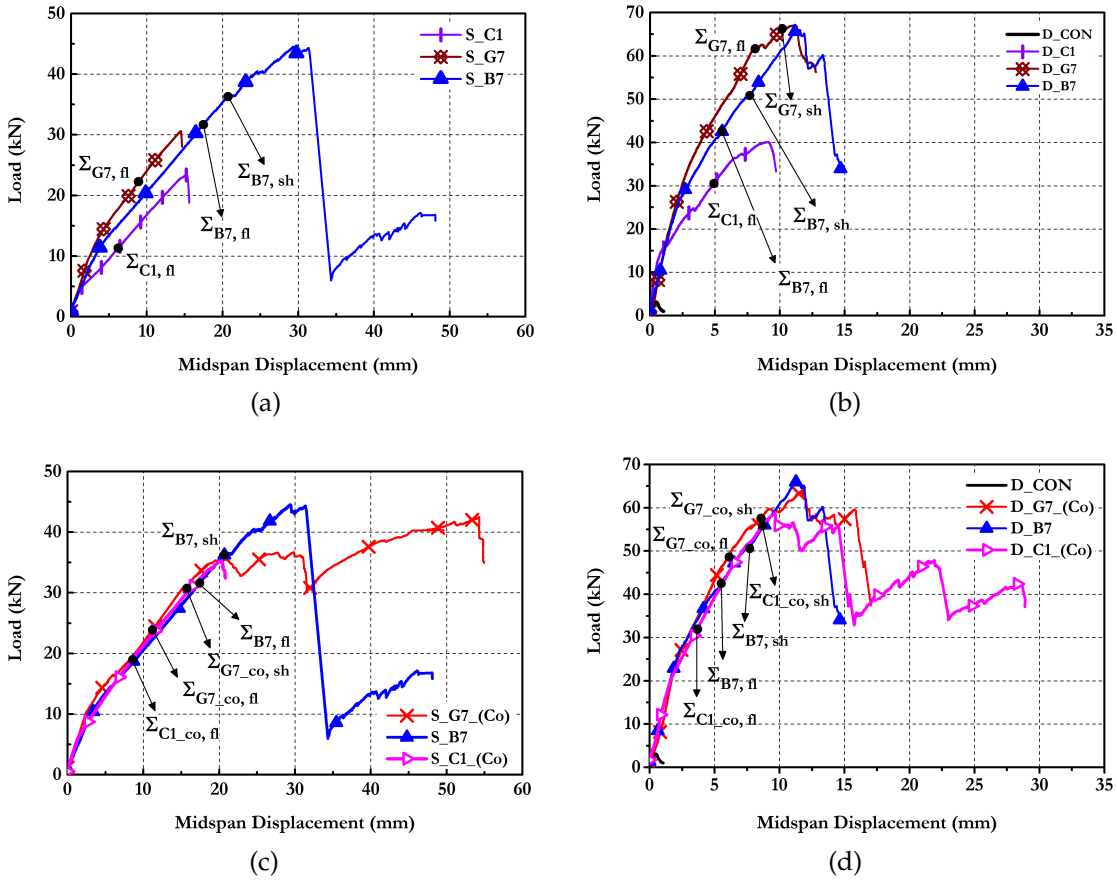
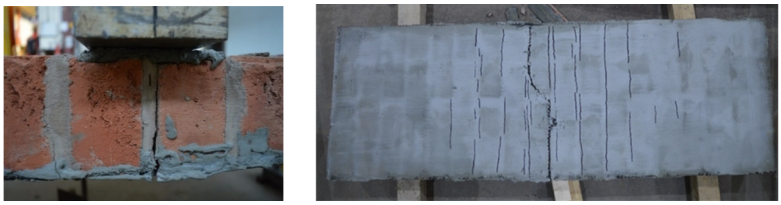


FIGURE 6.5: Experimental load-displacement response curves of single and double-wythe walls grouped in terms of (a)-(b) one layer of carbon fibre textile vs seven layers of glass and coated basalt textile, (c)-(d) one layer of carbon coated fibre textile vs seven layers of glass coated and coated basalt textile



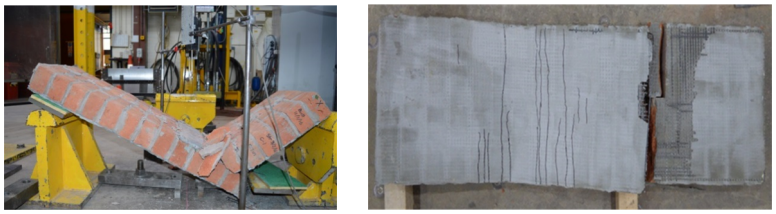
(a) (b)

FIGURE 6.6: Textile slippage of specimen S_C1; (a) side view (b) TRM surface after collapse

include textile rupture, slippage of the textile fibres within the mortar matrix, flexural-shear failure of the masonry wall, and shear failure of the masonry wall as summarized in Table 6.3.

The maximum load recorded in specimen S_C1, strengthened with 1 carbon TRM layer, was 23.4 kN and its corresponding deflection was 15.2 mm as shown in Fig. 6.5a. Fine flexural cracks along the mortar joints initiated in the vicinity of the loading line at a load level approximately 50% (point $\Sigma_{C1,fl}$ in Fig. 6.5a) of the maximum load. Further increasing the load, transversal cracks appeared in the TRM with a principal crack opening at mid-span as shown in Fig. 6.6. At peak load, damage concentrated at the mid-span. The main TRM crack at mid-span shown in Fig. 6.6a eventually led to textile slippage through the mortar and finally to collapse of the specimen. Visual inspection at the end of the test, revealed transversal cracks due to flexure at the TRM composite surface as shown in Fig. 6.6b.

S_C1_(Co), comprising one layer of coated carbon-fibre textile, failed due to the textile rupture (Fig. 6.7) at a maximum load of 35.3 kN and a corresponding out-of-plane displacement of 20.1 mm. In observing the response up to failure, hairline flexural cracks developed at 54% of the maximum load (point $\Sigma_{C1_co,fl}$ in Fig. 6.5c), at the mid-span area and along the mortar joints. Similar cracks also appeared at the surface of the composite material at the same region (Fig.



(a) (b)

FIGURE 6.7: Failure of specimen S_C1_(Co); (a) side view (b) TRM surface after collapse



(a) (b)

FIGURE 6.8: Failure of specimen S_G3; (a) side view (b) TRM surface after collapse

6.7b).

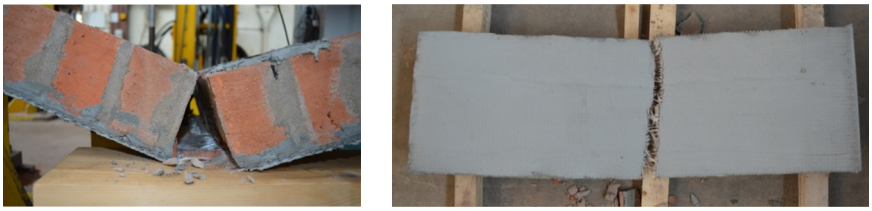
The maximum load and corresponding displacement of specimen S_G3 were 14.3 kN and 12.1 mm, respectively. Damage initiated with a single fine flexural crack at 82% of the peak load (point $\Sigma_{G3,fl}$ in Fig. 6.4c), appearing at the mid-span mortar joint at the tensile face of the masonry wall. This propagated along the thickness of the wall. At peak load, tensile fracture of the glass fibres occurred (Fig. 6.8a) resulting in the wall's collapse (see also Fig. 6.8b).

Specimen S_G3_(Co) failed at an applied load of 25.8 kN and a corresponding displacement of 29.3 mm. Failure initiated by tensile cracks at the mortar joints of the central region at 60% of the maximum load (point $\Sigma_{G3_co,fl}$ in Fig. 6.4c). At peak load, tensile fracture of the coated glass-fibre textile material occurred resulting in wall collapse as shown in Fig. 6.9.



(a) (b)

FIGURE 6.9: Failure of specimen S_G3_(Co); (a) side view (b) TRM surface after collapse



(a) (b)

FIGURE 6.10: Failure of specimen S_G7; (a) side view (b) TRM surface after collapse

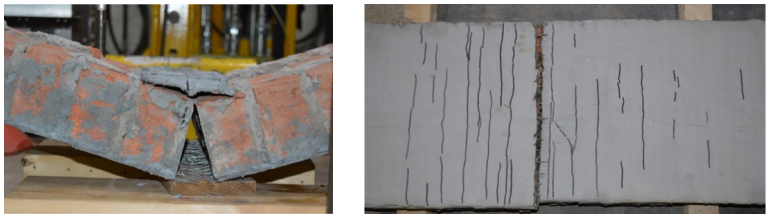
Specimen S_G7 attained a maximum load equal to 30.6 kN. The corresponding peak load displacement was 14.5 mm. Visual inspection during the test, revealed that at 73% of the maximum load (point $\Sigma_{G7,fl}$ in Fig. 6.5a), a minor flexural crack first developed at brick – bed joint, at the vicinity of the central bed-joint. At the peak load stage a wide flexural crack propagated which led to the instantaneous textile rupture at the mid-span of the wall (Fig. 6.10).

Specimen S_G7_(Co) failed in shear diagonal tension at a maximum load and corresponding mid-span displacement of 42.5 kN and 54.3 mm, respectively. At 56% of the peak load (at point $\Sigma_{G7_co,fl}$ in Fig. 6.5c), minor flexural cracks formed. At a load corresponding to 73% of the maximum load (point $\Sigma_{G7_co,sh}$ in Fig. 6.5c), the first fine diagonal crack initiated on the right side of the wall close to the TRM layer. This was followed by a diagonal crack on the left side of the wall. After the first peak load and during the second ascending non-linear branch, the diagonal cracks grew wider and gradually propagated to the point



(a) (b)

FIGURE 6.11: Failure of specimen S_G7_(Co); (a) side view (b) TRM surface after collapse



(a) (b)

FIGURE 6.12: Failure of specimen S_B3; (a) side view (b) TRM surface after collapse

of load-application (at both sides). The post-peak behaviour was generally characterised by a gradually increasing but fluctuating load, which led to extended diagonal crack through the wall-TRM interface and gradual debonding (with cohesive failure of the surface) of the TRM towards both supports as shown in Fig. 6.11.

Specimen S_B3 failed at a peak load of 23.2 kN with a corresponding displacement of 23.3 mm. Flexural cracks formed along the mortar joints of the mid-span region at 44% of the maximum load (point $\Sigma_{B3,fl}$ in Fig. 6.4c). The response was dominated by sudden rupture of basalt textile fibres at peak load leading to collapse of the wall as shown in Fig. 6.12a. Transversal crack patterns (Fig. 6.12b) along the length of the wall were identified through visual observation of the TRM surface.



(a) (b)

FIGURE 6.13: Failure of specimen S_B7; (a) side view (b) TRM surface after collapse

S_B7 collapsed at a maximum load of 44.5 kN. The corresponding displacement at collapse was 29.3 mm. A shear diagonal tension failure mode was observed, which as in the case of specimen SG7_(Co), is indicative of the increased reinforcement ratio utilised. At load levels from about 70% of the maximum load (point $\Sigma_{B7,fl}$ in Fig. 6.5c), hairline flexural cracks were formed, but not propagated further. Fine diagonal cracks initiated adjacent to the middle region of the wall at 82% of the maximum load (point $\Sigma_{B7,sh}$ in Fig. 6.5c). These gradually propagated from the TRM-masonry interface towards the loading line. After reaching the maximum load, the diagonal crack grew wider. Immediately, the load dropped at 6 kN. Contrary to S_G7_(Co), debonding at the TRM interface did not occur in S_B7. As a result, the load gradually increased again to 17.1 kN leading eventually to the diagonal crack shown in Fig. 6.13a.

6.3.2 Double-wythe walls

As in the case of the single wythe specimens, strengthened double wythe specimens demonstrated a significantly improved response with respect to their maximum attained loads and corresponding deflections.

The control specimen D_CON failed in flexure. The maximum load and corresponding displacement was 3.1 kN and 1 mm, respectively. The overall response was very brittle as the specimen failed abruptly due to a single flexural



FIGURE 6.14: Failure of D_CON specimen



(a)



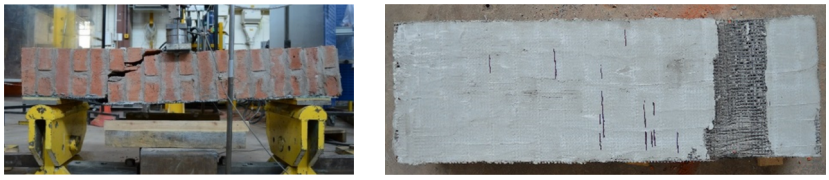
(b)

FIGURE 6.15: Failure of specimen D_C1; (a) side view (b) TRM surface after collapse

crack (Fig. 6.14), which occurred at the mid-span of the wall, when the developed tensile stresses at that cross-section overcome the mortar strength.

Specimen D_C1 attained a maximum load of 40.1 kN with a corresponding mid-span displacement of 9.0 mm. The failure mechanism of this specimen was controlled by the sudden rupture of the textile. A hairline flexural crack initiated at the mid-span mortar joint at 76% of the maximum load (point $\Sigma_{C1,fl}$ in Fig. 6.5b). As the load increased, further flexural cracks initiated along the specimen at four mortar joint locations of the middle region. Corresponding transversal cracks initiated at the surface of the TRM. Upon reaching the maximum load, a wide single mortar joint crack developed while the specimen strength rapidly degraded until the textile ruptured; see also Fig. 6.15.

Specimen D_C1_(Co) strengthened with one layer of coated carbon fibre textile, failed due to shear failure of the bricks located at the mid-distance between the point load and the left support in a typical zig-zag pattern. The maximum load and corresponding mid-span displacement were 58.8 kN and 9.7 mm, respectively. At early stage of loading (54% of maximum load at point $\Sigma_{C1_co,fl}$ in



(a) (b)

FIGURE 6.16: Failure of specimen D_C1_(Co); (a) side view (b) TRM surface after collapse

Fig. 6.5d), fine flexural cracks were distributed along the mortar joints in proximity to the central bed-joint region. Further increasing the load to 95% of the maximum load (point $\Sigma_{C1_co,sh}$ in Fig. 6.5d), a diagonal crack propagated primarily along the block-mortar interface and the brick shell. Following, the load gradually dropped to 33.2 kN, while the crack grew wider. Eventually, relative slip of the clay bricks resulted to the debonding of the textile at the textile to mortar interface along its principal direction Fig. 16a. At the same time partial rupture of the coated carbon-fibre textile and tensile rupture of the TRM mortar was observed approximately at the quarter span; see also Fig. 6.16b.

Specimen D_G3, strengthened with three layers of glass fibre textile, reached a maximum load of 32 kN with the corresponding displacement being equal to 5.7 mm. During the pre-peak load regime and in particular at 83% of the maximum load (point $\Sigma_{G3,fl}$ in Fig. 6.4d), visual observation revealed minor flexural cracks initiating in the middle bed joint region. At the maximum load the textile fibres fractured suddenly leading to the collapse of the specimen (Fig. 6.17).

Specimen D_G3_(Co), failed in a combined shear – flexure failure mode. During the ascending linear branch at 72% of the maximum load (point $\Sigma_{G3_co,fl}$ in Fig. 6.4d), hairline flexural mortar joints cracks initiated and propagated along the bottom central brick-wall region. At 86% of the peak load (point



(a) (b)

FIGURE 6.17: Failure of specimen D_G3; (a) side view (b) TRM surface after collapse



(a) (b)

FIGURE 6.18: Failure of specimen D_G3_(Co); (a) side view (b) TRM surface after collapse

$\Sigma_{G3_co,sh}$ in Fig. 6.4d) the first minor diagonal crack initiated at the right support at the TRM-wall interface and started propagating towards the mid-span. This resulted in a sudden drop on the applied load to 24.2 kN accompanied by a fine shear crack initiating at the bottom section near the left support. Thereafter, the load further increased at the maximum value of 40.4 kN with the width of the right diagonal crack increasing accordingly. The load subsequently dropped and fluctuated at 38.6 kN, where the left shear crack propagated to the mid-span (Fig. 6.18a). Finally, debonding of the TRM composite at the textile to mortar interface occurred lead to collapse. Flexural cracks also appeared at the external surface of the TRM composite (Fig. 6.18b).

Specimen D_G7, reinforced with seven layers of glass-fibre textile, failed in a combined shear-flexure mode, at a maximum load of 67.1 kN with the corresponding midspan displacement equal to 12.8 mm. At a load equal to 92% of



(a) (b)

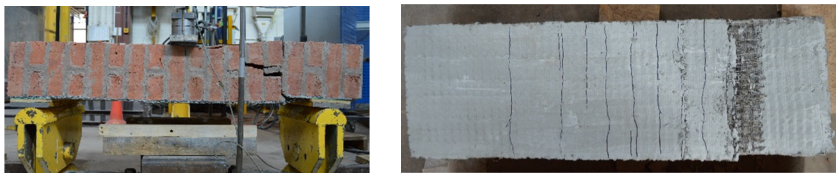
FIGURE 6.19: Failure of specimen D_G7; (a) side view (b) TRM surface after collapse



FIGURE 6.20: Failure of specimen D_G7_(Co)

the peak load (point $\Sigma_{G7,fl}$ in Fig. 6.5b) hairline flexural cracks started propagating along the mortar joints, close to the mid-span region. At the maximum load (99% of the peak load at point $\Sigma_{G7,sh}$ in Fig. 6.5b), a diagonal crack initiated from the TRM-masonry substrate interface and propagated towards the point load (mainly at the mortar line and the brick shell). The diagonal crack propagated towards the left support resulting in the failure of the masonry wall and eventually to the abrupt rupture of the textile (Fig. 6.19).

Specimen D_G7_(Co) reached a maximum load of 63.8 kN with the corresponding displacement being equal to 11.8 mm. Hairline flexural cracks and a diagonal crack initiated at 77% (point $\Sigma_{G7_co,fl}$ in Fig. 6.5d) and 90% (point $\Sigma_{G7_co,sh}$ in Fig. 6.5d) of the maximum load, respectively; these propagated from the TRM-wall interface (close to the right support) towards the loading line (on bricks and along mortar joints). After the peak load suddenly dropped to 38.5 kN, debonding of the TRM composite at the textile to mortar interface occurred due to shear sliding of the masonry blocks (Fig. 6.20).

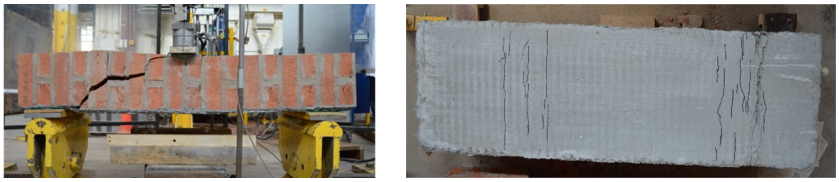


(a) (b)

FIGURE 6.21: Failure of specimen D_B3; (a) side view (b) TRM surface after collapse

Specimen D_B3 attained a load of 43.1 kN and at 14.6 mm corresponding mid-span deflection. Failure of this specimen attributed to combination of shear sliding and flexure (partial textile rapture). At the early stage of loading at 56% of the peak load (point $\Sigma_{B3,fl}$ in Fig. 6.4d), minor flexural cracks were initiated along the mortar joints and on the TRM external face of the wall. From 92% of the peak load (point $\Sigma_{B3,sh}$ in Fig. 6.4d) and after that, diagonal cracks were noticeable close to both sides of the supports towards the load application. Then a descending branch followed, where the diagonal crack grew wider towards the right support, and transverse displacement of the bricks lead to debonding (at the textile-mortar interface), rupture of the TRM mortar and partial collapse of the basalt textile (Fig. 6.21).

Specimen D_B7 failed at 66.2 kN due to shear diagonal tension. Minor flexural cracks initiated at the 64% of the maximum load (point $\Sigma_{B7,fl}$ in Fig. 6.5b). At 77% of the maximum load (point $\Sigma_{B7,sh}$ in Fig. 6.5b) the first diagonal crack was developed. Reaching the maximum load, diagonal crack penetrated from the TRM-wall interface of the left support (minor diagonal crack of the right support) towards the point of load application. Following the gradual decrease of the load, the diagonal crack grew wider in combination with minor debonding of the TRM (at the textile to mortar interface) until drop of the load to 34 kN



(a) (b)

FIGURE 6.22: Failure of specimen D_B7; (a) side view (b) TRM surface after collapse

(6.22a). Tensile cracks were identified at the surface of the strengthening material by visual inspection at the end of the test as shown in Fig. 6.22b.

6.4 Discussion

6.4.1 Ductility of strengthened masonry walls

The ductility of the strengthened masonry wall specimens is quantified in Table 6.4 by means of the d_{ult} to d_{max} ratio. The strengthened masonry wall specimens failed due to textile rupture did not develop any ductility. Pseudo-ductility was observed in single and double-wythe masonry wall specimens failed due to shear and shear-flexure failure mode followed by debonding or partial textile rupture. Shear failue in masonry is a brittle failure mode, which developed quickly, therefore is referred as pseudo-ductility. The effect of the TRM to increase the ductility of the structure, therefore delaying collapse can be very beneficial in case of an adverse environmental action or earthquake.

6.4.2 Effect of the experimental setup

The masonry walls were tested horizontally instead of vertically, due to the simplicity of the experimental setup. Therefore, the self-weight of the walls

TABLE 6.3: Summary of experimental results

		Maximum Load P_{max} [kN]	Midspan Deflection maximum load d_{max} [mm]	Ultimate load P_{ult} [kN]	Ultimate midspan deflection d_{ult} [mm]	P_{max}/P_{con}	Failure mode
Single Wythe walls	S_CON	0.7*				1.0	Failed under its own weight
	S_C1	23.4	15.2	18.8	15.6	33.4	Slippage between textile fibre-mortar
	S_C1_(Co)	35.3	20.1	32.4	20.8	50.4	Textile rupture
	S_G3	14.3	12.1	14.1	12.2	20.4	Textile rupture
	S_G3_(Co)	25.8	29.3	20.6	30.0	36.9	Textile rupture
	S_G7	30.6	14.5	28.0	14.7	43.7	Textile rupture
	S_G7_(Co)	42.5	54.3	35.0	55.0	60.7	Shear failure[1]
	S_B3	23.2	23.3	18.6	24.7	33.1	Textile rupture
	S_B7	44.5	29.3	35.6	32.1	63.6	Shear failure[1]
Double Wythe walls	D_CON	3.1	0.5	2.5	0.6	1.0	
	D_C1	40.1	9.0	33.3	9.7	12.9	Textile rupture
	D_C1_(Co)	58.8	9.7	47.0	14.9	19.0	Shear-flexure[4]
	D_G3	32.0	5.7	31.3	5.8	10.3	Textile rupture
	D_G3_(Co)	40.4	18.9	32.3	28.8	13.0	Shear-flexure[2]
	D_G7	67.1	11.2	56.3	12.8	21.6	Shear-flexure[3]
	D_G7_(Co)	63.8	11.8	51.0	16.2	20.6	Shear-flexure[2]
	D_B3	43.1	14.6	34.5	16.7	13.9	Shear-flexure[4]
	D_B7	66.2	11.3	53.0	13.6	21.4	Shear-flexure[1]

[1]Diagonal tension, [2]Shear-flexure followed by debonding of TRM
[3]Shear-flexure followed by textile rupture, [4]Shear-flexure followed by brick sliding and partial textile rupture
*Calculated from EC 6 based on the value of f_{xk1} derived from D_CON

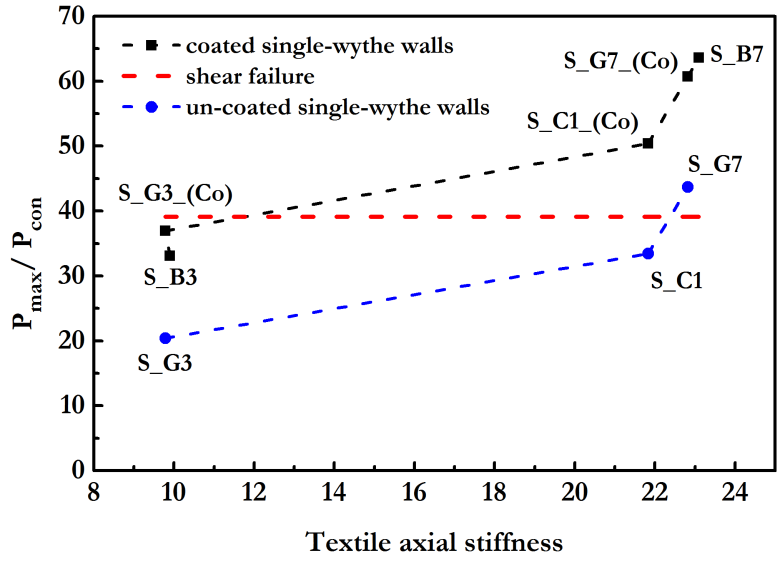
TABLE 6.4: Ductility of masonry walls

Single-wythe walls	
Specimen	d_{ult}/d_{max}
S_CON	
S_C1	1.03
S_C1_(Co)	1.03
S_G3	1.01
S_G3_(Co)	1.02
S_G7	1.01
S_G7_(Co)	1.01
S_B3	1.06
S_B7	1.10
Double-wythe walls	
D_CON	1.20
D_C1	1.08
D_C1_(Co)	1.54
D_G3	1.02
D_G3_(Co)	1.52
D_7	1.14
D_G7_(Co)	1.37
D_B3	1.14
D_B7	1.20

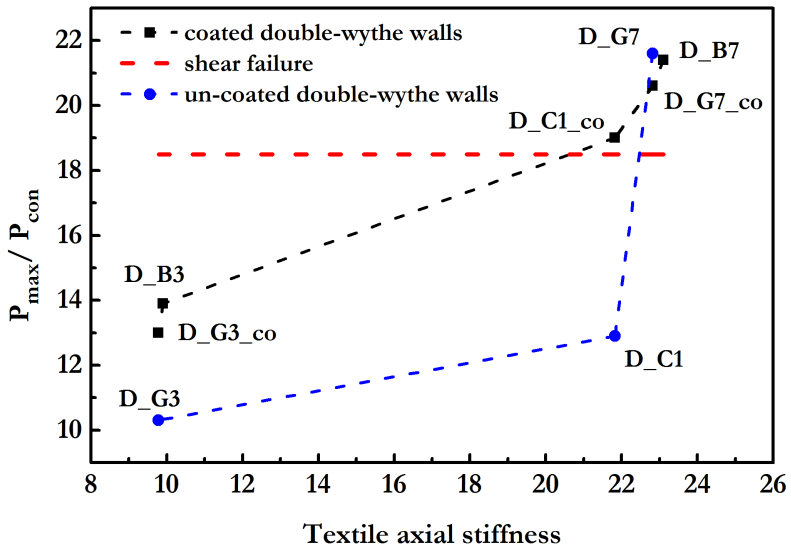
TABLE 6.5: Horizontal vs vertical experimental setup

Specimen	P_{max} [kN]	d_{max} [mm]	M_{exp} [kNm]	M_w [kNm]
Single-wythe walls				
S_CON	0.7			
S_C1	23.4	15.2	6.6	0.01
S_C1_(Co)	35.3	20.1	9.9	0.01
S_G3	14.3	12.1	4.0	0.01
S_G3_(Co)	25.8	29.3	7.3	0.02
S_G7	30.6	14.5	8.6	0.01
S_G7_(Co)	42.5	54.3	12.0	0.03
S_B3	23.2	23.3	6.5	0.01
S_B7	44.5	29.3	12.5	0.02
Double-wythe walls				
D_CON	3.1	0.5	0.9	0.001
D_C1	40.1	9.0	11.3	0.01
D_C1_(Co)	58.8	9.7	16.5	0.01
D_G3	32.0	5.7	9.0	0.01
D_G3_(Co)	40.4	18.9	11.4	0.02
D_7	67.1	11.2	18.9	0.01
D_G7_(Co)	63.8	11.8	17.9	0.01
D_B3	43.1	14.6	12.1	0.02
D_B7	66.2	11.3	18.6	0.01

was not taken into account during the test, which could have a detrimental effect in the out-of-plane performance of the wall. However, the load capacity of the strengthened masonry walls was increased substantially due to the TRM composite material, as indicated by the P_{max}/P_{con} ratio, which means that the presence of self-weight would not affect the experimental results. To enhance this argument, Table 6.5 presents the experimental moment M_{exp} and the additional moment M_w due to the self-weight of the wall. The minimal M_w values verify the assumption that the results were not affected by the horizontal experimental setup.



(a)



(b)

FIGURE 6.23: Ratio of strengthened specimen maximum load to control specimen maximum load (a) single-wythe walls (b) double-wythe walls

6.4.3 The effect of wall thickness

The evaluation of the results obtained is based on the various parameters investigated in this series of experiments. All specimens demonstrated a significant increase in the out-of-plane flexural capacity, compared to their corresponding control specimens. In Fig. 6.23a, 6.23b the strengthened to control specimen maximum load ratios versus the stiffness of the reinforcement layers are plotted for single- and double- wythe walls, respectively. An estimated shear capacity normalised to the control specimen maximum load is also shown. Shear capacity was calculated per TMS 402–02 (MSJC, 2002) as this provides an estimate more consistent to the experimental results than EC6.

In coated single-wythe specimens, S_B7 demonstrated the highest ratio, i.e., 63.6 times the maximum load of the corresponding control specimen S_CON. The lowest ratio was recorded for specimen S_B3 and was equal to 33.1. Conversely, in uncoated specimens the highest increase was recorded for specimen S_G7, i.e., 43.7, whereas the lowest increase was recorded for specimen S_G3, i.e., 20.4. In double-wythe walls strengthened with uncoated textile fibre materials, the highest and lowest recorded ratios were 21.6 and 10.3 for specimens D_G7 and D_G3 respectively. For the case of coated textile fibre materials, the corresponding ratios were 21.4 for specimen D_B7 and 13 for specimen D_G3_(Co).

Double-wythe walls demonstrated lower ratios compared to their single-wythe counterparts. The increased thickness of the wall resulted in increased effective depths when compared to the single-wythe specimens thus leading to better utilization of the additional textile reinforcement. Hence, almost in all cases, the maximum load of the strengthened double-wythe specimens was bounded by the masonry shear capacity as shown by the corresponding failure

modes reported in Table 6.3 and Fig. 6.23b where the shear capacity estimate is indeed close to the recorded experimental results.

6.4.4 The effect of coating

The effect of coating on the maximum load of the single-wythe specimens is highlighted in Fig. 6.24. Specimens S_C1_(Co), S_G3_(Co), and S_G7_(Co) demonstrated increased values of the maximum load by 51%, 81% and 39%, with respect to their corresponding non-coated counterparts, i.e., S_C1, S_G3, and S_G7, respectively.

Specimen S_C1 failed due to slippage of the textile through the mortar contrary to the corresponding coated specimen S_C1_(Co) where failure occurred through tensile rupture of the textile. Although slippage did not occur for the case of the specimens retrofitted with three and seven uncoated glass-fibre textile layers, yet the contribution of the fibre textile in the coated case was significantly enhanced, as manifested by the overall increase in their corresponding maximum strength (see also Fig. 6.3a). This beneficious impact of coating is attributed to the improved mechanical interlocking conditions obtained through the enhanced stress transfer mechanism from the fibres to the cementitious matrix; this eventually improves the contribution of roving filaments at the time of failure (see also, (Raoof et al., 2016; Papanicolaou et al., 2011)).

With the exception of D_C1_(Co), coating had a reduced effect in double-wythe walls as shown in Fig. 6.23b. For specimens D_C1_(Co) and D_G3_(Co) the maximum load was increased by 47% and 26% when compared to D_C1 and D_G3 respectively. The maximum recorded load of D_G7_(Co) was 5% lower than D_G7.

D_C1_(Co) demonstrated an increase in its maximum load that is comparable to the 51% increase recorded in the case of S_C1_(Co) versus S_C1. This could potentially mean, that full utilization of textile fibre strength was not achieved in D_C1 (which would increase its corresponding maximum load); although the failure mechanism of D_C1 was textile rupture, partial slippage must have occurred as in the case of S_C1. Thus, further tests are required in the future to examine and highlight this behaviour. In the case of D_G3_(Co) and D_G7_(Co) the maximum load was bounded by the shear capacity of the masonry. Hence, although the coating enhanced the properties of the corresponding TRM layers, full utilization of its tensile capacity was not feasible.

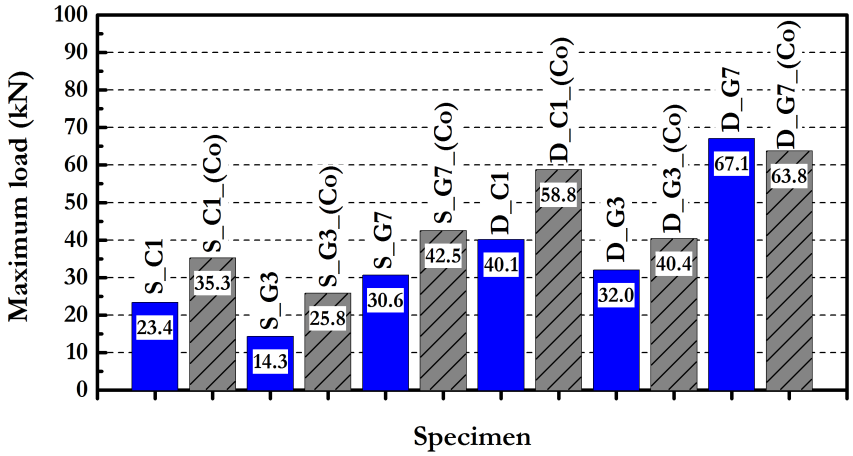


FIGURE 6.24: The effect of coating on the out-of-plane bearing capacity

In terms of deformation capacity, coating enhanced the deformability of all specimens as the enhanced interlocking conditions mitigated textile slippage and allowed for better crack distribution along the length of the wall. Single-wythe walls specimens S_C1_(Co), S_G3_(Co), and S_G7_(Co) demonstrated a 32%, 142%, and 275% increase in their deflection at maximum load when compared to S_C1, S_G3, and S_G7, respectively. Specimens D_C1_(Co),

D_G3_(Co), and D_G7_(Co) also demonstrated increased displacements at maximum load, i.e., 8%, 232%, and 5% when compared to D_C1, D_G3, and D_G7, respectively.

The marginal increase observed in the deformability of specimens D_C1_(Co) and D_G7_(Co) when compared to their uncoated counterparts is attributed to different reasons. In the case of 1 layer of carbon fibre textile TRM, coating improved bonding between the textile and the mortar matrix and resulted in a much stiffer configuration than D_C1. Indeed, the post-cracking stiffness of D_C1_(Co) is significantly larger than the corresponding stiffness of D_C1 (see also Fig. 6.3b); it should be highlighted that such pronounced increase is not observed in all other specimens. This further supports the hypothesis previously made that partial textile slippage occurred in D_C1. When 7 layers of glass fibre textile were used, both D_G7 and D_G7_(Co) failed in shear dominated modes; hence coating did not provide any significant advantage to an already over-reinforced specimen.

6.4.5 The effect of number of layers

Increasing the number of layers resulted in a significant increase in the load bearing-capacity of both single and double-wythe walls as demonstrated in Fig. 6.25. Single-wythe walls specimens strengthened with 7 layers of TRM, i.e., S_G7, S_G7_(Co) and S_B7 demonstrated an increase in their corresponding maximum loads of 114.0%, 65% and 92%, respectively when compared to the specimens strengthened with three layers of TRM, i.e., S_G3, S_G3_(Co), S_B3. The corresponding load-deflection paths are shown in Fig. 6.4a. Furthermore, in double-wythe walls specimens, i.e., D_G7, D_G7_(Co), D_B7 the maximum load increased by 110%, 58%, 54%, respectively, compared to the specimens

strengthened with three layers of TRM composite, i.e., D_G3, D_G3_(Co), and D_B3; see also Fig. 6.4b.

The maximum load was increased proportionally to the additional reinforcement when uncoated glass textile was utilised. Since textile rupture finally occurred in single and double-wythe walls (after shear failure initiation) the maximum tensile strength of the fibre-textile was attained. This was not the case when coated textiles were used where shear/ shear-flexure failure of the wall preceded the flexural strength of the fibre textile and complete utilisation of the fibre textile material did not occur. However, even in those cases where increasing the number of layers did not alter the failure mode, the increase in maximum load has been substantial, as shown in Fig. 6.23a and 6.23b. This highlights the fact that adding reinforcement layers enhances bonding of the textile fibre reinforcement within the matrix thus minimizing roving slippage hence increasing the textile reinforcement effective strength.

In terms of deformability, single-wythe specimens S_G7, S_G7_(Co), and S_B7 demonstrated increased deflection at maximum load, namely 20%, 85%, and 26%, compared to S_G3, S_G3_(Co), and S_B3 respectively as shown in Fig. 6.4a. The increase is more pronounced in the case where the specimen response was governed by a drastic shift from a bending to a shear dominated failure mode which is also consistent with the recorded increase in the corresponding maximum loads.

This response however was not confirmed in the case of stiff double-wythe configurations. The deformability of D_G7 was increased by 97% compared to D_G3 (Fig. 6.4b); this again is consistent with the shift in the failure mode. On the contrary, displacement at the maximum load for D_G7_(Co) and D_B7

was decreased by 38% and 23%, when compared to D_G3_(Co) and D_B3 respectively. These specimens failed in a shear dominated mode hence in terms of deformability, the additional TRM layers led to a stiffer configuration due to the increased axial stiffness of the strengthening layer. This is indeed verified by the initial and post-cracking stiffness of specimens that significantly increased in the case of D_G7_(Co) and D_B7 compared to D_G3_(Co) and D_B3 respectively as shown in Fig. 6.3b.

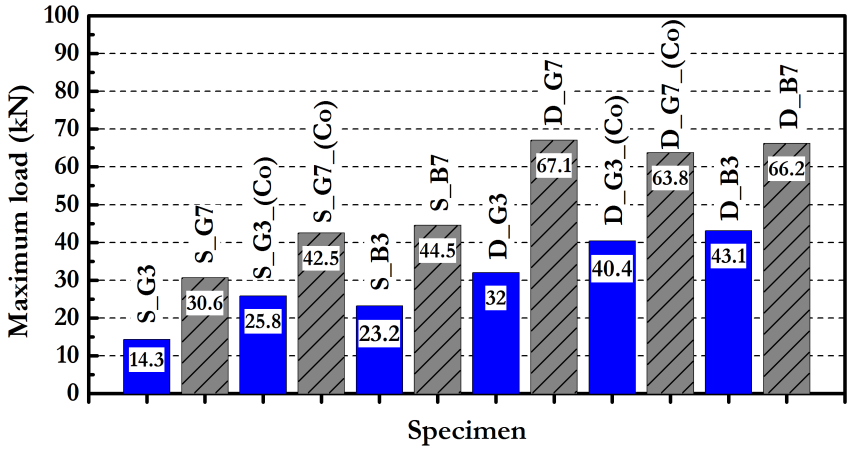


FIGURE 6.25: The effect of number of layers in the out-of-plane bearing capacity

6.4.6 The effect of the textile material

The effect of the textile material in the overall response of the TRM strengthened specimens is shown in Figs. 6.5a, 6.5c and Figs. 6.5b, 6.5d for single- and double-wythe walls, respectively. The maximum loads recorded for each specimen are summarized in Fig. 6.26 with respect also to the comparisons discussed in this Section.

S_G3_(Co) achieved a 11% higher maximum load, in comparison to S_B3. Furthermore, S_B7 attained a 5% larger value of the maximum load as compared to S_G7_(Co). In double-wythe walls, D_B7 and D_B3 reached a 4% and 7% higher maximum load, compared to D_G7_(Co) and D_G3_(Co), respectively. The similar response of coated glass and coated basalt specimens with respect to the attained maximum loads, also corroborated by the similar failure modes, highlights the effectiveness of the applied coating procedure for the case of the glass fibre textile.

The maximum load of S_G7 was increased by 31% compared to S_C1. This increase is consistent with the different failure modes observed, i.e., textile rupture as opposed to textile slippage of the roving filaments through the mortar; this occurs even though the axial stiffness of 1 carbon fibre textile layer is equivalent to the axial stiffness of 7 glass fibre textile layers. Hence, this further highlights the enhanced interlocking mechanisms that the additional number of textile fibre layers benefit from.

A similar trend is observed between S_G7_(Co) and S_C1_(Co) where the former failed at a maximum load 20% higher than the latter. Although S_G7_(Co) failed in shear (shear diagonal tension), S_C1_(Co) failed due to textile rupture; thus, even though the two specimens involve textile material of comparable axial stiffness, employing additional layers of coated glass gave rise to an over-reinforced specimen. This indicates that the single carbon textile composite layer has a lower tensile fracture capacity compared to the 7 layers of coated glass fibre textile composite highlighting now the enhanced interlocking mechanisms between the textile fibre composites themselves.

Double-wythe wall specimen D_G7 resulted in a 67% higher load than D_C1. Although the axial stiffness of the G7 and C1 TRM layers is equivalent, such

a difference is manifested due to the lack of interlocking when a single uncoated layer of fibre-textile is used. DG_7 failed in a shear-flexure failure mode whereas D_C1 failed due to textile rupture; 7 layers of glass fibre textile again resulted in an over-reinforced specimen as in the case of the single-wythe specimens. The corresponding increase in the maximum load of D_G7_(Co) when compared to D_C1_(Co) was 9%. These specimens failed in a similar failure mode, i.e., shear - flexure failure followed by brick sliding and partial textile rupture or debonding of TRM respectively. Coating in this case dominated the mechanical response of the textile fibre material.

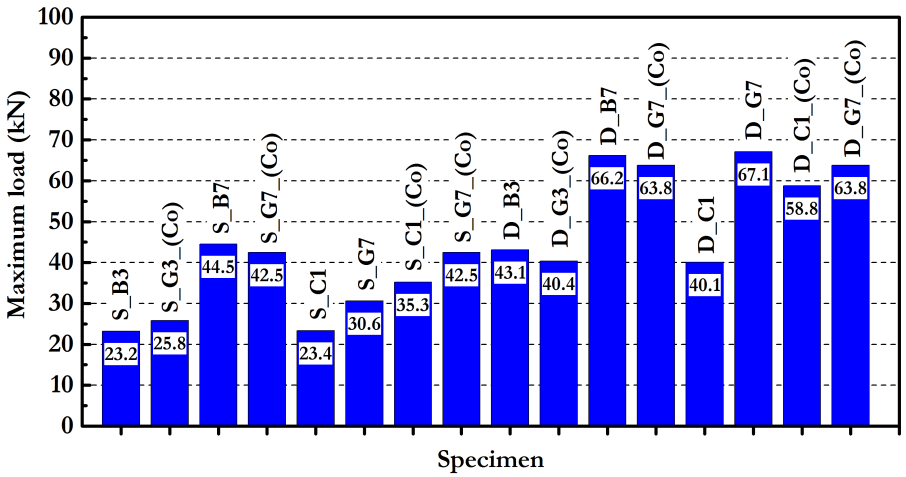


FIGURE 6.26: The effect of textile material in the out-of-plane bearing capacity of single and double-wythe walls

In terms of deformation capacity, single-wythe specimens S_G3_(Co) and S_G7_(Co) resulted in 26% and 85% increased displacement at maximum load, compared to S_B3 and S_B7 specimens respectively as shown in Fig. 6.4a. Double-wythe specimens D_G3_(Co) and D_G7_(Co) lead to 30% and 4% increased corresponding displacement of the maximum load, compared to D_B3

and D_B7 specimen, respectively (see also Fig. 6.4b). With the marginal exception of specimen D_G7_(Co), coated glass fibre textile specimens were significantly more deformable than the corresponding basalt fibre textile specimens although the axial stiffness of the corresponding TRM layers is comparable. This hints to a potential advantage of coated glass fibre textile reinforced mortars that should be further investigated in the future.

6.4.7 Comparison between bond and tensile tests results

A comparison among the masonry wall specimens failed due to textile rupture has been adopted based on the cross-sectional analysis and stress-strain compatibility of the design model for the FRP strengthened specimen reported in Triantafillou (1998b) and Matthys (2000) and the masonry walls experimental results. In this model, the force equilibrium in Eq. 6.1 and strain compatibility (see Eq. 6.4) were used for the case of FRP failure when the textile strain was equal to the ultimate tensile strain (ϵ_{fu}) before the compression failure of masonry (see also Fig. 6.27). The depth of the neutral axis is defined in Eq. 6.7, where (F_m) is the compression force of masonry, (F_f) is the tensile force of the FRP, ($f_m^{'}$) is the masonry compressive strength, (A_f) is the cross-section area of the FRP, (E_f) is the Young's modulus of FRP, (ϵ_f) is the strain of the FRP, (l) is the masonry width, (t) is the thickness of masonry and (x) is the neutral axis depth. Next, the design moment resistant is determined in Eq. 6.5, where (γ_M) is the partial safety factor for masonry, (ψ) is the ratio of the average over the maximum concrete compressive stress and (δ_G) is the distance from the compression face to the compression force divided by the depth of the compression zone, (w_f) is the mechanical FRP reinforcing ratio, and (ϵ_{mu}) is the ultimate strain of masonry (see Eq. 6.6, Eqs. 6.8-6.11).

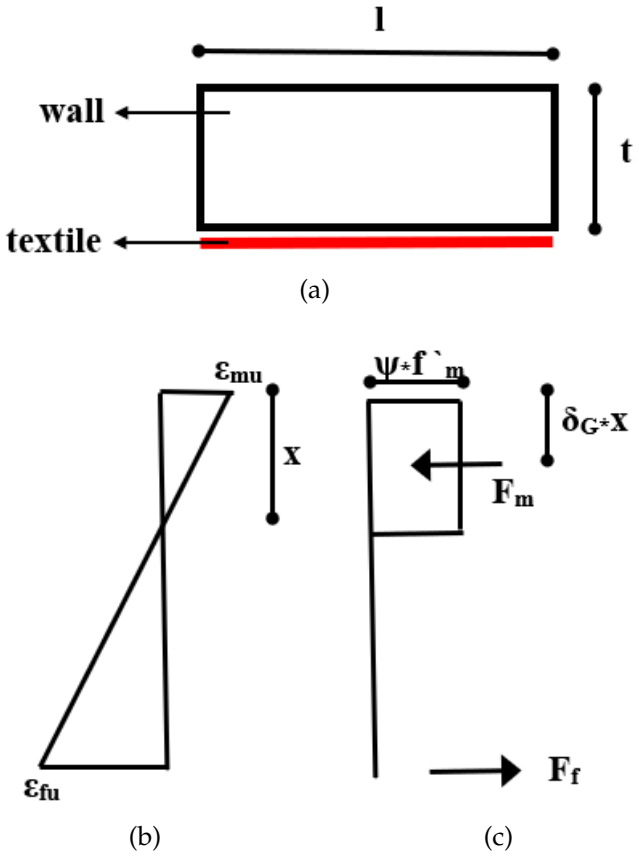


FIGURE 6.27: Cross-section analysis in out-of-plane bending (a) geometry, (b) strain distribution and (c) internal force distribution

$$F_m - F_f = 0 \tag{6.1}$$

$$F_m = \psi.f_m^{'}.l.x \tag{6.2}$$

$$F_f = A_f.E_f.\epsilon_{fu} \tag{6.3}$$

$$\frac{F_f}{E_f} = \epsilon_{mu}\frac{t-x}{x} = \epsilon_{fu} \tag{6.4}$$

$$\frac{M_{Rd}}{l.t^2.f_m^{'}} = 0.5w_f\frac{\epsilon_{fu}}{\epsilon_{mu}} + \frac{\psi.x}{2\gamma_M.t}(1-2\delta_G\frac{x}{t}) \tag{6.5}$$

$$w_f = \frac{A_f.\epsilon_m.E_f}{l.t.f_m^{'}} \tag{6.6}$$

$$\frac{x}{t} = \frac{1}{\psi}(w_f\frac{\epsilon_{fu}}{\epsilon_{mu}} + \frac{N_{Rd}}{l.t.f_m^{'}}) \tag{6.7}$$

$$\psi = 1000\epsilon_m(0.5 - \frac{1000}{12}\epsilon_m), \quad if \quad \epsilon_m \leqslant 0.002 \tag{6.8}$$

$$\psi = 1 - (\frac{2}{3000.\epsilon_m}), \quad if \quad 0.002 \leqslant \epsilon_m \leqslant 0.0035 \tag{6.9}$$

$$\delta_G = \frac{8 - 1000\epsilon_m}{4(6 - 1000\epsilon_m)}, \quad if \quad \epsilon_m \leqslant 0.002 \tag{6.10}$$

$$\delta_G = \frac{1000\epsilon_m(3000\epsilon_m - 4) + 2}{2000\epsilon_m(3000\epsilon_m - 2)}, \quad if \quad 0.002 \leqslant \epsilon_m \leqslant 0.0035 \tag{6.11}$$

In this study, the TRM properties were implemented instead of the FRP, where the ϵ_{fu} and E_f were set equal to the ultimate strain and Young Modulus of the coupon tests, respectively (see Table 6.6). Following that, an iterative procedure was applied for different values of x and the flexural resistance was defined in Eq. 6.5. Then, the maximum load $P_{max,cs}$ was defined based on the flexural resistance of a simply supported beam ($P_{max,cs}$=4M_{Rd}/L, where L is the length of the wall).

Table 6.6 presents the ultimate tensile stress of the coupon tests f_{fu}, the corresponding ultimate strain ϵ_{fu}, the experimental maximum load P_{max} and the $P_{max,cs}$ obtained using the cross-sectional analysis and stress-strain compatibility of the TRM strengthened specimen.

In single-wythe walls, almost identical values have been observed among the $P_{max,cs}$ and the P_{max} (see Table 6.6 and Fig. 6.28). In double-wythe walls, the experimental maximum load P_{max} was higher compared to the $P_{max,cs}$, due to the shear failure preceded before textile rupture occurred (see Table 6.6 and Fig. 6.28). The similar values observed show that the coupon test results can be used to predict the maximum load the TRM strengthened wall can attain. This means that this model can be used to design the TRM strengthened masonry walls which are subjected in out-of-plane bending using the TRM coupon test results for different strengthening configurations.

The results obtained from the bond tests in Chapter 5 verify the behaviour of masonry walls specimens. In particular, the dry carbon fibre-textile TRM, resulted in similar failure mode in masonry wall and bond specimens tests, where slippage between the fibre-textile and the mortar occurred. In addition, the axial stress developed for the different bond lengths was 32%-49% of the ultimate

TABLE 6.6: Tensile tests vs cross-section analysis results

Specimens	f_{fu} [MPa]	ϵ_{fu} [%]	$P_{max,cs}$ [kN]	P_{max} [kN]
S_C1_(Co)	2843	1.390	37.1	35.3
S_G3	794	1.660	11.5	14.3
S_G3_(Co)	1107	1.624	19.7	25.8
S_B3	1190	1.825	19.0	23.2
S_G7	794	1.660	30.8	30.6
D_C1	1518	0.793	25.1	40.1
D_G3	794	1.660	19.9	32.0
D_G7	794	1.660	56.6	67.1

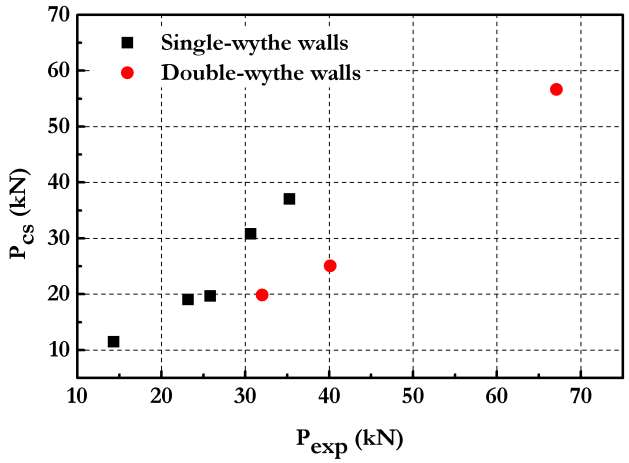


FIGURE 6.28: Cross-sectional analysis vs Experimental results

tensile stress of the carbon fibre textile, which also demonstrates low exploitation of the carbon textile strength of the S_C1 specimen.

The effect of coating on masonry walls specimens is also shown by the bond tests results. In bond tests, carbon coating increased the ultimate bond stress significantly by 151%, 112%, 76%, for bond lengths equal to 100 mm, 150 mm and 200 mm, respectively, compared to the dry carbon specimens. In this case, the failure mode modified from slippage to debonding between textile-mortar interface and tensile rupture of the mortar. Similarly, in masonry wall specimen S_C1_(Co), debonding at the textile to mortar interface with rupture of the TRM mortar occurred at the same region where textile rupture occurred as shown in Fig. 6.7b. In addition, a similar phenomenon was observed in DC1_(Co) specimen as presented in Fig. 6.16b.

The effect of coating in S_G3_(Co) is also verified by the coated glass bond tests, where increased axial stress (35%-110%) was observed compared to the uncoated glass specimens. Similar failure mode, namely textile rupture was observed in both bond tests and S_G3_(Co) specimen. This is also shown by the high exploitation of the textile strength, which was 88% for the effective bond length of 200 mm.

The coated basalt demonstrated 20%-25% higher axial bond stress compared to the coated glass corresponding specimens. This shows the superior behaviour of the coated basalt with respect to the coated glass fibre textile. Textile rupture failure mode was observed in both bond tests, coated basalt/coated glass bond tests and S_B3_(Co)/S_G3_(Co) specimens. The exploitation of the coated basalt and coated glass fibre textile was maximised to 103% and 88%, respectively, of the ultimate tensile stress of the basalt TRM coupon, at the bond length of 200 mm. In addition, the coupon test results presented in Section 4.6.1

demonstrated that the coated basalt resulted in slightly higher ultimate tensile stress (f_{fu}) and corresponding ultimate strain (ϵ_{fu}), respectively, with respect to the coated glass fibre textile.

6.5 Conclusions

In this work, an experimental campaign was carried out on single and double-wythe masonry walls strengthened with TRM composite material. The objective of this experimental work was to examine and quantify the effect of i) the textile fibres coating; ii) the number of TRM layers and; iii) the type of the textile fibre material utilised, on the out-of-plane flexural response of TRM-strengthened masonry walls. The experimental results obtained are analysed and discussed in terms of maximum load capacity, the deformation capacity and the different failure modes observed due to the aforementioned investigated parameters. Conclusions drawn from the preceding analysis are summarised as follows:

- The application of epoxy-resin coating resulted in specimens of increased maximum load capacity with respect to their uncoated counterparts, both in single and double-wythe walls. This is attributed to i) the enhanced bonding between the textile fibre and the mortar matrix due to the stiffening of the rovings and their increased surface roughness and ii) increase in the tensile strength of the fibre textile due to improved friction conditions between individual fibres within a roving.

- This was not the case for the D_G7 and D_G7_(Co) specimens where the difference in the recorded maximum loads was marginal. In both specimens, the shear capacity of the masonry wall controlled the corresponding

failure modes.

- Increasing the number of TRM layers by 2.3 times, i.e., from 3 to 7, resulted in a maximum load increase of 2.1 times for the case of the uncoated glass fibre textile material, both in single and double-wythe walls. However, the maximum load increase achieved in the case of the coated glass fibre textile TRM was 1.6 times in both single and double-wythe walls. In the case of coated basalt fibre textile TRM the corresponding increase of the load capacity was 1.9 and 1.5 times in single and double walls, respectively. Employing 7 layers of coated textile fibre TRM led to over-reinforced specimens whose strength was bounded by the masonry shear strength. Hence, increasing the number of layers has an impact similar to the application of coating by improving interlocking conditions between the fibre textile reinforcement and the matrix.

- Coated Basalt and coated glass fibre textile performed similarly in terms of load bearing capacity, both in single and double-wythe walls. Hence, the custom coating procedure described in this work, which can also be implemented on site, results in a strengthening configuration that is equivalent to that of an industrially manufactured textile composite material.

- The deformability of S_G7_(Co) was significantly increased compared to S_B7 specimen. Although the axial stiffness and strength of the TRM in both cases was practically identical, glass textile fibre reinforcement seems to be providing an advantage that should be further investigated in the future.

- In all cases examined bonding achieved between the TRM and the masonry substrate was optimum as debonding only occurred after the maximum load was attained.

- As manifested by P_{max} to P_{con} ratio TRM effectiveness was more pronounced in single-wythe walls compared to the much stiffer double-wythe walls. In the latter, the maximum load of the strengthened specimens was bounded by the masonry shear capacity.

Chapter 7

Strengthening of masonry arches with TRM material

7.1 Introduction

In this Chapter, an extensive experimental work on masonry arches strengthened with TRM is provided. The aim of this study was to examine the effectiveness of the TRM composite system on the masonry arches specimens when monotonic load is applied at the quarter length of the span comprising several investigating parameters (e.g., different composite materials, different amount of the composite material).

In this study, the effect of the wall buttresses and backfill, has not been considered. This assumption has been made for the simplicity of the experimental setup. The presence of the backfill could modify the failure modes and prevent the sliding occurred at the supports of the arch. However, the scope of this experimental work was to quantify the effectiveness of each fibre textile material for all the investigated parameters and not to study the effect of the backfill on the masonry arches.

In the following, the experimental program is described. Next, the experimental results are presented and then the discussion is provided based on the experimental results obtained. Finally, the conclusions are drawn based on the experimental results and discussion.

7.2 Experimental Program

7.2.1 Test specimens and investigated parameters

Eight half-scaled masonry arches specimens were built with a 2.0 m span, 0.5 m rise, 0.1025 m thickness, and 0.44 m width. Half-scale was selected to better reflect typical geometries of masonry arches also as suggested in the relevant literature, see, e.g., Borri et al. (2009). Solid clay bricks were used along with a general purpose masonry cement mortar of 10 mm thickness for both bed and head joints.

The key investigated parameters of this study were: (a) the textile fibre material used, i.e., coated glass and coated basalt, (b) the number of TRM layers, and (c) the strengthening configuration (intrados versus extrados). The control specimen (CON) was not strengthened. The remaining 7 specimens were strengthened at either their internal or external surface, i.e., intrados and extrados, respectively. Three and seven layers of coated glass or coated basalt TRM were applied as strengthening material at the intrados or the extrados of each masonry arch. The case of seven layers of coated glass and basalt TRM is considered as these have been shown to have an axial stiffness equivalent to a single carbon TRM layer (see Chapters 4, 6). This can hence provide a comparative basis with previous works where the case of carbon fibre textile material is considered, (see, e.g., Zampieri et al., 2018). The case of three layers

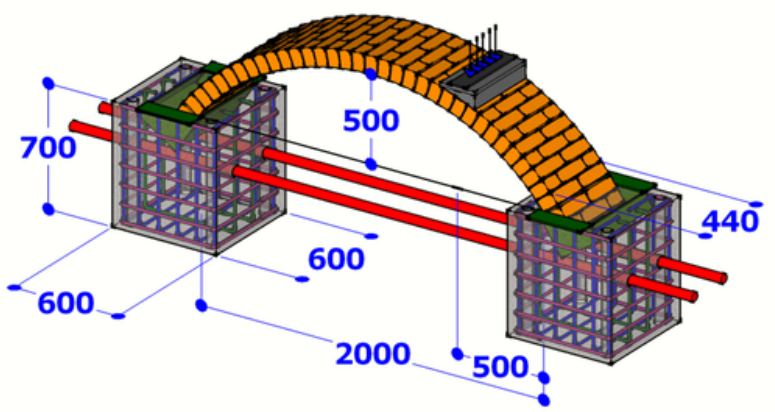
TABLE 7.1: Specimens and investigated parameters

Specimen	TRM material	Strengthened at the	Number of TRM layers	TRM thickness [mm]	In-house coating applied
CON		-			No
G3_I	Coated glass	Intrados	3	7	Yes
G7_I	Coated glass	Intrados	7	9	Yes
B3_I	Coated basalt	Intrados	3	9	No
G3_E	Coated glass	Extrados	3	7	Yes
G7_E	Coated glass	Extrados	7	9	Yes
B3_E	Coated basalt	Extrados	3	9	No
B7_E	Coated basalt	Extrados	7	13	No

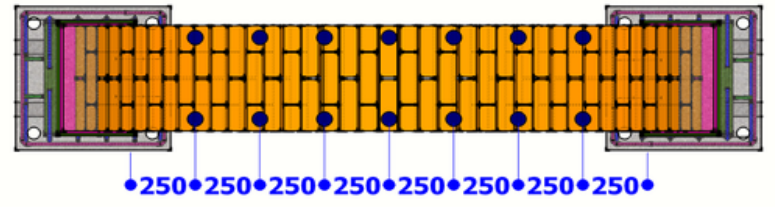
is further considered to investigate the influence of the amount of reinforcement when this is practically halved. The glass textile fibre material was coated using an in-house coating procedure whereas coated basalt textile-fibre material was a commercially coated material. The in-house coating procedure employed is discussed in Section 7.2.2.

The specimens together with the corresponding investigated parameters are summarized in Table 7.1. The notation adopted for the strengthened arches is MN_Cf, where M denotes the fibre textile material (G for coated glass and B for coated basalt), N denotes the number of TRM layers (3 and 7) and Cf denotes the strengthening configuration (E for Extrados and I for Intrados).

It is of interest to note that, although attempted, the application of 7 layers of basalt textile fibre material at the intrados of the arches was not feasible; due to the the large mesh spacing of 25 mm the textile fibre material was slipping while the mortar was still in fresh state.



(a)



(b)



(c)

FIGURE 7.1: Experimental setup - all units are in mm (a) geometry and load configuration (b) plan view and position of displacement transducers (c) actual setup

7.2.2 Materials

The arches were built using solid clay bricks with UK typical nominal dimensions. The properties of the bricks and masonry walletes are presented in Sections 4.2 and 4.4, respectively.

Joint and strengthening mortar prisms were tested for each specimen, under flexure and compression as described in Sections 4.3 and 4.5. Table 7.2 presents the mean values of the compressive and tensile strength. The variability was similar for the compressive strength of both casting and strengthening mortar and marginally increased for casting mortar tensile strength. In any case, the observed variabilities did not affect the observed failure modes.

The strengthening of masonry arches was performed using either coated glass or coated basalt textile fibre material. The corresponding material properties and the fibre-textiles configurations per the manufacturer datasheets and from tensile tests on bare textiles and TRM coupons used are demonstrated in Section 4.6.

The glass textile fibre material was coated in-house using a two part commercial epoxy resin as presented in Section 4.7. On the other hand, coated basalt fibre-textile was a commercial product manufactured with 10% bituminous binder.

The strengthening mortar used for the application of the TRM is described in Section 4.5. The mean values of the flexural and compressive strength were determined on the day of testing and found equal to 9.8 MPa and 32.8 MPa, respectively.

7.2.3 Strengthening procedure

TRM strengthening was implemented according to the following procedure:

TABLE 7.2: Casting and strengthening mortar of masonry arches specimens

Specimens	Casting mortar		Strengthening mortar	
	Compressive Strength f_m [MPa]	Tensile Strength f_{mt} [MPa]	Compressive Strength f_m [MPa]	Tensile Strength f_{mt} [MPa]
CON	9.2	3.5		
G3_I	9.0	2.8	38.6	9.2
G7_I	8.1	3.0	30.9	8.6
B3_I	7.2	2.5	32.1	10.2
G3_E	6.8	2.6	37.4	10.2
G7_E	6.7	2.7	37.1	10.5
B3_E	9.7	2.8	25.6	8.9
B7_E	7.8	2.8	28.2	11.1
Mean value	8.1 (1.2* / 0.14**)	2.8 (0.3* / 0.11**)	32.8 (5.0* / 0.15**)	9.8 (0.9* / 0.09**)
*Standard deviation/ **Coefficient of Variation				

- Dust from the surface to be strengthened was removed using air pressure.
- After dampening the specimen, the mortar was applied to cover the entire surface of the masonry arch.
- One layer of the fibre textile was impregnated into the mortar using hand pressure (Fig. 7.2a).
- The textile was completely covered by one layer of mortar. The described procedure was repeated for each additional TRM layer. Figure 7.2b and Fig. 7.2c present the final strengthening layout for extrados and intrados strengthening configuration, respectively. To obtain sufficient adhesion between the TRM layers the strengthening procedure is required to be completed while the mortar is in fresh state.



(a) (b) (c)

FIGURE 7.2: (a) Application of basalt textile into the mortar (b) Extrados and (c) Intrados final strengthening configuration

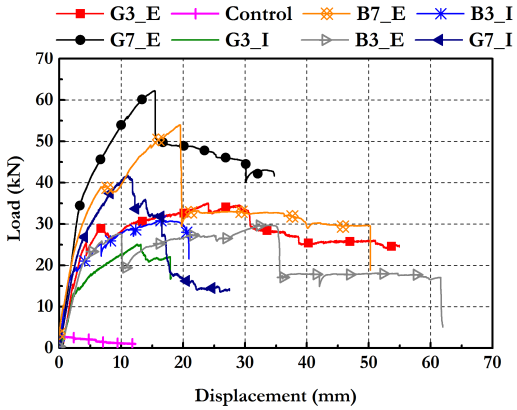
7.2.4 Experimental setup and procedure

A vertically positioned servo-hydraulic actuator of 100 kN capacity was fastened to a stiff steel reaction frame at the quarter length of the span as shown in Fig. 7.1c. The load was applied monotonically under displacement control at a rate of 0.005 mm/s and 0.015 mm/s for the control and strengthened specimens, respectively. The loading rate chosen for the strengthened specimens (approximately equal to 1mm/sec) is typical for static tests on masonry and concrete structures. A lower rate was chosen for the control specimen to accommodate for its significantly lower strength and deformability. The masonry arches were fixed on concrete blocks. The latter were tied to the strong floor via steel threaded rods. The concrete blocks were further tied together to prevent longitudinal displacements using two steel rods as presented in Fig. 7.1a. Fourteen displacement transducers were positioned every 250 mm lengthwise to measure the vertical displacement profile of the arch as shown in Fig. 7.1b. Data was collected at a frequency of 4 Hz, synchronised and recorded using a fully-computerized data acquisition system.

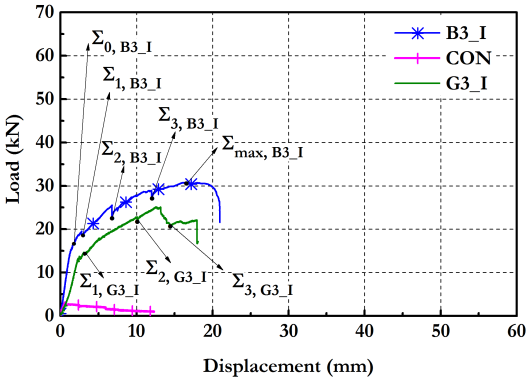
7.3 Experimental Results

The load-displacement response plots for all specimens are presented in Fig. 7.3a. The data presented in these plots were obtained from the actuator feedback to the controller. The measurements from the displacement transducers positioned on either side of the actuator (Figure 7.1c) were used to confirm that the load was applied uniformly along the width of the arch. Table 7.3 summarizes the experimental results in terms of the maximum load P_{max}, the displacement at maximum load d_{max}, the ultimate load P_{ult}, the displacement at ultimate load d_{ult}, the strength increase ratio defined as $SIR = P_{max}/P_{CON}$, the displacement increase ratio defined as DIR=d_{ult}/d_{CON} and the observed failure modes. The ultimate load is defined as P_{ult} = max(0.8P_{max}, P_{final}), where P_{final} is the last recorded load value as shown in the Load vs Displacement curves (Fig. 7.3a). The reported displacements correspond to mean values of the displacement transducers at the position of the actuator. The vertical displacement profiles at P_{ult} are shown in Fig. 7.4.

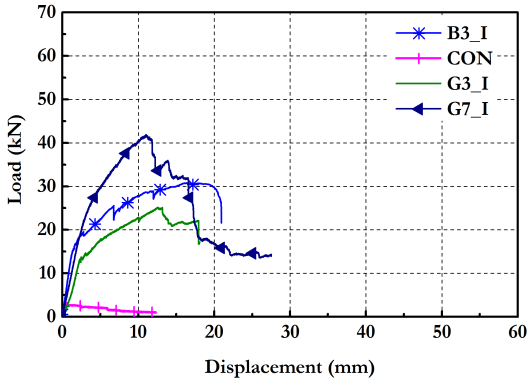
Failure modes varied according to the strengthening configuration, the ratio of the strengthening material, and the fibre-textile material utilised. The control specimen failed in a four-hinge collapse mechanism shown in Fig. 7.5b; as expected the four hinges formed in alternate positions of intrados and extrados. The control specimen peak load and the corresponding displacement was 3.2 kN and 0.7 mm, respectively (see Fig. 7.3c). The first crack initiated under the point load when the maximum load was attained from the intrados towards the extrados, where the first hinge formed (point $\Sigma_{1,CON}$ in Fig. 7.3d). Subsequently, a hairline crack initiated from the extrados towards the intrados of the crown where the second hinge formed ($\Sigma_{2,CON}$ in Fig. 7.3d). Both hinges



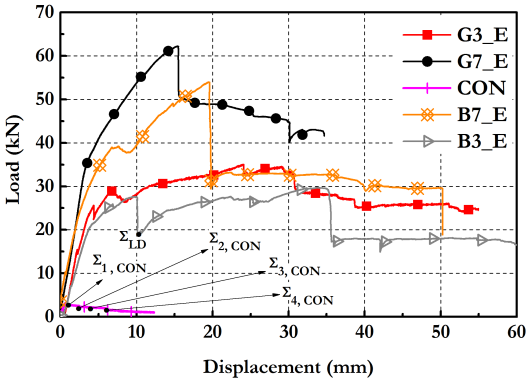
(a) All specimens



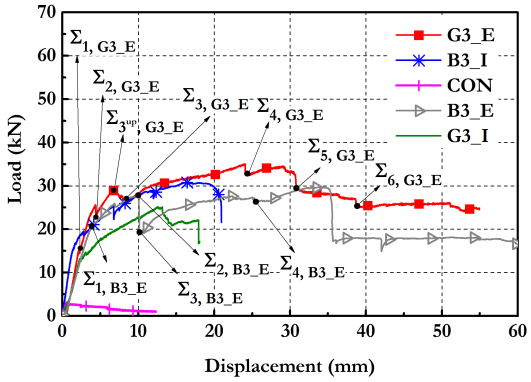
(b) Intrados: Basalt Vs glass textile



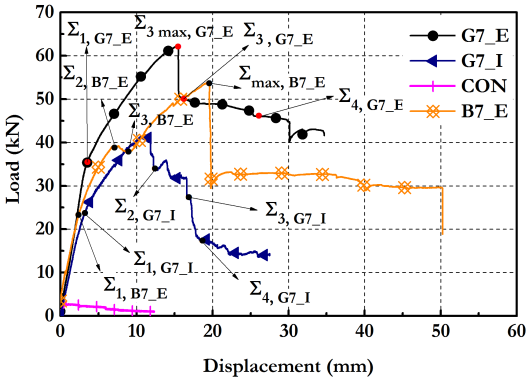
(c) Intrados: 3 and 7 TRM layers



(d) Extrados: 3 and 7 TRM layers



(e) Extrados Vs Intrados 3 TRM layers



(f) Extrados Vs Intrados 7 TRM layers

FIGURE 7.3: Experimental load-displacement curves in terms of the number of layers, textile material, and the position of the strengthening

TABLE 7.3: Summary of experimental results

	P_{max} [kN]	d_{max} [mm]	P_{ult} [kN]	d_{ult} [mm]	SIR	DIR	Failure mode
CON	3.2	0.7	2.6	1.9	1.0	1.0	4-hinge mechanism
G3_I	25.1	13.2	20.1	18.0	7.8	9.7	2 hinges[5,6], shear sliding[1,2]
G7_I	41.9	11.0	33.5	12.4	13.1	6.7	2 hinges[5,6], shear sliding[1,2]
B3_I	30.8	16.5	24.6	21.0	9.6	11.3	2 hinges[5,6], masonry crushing shear sliding[1,3,4]
G3_E	35.1	24.1	28.1	35.0	11.0	18.8	Shear sliding[1,4], cracks[5,6]
G7_E	62.2	15.4	49.8	16.8	19.4	9.0	2 hinges[1,4], shear sliding [5] cracks[6]
B3_E	29.7	33.9	23.8	35.6	9.3	19.1	Shear sliding [1,4], cracks [5,6] hinge[5]
B7_E	54.0	19.4	43.2	19.7	16.9	10.6	2 hinges[4,5], shear sliding[1] cracks[6]

[1]left support, [2]followed by TRM debonding under point load, [3]partial textile rupture [4]under point load, [5]right support, [6]left haunch

gradually grew wider until the end of the test (Fig. 7.5a and Fig. 7.5c). After the onset of point $\Sigma_{2,CON}$ in Fig. 7.3d a crack initiated at the left support from the intrados towards the extrados until point $\Sigma_{4,CON}$ in Fig. 7.3d, where the third hinge formed (Fig. 7.5d). At point $\Sigma_{3,CON}$ in Fig. 7.3d a crack initiated at the right support from the extrados and gradually propagated to the intrados. Finally the collapse occurred when the fourth hinge formed at the intrados of the right support at the end of the test (Fig. 7.5e).

The failure of G3_I specimen was manifested by the formation of two flexural hinges, shear sliding at the left support and under the point load, followed by debonding of the TRM material from the masonry substrate (Fig. 7.6). The maximum recorded load was 25.1kN and the corresponding displacement 13.2mm (Table 7.3). Approaching the load at point $\Sigma_{1,G3_I}$ in Fig. 7.3b a hairline crack initiated from the extrados of the left support and gradually propagated towards the intrados. Subsequently, a crack formed at the extrados of the left haunch and propagated until the intrados where the first hinge formed (Fig.

7.6a). At the meantime of load points $\Sigma_{1,G3_I}$ and $\Sigma_{2,G3_I}$ in Fig. 7.3b, a crack initiated at the right support from the extrados and propagated towards the intrados of the arch, where the second hinge formed. Approaching the maximum load (point $\Sigma_{3max,G3_I}$ in Fig. 7.3b) the hinge widened until the end of the test (Fig. 7.6e). At the same time, a shear diagonal crack initiated from the TRM interface and propagated diagonally, crossing the adjacent bricks towards the point load (Fig. 7.6c). Thereafter, debonding of the TRM (point $\Sigma_{4,G3_I}$ in Fig. 7.3b) resulted in complete collapse of the arch, followed by significant outward movement at the mortar joint of the left support (Fig. 7.6d).

The failure mechanism G7_I specimen was subjected involved two flexural hinges, shear sliding among the mortar joint of the left support and at the region of the point load with subsequent debonding of the TRM material from the masonry substrate (Fig. 7.7). The maximum load and the corresponding displacement attained was 41.9kN and 11.0mm, respectively as presented in load-displacement curve in Fig. 7.3 (see also Table 7.3). At early stage of loading (point $\Sigma_{1,G7_I}$ in Fig. 7.3f) a crack initiated from the extrados of the right support towards the intrados, where the first hinge formed (Fig. 7.7e). The hinge continued growing wider until load point $\Sigma_{2,G7_I}$ in Fig. 7.3f was attained. After the onset of point $\Sigma_{1,G7_I}$ in Fig. 7.3f cracks at the left support and left haunch appeared almost at the same time. The crack at the left support initiated from the TRM-masonry interface towards the extrados. Approaching the maximum load the crack gradually grew wider which resulted in a significant shear sliding mode at points $\Sigma_{3,G7_I}$ and $\Sigma_{4,G7_I}$ in Fig. 7.3f (see also Fig. 7.7d). Subsequently, a hairline crack initiated from the extrados of the left haunch towards the intrados where the second hinge formed and gradually widened when the maximum load was attained (Fig. 7.7a). At the onset of the maximum load a

shear crack propagated diagonally crossing the mortar joint and brick towards the point load. The crack gradually broadened and propagation of the crack towards the interface of TRM-masonry substrate occurred which resulted in TRM debonding (Fig. 7.7c).

The specimen B3_I failed due to the formation of two flexural hinges, shear sliding at the left support and masonry crushing followed by shear sliding and partial textile rupture at the loaded region of the arch (Fig. 7.8). The peak load and corresponding displacement recorded were 30.8 kN and 16.5 mm, respectively (Table 7.3). Approaching point $\Sigma_{0,B3_I}$ in Fig. 7.3b a hairline crack initiated from the extrados of the left haunch and increasing the load until point $\Sigma_{2,B3_I}$ in Fig. 7.3b propagated towards the intrados where the first hinge gradually formed. Subsequently, the adjacent bricks of the hinge jointed back together and another hinge formed at the intrados of the left haunch, which gradually grew wider until the end of the test (Fig. 7.8a). After point $\Sigma_{0,\ B3_I}$ in Fig. 7.3b a crack initiated at the left support from the intrados and further increasing the load until point $\Sigma_{2,B3_I}$ in Fig. 7.3b the crack crossed the mortar joint. When the maximum load was attained (point Σ_{maxB3_I} in Fig. 7.3b) a significant outward movement (shear sliding) gradually occurred at the left support. The second hinge formed at the right support. At the meantime of loading point $\Sigma_{1,B3_I}$ and $\Sigma_{2,B3_I}$ in Fig. 7.3b a crack initiated from the extrados towards the intrados. Approaching the load point $\Sigma_{3,B3_I}$ in Fig. 7.3b the second hinge formed at the intrados of the mortar joint at the right support (Fig. 7.8e). The failure of the arch gradually developed under the point load. During the points $\Sigma_{2,B3_I}$ and $\Sigma_{3,B3_I}$ in Fig. 7.3b a crack initiated from the TRM-masonry substrate interface towards the extrados of the arch. Further increasing the load until the maximum point $\Sigma_{max,B3_I}$ in Fig. 7.3b the crack propagated crossing the adjacent

brick, where masonry crushing occurred. Subsequently, the cracks grew wider and the end of the test manifested when shear sliding along the mortar joint occurred, which resulted in partial rupture of the textile (Fig. 7.8c). At this stage, further shear sliding at left support of the arch also occurred (Fig. 7.8d).

Specimen G3_E failed due to shear sliding at the left support and under the loaded cross-section. Instead of the hinges appeared at the control specimen cracks formed at the adjacent mortar joints of the right support and left haunch. The maximum recorded load was 34.9kN and the corresponding displacement 24.1mm as shown in Fig. 7.9 (see also Table 7.3). At early stage of loading cracks appeared under the point load and left support almost simultaneously. At point $\Sigma_{1,G3_E}$ in Fig. 7.3e, a hairline crack appeared under the loaded region of the intrados and approaching the point ${\Sigma_3}^{up}{}_{G3_E}$ in Fig. 7.3e propagated until the TRM-masonry substrate interface. A crack initiated at the left support from the intrados and propagated towards the interface of TRM-masonry substrate (between points $\Sigma_{2,G3_E}$ -$\Sigma_{3,G3_E}$ in Fig. 7.3e). Further increasing the load (between points $\Sigma_{3,G3_E}$ and $\Sigma_{4,G3_E}$ in Fig. 7.3e) the crack crossed the adjacent brick, grew wider and shear sliding at the left support took place. It is noted that at the onset of point $\Sigma_{3,G3_E}$ a minimal shear sliding along the mortar joint under the point load resulted in the left support outward movement. Approaching the point $\Sigma_{4,G3_E}$ in Fig. 7.3e shear sliding further developed in both mortar joint of the loaded cross-section and the left support (Figs. 7.9c and 7.9d). Additionally, cracks developed at left haunch and right support (between points $\Sigma_{3,G3_E}$ - $\Sigma_{4,G3_E}$), as shown in Fig. 7.3e (see also Figs. 7.9a and 7.9e). The complete failure mechanism of the arch was developed due to shear sliding of the loaded cross-section(Fig. 7.9c).

Specimen G7_E failed due to the formation of two hinges (under the point

load and left support) and shear sliding at the mortar joint of the right support. The hinge formed at the left haunch of the control specimen was prevented by cracks developed on the TRM surface (Fig. 7.11b). The maximum recorded load was 62.2kN and the corresponding displacement 15.4 mm as shown in fig (see also Table 7.3). At early stage of loading (point $\Sigma_{1,G7_E}$ in Fig. 7.3f) a hairline crack initiated at the intrados under the point load and gradually propagated towards the extrados. The first hinge finally formed at the extrados which gradually grew wider until the end of the test (Fig. 7.11c). Further increasing the load during the post-elastic branch (point $\Sigma_{1,G7_E} - \Sigma_{3max,G7_E}$ in Fig. 7.3f), the second hinge formed at the extrados of the left support. Thereafter the hinge gradually grew wider due to a subsequent upward movement of the entire support, which developed until the completion of the test (Fig. 7.11d). At the meantime of points $\Sigma_{1,G7_E}$ and $\Sigma_{4,G7_E}$ in Fig. 7.3f, cracks formed at the mortar joints of the left haunch, right support and crown of the arch (Figs. 7.11a and 7.11e). Approaching the maximum load (point $\Sigma_{3,max,G7_E}$ in Fig. 7.3f), a crack initiated at the right support which broadened until point $\Sigma_{4,G7_E}$ in Fig. 7.3f. The complete failure of the arch developed when the hinge under the point load was significantly enlarged, to provoke shear sliding at the right support (Fig. 7.11e).

Specimen B3_E failed due to shear sliding at the mortar joint of the left support and under the loaded region of the arch as shown in Fig. 7.10b. Cracks formed at the left haunch and right support where a hinge finally formed. The maximum recorded load was 29.7 kN and the corresponding displacement 33.8 mm (see also Fig. 7.3e and Table 7.3). At early stage of loading the first hairline crack propagated under the loaded cross-section from the intrados towards the extrados of the arch, when the point $\Sigma_{1,B3_E}$ in Fig. 7.3e was attained. Subsequently, the second crack initiated at the left support from the intrados towards

the extrados. Further increasing the load between points $\Sigma_{1,B3_E}$ - $\Sigma_{2,B3_E}$ in Fig. 7.3e, the crack reached the extrados and then propagated through the masonry substrate - TRM interface. At the same time, another crack initiated from the intrados under the point load and reached the extrados at point $\Sigma_{3,B3_E}$ in Fig. 7.3e, where it also grew wider. Additionally, cracks formed at the left haunch and the right support among points $\Sigma_{1,B3_E}$, $\Sigma_{2,B3_E}$ in Fig. 7.3e at the positions where hinges formed at the control specimen (see also 7.10a and 7.10e). Further increasing the load between points $\Sigma_{3,B3_E}$ - $\Sigma_{4,B3_E}$ in Fig. 7.3e shear sliding occurred at the mortar joint of the loaded region and the crack of the left support gradually grew wider. Approaching the maximum load, significant shear sliding at the left support and under the point load gradually occurred, which further expanded until the end of the test (7.10c and 7.10d). Subsequently, a hinge gradually formed at the right support. The complete failure of the specimen was pronounced due to shear sliding of the left support (Fig. 7.10d).

Specimen B7_E failed due to the formation of two hinges (under the point load and right support) and due to shear sliding at the left support mortar joint (Fig. 7.12). Cracks formed at the TRM surface of the left haunch of the arch. The maximum load attained was 54.0 kN and the corresponding displacement 19.4 mm (see also Fig. 7.3 and Table 7.3). The first crack formed under the loaded cross-section of the arch during the linear part of the load-displacement curve (Fig. 7.3f). Subsequently, another crack initiated from the intrados towards the extrados (at point $\Sigma_{2,B7_E}$ in Fig. 7.3f) and propagated until TRM-masonry interface of the loaded region where the first hinge formed (Fig. 7.12c). Approaching the maximum load ($\Sigma_{max,B7_E}$), the hinge gradually grew wider until the end of the test. A crack initiated at the left support (in point $\Sigma_{2,B7_E}$ in

Fig. 7.3f), which further increasing the load to the maximum $\Sigma_{max,B7_E}$ significant shear sliding developed (Fig. 7.12d). In the meantime of points $\Sigma_{3,B7_E}$-$\Sigma_{max,B7_E}$ (Fig. 7.3f) cracks formed at the right support and the left haunch of the arch (Figs. 7.12a and 7.12e). After the maximum load was attained the second hinge gradually developed at the right support of the arch (Fig. 7.12e). The failure of the arch was pronounced when complete shear sliding occurred at the left support of the arch as shown in Fig. 7.12d.

7.4 Discussion

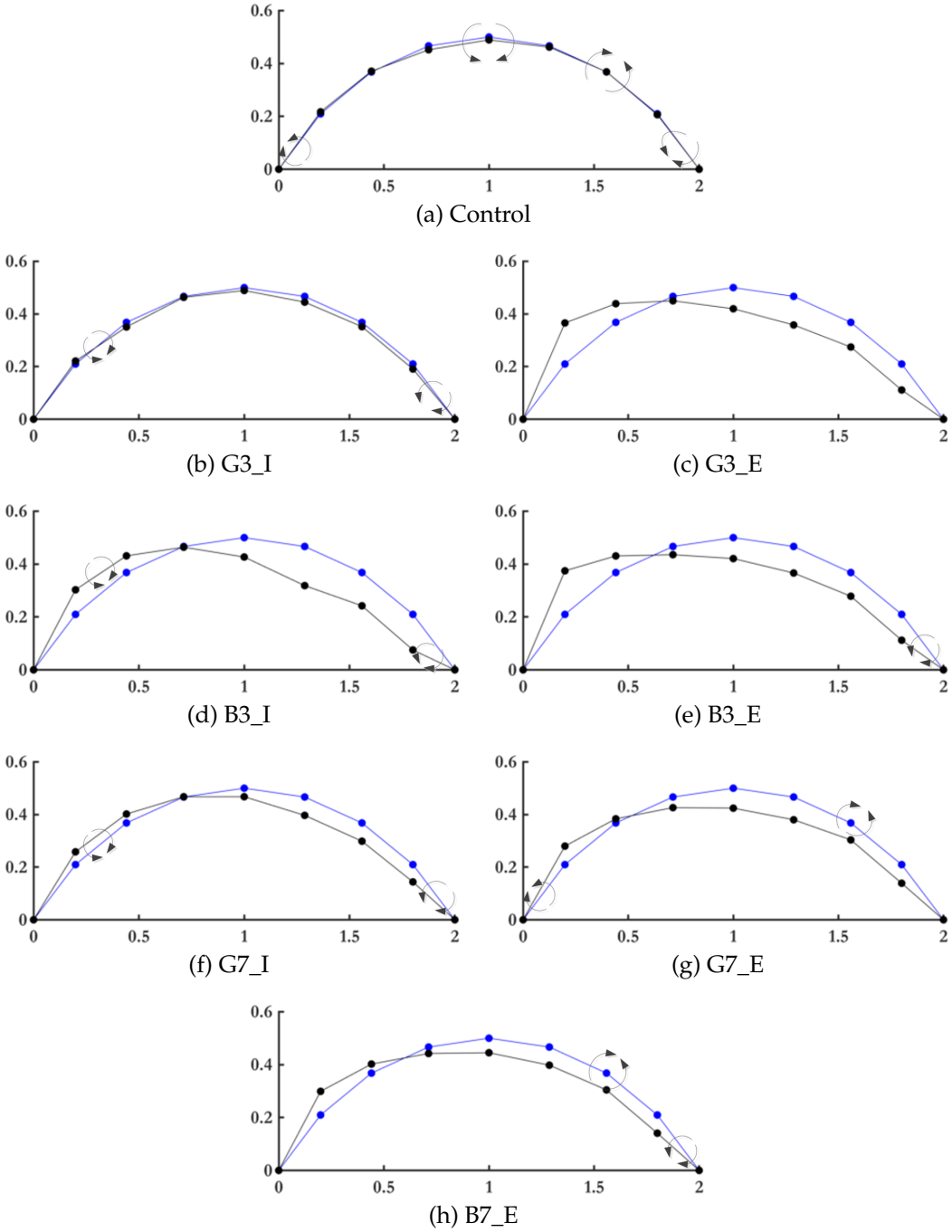
7.4.1 Overview

Compared to the control specimen, all strengthened specimens demonstrated increased values of their maximum load and deformation capacity. The maximum SIR was recorded for G7_E, i.e., 19.4 whereas the minimum SIR was recorded for G3_I, i.e., 7.8 as shown in Fig. 7.13.

Among the specimens strengthened at the extrados, G7_E demonstrated the highest SIR, whereas B3_E the lowest, i.e., 9.3. The corresponding SIRs for arches strengthened at the intrados were 13.1 and 7.8 for G7_I and G3_I, respectively.

7.4.2 The effect of the textile material

The utilisation of coated glass textile fibre material resulted in marginally increased values of P_{max} when compared to the coated basalt specimens. In particular, G3_E and G7_E attained increased maximum loads by 18% and 15% when compared to B3_E and B7_E, respectively (see also Fig. 7.14a). The failure modes in both glass and basalt specimens were similar as reported in Table 7.3.



(a) Control

(b) G3_I

(c) G3_E

(d) B3_I

(e) B3_E

(f) G7_I

(g) G7_E

(h) B7_E

FIGURE 7.4: Vertical Displacement profiles - Displacements are scaled by a factor of 5 and units are in m

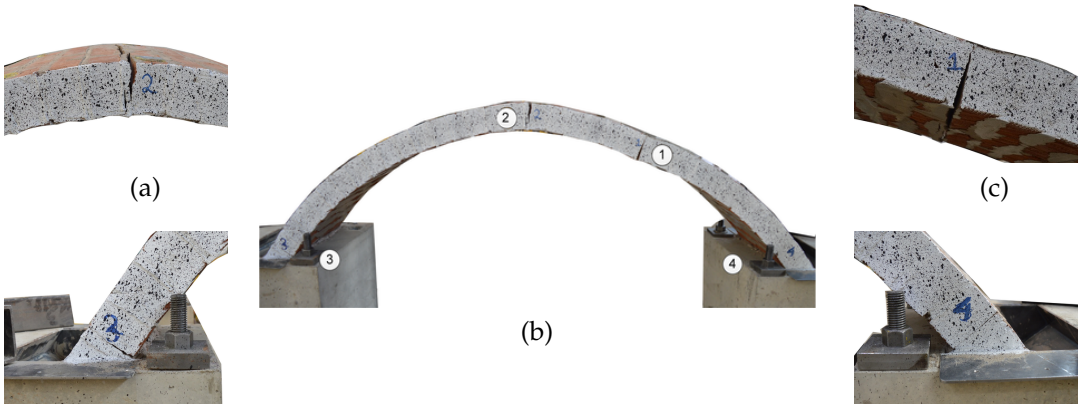


FIGURE 7.5: Collapse mechanism of control specimen (a) Section 2, (c) Section 1, (d) Section 3, (e) Section 4

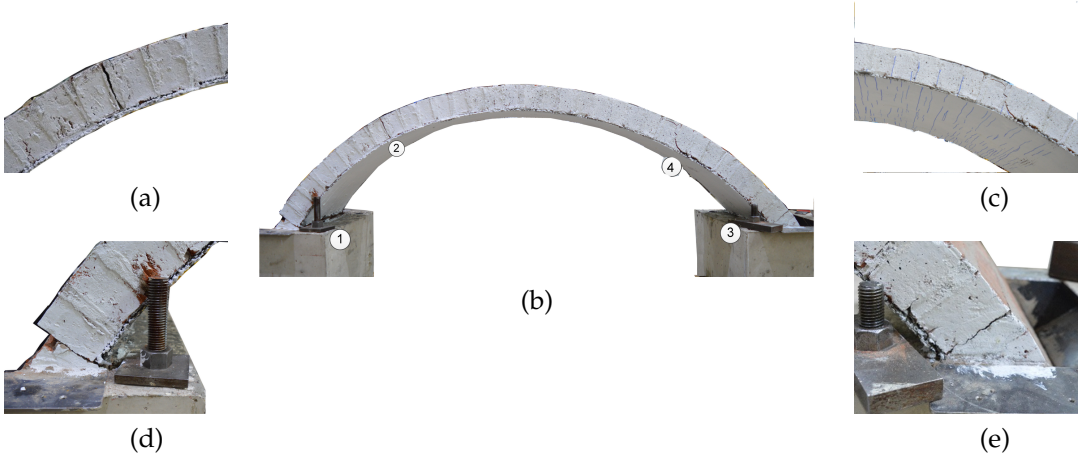


FIGURE 7.6: Collapse mechanism of specimen G3_I (a) Section 2, (c) Section 4, (d) Section 1, (e) Section 3

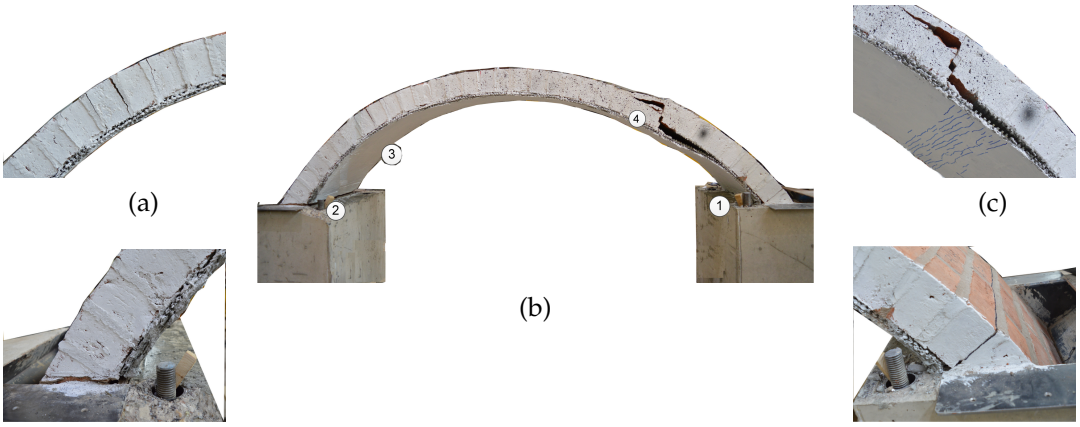


FIGURE 7.7: Collapse mechanism of specimen G7_I (a) Section 3, (c) Section 4, (d) Section 2, (e) Section 1

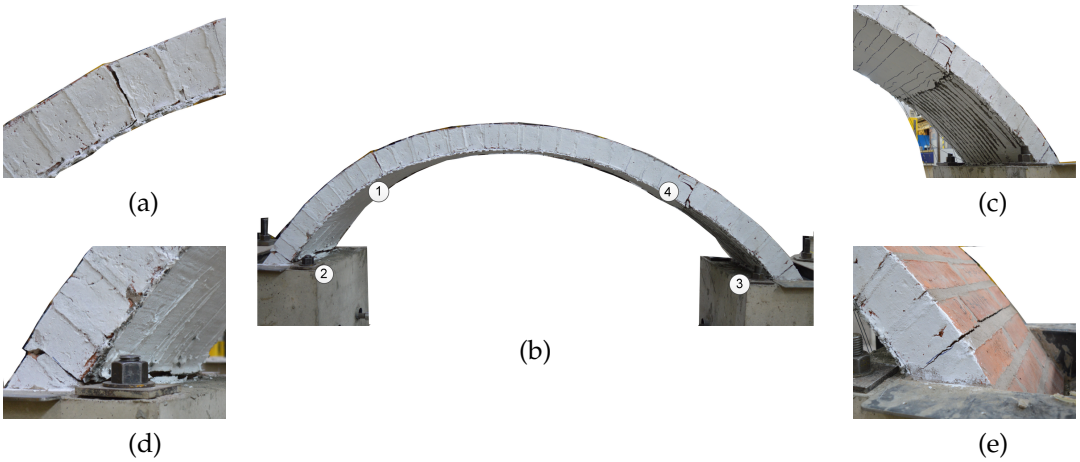


FIGURE 7.8: Collapse mechanism of specimen B3_I (a) Section 1, (c) Section 4, (d) Section 2, (e) Section 3

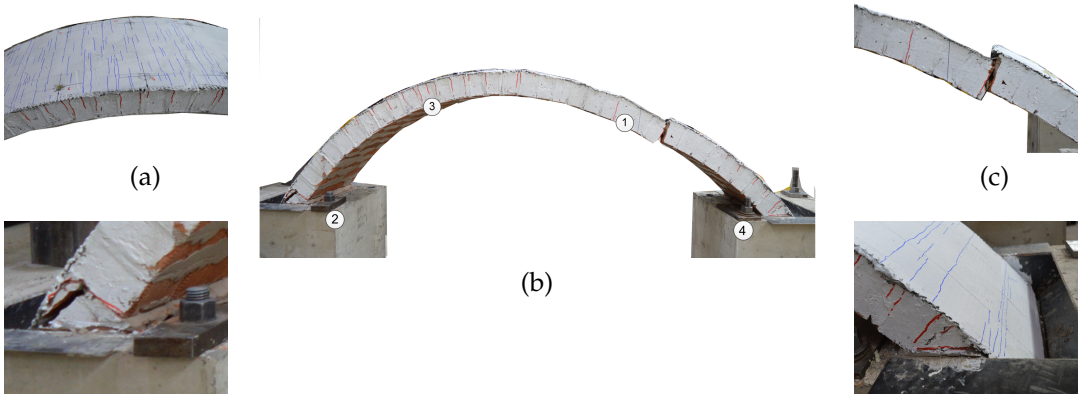


FIGURE 7.9: Collapse mechanism of specimen G3_E (a) Section 3, (c) Section 1, (d) Section 2, (e) Section 4

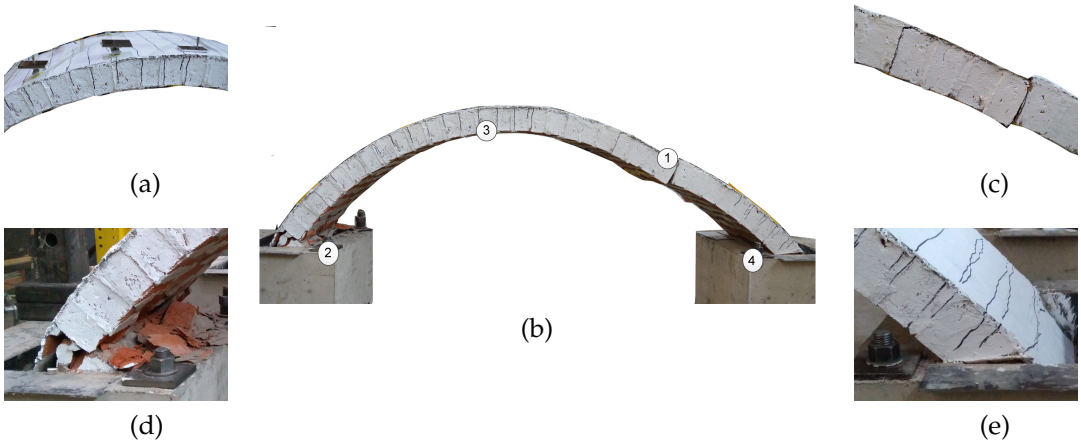


FIGURE 7.10: Collapse mechanism of specimen B3_E (a) Section 3, (c) Section 1, (d) Section 2, (e) Section 4

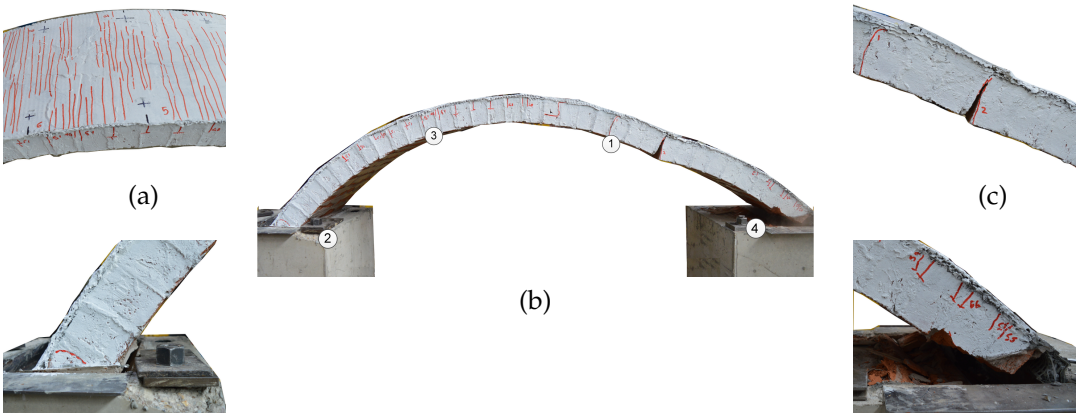


FIGURE 7.11: Collapse mechanism of specimen G7_E (a) Section 3, (c) Section 1, (d) Section 2, (e) Section 4

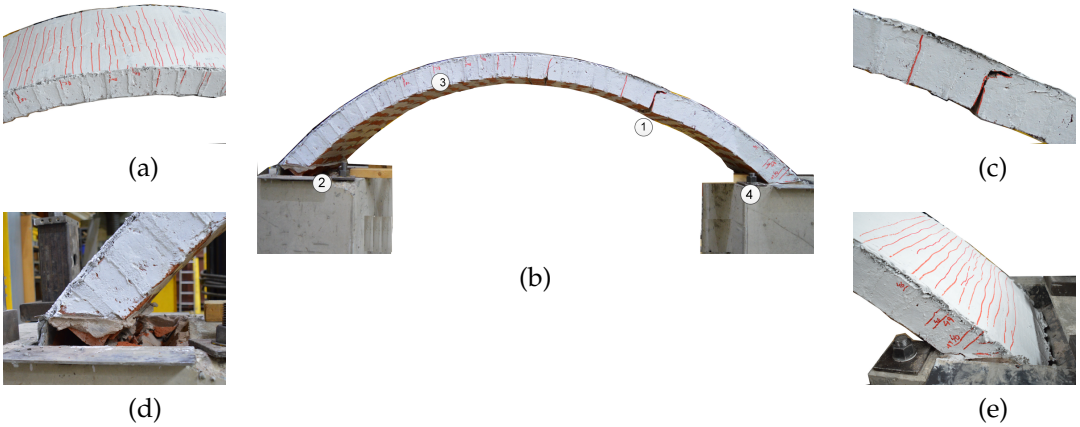


FIGURE 7.12: Collapse mechanism of specimen B7_E (a) Section 3, (c) Section 1, (d) Section 2, (e) Section 4

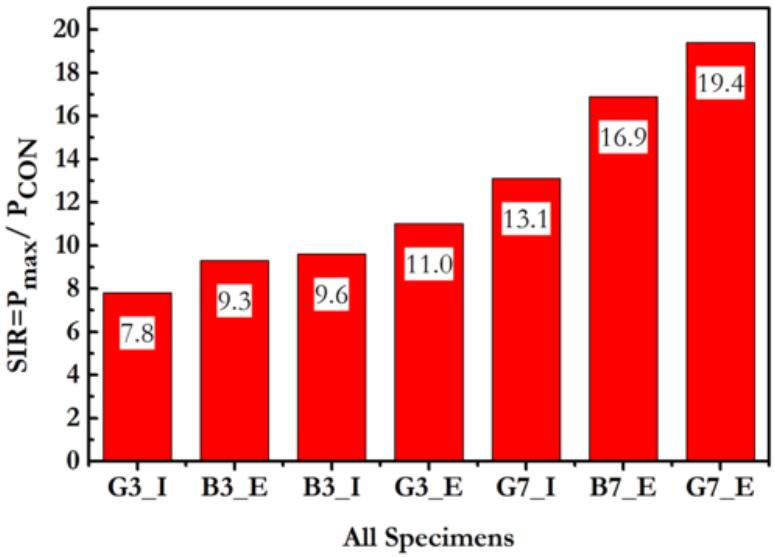


FIGURE 7.13: Ratio of the maximum strength effectiveness

In the intrados case, B3_I demonstrated a higher P_{max} by 23% compared to G3_I; however the maximum loads recorded in these specimens correspond to different failure mechanisms. In B3_I, brick crushing and partial textile rupture occurred at P_{max}, then followed by shear sliding whereas in G3_I shear sliding was observed at P_{max} leading to immediate collapse. Brick crushing significantly altered the development length of sagging regions in the arch, (see Figs. 7.4d for B3_I and 7.4b for G3_I, respectively) hence activating larger TRM lengths. Furthermore, the debonding of the TRM under the point load in G3_I, prevented the development of the masonry crushing zone and hints to poorer bonding conditions for the glass fibre textile.

Conversely, the larger development length of the TRM in the extrados region provided the necessary bond length to the glass fibre textile; this led to a better utilisation of the composite system stiffness and strength. The tensile cracks in the TRM surface of the coated glass specimens (G3_I, G3_E, G7_E) were more uniformly distributed than in the case of coated basalt specimens (B3_I, B3_E, B7_E); this also highlights the improved bonding conditions in G3_E compared

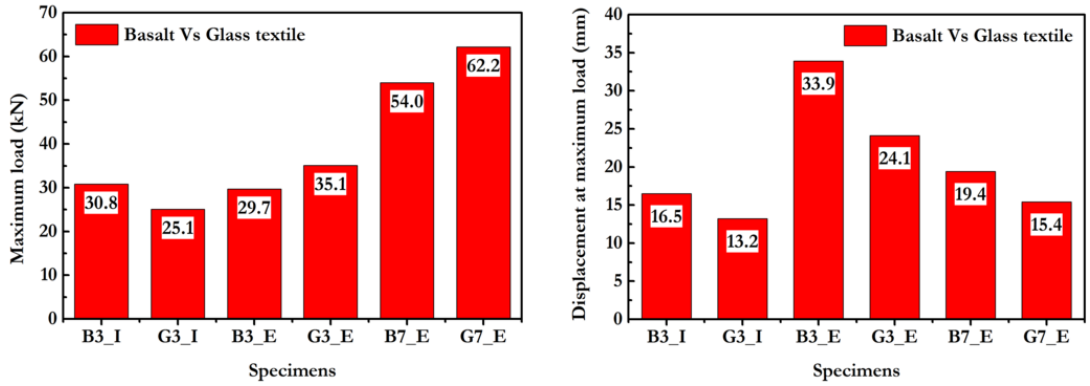


FIGURE 7.14: The effect of textile material in terms of (a) the maximum load and (b) the corresponding displacement

to B3_E.

In terms of deformation capacity, specimens B3_I, B3_E, and B7_E demonstrated increased values of displacement at the maximum load, i.e., by 25%, 41%, and 26%, respectively compared to their glass fibre strengthened counterparts, i.e., G3_I, G3_E, and G7_E (see also Fig. 7.14b). The enlarged value obtained in B3_E with respect to G3_E is attributed to the initiation of shear sliding at the first load drop (Σ_{B3_E}) of the left support in B3_E, which resulted in a less stiff strengthening system as shown in the post-elastic part of the load displacement curve in Fig. 7.3d.

The consistently larger values of d_{max} for the basalt fibre textile strengthened specimens are attributed to the coarser mesh size of the textile that allows for larger slippage within the mortar before bond is activated. It is of interest to note however that the overall effectiveness of both materials with respect to deformability which is quantified by their corresponding DIRs (Table 7.3) is similar. This is consistent with the fact that the tensile strength and the axial stiffness of the coated glass and coated basalt TRM layers is equivalent (Section 4.6).

7.4.3 The effect of number of layers

The transition from 3 to 7 TRM layers in masonry arches resulted in similar enhancement of the load bearing capacity, irrespective of the strengthening configuration. In particular, specimens G7_I, G7_E, B7_E demonstrated increased values of P_{max} by 67% and 77%, and 82% compared to specimens G3_I, G3_E, and B3_E, respectively (see also Fig. 7.15a). A similar trend has been shown in Chapter 6 for the case of out of plane flexure of plane masonry walls strengthened with 3 and 7 TRM layers.

The maximum load was increased substantially but not proportionally to the additional reinforcement used. Compared to the control specimen, all strengthened specimens demonstrated a substantial increase of the maximum attained load as manifested by the corresponding SIR factors shown in Fig. 7.13. Moving from 3 to 7 TRM layers resulted in increased values of P_{max} ranging from 1.67 times in the case of G3_I with respect to G7_I, 1.78 in the case of G3_E with respect to G7_E, and 1.81 times in the case of B3_E with respect to B7_E specimens (see Figs. 7.3c- 7.3d).

The increase achieved in the extrados glass and basalt specimens is practically identical. Since no textile rupture occurred, this trend is indicative of the beneficial effect of the improved mechanical interlock between the additional number of TRM layers that imposes the same improvement ratio in the two materials (Raoof et al., 2017).

This increase however is not proportional to the increase in the amount of reinforcement used, i.e., 7/3=2.3 times. All intrados and extrados strengthened specimens failed in a shear dominated mode both in the case of 3 and 7 TRM layers. This highlights that the upper bound of the flexural strength of the arch has been reached even at the case of 3 layers of TRM (see also Fig. 7.15a) and

justifies the fact that the 2.3 times increase in the amount of reinforcement resulted in a slightly reduced increase in P_{max}. Furthermore, in all cases the SIR values are much higher than the relative increase in the arch thickness due to the strengthening mortar alone. Hence we consider the effect of the high compressive strength mortar alone to be negligible, compared to the composite effect of the TRM.

The displacement at the maximum load of specimens G7_E and and B7_E decreased substantially by 36%, and 43%, with respect to specimens G3_E and B3_E, respectively (Fig. 7.15b). This is attributed to the increased axial stiffness provided by the seven TRM layers that resulted in increased tensile capacities at the hogging regions of the arch, effectively altering the failure mode to a shear dominated one. The increased number of TRM layers resulted in a more distributed cracking pattern at the left haunch in specimens G7_E (Fig. 7.11a) and B7_E (Fig. 7.12a).

In specimen G7_I, the displacement at maximum load was slightly lower, namely by 16% with respect to G3_I (Fig. 7.3c). Indeed, cracks on the TRM surface were more distributed in the latter (see, e.g., Fig. 7.6c) than in the former case (see, e.g., Fig. 7.7c). Similar to the extrados strengthening, the increase in the number of layers appears detrimental for the deformability of the specimens, see also Fig. 7.4; contrary to the extrados strengthening, the change in the number of layers did not alter the failure mechanism indicating that in this case 3 layers of textile reinforced fibre material already lead to an over-strengthened specimen with respect to flexure.

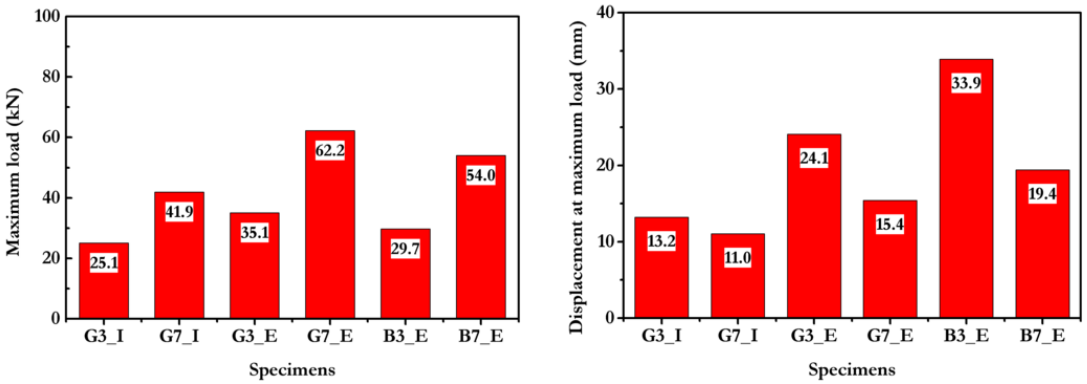


FIGURE 7.15: The effect of number of layers in terms of (a) the maximum load and (b) the corresponding displacement

7.4.4 The effect of the strengthening layout

The strengthening layout had a significant impact on the effectiveness of the TRM composite and the corresponding failure mode. Masonry arches strengthened at the extrados with coated glass fibre-textile indicated higher SIR and DIR compared to the corresponding specimens strengthened at the intrados, as shown in Fig. 7.16. This was not the case for specimens strengthened with 3 TRM layers of coated basalt fibre-textile (B3_I, B3_E) where similar values of P_{max} were reported (see also Figs. 7.17, 7.13).

At the maximum load was attained both B3_I and B3_E demonstrated a significant shear sliding at the left support. In B3_I, this was followed by brick crushing (Fig. 7.8) that increased the active TRM region as discussed in Section 7.4.2; conversely, in B3_E sliding at the left support was followed by shear sliding under the point load (see Figs. 7.10) and the specimen failed pre-maturely without being able to reach the loads attained by the coated glass extrados specimens. We believe that the relatively large mesh spacing of the coated basalt textile has a detrimental impact on the bonding conditions achieved. Hence,

further experimental work should be conducted to examine the bonding conditions and corresponding performance of the basalt textile fibre material. The improved performance of B7_E further supports this hypothesis, as it has been shown that increasing the number of textile fibre material layers enhances bonding through the action of the inter-locking mechanism (see also discussion in Section 7.4.3).

The highest SIR observed in extrados strengthened coated glass specimens can be explained by observing the corresponding failure modes. In particular, the dominating failure mode in G3_I and G7_I was shear sliding followed by debonding of the TRM under the point load. However, in the case of G3_E and G7_E debonding did not occur hence the TRM was able to sustain additional load. Debonding was prevented due to better bonding conditions obtained by the increased anchorage length at the extrados with respect to the intrados. Specimens G3_E and G7_E attained increased values of the maximum load by 39.7% and 48.4%, with respect to G3_I and G7_I, respectively (see also Fig. 7.17a and Table 7.3).

With regards to their deformation capacity d_{max}, specimens B3_E, G3_E and G7_E demonstrated increased values by 105%, 83% and 40% respectively when compared to their corresponding intrados specimens, i.e., B3_I, G3_I, and G7_I respectively (see also, Fig. 7.17b). At d_{max}, the collapse mechanism in all cases involves well developed sagging lengths which allow for larger portions of the TRM to be activated when this is placed at the extrados. The increased deformation capacity d_{ult} mainly manifested at the extrados layout, highlights the capability of the TRM composite to delay brick separation along the mortar joints.

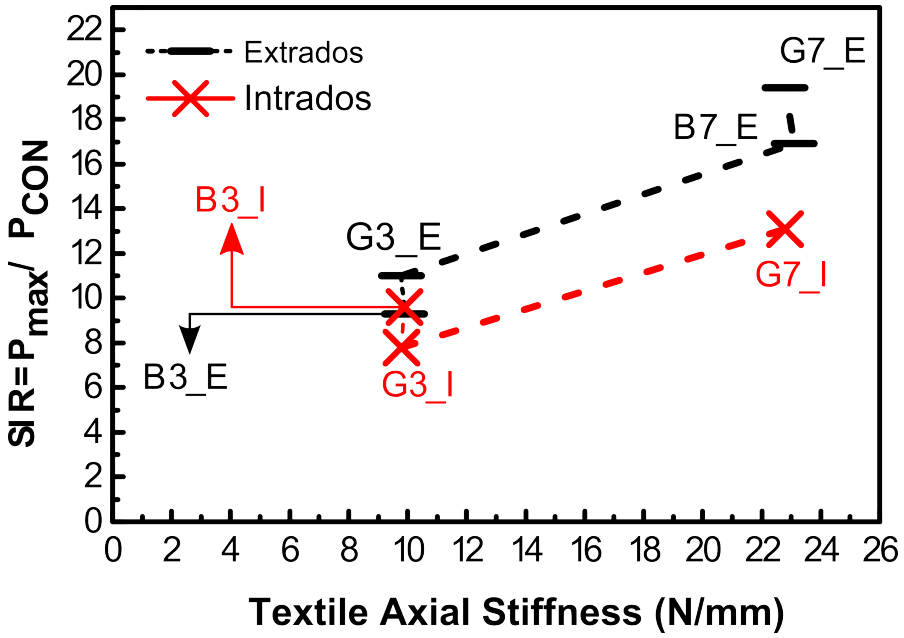
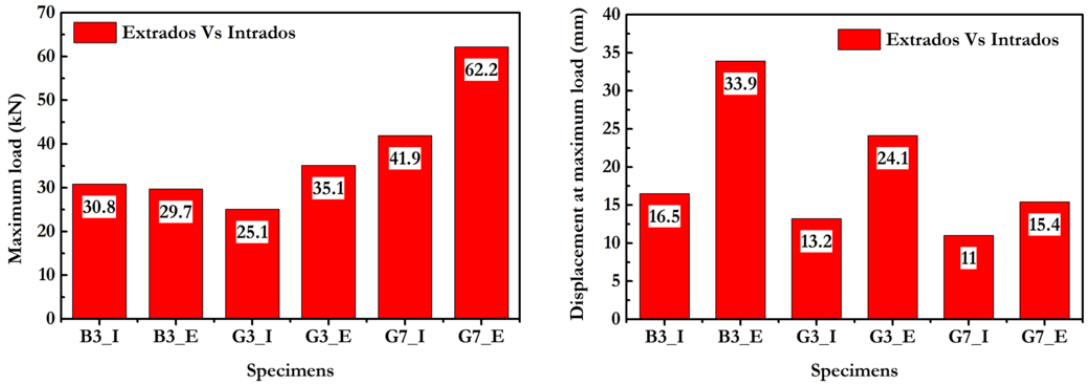


FIGURE 7.16: Ratio of the maximum strength effectiveness: Strengthening configuration

Macroscopically, this enhances the deformability of the structure hence delaying collapse which can be beneficial especially for the case of earthquake excitation. In addition, Table 7.4 presents the d_{ult} to d_{max} ratio for all the strengthened masonry arches.

TABLE 7.4: Ductility of masonry arches

Specimen	d_{ult}/d_{max}
CON	2.7
G3_I	1.4
G7_I	1.1
B3_I	1.3
G3_E	1.5
G7_E	1.1
B3_E	1.1
B7_E	1.0



(a) (b)

FIGURE 7.17: The effect of the strengthening configuration in terms of (a) the maximum load and (b) the corresponding displacement

7.5 Conclusions

This study investigated the effect of the cement-based TRM strengthening system on medium-scaled masonry arches. The objective of this experimental campaign was to study the effect of i) the strengthening configuration; ii) the number of TRM layers; iii) coated glass and coated basalt fibre-textile composite, on the monotonically loaded TRM-strengthened masonry arches.

According to the analysed and discussed experimental results in terms of maximum load, deformation capacity and different failure modes conclusions are summarised as follows:

- By increasing the TRM layers from 3 to 7, which is equal to 2.3 times, the maximum attained load increased by 1.7 and 1.8 times for the specimens strengthened at the intrados and extrados, respectively. The failure mechanism of shear sliding among the corresponding specimens indicated that after a certain amount of strengthening material, this system cannot be further enhanced unless shearing along the mortar joints is avoided.

- Increasing the amount of textile fibre material by 2.3 times resulted in decreased deformation capacities. This was mainly manifested at the extrados strengthened specimens where TRM development lengths were larger and is consistent with the increased axial stiffness of the TRM strengthening layer and the resulting shear driven failure modes.

- Specimens strengthened at the extrados with coated glass textile fibre material outperformed the corresponding intrados strengthened specimens. TRM placed on the extrados results in larger development lengths and further improves the performance of hogging regions that are critical in this asymmetric loading scenario.

- Specimens strengthened at the extrados with basalt textile fibre material resulted in practically identical SIRs compared to the corresponding intrados strengthened specimens. Given that the coated glass and basalt material parameters are practically identical, this result is indicative of reduced bonding conditions that are attributed to the large mesh size of the basalt textile fibre.

- Of interest is the improved load capacities of specimen B3_I compared to G3_I. B3_I was characterized by brick masonry crushing under the point load which proved beneficial as it increased the length of the sagging zones and inevitably led to enhanced utilisation of the TRM strengthening.

- All the extrados strengthened specimens demonstrated a significantly increased deformation capacities when compared to the intrados strengthened systems as manifested by the corresponding DIR values.

- Specimens strengthened with coated basalt textile demonstrated higher deformation capacity with respect to their coated glass counterparts. This is attributed to the coarser mesh size which resulted in larger slippage within the mortar.

Chapter 8

Finite element analysis

8.1 Introduction

In this Chapter, a numerical study on the out-of-plane response of masonry walls strengthened with TRM is provided. For this purpose, a detailed finite element model of single and double wythe walls is constructed using the cohesive method to account for the nonlinear response at the interface of the constituents. The overarching aim of this work was to provide a numerical tool for the simulation of TRM strengthened structures employing tools available in the commercial code Abaqus (SIMULIA, 2016).

In the following, a literature review is provided on the methods available for the simulation of the nonlinear response of masonry components. Next, a discussion is provided on the constitutive models employed. The models are calibrated based on the experimental results. At the end, the conclusions are drawn between the experimental and numerical analysis results.

8.2 Simulation approaches for masonry structures

Masonry is a composite material composed by masonry units and mortar joints. Numerical modelling of masonry structures is a complex procedure as the mechanical response is dependant on several parameters. These are the anisotropy and dimension of units, the material properties of units and mortar, the arrangement of bed and head joints and the quality of workmanship (Lourenco and Rots, 1997).

Heterogeneous and homogeneous approach can determine the applied modelling on the structure, according to the required level of accuracy and simplicity. The available modelling strategies for different application fields, include the detailed micro-modelling, simplified micro-modelling and macro-modelling.

In the micro-modelling approach, mortar joints and units are represented by continuum elements, such as quadrilateral plane stress elements or 3D hexahedral elements (Abaqus manual, 2014). The interface between the unit and the mortar is modelled using interface elements (Abaqus manual, 2014). The discontinuous elements account for any potential crack, slip or crushing plane that can occur at the interface of the mortar joints. Different properties of units and mortar such as Young's modulus, Poisson's ratio and inelastic characteristic are considered, and the mechanical properties such as the compressive, bending and shear response of masonry assemblages are obtained from experimental tests. This method is realistic, predicts the local response of masonry and provides high level of accuracy. However, is inefficient and uneconomic (Zucchini and Lourenco, 2004; Bolhassani et al., 2015).

Macro-modelling is used for large and practice-oriented analyses to obtain an overall behaviour of the structure; the interaction between units and mortar

is usually neglected, considering the structure as a homogeneous anisotropic continuum material, where average values of the mechanical properties of the mortar and units are adopted. Mortar joints and units are considered smeared within an isotropic or anisotropic material (Bolhassani et al., 2015). The precision provided by this method is limited compared to the micro-modelling approach in terms of the maximum load obtained and the crack pattern reproduction.

Lourenço et al. (1998) studied the in-plane behaviour of masonry structures and developed a yield criterion for macro-models considering different strengths at each material axis. The geometrical arrangement of units and mortar results in the anisotropy of masonry, must be considered in the analyses. The material parameters are obtained from large size masonry tests. Different tensile and compressive strengths and different inelastic behaviours for each material axis must be considered to reproduce an orthotropic material. Dhanasekar et al. (1985), Berto et al. (2002), and Lourenço et al. (1998) used different inelastic criteria in tension and compression.

The homogenisation approach can be applied in cases where masonry comprises a regular texture which repeats periodically. This method relies on the definition of average stress and strain of the masonry constituents (Maier et al., 1991; Pande et al., 1989; Zucchini and Lourenco, 2002; Zucchini and Lourenco, 2004; Milani et al., 2006a; Milani et al., 2006b; Casolo and Milani, 2010). Zucchini and Lourenco (2002) developed an one-step micro-mechanical homogenisation model where small errors occurred, with respect to the two-step homogenisation process of Lourenço et al. (1998) approach. In Zucchini and Lourenco (2004) an improvement of the proposed model is presented applicable in non-linear problems. Milani et al. (2006a) and Milani et al. (2006b) proposed a simple

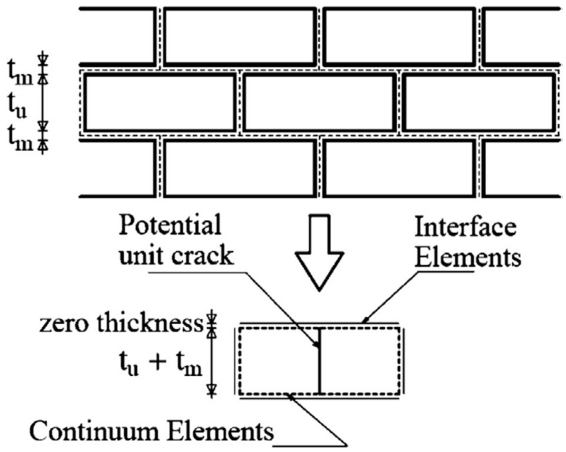


FIGURE 8.1: Simplified micro-modelling (Lourenco and Rots, 1997)

micro-mechanical model for the homogenised limit analysis of in-plane loaded masonry.

In the simplified micro-modelling approach, masonry units are expanded up to the half of both head and bed mortar joints (see Fig. 8.1). Continuum elements are used to model units, while interface elements are utilised for mortar joints (Page, 1978; Rots, 1991). This method can capture accurately the response of masonry by simulating the behaviour of masonry components. This method is extensively used in the literature (Shing et al., 1992; Berto et al., 2004; Milani, 2008; Stavridis and Shing, 2010; La Mendola et al., 2014; Bolhassani et al., 2015; Chaimoon and Attard, 2007; Shing et al., 1990; Lotfi and Shing, 1994; Lourenco and Rots, 1997).

Lotfi and Shing (1994) developed an interface model for modelling the behaviour of mortar joints and a smeared crack model for masonry units. An interface model was used, developed by Lourenco and Rots (1997) to capture all the possible failure mechanisms (e.g., joint cracking, sliding along bed and head joint, cracking of masonry units in tension, diagonal tension cracking of masonry units, splitting of units in tension).

Stavridis and Shing (2010) studied the behaviour of masonry infilled RC frames using smeared and discrete crack approaches to produce the mixed-mode fracture of mortar joints and the shear failure of RC members. The masonry infill was modelled using the simplified micro-modelling with a zero-thickness cohesive interface model which allowed tensile failure of the bricks and sliding among the units (Lotfi and Shing, 1994). This approach resulted in a good fit among experimental and finite element (FE) modelling, in terms of failure modes and load-displacement response.

Macorini and Izzuddin (2011) developed an innovative interface element of brick masonry structures which considers opening in tension, sliding in shear/ tension and shear/ compression and crushing in compression. Good agreement was observed between experimental and numerical examples for the case of in-plane and out-of-plane response of masonry walls.

Bolhassani et al. (2015) used the cohesive surface-based approach to model the interface between the RC units. The mortar joints response was modelled using traction-separation of the cohesive element, where the damage initiation was based on mortar strength. The response of masonry bricks was modelled using the concrete damage plasticity model.

Chaimoon and Attard (2007) studied the response of unreinforced masonry walls under axial compression, using a simplified micro-modelling approach with zero-thickness interface elements. Triangular units were grouped to rectangular to model the bricks and mortar joints. The mortar-joint interface was modelled with the Mohr-Coulomb failure surface with a tension cut-off and a linear compression cap while the brick interface with a Mohr-Coulomb failure surface with a tension cut-off. Good agreement was observed between the model and the experiment in terms of pre-peak and post-peak response.

Numerical simulation of strengthened masonry components with the aforementioned methods has also received considerable attention. Gattesco and Boem (2017) performed an experimental and analytical work on the out-of-plane response on a four-point bending test setup of strengthened masonry walls. The masonry walls were strengthened with GFRP mesh composite combined with coating of mortar. A 2D numerical model comprised plane strain elements for masonry and mortar coating, while the GFRP mesh was modelled with truss elements. A good fit was achieved between numerical and experimental results.

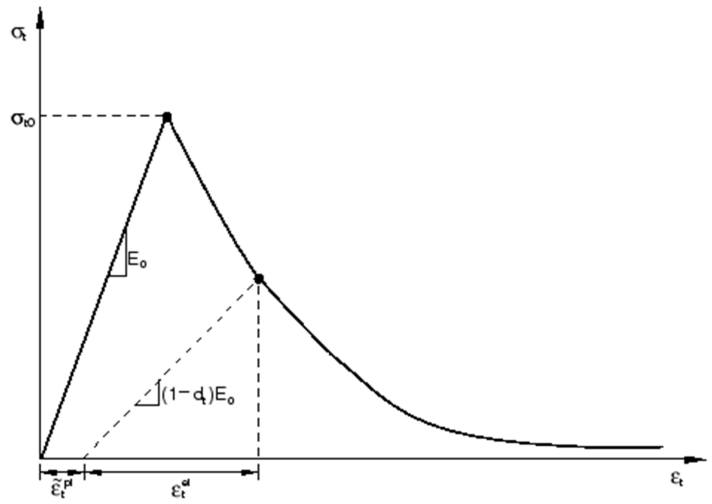
Fedele and Milani (2010) studied the bond behaviour of a numerical model of masonry strengthened with FRP strips. An heterogeneous model at the meso-scale was adopted, where bricks and mortar simulated separately in tension and compression. The bond-slip behaviour between FRP and the support was modelled using the italian code CNR-DT200 (2006), comprising a linear function of average shear stress versus tangential slip, followed by a linear decrease until full detachment of the composite.

Ghiassi et al. (2013) executed a 3D numerical work on the bond behaviour of FRP-strengthened masonry. Bricks and epoxy resin were represented with solid elements and simulated with the smeared crack model. Shell elements were utilised for the FRP strips. A smeared crack model was adopted for the debonding and crack propagation, and a linear elastic response for the FRP and epoxy-resin layer. Good agreement was achieved between numerical and experimental results in terms of failure mode and crack distribution.

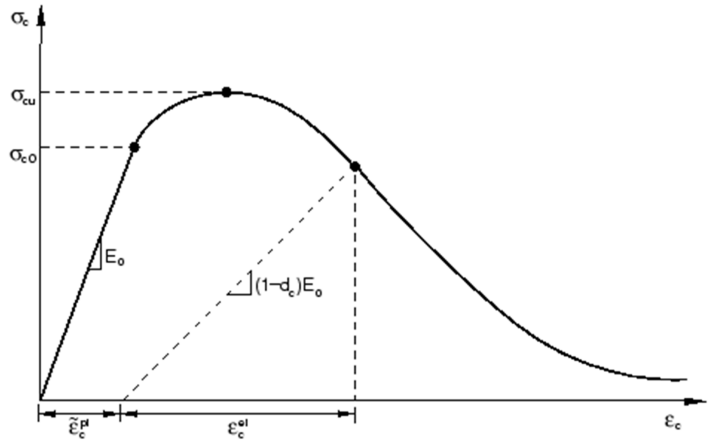
Meriggi et al. (2019) studied the seismic out-of-plane response of masonry walls using the distinct element model (DEM). The DEM modelling approach is a micromodelling approach where masonry is modelled using an assembly

of discrete (rigid or deformable) blocks, separated with zero-thickness joints. It interacts at contact points, which include all the properties of the rigid blocks (e.g., stiffness and deformations) concentrate in the contact points. In addition, it takes into account the geometry and configuration of masonry components together with cracking and shear sliding. It uses explicit integration of the equations of motion, therefore is suitable for dynamic analysis. The analytical results were compared with the experimental work conducted on tuff and stone masonry. Good agreement was observed on the shape of the collapse mechanism, which shows that DEM method can predict the response of masonry wall under earthquake motion even with limited results in strength properties.

Malena et al. (2019) examined the response of masonry structures using a macroscopic model in a FE code derived from the Haar-Karman principle. The masonry wall was modelled as an elasto-plastic homogenized Love-Kirchhoff plate with an associated flow rule. The model was implemented for a numerical case study of a masonry church subjected to horizontal seismic action. The results obtained were compared with a discrete rigid block model, where the contact interaction is a point-based contact model. This is an alternative to the surface based contact, which simplifies the mathematical programming problems (Portioli et al., 2013). The two modelling approaches are discussed and analysed by highlighting their simplicity compared to the available models in the literature.



(a)



(b)

FIGURE 8.2: (a) Tensile and (b) compressive behaviour described by the CDP model for concrete (SIMULIA, 2016)

8.3 Concrete damage plasticity model

The concrete damage plasticity model (CDP) was initially proposed by Lubliner et al. (1989) and Lee and Fenves (1998) and among others it was used for reinforced concrete and masonry structures applications, respectively (Genikomsou and Polak, 2015; Agnihotri et al., 2013). The CDP assumes two main failure mechanisms, namely tensile cracking and masonry crushing. Therefore, the compressive and tensile stress-strain behaviour of the material is described within this model (see Fig. 8.2). In particular, the uniaxial tension response is described by a linear response until the failure stress (σ_{t0}) is attained (Fig. 8.2a). At this point micro-cracking of masonry initiates, which is followed by stress-strain softening behaviour, where micro-cracks are developed. The uniaxial compression diagram is linear until the yield stress (σ_{c0}) is attained. The plastic regime comprises stress hardening, followed by strain softening after reaching the ultimate stress (σ_{cu}) (Fig. 8.2b). The yield function of the CDP is controlled by two hardening variables, namely equivalent tensile plastic strain ($\tilde{\epsilon}_t^{pl}$) and equivalent compressive plastic strain ($\tilde{\epsilon}_c^{pl}$). (E_0) is the initial (undamaged) elastic stiffness of the material, (d_t) and (d_c) are the damage variables for tension and compression, respectively, which describe the degradation of the elastic stiffness in case of uniaxial cyclic loading.

In cases where reinforcement is not applied on the model, as in the case of unreinforced masonry, SIMULIA (2016) proposed to use the fracture energy cracking criterion as reported in Hillerborg et al. (1976). In this case, the fracture energy (G_f) and the failure stress (σ_{t0}) are defined, where a linear response of this models is assumed after cracking has occurred (Fig. 8.3). The corresponding displacement, where cracking occurs until complete loss of the tensile

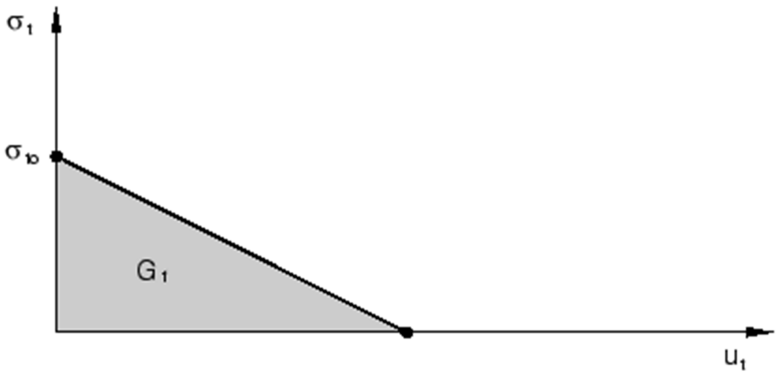


FIGURE 8.3: Stress-fracture energy curve SIMULIA (2016)

strength is calculated by Eq. 8.1.

$$u_{t0} = \frac{2G_f}{\sigma_{t0}} \tag{8.1}$$

The hardening data of the compressive behaviour defined in the Abaqus software are given in terms of inelastic strain ($\tilde{\epsilon}_c^{in}$). The inelastic strain is defined as the total strain (ϵ_c) minus the elastic strain (ϵ_{0c}^{el}) for undamaged material (Eqs. 8.2-8.3). The Abaqus software automatically converts the inelastic stain values to plastic strain values according to Eq. 8.4. In case where there is no damage d_c=0, the plastic strain is equal to inelastic strain $\tilde{\epsilon}_c^{pl}$=$\tilde{\epsilon}_c^{in}$.

$$\tilde{\epsilon}_c^{in} = \epsilon_c - \epsilon_{0c}^{el} \tag{8.2}$$

$$\epsilon_{0c}^{el} = \frac{\sigma_c}{E_0} \tag{8.3}$$

$$\epsilon_{0c}^{el} = \tilde{\epsilon}_c^{in} - \frac{d_c}{1-d_c}\frac{\sigma_c}{E_0} \tag{8.4}$$

In addition, the description of this model requires the definition of the hyperbolic Drucker-Prager plastic flow function (Eq. 8.8) and the yield function

(Eqs. 8.9-8.12), where ($\bar{p}$) is the hydrostatic pressure stress (Eq. 8.14 and Eq. 8.13), ($\bar{q}$) is the Von Mises equivalent stress (Eqs. 8.15-8.16), (ψ) is the dilation angle measured in the p-q plane, (σ_{t0}) is the uniaxial tensile stress at failure, and (ϵ) is the eccentricity, which defines the rate at which the flow potential function approaches the asymptote. The dilation angle was introduced by Hansen (1958) and represents the change in volume that is associated with shear distortion of an element in the material. Dilation angle is defined in Eq. 8.5, where ($\dot{\gamma}^{pl}$) is the rate of the plastic distortion (see Eq. 8.7), and ($\dot{\epsilon}_v^{pl}$) is the rate of the plastic volumetric strain (see Eq. 8.6). Experimental studies on the concrete and rock material showed that during the hardening response of the material, the dilation volume is increased due to frictional sliding along the micro-cracks.

$$\sin\psi = \frac{\dot{\epsilon}_v^{pl}}{\dot{\gamma}^{pl}} \tag{8.5}$$

$$\dot{\epsilon}_v^{pl} = \dot{\epsilon}_{11}^{pl} + \dot{\epsilon}_{22}^{pl} + \dot{\epsilon}_{33}^{pl} \tag{8.6}$$

$$\dot{\gamma}^{pl} = \sqrt{(\dot{\epsilon}_{11}^{pl} - \dot{\epsilon}_{22}^{pl})^2 + (\dot{\gamma}_{12}^{pl})^2} \tag{8.7}$$

The yield function (Eqs. 8.9-8.12) is described by the maximum principal effective stress ($\hat{\sigma}_{max}$), the ratio of the initial equibiaxial compressive yield stress to the initial uniaxial compressive yield stress (σ_{b0}/σ_{c0}), where the default value is 1.16. (K_c) is the ratio of the second stress invariant ($q(TM)$) on the tensile meridian to that on the compressive meridian ($q(CM)$), at initial yield for any given value of the pressure invariant (p), where ($\hat{\sigma}_{max}$) is negative. The default value is (2/3) and must satisfy the condition of $0.5 \leq K_c \leq 1.0$ (see Fig. 8.4). In addition, $\bar{\sigma}_t(\tilde{\epsilon}_t^{pl})$ is the effective tensile cohesion stress, and $\bar{\sigma}_c(\tilde{\epsilon}_c^{pl})$ is the effective

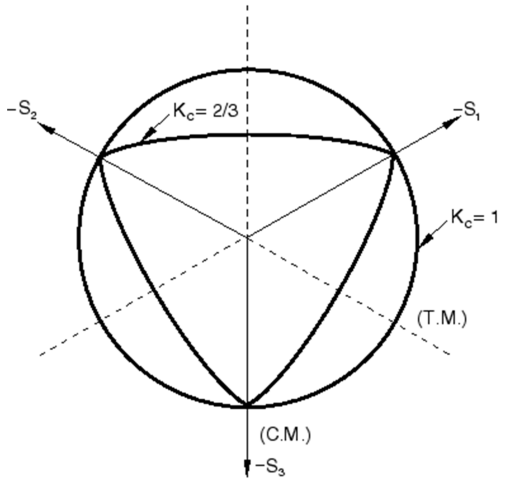


FIGURE 8.4: Yield surfaces in the deviatoric plane for different K_c values (SIMULIA, 2016)

compressive cohesion stress. The Yield surface in plane stress is shown in Fig. 8.5. A viscoplastic regularization of the constitutive equations is used to overcome convergence difficulties, which permits stresses to be outside of the yield surface.

$$G = \sqrt{(\epsilon\sigma_{t0}tan\psi)^2 + \bar{q}^2} - \bar{p}\tan\psi \tag{8.8}$$

$$F = \frac{1}{1-\alpha}(\bar{q} - 3\alpha\bar{p} + \beta(\tilde{\epsilon}_c^{pl})\langle\hat{\sigma}_{max}\rangle - \gamma\langle\hat{\sigma}_{max}\rangle) - \bar{\sigma}_c(\tilde{\epsilon}_c^{pl}) = 0 \tag{8.9}$$

$$\alpha = \frac{(\frac{\sigma_{b0}}{\sigma_{c0}}) - 1}{2(\frac{\sigma_{b0}}{\sigma_{c0}}) - 1} \tag{8.10}$$

$$\beta = \frac{\bar{\sigma}_c(\tilde{\epsilon}_c^{pl})}{\bar{\sigma}_t(\tilde{\epsilon}_t^{pl})}(1-\alpha) - (1+\alpha) \tag{8.11}$$

$$\gamma = \frac{3(1-K_c)}{2K_c - 1} \tag{8.12}$$

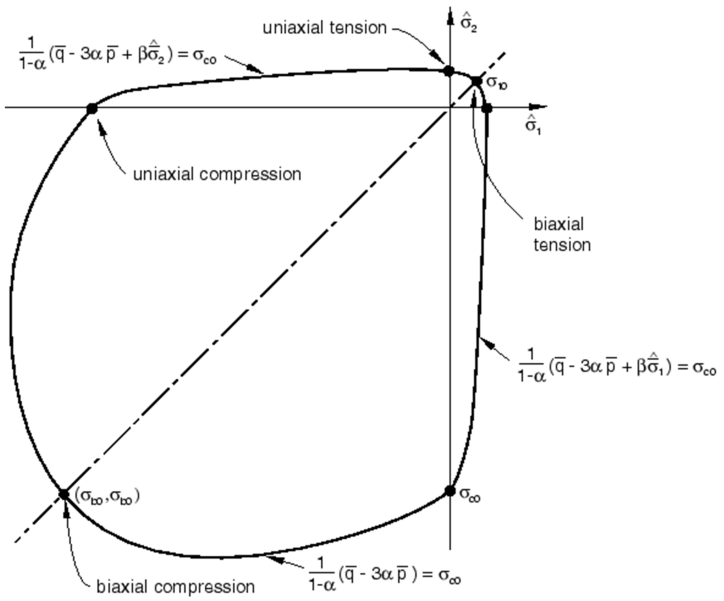


FIGURE 8.5: Yield surfaces in the deviatoric plane for plane stress condition (SIMULIA, 2016)

$$\sigma = \begin{pmatrix} \sigma_{11} & \sigma_{12} & \sigma_{13} \\ \sigma_{21} & \sigma_{22} & \sigma_{23} \\ \sigma_{31} & \sigma_{32} & \sigma_{33} \end{pmatrix} \tag{8.13}$$

$$\bar{p} = -\frac{I_1}{3} = -\frac{\sigma_{11} + \sigma_{22} + \sigma_{33}}{3} \tag{8.14}$$

$$\bar{q} = \sqrt{3J_2} \tag{8.15}$$

$$J_2 = \frac{1}{2}(\sigma_{11} + \sigma_{22} + \sigma_{33})^2 - \frac{1}{3}(\sigma_{11} + \sigma_{22} + \sigma_{33})^2 \tag{8.16}$$

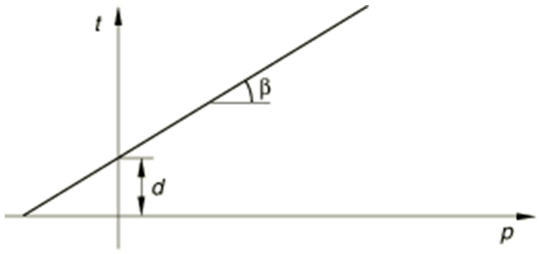


FIGURE 8.6: Yield surface of linear Drucker-Prager (SIMULIA, 2016)

8.4 Drucker-Prager

The yield surface of the linear Drucker-Prager criterion is given by Eq. 8.17 (see Fig. 8.6), where (t) is the deviatoric stress measure (Eq. 8.18), (p) is the hydrostatic or volumetric stress tensor (Eq. 8.19), (q) is the Von Mises criterion equivalent stress (Eq. 8.20), (d) is the cohesion of the material (Eq. 8.22), and (β) is the friction angle of the material, which is the slope of the linear yield surface in the p-t stress plane (Fig. 8.6). In addition, (r) is the third invariant of deviatoric stress, (K) is the ratio of the yield stress in triaxial tension to the yield stress in triaxial compression. The values of (K) required to be 0.778≤K≤1.0 to ensure that the yield surface is convex.

$$F = t - p\tan\beta - d = 0 \tag{8.17}$$

$$t = \frac{1}{2}q[1 + \frac{1}{K} - (1 - \frac{1}{K})(\frac{r}{q})^3] \tag{8.18}$$

$$p = -\frac{I_1}{3} = -\frac{\sigma_{11} + \sigma_{22} + \sigma_{33}}{3} \tag{8.19}$$

$$q = \sqrt{3J_2} \tag{8.20}$$

$$r = J_3 = \frac{1}{3}[(\sigma_{11}+\sigma_{22}+\sigma_{33})^3 - (\sigma_{11}+\sigma_{22}+\sigma_{33})^2(\sigma_{11}+\sigma_{22}+\sigma_{33}) + \frac{2}{9}(\sigma_{11}+\sigma_{22}+\sigma_{33})^3] \tag{8.21}$$

$$d = (\frac{1}{K} + \frac{1}{3}\tan\beta)\sigma_t \tag{8.22}$$

The flow potential (G) chosen for this model is given in Eq. 8.23, where (ψ) is the dilation angle in the p–t plane and (p) the hydrostatic or volumetric stress tensor. A geometric representation of the dilation angle is given in Fig. 8.7.

Both flow potential (G) and the yield surface (F) have functional dependence on (t), which shows that (G) is associated in the deviatoric plane. On the other hand, the dilation angle (ψ) and the material friction angle(β) can be different, which means that the model will be not associated in the p-t plane. For granular materials such as concrete or masonry, the linear model is used with non-associated flow in the p-t plane, where the flow potential (G) is assumed to be normal to the yield surface in the deviatoric Π plane but there is a dilation angle (ψ) to the t-axis, which is ψ<β (Fig. 8.7). In this study was set ψ=β and K=1, where the original Drucker-Prager model is recovered, for simplicity of the model.

$$G = t - p\tan\psi \tag{8.23}$$

The original Drucker-Prager criterion yield surface is presented in Eq. 8.24 (Drucker and Prager, 1952; Alejano and Bobet, 2012). To calibrate the friction

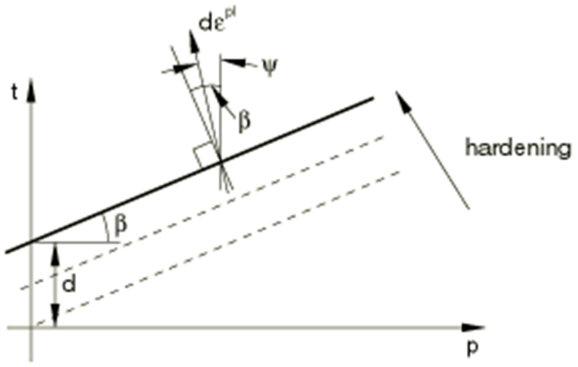


FIGURE 8.7: Geometric representation of the dilation angle (SIMULIA, 2016)

angle (β) Eqs. 8.24, 8.17 and 8.19 were used, which resulted in Eq. 8.29. The values of (A) (Eq. 8.27) and (B) (Eq. 8.28) were found using Eq. 8.24 and Eq. 8.25 under uniaxial tension (σ_1=σ_t) and uniaxial compression (σ_2=σ_c), respectively, where (σ_t) is the yield stress in tension and (σ_c) is the yield stress in compression.

$$F = t - BI_1 - A \tag{8.24}$$

$$\sqrt{J_2} = BI_1 + A \tag{8.25}$$

$$I_1 = \sigma_{11} + \sigma_{22} + \sigma_{33} \tag{8.26}$$

$$A = \frac{2}{\sqrt{3}} \frac{(\sigma_c \sigma_t)}{(\sigma_t + \sigma_c)} \tag{8.27}$$

$$B = \frac{1}{\sqrt{3}} \frac{(\sigma_t - \sigma_c)}{(\sigma_t + \sigma_c)} \tag{8.28}$$

$$B = -\frac{1}{3} tan\beta \tag{8.29}$$

8.5 Cohesive surface-based element approach

8.5.1 Contact pairs

A pair of contact is defined using pairs of surfaces which interact between them, and refers to interaction property. Each surface is assigned as 'master' or 'slave', using the following basic rule:

- The larger of the two surfaces should be the master surface.
- When the two surfaces are of comparable size, the stiffer body should act as a master surface.
- In case the two surfaces have comparable size and stiffness, the coarser mesh surface should be assigned as the master surface.

8.5.2 Traction-separation of the cohesive elements

The cohesive elements are used to model adhesives or bonded surfaces and their response depends on the application and the assumptions about their deformation and stress state. Continuum based modelling can be used in cases where the adhesive material has a finite thickness and the traction-separation-based modelling where the intermediate glue material is very thin and can be considered of zero thickness. The traction-separation-based modelling comprises model of the initial loading, initiation of damage, and propagation of damage, which leads to failure of the bonded interface. The response of the interface before the initiation of the damage is usually described as linear elastic in terms of penalty stiffness, which degrades under tensile or shear loading.

In particular, the damage initiation, is the beginning of the degradation of the response of the material. In this case, the maximum nominal stress criterion

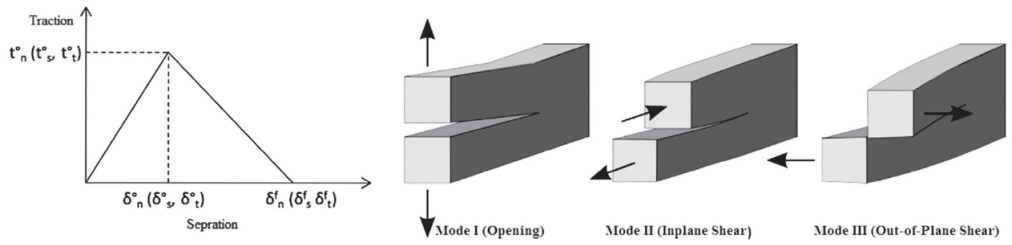


FIGURE 8.8: Typical traction-separation response (Bolhassani et al., 2015)

was chosen, where (t_n, t_s, t_t) are the peak values of the nominal stress when the deformation is normal to the interface, in the first (in-plane) and second (out-of-plane) shear direction, respectively. The corresponding components δ_n, δ_s and δ_t represent the displacement in the normal and in two shear directions (see Fig. 8.8). When the maximum nominal stress ratio reaches the value of 1 (see Eq. 8.30), the damage initiates. The interface elastic stiffness for the traction-separation model before the initiation of the damage is also defined normal to the interface (K_n), and in the two shear directions (K_s) and (K_t).

$$max(\frac{t_n}{t^0}, \frac{t_s}{t_s^0}, \frac{t_t}{t_t^0}) = 1 \tag{8.30}$$

A linear damage evolution can be determined in the Abaqus software using the effective displacement at complete failure (δ_m^f) relative to the displacement at the initiation of the damage, (δ_m^0), or the energy dissipated due to failure (G^c), known as fracture energy. Figure 8.9 shows a schematic representation of the linear damage evolution, after the peak of the maximum nominal stress. The area under the aforementioned curve is equal to the fracture energy.

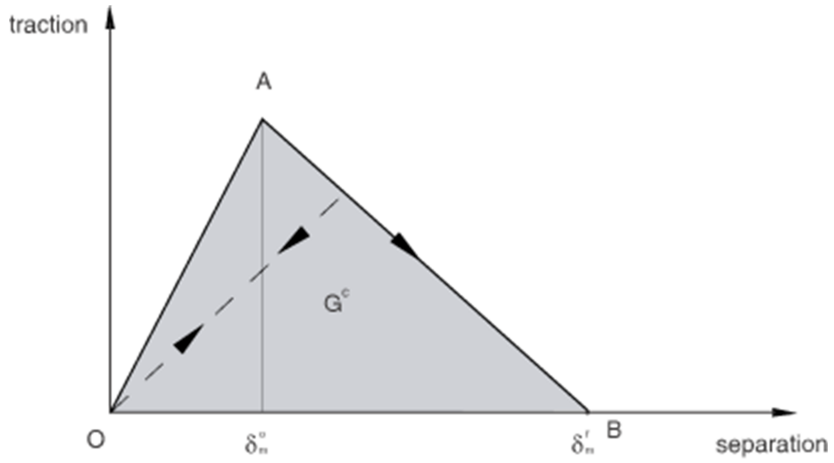


FIGURE 8.9: Linear damage evolution (SIMULIA, 2016)

8.5.3 Behaviour normal to the contact surface

A 'hard' contact pressure-overclosure is used for surface-based contact as shown in Fig. 8.10. In case the surfaces are in contact, contact pressure can be developed between them, and when the contact pressure is minimised to zero the surfaces separate. In addition, if the clearance between the two surfaces is reduced to zero the separate surfaces come into contact. The 'hard' type of contact minimizes the penetration of the slave surface into the master surface and does not allow the transfer of tensile stress across the interface.

The default constraint enforcement method is the direct method, which is based on the interaction characteristics. When the small sliding is adopted between the contact surfaces, a relatively little sliding of one surface along the other is assumed.

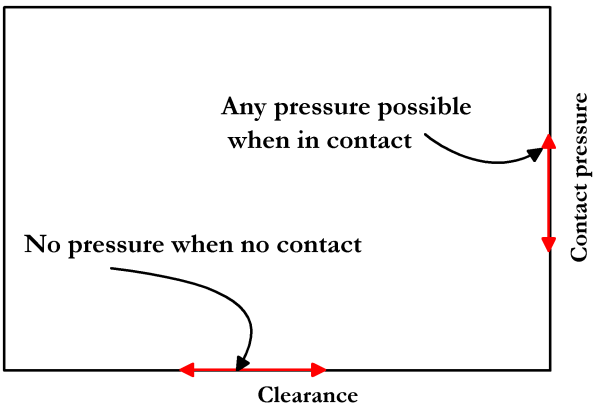


FIGURE 8.10: Contact Pressure-Overclosure relationship (SIMULIA, 2016)

8.5.4 Tangential behaviour - Coulomb friction model

Coulomb friction model comprises two contacting surfaces which can carry shear stresses up to a critical value before they start sliding. In particular it determines the critical shear stress (τ_{crit}), where sliding of the surfaces starts (Eq. 8.31). The parameters describe the Coulomb friction model are the coefficient of friction (μ), and the contact pressure between the two surfaces (p).

Incremental slip might occur even though the frictional state of the friction model is sticking. This means that the slope of the shear stress versus total slip can be finite in the sticking state as presented in Fig. 8.11, where (τ_{crit}) is the yield stress. This relationship follows the elastic-plastic material behaviour, where the sticking friction corresponds to the elastic regime and the slipping friction to the plastic regime. The finite value of the sticking stiffness is defined by default using the penalty method in the Abaqus/Standard. The penalty method allows an elastic slip of the surfaces when they should be sticking. The default value of the allowable elastic slip (γ_i) is defined using Eq. 8.32, where

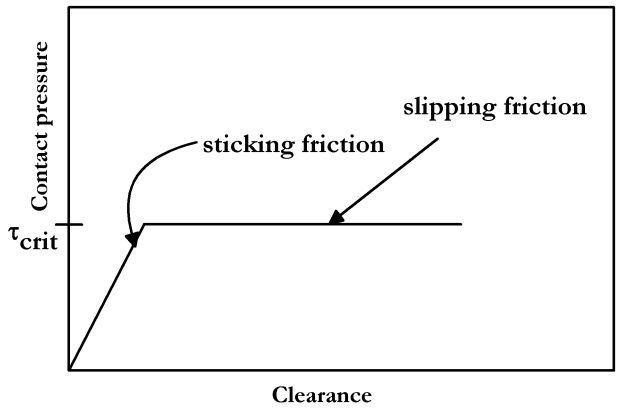


FIGURE 8.11: Shear stress versus total slip (SIMULIA, 2016)

(F_f) is the slip tolerance equal to 0.005 (default value) and (l_i) is the characteristic contact surface length.

$$\tau_{crit} = \mu.p \tag{8.31}$$

$$\gamma_i = l_i.F_f \tag{8.32}$$

8.5.5 Tie-constraint

The surface-based tie constraint is used to make the translational and rotational motion and all the active degrees of freedom equal for a pair of surfaces. One surface in the constraint is assigned as the slave surface and the other as the master surface. The default position tolerance criterion ensures that nodes are tied only where the master and slave surfaces are close to one another in the initial configuration.

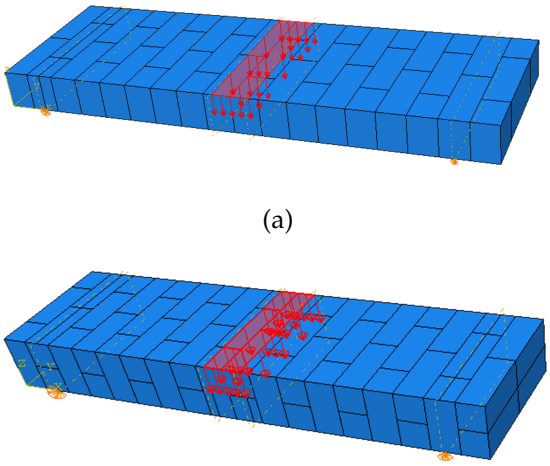
8.5.6 Ductile damage

The ductile damage initiation criterion is a model to predict the onset of a damage in ductile metals. It assumes that the equivalent plastic strain at the onset of damage is a function of stress triaxiality and strain rate. This criterion can be used in combination with the Drucker-Prager, and the Von Mises plasticity model. The ductile damage initiation requires to define the fracture strain, which is the equivalent fracture strain at damage initiation, the stress triaxiality, and strain rate, which is the equivalent plastic strain rate. The stress triaxiality is defined as n=-p/q, where (p) is the pressure stress and (q) is the Mises equivalent stress (see Eqs. 8.19-8.20).

8.6 Modelling of single and double wall specimens

8.6.1 Description of the model

The mechanics of the TRM strengthened masonry walls was investigated using the Abaqus commercial code (SIMULIA, 2016). A simplified micro-modelling approach was adopted, where brick units were expanded up to the half of both head and bed mortar joints and mortar joints were represented by zero-thickness interface elements (see Fig. 8.1). Full integration 20-node hex-elements were utilised to model the brick units. A full integration quadrilateral layered shell element was used to model the TRM strengthening material, where the fibre-textile material was embedded as longitudinal reinforcement. The distance of the reinforcement was set equal to the rovings distance for each fibre-textile (see Fig. 4.1). The TRM thickness was determined equal to 2.5 mm, 2.5 mm and 5 mm for 1, 3 and 7 TRM layers, respectively. The mesh size was set



(a)

(b)

FIGURE 8.12: Loading of (a) single walls, (b) Loading of double walls

equal to 0.04 m along the mortar layer and along the height of the masonry wall. A displacement control static analysis procedure was implemented with a maximum incremental displacement step-size equal to 0.1 and 0.05 for the single and double walls specimens, respectively.

The application of the load was performed in the middle of the wall, covering an area of 100 mm x 440 mm, which was the metal plate dimensions used for the application of the load at the experiment, as shown in Fig. 8.12. The supports were positioned 107.5 mm from the ends of the masonry wall as occurred during the experiment. In particular, a pinned and roller support was positioned at the left and right of the specimen, respectively, as shown in Fig. 8.12.

8.6.2 Modelling of the brick masonry units using the CDP

The concrete damage plasticity model (CDP) was used to account for the inelastic constitutive behaviour of the brick masonry units. The compressive behaviour of the bricks was represented using the constitutive relation introduced by Saenz, 1964 for plain concrete (Eq. 8.33) where (σ_c), and (ϵ_c) are the compressive stress and strain, respectively, (σ_p), and (ϵ_p) are the maximum stress and its corresponding strain, respectively, and (E_0) is the Young's modulus of elasticity of the bricks. The experimental brick compressive strength is equal to f_b=21.2 MPa (see Section 4.2) and the corresponding strain equal to ϵ_p=0.0022 as used in Tao et al. (2012). Table 8.1 shows the brick compressive stress used in all the single and double-wythe walls specimens. The brick compressive stress was minimally increased to 25 MPa in case of S_G3_(Co) specimen to allow further increase of the textile ultimate tensile stress, and subsequently higher maximum load close to the experimental value, when the textile rupture failure mode occurred (see Fig. 8.14d). The Young's modulus (E_0) used to account for the elastic behaviour of the bricks was 8 GPa (Nazir and Dhanasekar, 2013). The stress-strain curve was considered linear up to about one-third of the compressive stress (σ_c) as described in Kaushik et al. (2007) and EN (1996) (see Fig. 8.13).

$$\sigma_c = \frac{E_0 \epsilon_p}{1 + (\frac{E_0 \epsilon_p}{\sigma_p} - 2)(\frac{\epsilon_c}{\epsilon_p}) + (\frac{\epsilon_c}{\epsilon_p})^2} \tag{8.33}$$

The brick tensile strength (σ_t) and the corresponding fracture energy (G_f) were set equal to 500 KPa and 0.25 kN/m, respectively. It should be emphasised that the value of the fracture energy utilized in this study was again chosen to ensure numerical stability of the solution procedure as in all cases the interface

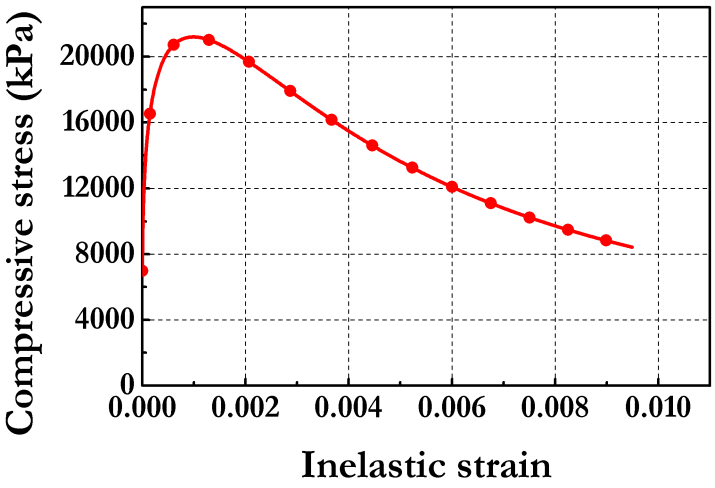


FIGURE 8.13: Compressive response of brick masonry unit

cohesive strength dictates the actual response of the masonry specimen under tension.

8.6.3 Plasticity parameters of the CDP model

The CDP plasticity parameters used in single and double-wythe walls were the common values used in the literature and the manual of the Abaqus software (SIMULIA, 2016). In particular, the dilation angle (β) was assumed to be 15° for all the single and double-walls, apart from S_G7_(Co) and S_B7 specimens, where it was increased to 45° due to the compressive damage of the brick as discussed in Section 8.7 (see Fig. 8.14d and Fig. 8.14e and Table 8.1). Vermeer and De Borst (1984) reported that the common values of the dilation angle are between 0° and 20° for concrete and rocks. In addition, zero eccentricity value was adopted for all the single and double-wythe walls.

The ratio of the second stress invariant on the tensile meridian, to that on the compressive meridian (K_c) was set equal to 0.77. In addition, the default value of the ratio (σ_{b0}/σ_{c0}) was used equal to 1.16. Finally, a viscosity parameter

TABLE 8.1: Brick properties for single and double-wythe walls

FE model	f_b [MPa]	β [°]	FE model	f_b [MPa]	β [°]
S_CON	21.2	15	D_CON	21.2	15
S_C1	21.2	15	D_C1	21.2	15
S_C1_(Co)	21.2	15	D_C1_(Co)	21.2	15
S_G3	21.2	15	D_G3	21.2	15
S_G7	21.2	15	D_G7	21.2	15
S_G3_(Co)	25.0	15	D_G3_(Co)	21.2	15
S_G7_(Co)	21.2	45	D_G7_(Co)	21.2	15
S_B3	21.2	15	D_B3	21.2	15
S_B7	21.2	45	D_B7	21.2	15

(r) determined as 10^{-6} was utilized to ensure stability of the numerical solution procedure.

8.6.4 Application of the cohesive modelling approach on the mortar joints of the masonry wall specimens

The cohesive modelling approach was implemented to account for the joint mortar separation between the initially bonded brick surfaces. Cohesive elements can be implemented in cases where the interface strength is lower with respect to the adjacent materials and a crack is expected to propagate as happens at the head and bed mortar joints.

The traction-separation constitutive model was adopted to model the response of cohesive elements as described in Section 8.5. The stresses define the maximum nominal stress damage initiation criterion (t_n, t_s, t_t) and the elastic stiffness (K_n, K_s, K_t) describes the response of the interface among the bricks

before the initiation of the damage were determined using a curve fitting procedure on the double wall control specimen, namely D_CON. The S_CON specimen failed under the action of its own weight during placement on the test-setup. Similar interface values were applied for all the single and double wall specimens as shown in Table 8.2. The fracture energy used to describe the linear damage evolution after the peak traction was calibrated for each model and is presented in Table 8.2. It should be mentioned that the actual value of the critical fracture energy is associated with a large variability. Furthermore, its value affects the post peak response of the specimen. Hence, for the purpose of this study, the variability considered is deemed reasonable. In addition, the viscosity coefficient used was 10^{-5}.

A hard type of contact was chosen among the bricks to minimize the penetration of the slave surface into the master surface at the constrained locations without transferring stresses at the interface. The default constraint enforcement method was adopted. The tangential behaviour among the bricks was described using the Coulomb friction model, using a coefficient of friction equal to 0.7 (Bolhassani et al., 2015; Nazir and Dhanasekar, 2013).

8.6.5 Modelling of TRM and masonry substrate interface

The TRM masonry substrate interface was modelled using a surface-based tie constraint as described in Section 8.5.5. This is a surfaced based constraint used to set all the active degrees of freedom equal between the masonry substrate and the composite material interface. The masonry substrate interface was defined as the master and the composite material interface as the slave. This type of constraint was used to model the response of the strengthened masonry wall when the TRM composite was fully bonded on the masonry substrate until textile

TABLE 8.2: Cohesive surface element properties

FE model	K_n [kN/m] [x10^6]	K_s [kN/m] [x10^7]	K_t [kN/m] [x10^7]	t_n [kPa]	t_s [kPa]	t_t [kPa]	G^c [kN/m]
Single-wythe walls							
S_CON	4	4	4	95	500	500	0.02
S_C1	4	4	4	95	500	500	0.046
S_C1_(Co)	4	4	4	95	500	500	0.075
S_G3	4	4	4	95	500	500	0.045
S_G7	4	4	4	95	500	500	0.045
S_G3_(Co)	4	4	4	95	500	500	0.063
S_G7_(Co)	4	4	4	95	500	500	0.09
S_B3	4	4	4	95	500	500	0.055
S_B7	4	4	4	95	500	500	0.09
Double-wythe walls							
D_CON	4	4	4	95	500	500	0.02
D_C1	4	4	4	95	500	500	0.12
D_C1_(Co)	4	4	4	95	500	500	0.152
D_G3	4	4	4	95	500	500	0.058
D_G7	4	4	4	95	500	500	0.30
D_G3_(Co)	4	4	4	95	500	500	0.16
D_G7_(Co)	4	4	4	95	500	500	0.20
D_B3	4	4	4	95	500	500	0.185
D_B7	4	4	4	95	500	500	0.16

rupture occurred. In addition tie-constraint cannot capture the response of the strengthened masonry walls when the failure mode was debonding of the textile at the textile to mortar interface. Therefore, in specimens S_B7, S_G7_(Co), D_B7, D_G7_(Co),D_C1_(Co) in Figs. 8.14-8.15 the FEM curve was not able to capture the entire post-peak behaviour of the experiment.

8.6.6 Modelling of the TRM composite material

The Drucker-Prager yield criterion was adopted to model the nonlinear constitutive behaviour of the TRM strengthening mortar. In this study the (K) value was chosen equal to 1, which results in t=q (see Eq. 8.18), for the simplicity of the model. Using the calibration procedure described Section 8.4, with yield stress in tension equal to σ_t=6 MPa and yield stress in compression equal to σ_c=37 MPa a friction angle of 52 $^\circ$ was adopted. A similar value was used for the dilation angle (ψ=β). The corresponding yield stress in tension and Young's Modulus (E_m) were set equal to σ_t=6 MPa and E_m=800 000 kPa, respectively. The mechanical properties of the strengthening mortar were adopted by the strengthening mortar experimental results presented in Table 6.2 in Section 6.2.2.

In addition, for the textile fibre reinforcement an isotropic hardening model was adopted using a yield stress based on the coupon test results and a curve fitting procedure. A ductile damage criterion was used to model the response of the textile after the yield stress was attained. Table 8.3 illustrates the input fracture strain ($\epsilon_{fr,FEM}$) and the corresponding displacement at failure ($d_{fail,FEM}$), which were used to describe the ductile damage criterion of each fibre-textile material. It is of interest to note that, even-though the damage model is intended to be used for ductile materials, the ($\epsilon_{fr,FEM}$) values used were small

TABLE 8.3: Damage properties of the fibre-textile

FE model	$\epsilon_{fr,FEM}$ [%]	$d_{fail,FEM}$ [m]	FE model	$\epsilon_{fr,FEM}$ [%]	$d_{fail,FEM}$ [m]
S_C1	0.2	0.002	D_C1	0.2	0.002
S_C1_(Co)	0.4	0.002	D_C1_(Co)	0.4	0.002
S_G3	0.1	0.001	D_G3	0.1	0.003
S_G7	0.2	0.002	D_G7	0.2	0.002
S_G3_(Co)	0.1	0.002	D_G3_(Co)	0.1	0.002
S_G7_(Co)	0.1	0.002	D_G7_(Co)	0.1	0.002
S_B3	0.2	0.002	D_B3	0.2	0.002
S_B7	0.2	0.002	D_B7	0.2	0.002

(see Table 8.3). This results indeed in a brittle envelope which is more consistent with the response anticipated from the textile.

The elastic and inelastic properties of the textile fibre composite materials have been identified through a curve fitting procedure based on the specimen elastic stiffness and ultimate strength capacity, respectively (see Table 8.4). Table 8.4 demonstrates the input ultimate tensile stress ($f_{fu,in,FEM}$) and output ($f_{fu,out,FEM}$) ultimate tensile stress, the Young's Modulus ($E_{f,FEM}$) and the coupon tests results described in Chapter 4. In addition, the TRM thickness was determined equal to 2.5 mm, 2.5 mm and 5 mm for 1, 3 and 7 TRM layers, respectively.

8.7 Finite element analysis results and discussion

The numerically derived load vs deflection curves are compared against the experimental results for single-wythe and double-wythe walls in Fig. 8.14 and Fig. 8.15, respectively, where a good fit is shown to be achieved. In particular, the specimens failed due to textile rupture (S_C1_(Co), S_G3, S_G7, S_G3_(Co), S_B3) resulted in good agreement between experimental and analytical results. They provide an accurate estimate of the actual maximum load and both, the

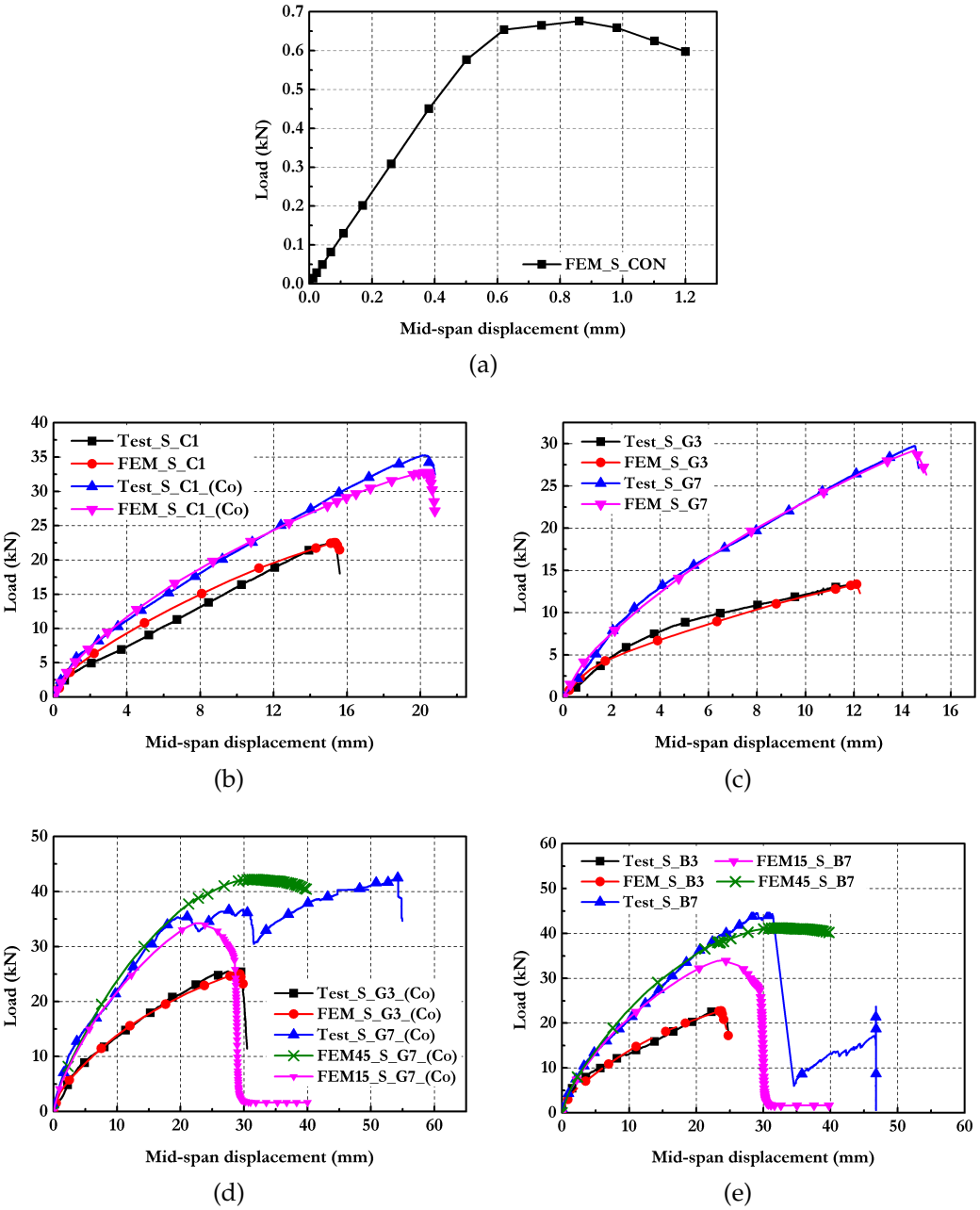


FIGURE 8.14: Load-displacement curves of single-wythe wall specimens

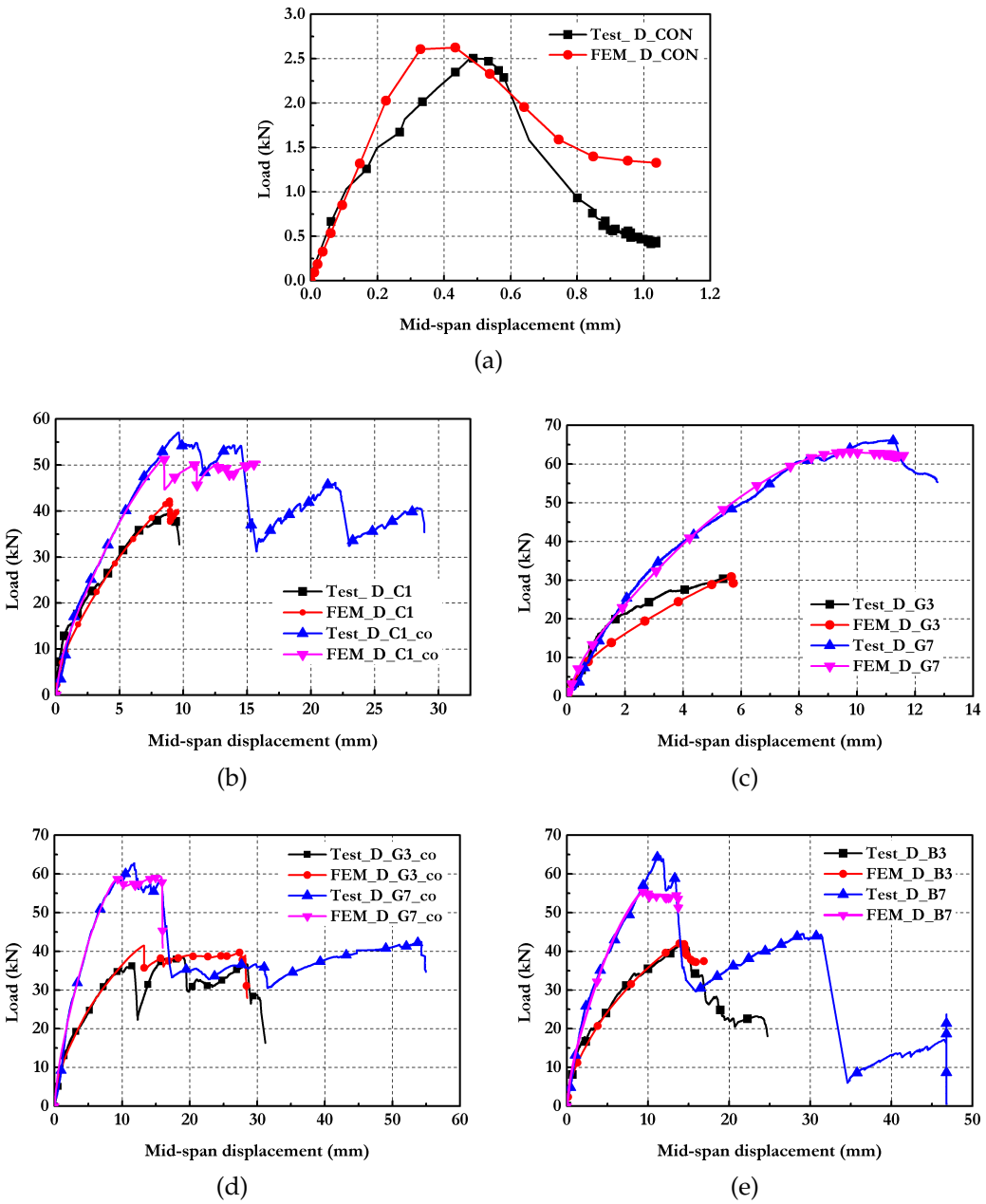


FIGURE 8.15: Load-displacement curves of double-wythe wall specimens

elastic and post-elastic stiffness of the masonry walls up to the peak load is accurately accounted for in all cases. In addition, the estimate on the displacements corresponding to the maximum and ultimate load also agrees well with the experimental results (see Figs. 8.14b-8.14e). The specimens failed due to shear failure in single-wythe walls (S_B7, S_G7_(Co)) and in double-wythe walls (D_B3, DG3_(Co), DG7_(Co), DC1_(Co), D_B7), demonstrated good fit among the experimental and numerical results, including the elastic and post-elastic stiffness up to the maximum or the ultimate load. The coated TRM models (S_G7_(Co), D_C1_(Co), D_G7_(Co), D_B7) did not capture the interlocking mechanics after shear damage of the wall occurred.

8.7.1 Single-wythe walls: Numerical vs experimental results

The S_CON specimen failed under the action of its own weight during placement on the test-setup (see Table 8.5). Therefore, the double-wythe wall control specimen D_CON was used to determine the interface properties of the single-wythe control specimen S_CON (see Fig. 8.14a). The FEM_S_CON failed when the mortar joints opened at the mid-span of the wall as shown in Fig. 8.16.

The S_C1 specimen failed due to slippage of the fibre-textile within the mortar (see Table 8.5). The E_f in FEM_S_C1 and FEM_S_C1_(Co) was decreased by 26% and 10%, respectively, compared to the TRM coupon (see Table 8.4). A higher decrease of E_f was observed in FEM_S_C1 due to the slippage of the fibres within the mortar. Both specimens, presented localised failure of the textile at the mid-span of the wall, which is shown in the longitudinal plastic strains contours in Fig. 8.17c and Fig. 8.18c, respectively, when the maximum load was attained (see also Fig. 8.14b). In FEM_S_C1_(Co) $f_{fu,in,FEM}$ and $f_{fu,out,FEM}$ are identical, which demonstrates that yielding of the textile occurred in the

model that corresponds to failure of the textile, when the maximum load was attained (see Table 8.4). In addition, the $f_{fu,out,FEM}$ for the FEM_S_C1 and FEM_S_C1_(Co) was 15% and 32% lower, with respect to the coupon test f_{fu}, respectively (see Table 8.4). This shows the reliability of the FE results with respect to the experimental results.

In specimens S_G3 and S_G7, textile rupture occurred (see Table 8.5, Fig. 8.19d, Fig. 8.20d and Fig. 8.14c). A similar failure mode was observed in the numerical model, where the $f_{fu,in,FEM}$ and $f_{fu,out,FEM}$ are equal, which shows that yielding of the textile was observed. This is equivalent of failure of the textile (see Table 8.4). The textile Young's modulus in FEM_S_G3 was similar to the TRM coupon, whereas in FEM_S_G7 higher value was obtained after the curve fitting procedure (see Table 8.4, and Fig. 8.14c). This occurred due to better interlocking mechanism among the 7 TRM layers compared to a single TRM layer as also reported in the experimental work of masonry walls in Chapter 6.

In addition, the $f_{fu,out,FEM}$ for the FEM_S_G3 and FEM_S_G7 was 43% and 41% decreased compared to the coupon test f_{fu}, respectively (see Table 8.4). This difference was observed due to the high variability among the glass coupon test results discussed in Section 4.6. Also, the longitudinal plastic strains of the textile, are localised at the mid-span of the wall as shown in Fig. 8.19c and Fig. 8.20c, where textile rupture was observed.

S_G3_(Co) and S_B3 specimens failed due to textile rupture (see Table 8.5, Fig. 8.21d, Fig. 8.24d, and Figs. 8.14d-8.14e). In FEM_S_G3_(Co) the $f_{fu,in,FEM}$ and $f_{fu,out,FEM}$ are similar, which illustrates that the textile yielded in the model by reaching the input value, when the peak load was attained. This corresponds to failure of the textile which is in agreement with the experimental results (Fig. 8.14d-Fig. 8.14e). The textile modulus of elasticity in FEM_S_G3_(Co) and

FEM_S_B3 was only 14% and 9% lower compared to the coupon test values E_f, respectively as shown in Table 8.4 (see also Figs. 8.14d-8.14e).

In addition, the $f_{fu,out,FEM}$ for the FEM_S_G3_(Co) and FEM_S_B3 was 9% and 20% lower than the coupon test f_{fu}, respectively (see Table 8.4). The similar values obtained demonstrate the reliability of the model. A similar distribution of the longitudinal plastic strains was observed among the specimens as shown in Fig. 8.21c and Fig. 8.24c.

S_G7_(Co) and S_B7 specimens failed due to shear (see Table 8.5, Fig. 8.23d, Fig. 8.26d and Figs. 8.14d-8.14e). In both specimens, the dilation angle found to be increased from 15° to 45°, to account that the failure mode of the wall did not occur due to compressive damage of the brick but due to shear damage of the wall. The load vs displacement curves for 15° and 45° are presented in Figs. 8.14d-8.14e for comparison. In FEM15_S_B7 the significant distribution of equivalent plastic strains at the top of the wall when the maximum load was attained is an evidence of compressive damage of the brick (see Fig. 8.25a). By increasing the dilation angle the compressive damage of the brick was prevented but also allowed the textile to reach higher strength. In particular, $f_{fu,out,FEM}$ was increased from 606 MPa to 791 MPa, in FEM15_SB7 and FEM45_SB7, respectively (see Table 8.4). Similar response was observed in FEM15_S_G7_(Co), where the increase of the dilation angle resulted in $f_{fu,out,FEM}$ equal to 572 MPa and 746 MPa in FEM15_SG7_(Co) and FEM45_SG7_(Co), respectively (see Table 8.4 and Fig. 8.22a). In addition, the load capacity is increased but without being able to capture the actual response up to the maximum load, where interlocking mechanics developed between the masonry bricks after the shear failure of the wall (see Fig. 8.14d).

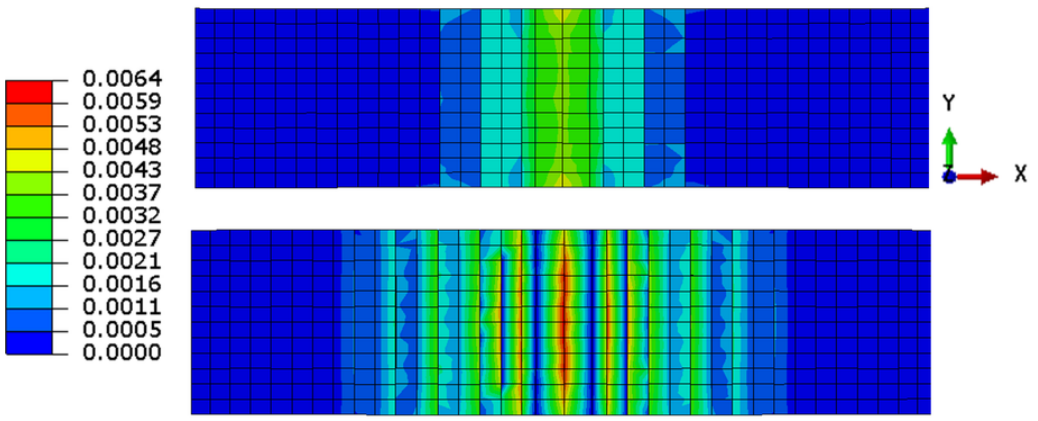


FIGURE 8.16: Deformed shape of FEM_S_CON

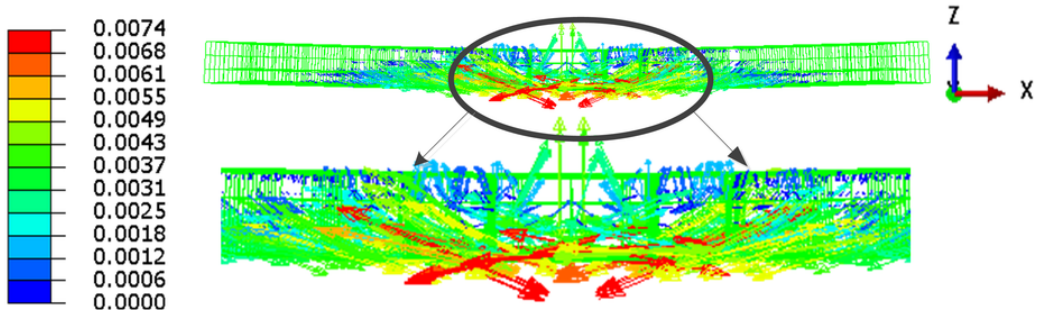
The shear damage of the brick in both specimens when the 45° dilation angle used was pronounced by the maximum principal plastic strain $PE_{max,princ}$ direction illustrated in Fig. 8.26b and Fig. 8.23b, respectively. Shear cracks are developed perpendicular to the maximum principal strain direction, which is at an angle of 45°. In addition, in FEM45_S_G7_(Co) and FEM45_S_B7 the $f_{fu,out,FEM}$ was 41% and 34%, lower compared to $f_{fu,in,FEM}$, respectively (see Table 8.4). This verify the fact that when the shear strength capacity of the wall was attained, the textile did not reach the maximum input strength and further increase of the fibre-textile strength did not occur, resulting in decreased exploitation of the textile strength. In addition, the modulus of elasticity in FEM45_S_G7_(Co) and FEM45_S_B7 was decreased by 23% and 25%, respectively, compared to the coupon test results (see Table 8.4) due to the shear failure observed in both specimens.

8.7.2 Double-wythe walls: Numerical vs experimental results

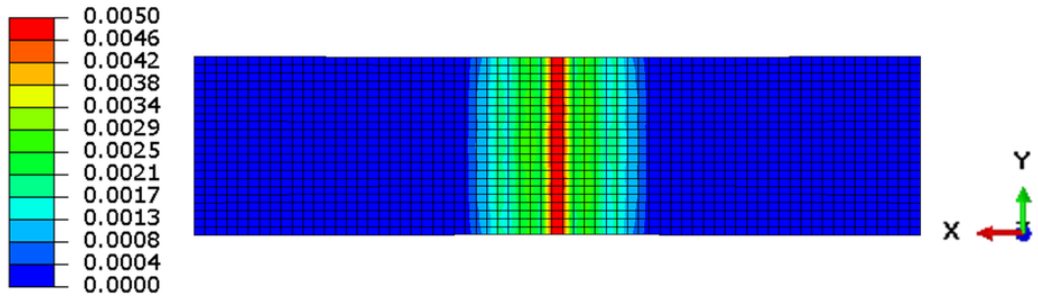
The $E_{f,FEM}$ in the specimens failed due to shear-flexure failure mode (D_C1_(Co), D_G3_co, D_G7_co, D_B3, D_B7) was decreased by 41%-48%, with respect to the coupon test results as presented in Table 8.4 (see also Table 8.6). The shear damage of the brick did not allow the textile to increase further its axial stress, but also resulted in decreased stiffness of the load displacement curve as shown in Fig. 8.15b, Fig. 8.15d and Fig. 8.15e (see also Table 8.4).



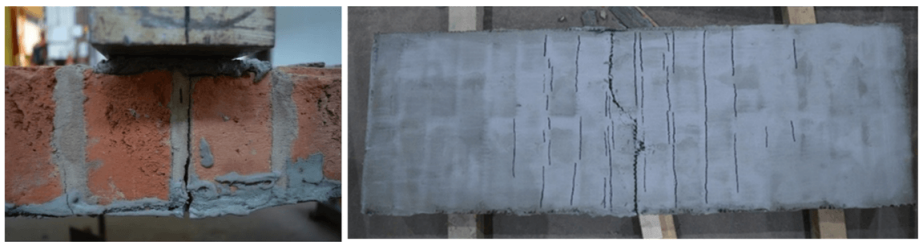
(a)



(b)



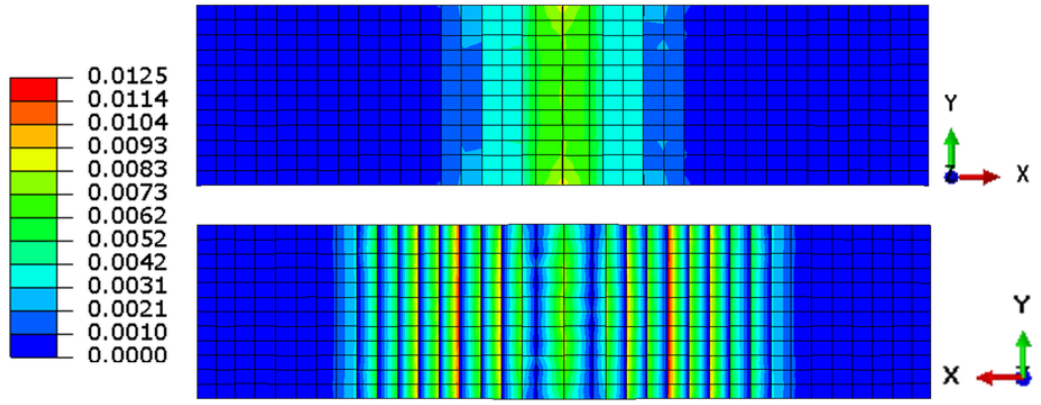
(c)



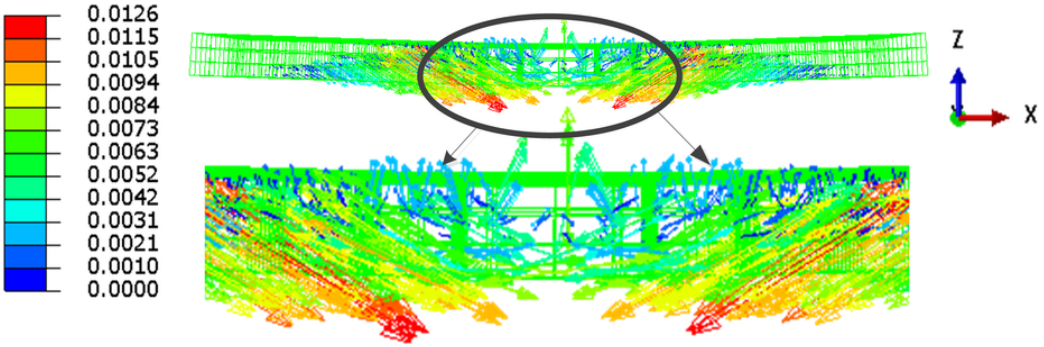
(d)

FIGURE 8.17: Strain contours of FEM_S_C1 including (a) equivalent plastic strain on the top and bottom of the wall, (b) maximum principal plastic strain and (c) longitudinal plastic strain in the x-axis (d) Failure mode of S_C1 specimen

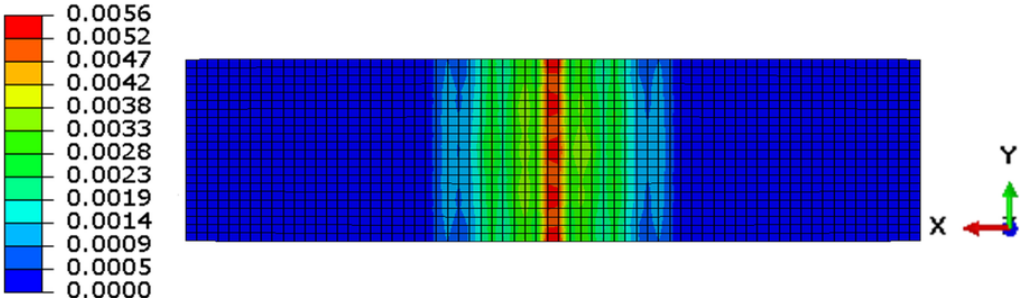
.



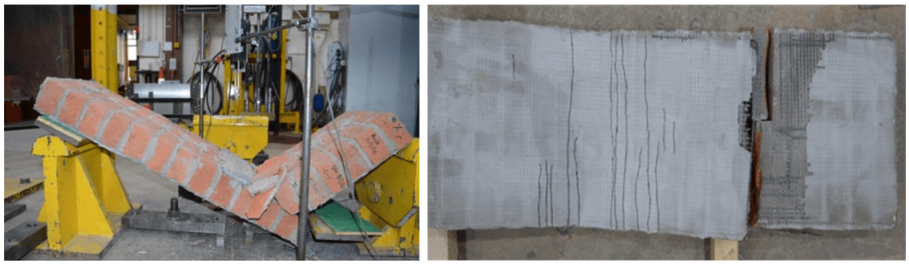
(a)



(b)

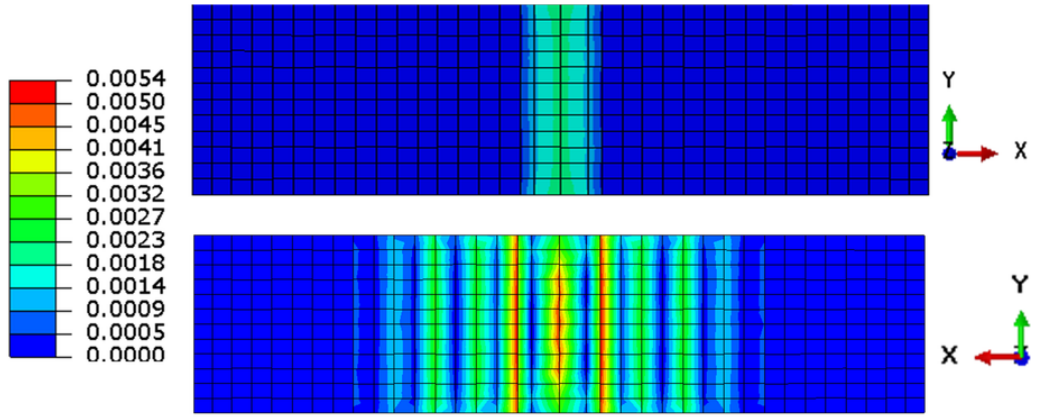


(c)

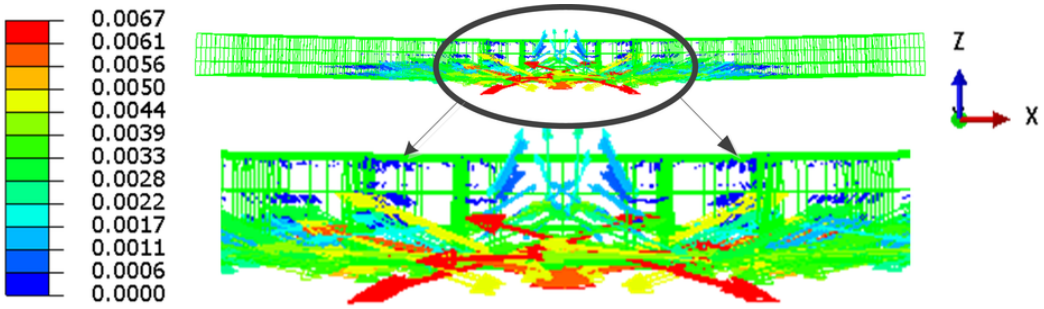


(d)

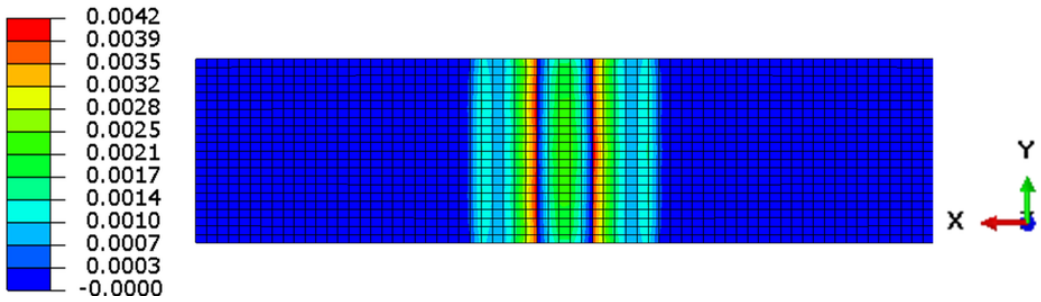
FIGURE 8.18: Strain contours of FEM_S_C1_(Co) including (a) equivalent plastic strain on the top and bottom of the wall, (b) maximum principal plastic strain and (c) longitudinal plastic strain in the x-axis, (d) Failure mode of S_C1_(Co) specimen



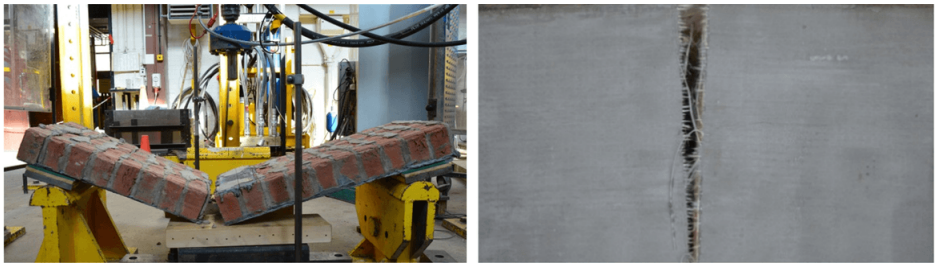
(a)



(b)

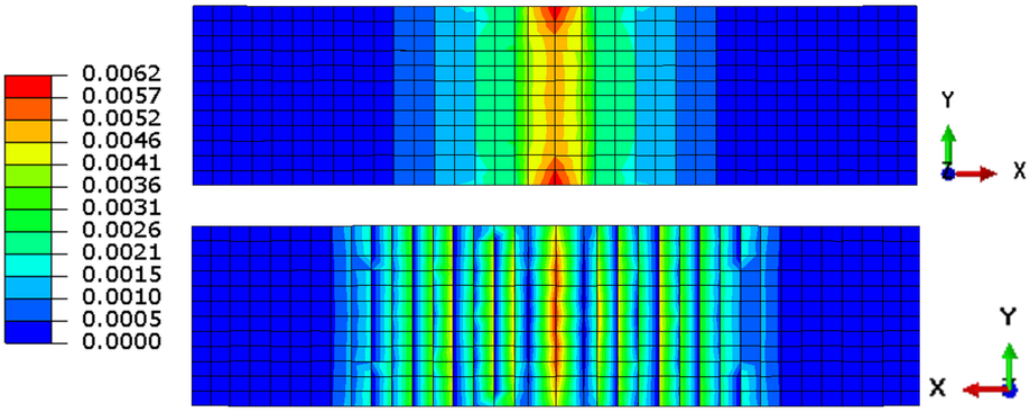


(c)

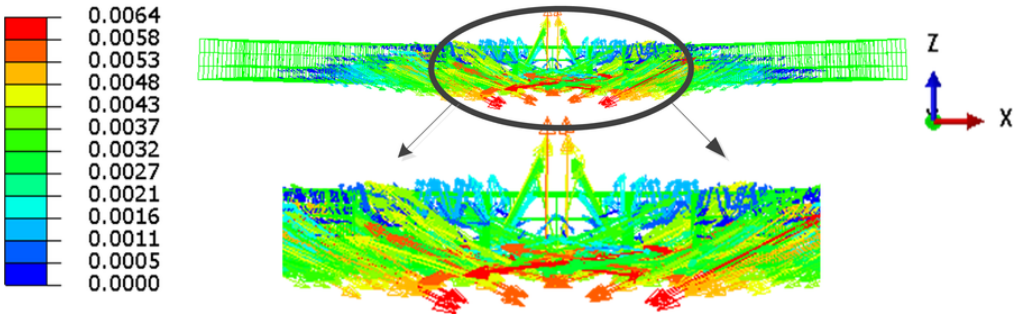


(d)

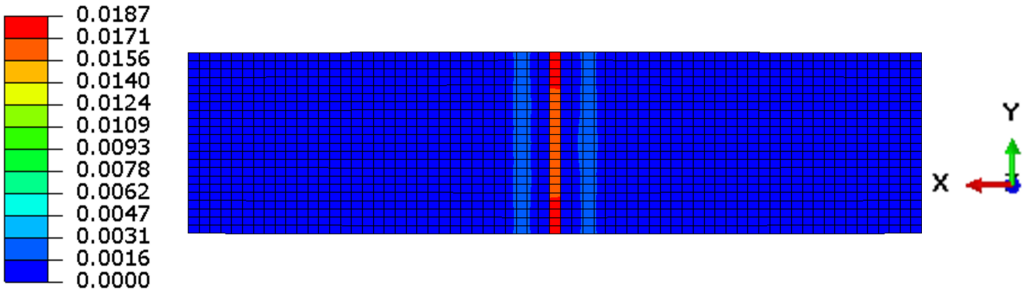
FIGURE 8.19: Strain contours of FEM_S_G3 including (a) equivalent plastic strain on the top and bottom of the wall, (b) maximum principal plastic strain and (c) longitudinal plastic strain in the x-axis, (d) Failure mode of S_G3 specimen



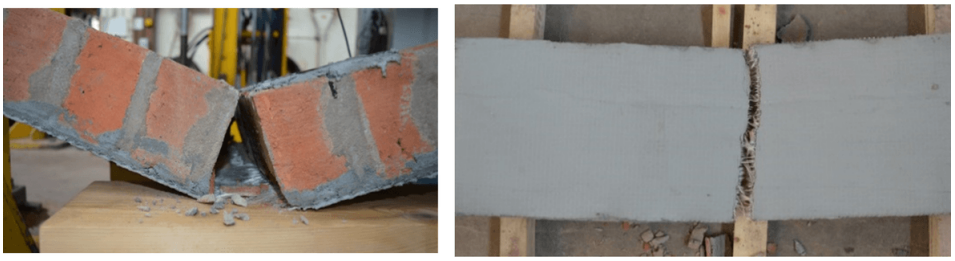
(a)



(b)

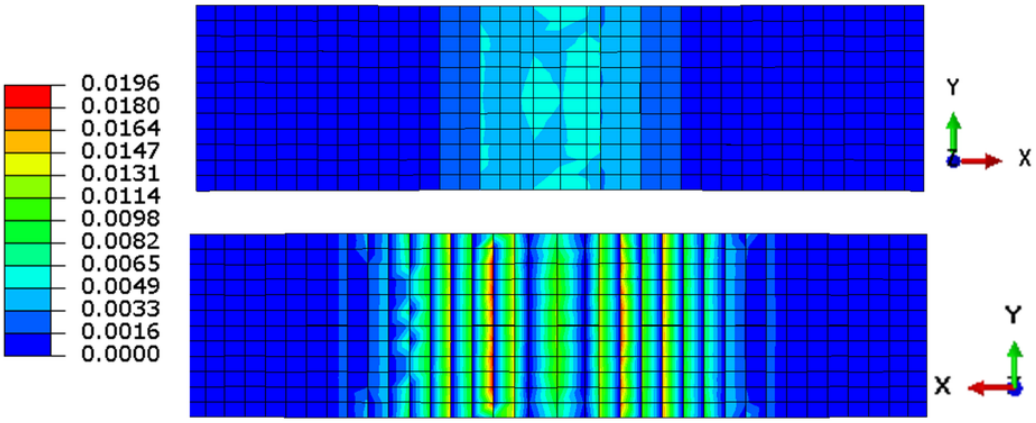


(c)

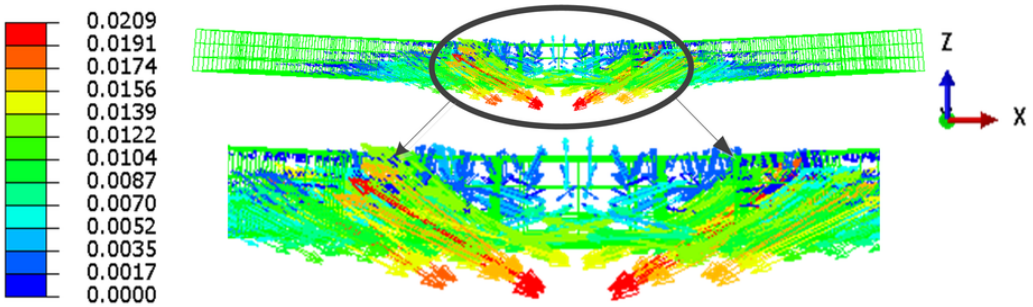


(d)

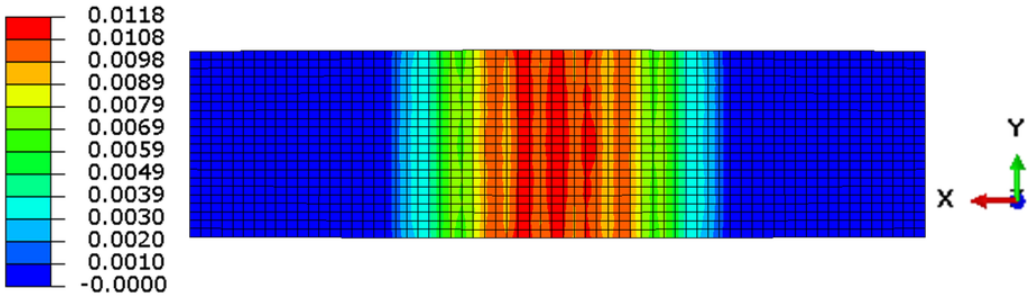
FIGURE 8.20: Strain contours of FEM_S_G7 including (a) equivalent plastic strain on the top and bottom of the wall, (b) maximum principal plastic strain and (c) longitudinal plastic strain in the x-axis (d) Failure mode of S_G7 specimen



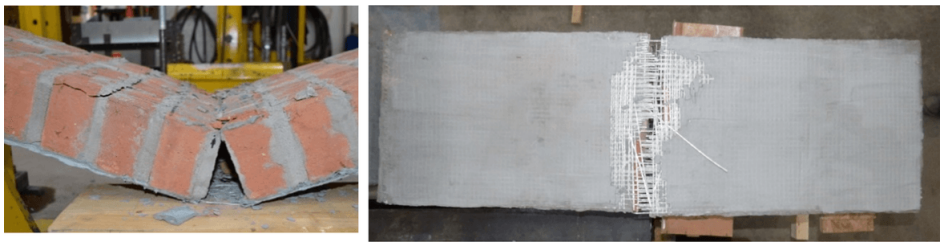
(a)



(b)

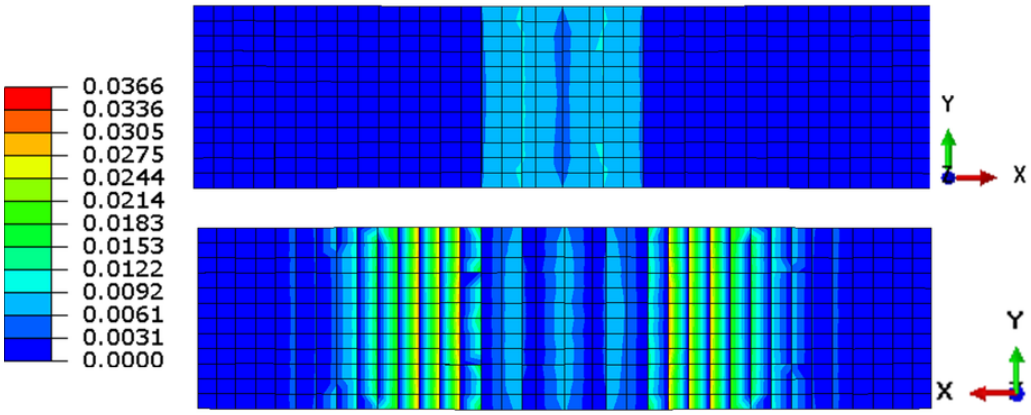


(c)

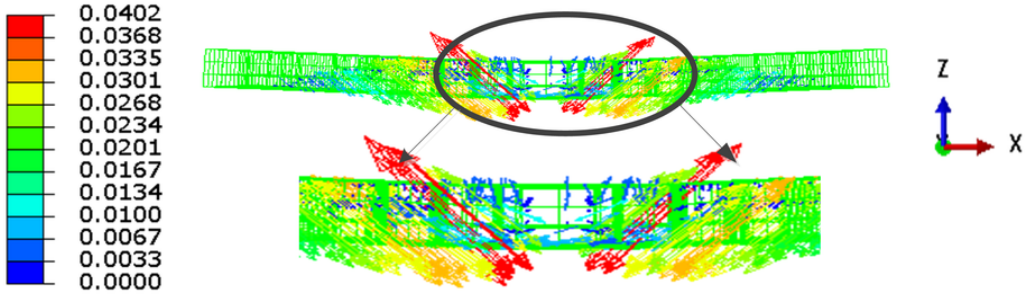


(d)

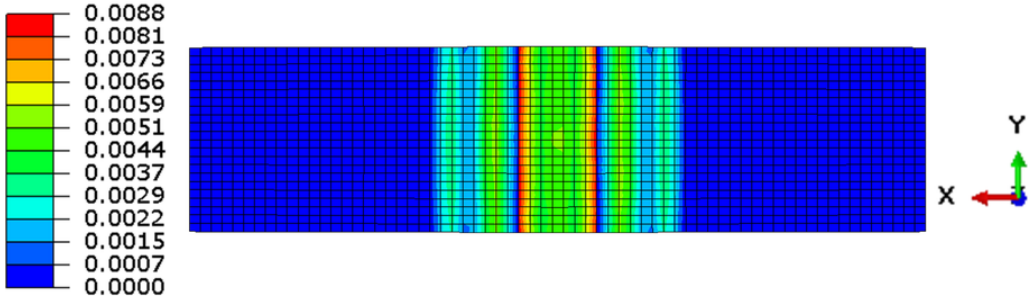
FIGURE 8.21: Strain contours of FEM_S_G3_(Co) including (a) equivalent plastic strain on the top and bottom of the wall, (b) maximum principal plastic strain and (c) longitudinal plastic strain in the x-axis, (d) Failure mode of S_G3_(Co) specimen



(a)



(b)

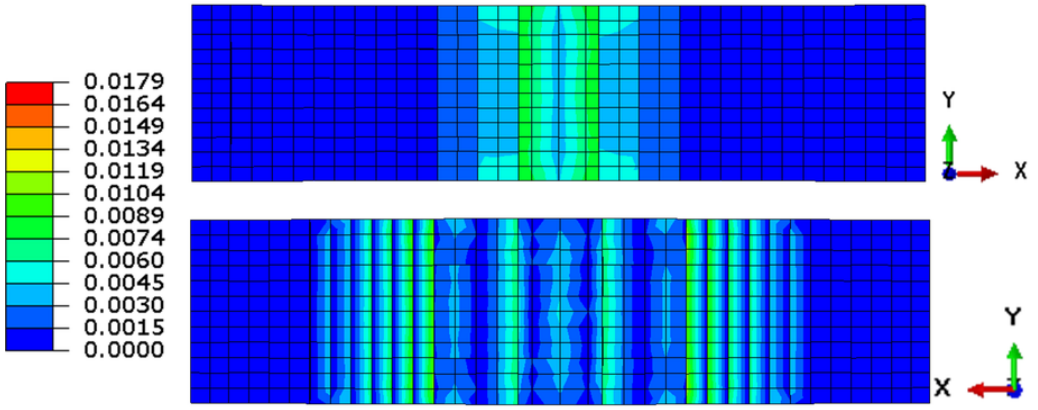


(c)

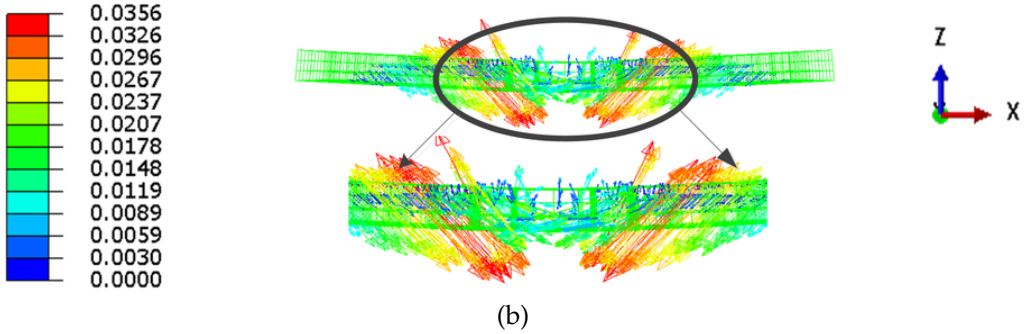


(d)

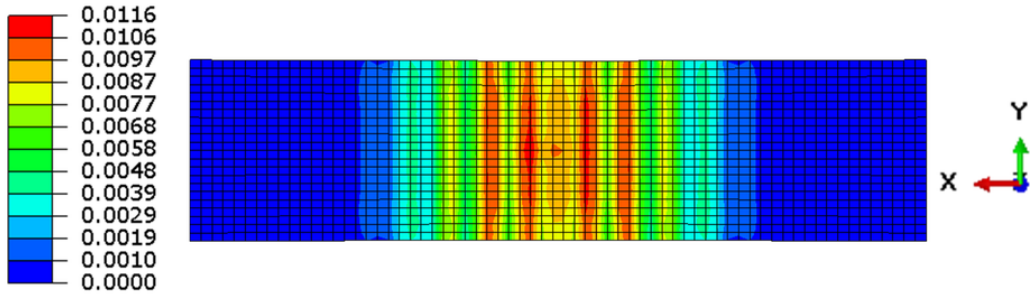
FIGURE 8.22: Strain contours of FEM15_S_G7_(Co) including (a) equivalent plastic strain on the top and bottom of the wall, (b) maximum principal plastic strain and (c) longitudinal plastic strain in the x-axis, (d) Failure mode of S_G7_(Co) specimen



(a)



(b)

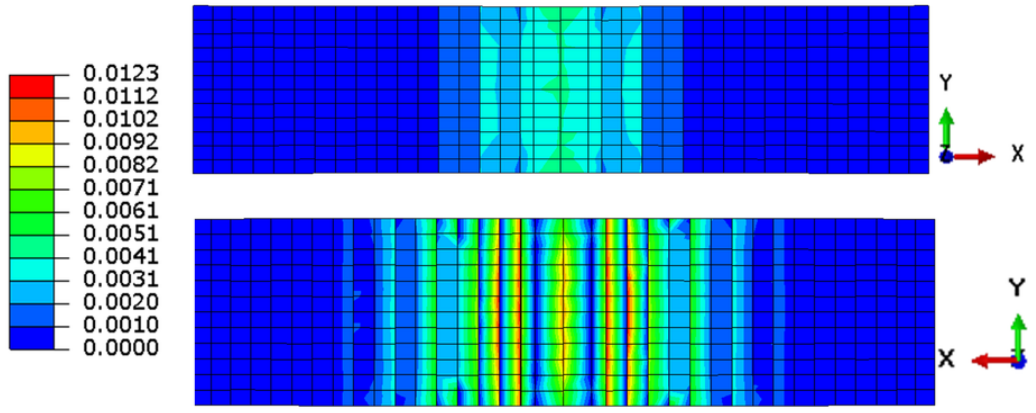


(c)

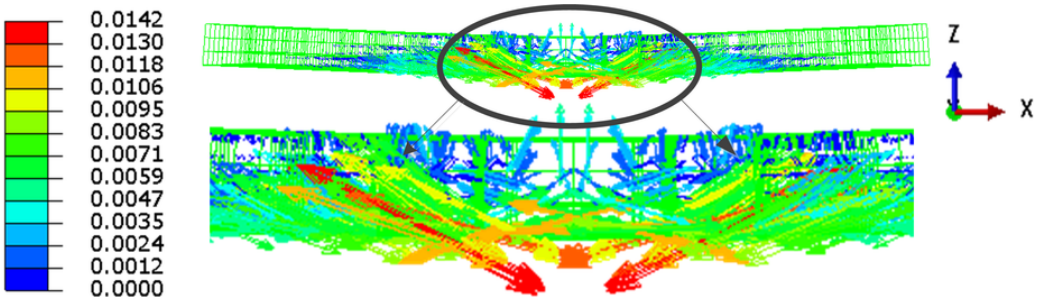


(d)

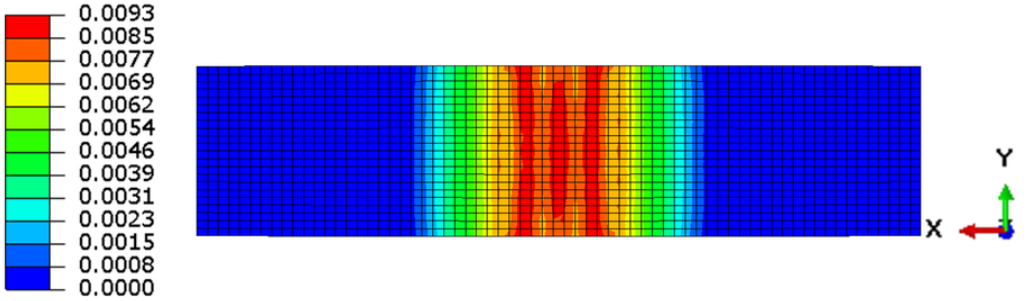
FIGURE 8.23: Strain contours of FEM45_S_G7_(Co) including (a) equivalent plastic strain on the top and bottom of the wall, (b) maximum principal plastic strain and (c) longitudinal plastic strain in the x-axis, (d) Failure mode of S_G7_(Co) specimen



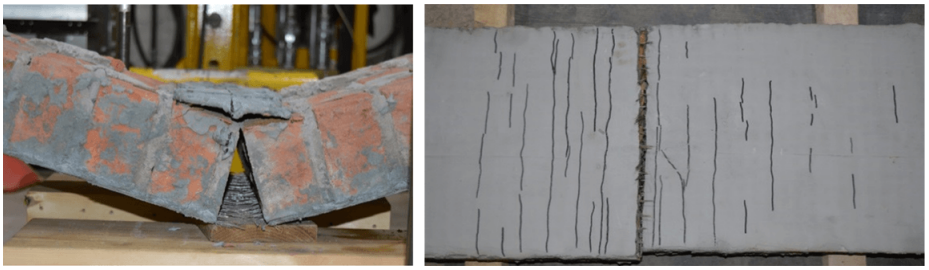
(a)



(b)

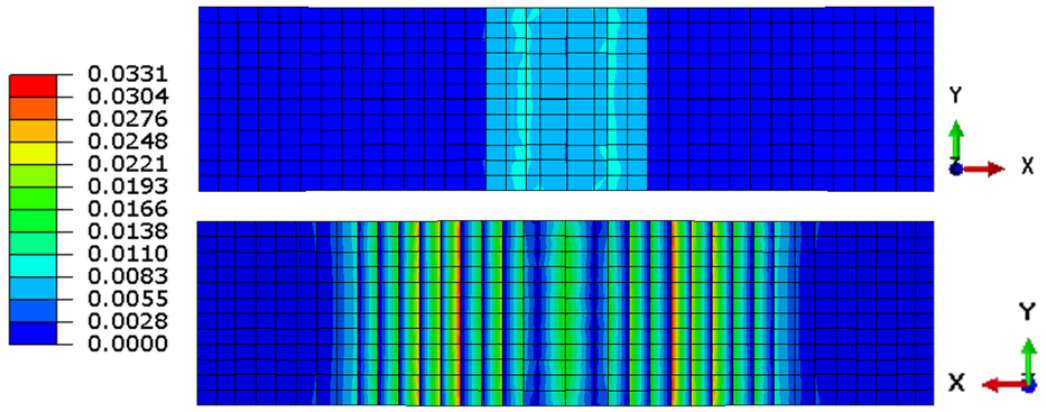


(c)

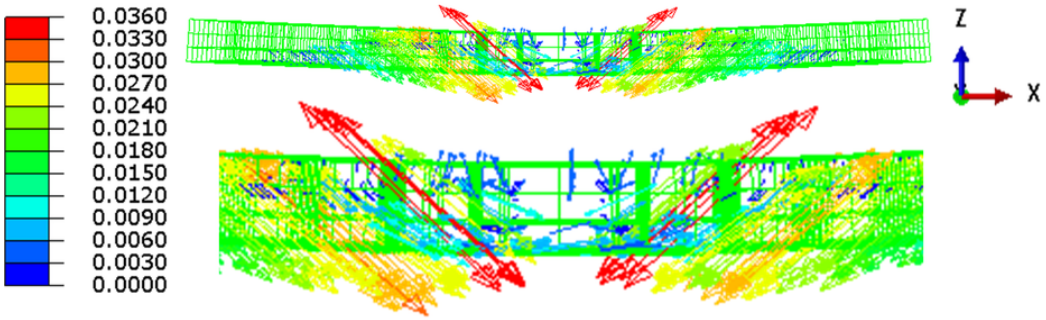


(d)

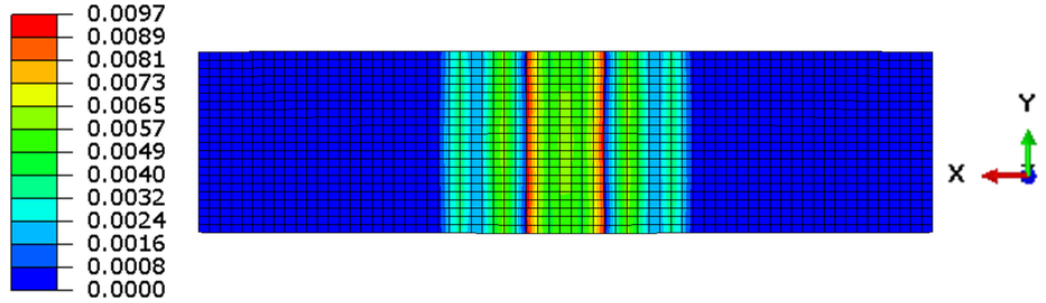
FIGURE 8.24: Strain contours of FEM_S_B3 including (a) equivalent plastic strain on the top and bottom of the wall, (b) maximum principal plastic strain and (c) longitudinal plastic strain in the x-axis, (d) Failure mode of S_B3 specimen



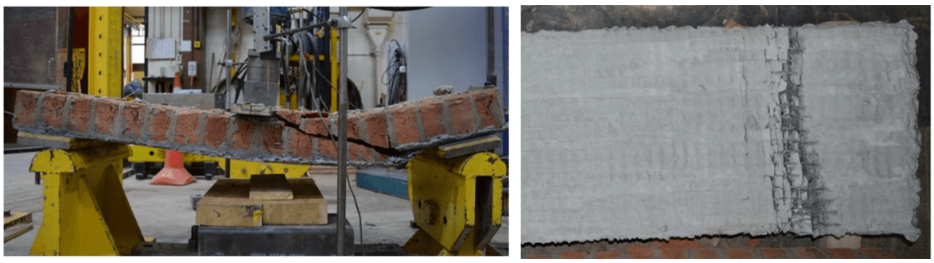
(a)



(b)

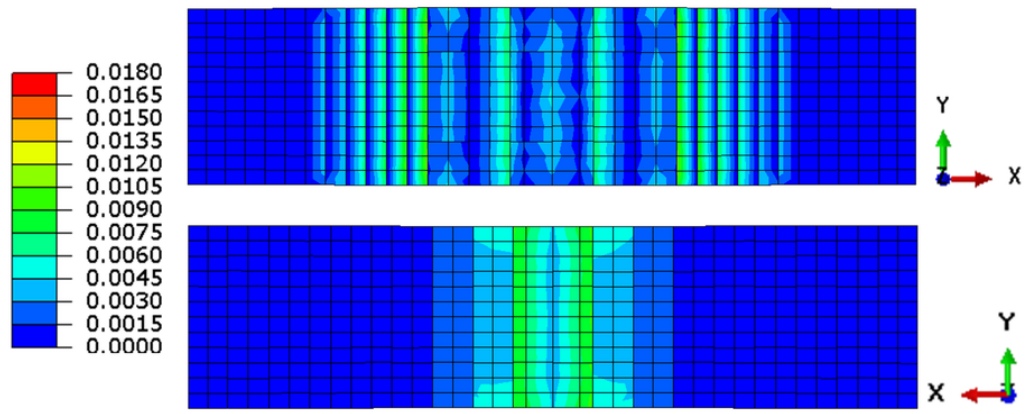


(c)

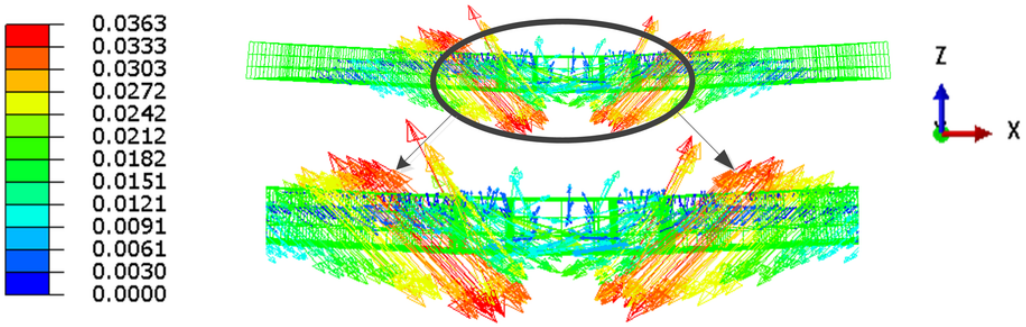


(d)

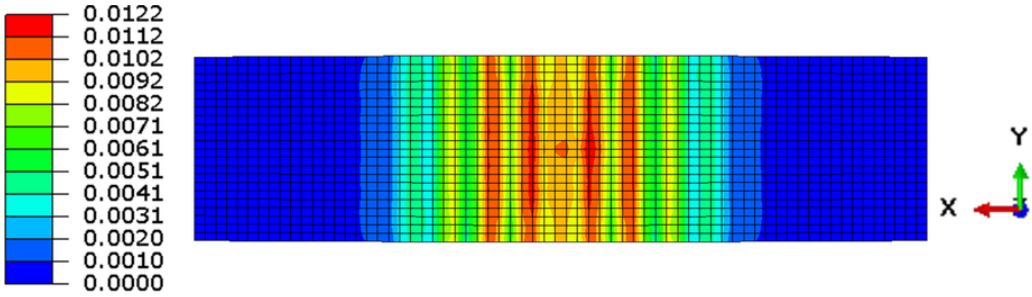
FIGURE 8.25: Strain contours of FEM15_S_B7 including (a) equivalent plastic strain on the top and bottom of the wall, (b) maximum principal plastic strain and (c) longitudinal plastic strain in the x-axis, (d) Failure mode of S_B7 specimen



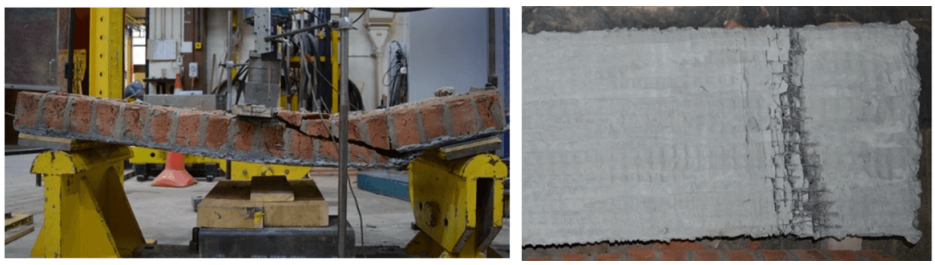
(a)



(b)



(c)



(d)

FIGURE 8.26: Strain contours of FEM45_S_B7 including (a) equivalent plastic strain on the top and bottom of the wall, (b) maximum principal plastic strain and (c) longitudinal plastic strain in the x-axis, (d) Failure mode of S_B7 specimen

The control specimen D_CON failed in flexure in an abrupt and brittle fashion as shown in Table 8.6 and Fig. 8.27b. The FEM_D_CON failed when the mortar joints opened at the mid-span of the wall as occurred at the experiment (see Table 8.6 and Fig. 8.27a).

The D_C1 specimen failed due to textile rupture as shown in Table 8.6 and Fig. 8.28d. A similar failure mode was observed in the numerical model. In particular, the similar values of $f_{fu,in,FEM}$ and $f_{fu,out,FEM}$ is an evidence that yielding of the textile occurred in the model (see Table 8.4). Also, the plastic strains in the x-axis of the textile are localised at the mid-span of the wall, where textile rupture occurred (Fig. 8.28c). The direction of $PE_{max,princ}$ in Fig. 8.28b also shows that flexural cracks were formed and shear damage did not occur. In addition, the $E_{f,FEM}$ was decreased substantially by 56% compared to the coupon E_f as shown in Table 8.4. This could be a result of the partial slippage of the textile within the mortar before textile rupture occurred as reported in Chapter 6, which also resulted in 24% decreased textile stress $f_{fu,out,FEM}$ compared to the coupon f_{fu}.

The D_C1_(Co) specimen failed due to shear-flexure failure mode, where shear failure of the brick occurred followed by partial textile rupture (see Table 8.6 and Fig. 8.29d). In FEM_D_C1_(Co) the textile did not reach the $f_{fu,in,FEM}$, since the output ultimate tensile stress $f_{fu,out,FEM}$ was 48% lower compared to the $f_{fu,in,FEM}$, when the maximum load was attained (see Table 8.4 and Fig. 8.29c). The shear damage of the brick is shown in Fig. 8.29b and Fig. 8.29a, where the maximum principal plastic strain $PE_{max,princ}$ and equivalent plastic strain, are maximised. The shear cracks are developed perpendicular to the direction of the $PE_{max,princ}$, which is approximately 45°.

The D_G3 specimen failed due to textile rupture as shown in Table 8.6 and

Fig. 8.30d. A similar failure mode was observed in the FE model, where the failure of the textile is localised at the mid-span of the wall as shown by the longitudinal plastic strains in Fig. 8.30c when the maximum load was attained (see Fig. 8.15c). The similar $f_{fu,in,FEM}$ and $f_{fu,out,FEM}$ is an evidence that yielding of the textile occurred in the model which corresponds to failure of the textile (see Table 8.4). Also, the angle between x-axis and $PE_{max,princ}$ is minimal, which is also illustrates that shear damage of the brick did not occur (see Fig. 8.30b). In addition, the $f_{fu,out,FEM}$ was 30% lower compared to the coupon test ultimate tensile stress f_{fu} (see Table 8.4). In addition, the $E_{f,FEM}$ was 27% lower compared to the E_f of the glass coupon (see Table 8.4). The similar values obtained with the coupon test results show the reliability of the model with respect to the experimental results.

The D_G7 failed due to shear-flexure failure, followed by textile rupture (see Table 8.6 Fig. 8.31d). A similar failure mode was observed in the numerical model. In particular, the similar values of $f_{fu,in,FEM}$ and $f_{fu,out,FEM}$, in the model FEM_D_G7 was evidence that yielding of the textile occurred in the model, which is equivalent of failure of the textile (see Table 8.4). In addition, the plastic strains in the x-axis, maximised at the mid-span of the wall illustrate rupture of the textile (Fig.8.31c). Shear damage of the brick is shown where the $PE_{max,princ}$ is maximised in Fig. 8.31b. Shear cracks are developed perpendicular to the maximum principal strain direction at an angle of 45°. In addition, the maximum equivalent plastic strain is maximised at the same region as presented in Fig. 8.31a.

The $E_{f,FEM}$ was identical to E_f as shown in Table 8.4. In addition, the $f_{fu,out,FEM}$ of D_G7 was 31% lower with respect to f_{fu} obtained by the TRM coupon test. The similar values obtained with the coupon test results show the

accuracy of the model with respect to the experimental results.

The DG3_(Co) specimen failed due to shear flexure failure mode as presented in Table 8.6 (see also Fig. 8.32d and 8.15d). In the model, FEM_D_G3_(Co) yielding of the textile did not occur since the $f_{fu,out,FEM}$ was 28% lower than the $f_{fu,in,FEM}$, and the textile did not reach its maximum tensile strength (see Table 8.4 and Fig. 8.32c). The shear damage of the brick is an evidence of the maximum principal plastic strain $PE_{max,princ}$ direction (Fig. 8.32b) and plastic equivalent strain (Fig. 8.32a), at the bottom of the wall, where both are maximised. In addition, shear cracks are developed perpendicular to the maximum principal strain direction at an angle of 45° as shown in Fig. 8.32b.

D_G7_(Co) failed due to shear-flexure failure mode as shown in Table 8.6 (see also Fig. 8.33d and Fig. 8.15d). In FEM_D_G7_co the $f_{fu,out,FEM}$ was 59% lower than $f_{fu,in,FEM}$, which shows that the textile did not attain its ultimate tensile stress (see Table 8.4). The $PE_{max,princ}$ direction in Fig. 8.33b and the plastic equivalent strain presented in Fig. 8.33a, show that shear damage of the brick occurred. The shear cracks are formed perpendicular to the maximum principal plastic strain direction at an angle of 45° as shown in Fig. 8.33b.

D_B3 specimen failed due to shear-flexure failure mode, followed by partial textile rupture as illustrated in Table 8.6 (see also Fig. 8.34d and Fig. 8.15e). In the model, FEM_D_B3 the $f_{fu,out,FEM}$ was 29% lower than $f_{fu,in,FEM}$, which shows that textile rupture did not occur (see Table 8.4). The shear damage of the brick is illustrated in Fig. 8.34b, where the $PE_{max,princ}$ is maximised. The direction of $PE_{max,princ}$ is approximately 45° (with respect to the x-axis) and the shear cracks are developed in a perpendicular direction of the maximum principal plastic strain. In addition, the maximum equivalent plastic strain in Fig. 8.34a, is also evidence of the shear damage of the brick.

TABLE 8.4: Textile properties of the FE models

Model	FEM results			Coupon results		
	$f_{fu,in}$ $_{FEM}$ [MPa]	E_f $_{FEM}$ [GPa]	$f_{fu,out}$ $_{FEM}$ [MPa]	f_{fu} [MPa]	ϵ_{fu} [%]	E_f [GPa]
Single-wythe walls						
S_C1	1270	123.5	1270	1518	0.793	166.8
S_C1_(Co)	1920	180.0	1920	2843	1.39	200.5
S_G3	450	40.5	450	794	1.66	41.1
S_G7	470	55.0	470	794	1.66	41.1
S_G3_(Co)	1010	54.0	1010	1107	1.624	62.7
45_S_G7_(Co)	1107	48.0	746	1107	1.624	62.7
15_S_G7_(Co)	1107	48.0	572	1107	1.624	62.7
S_B3	950	58.0	950	1190	1.825	63.7
45_S_B7	1190	48.0	791	1190	1.825	63.7
15_S_B7	1190	48.0	606	1190	1.825	63.7
Double-wythe walls						
D_C1	1158	74.0	1158	1518	0.793	166.8
D_C1_(Co)	2843	110.0	1481	2843	1.39	200.5
D_G3	556	52.0	556	794	1.66	41.1
D_G7	550	41.0	550	794	1.66	41.1
D_G3_(Co)	1107	37.0	802	1107	1.624	62.7
D_G7_(Co)	1107	35.0	458	1107	1.624	62.7
D_B3	1190	38.0	850	1190	1.825	63.7
D_B7	1190	33.0	452	1190	1.825	63.7

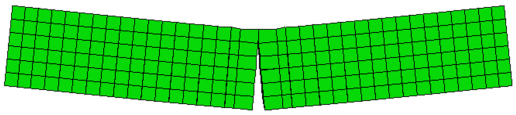
D_B7 failed due to shear failure mode as shown in Table 8.6 (see also Fig. 8.35d and Fig. 8.15e). FEM_D_B7 illustrate shear damage of the brick in Fig. 8.35b, where the $PE_{max,princ}$ direction is 45° with respect to x-axis. The shear cracks are developed perpendicular to the maximum principal plastic strain direction. In addition, the maximum equivalent plastic strain in Fig. 8.35a also illustrates shear damage of the brick. The $f_{fu,out,FEM}$ is 62% lower compared to $f_{fu,in,FEM}$, which shows that the textile did not reach its ultimate tensile strength and textile rupture did not occur (see Table 8.4).

TABLE 8.5: Experimental and simulated failure mode in single-wythe walls

Specimen	Simulated failure mode	Experimental failure mode
S_CON	Mortar joint opening	Failed under its own weight
S_C1	Textile yielding (failure)	Slippage between mortar-fibres
S_C1_(Co)	Textile yielding (failure)	Textile rupture
S_G3	Textile yielding (failure)	Textile rupture
S_G7	Textile yielding (failure)	Textile rupture
S_G3_(Co)	Textile yielding (failure)	Textile rupture
S_G7_(Co)	Shear brick damage	Shear failure
S_B3	Textile yielding (failure)	Textile rupture
S_B7	Shear brick damage	Shear failure

TABLE 8.6: Experimental and simulated failure mode in double-wythe walls

Specimen	Simulated failure mode	Experimental failure mode
D_CON	Mortar joint opening	Mortar joint opening
D_C1	Textile yielding (failure)	Textile rupture
D_C1_(Co)	Shear brick damage	Shear-flexure
D_G3	Textile yielding (failure)	Textile rupture
D_G7	Textile yielding (failure) shear brick damage	Shear-flexure textile rupture
D_G3_(Co)	Shear brick damage	Shear-flexure
D_G7_(Co)	Shear brick damage	Shear-flexure
D_B3	Shear brick damage	Shear-flexure
D_B7	Shear brick damage	Shear-flexure



(a)



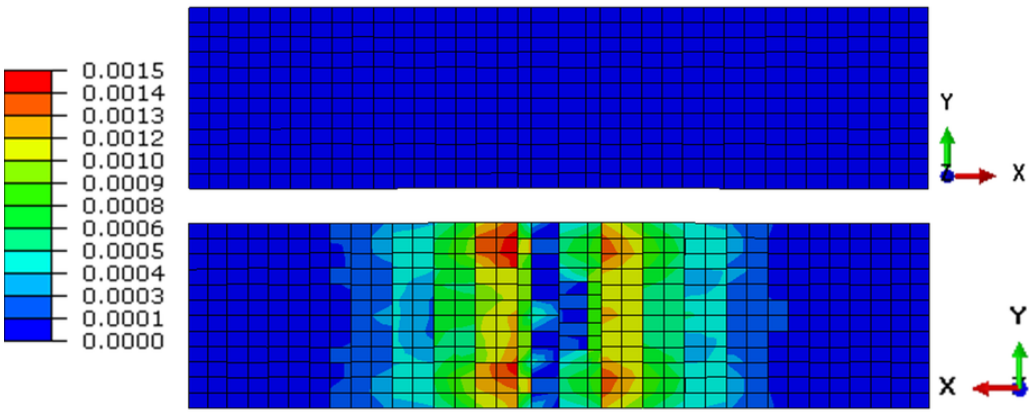
(b)

FIGURE 8.27: (a) Deformed shape of FEM_D_CON, (b) Failure mode of D_CON specimen

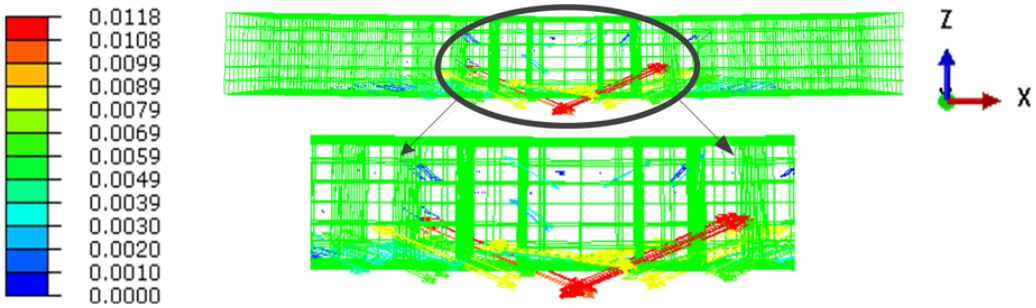
8.7.3 Effect of the dilation angle

The dilation angle adopted in single and double wythe specimens, was 15°, apart from S_B7 and S_G7_(Co) specimens, where a higher value of 45° provided the best fit, as discussed in Section 8.7.1. Therefore, a parametric analysis was performed to compare the results using 15° and 45° dilation angle in all the FE models of single-wythe walls. Figure 8.36 presents the load-displacement curves using both values of dilation angle, where a substantial difference was observed in the curves of the strengthened specimens (Figs. 8.36b-8.36e between the two different angles. A similar effect of the dilation angle was observed in all the single-wythe walls. In particular, by increasing the dilation angle from 15° to 45° increase of the load capacity of the load-displacement curve was observed.

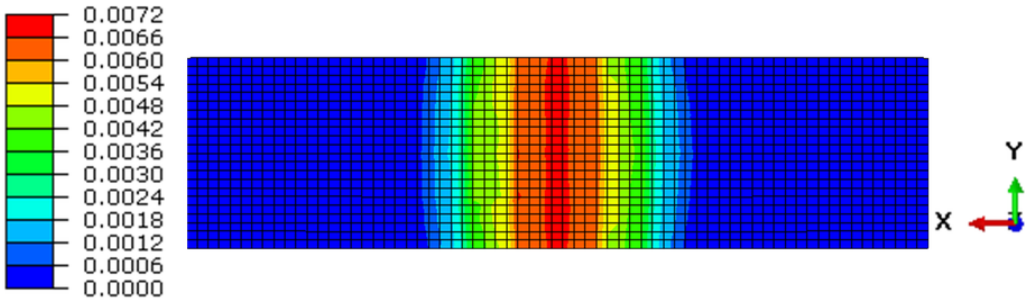
The dilation angle describes the plastic volumetric change of the material in relation with the plastic distortion. For a given shear distortion, increase of the dilation angle results in increase of the volume of the material. In S_B7



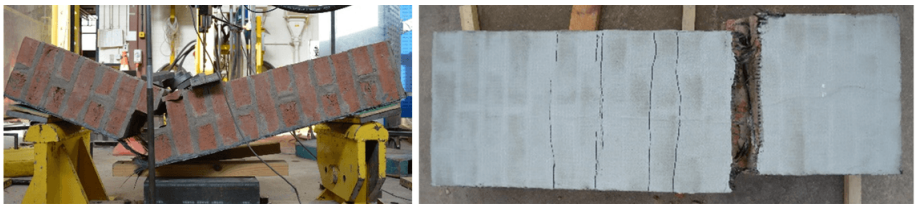
(a)



(b)

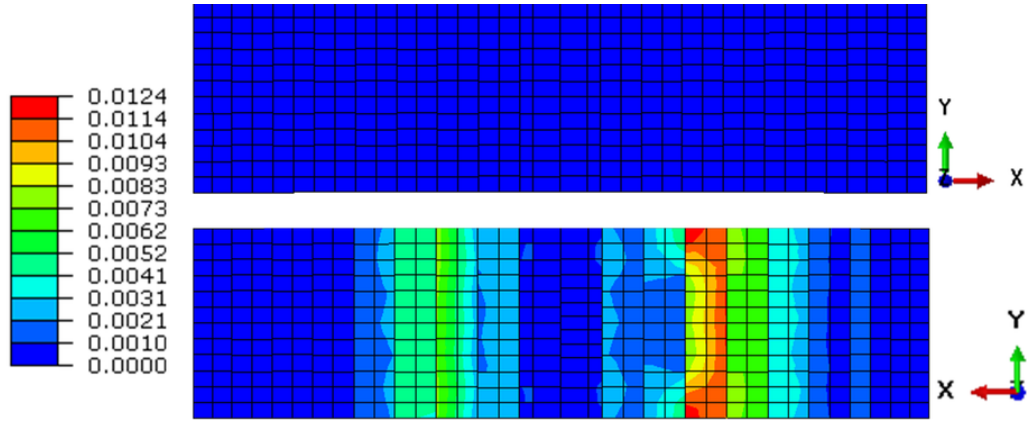


(c)

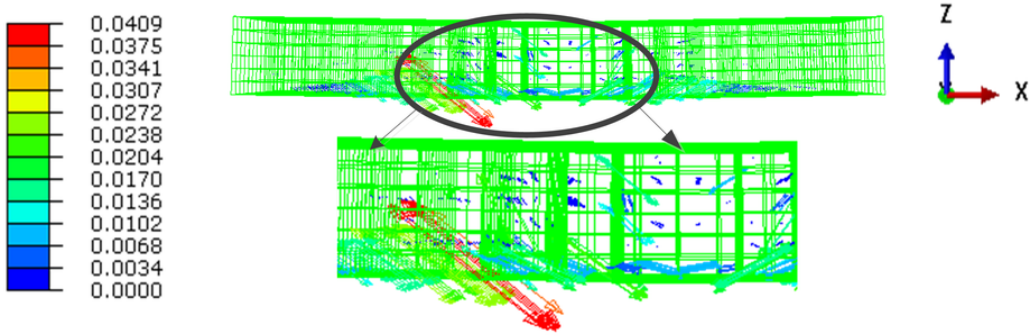


(d)

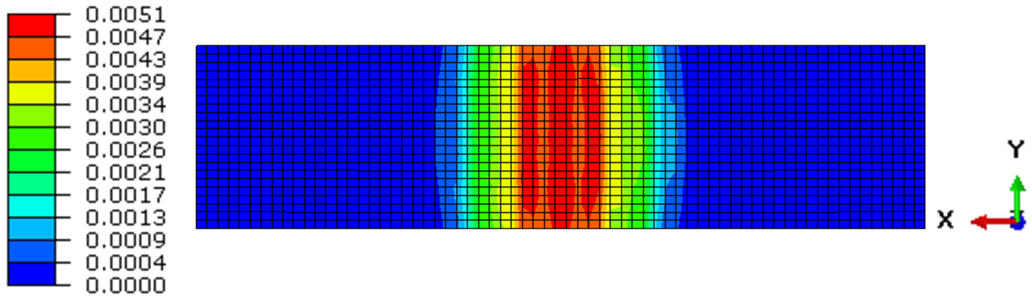
FIGURE 8.28: Strain contours of FEM_D_C1 including (a) equivalent plastic strain on the top and bottom of the wall, (b) maximum principal plastic strain and (c) longitudinal plastic strain in the x-axis, (d) Failure mode of D_C1 specimen



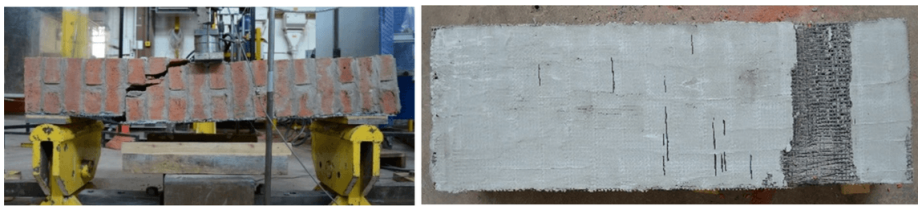
(a)



(b)

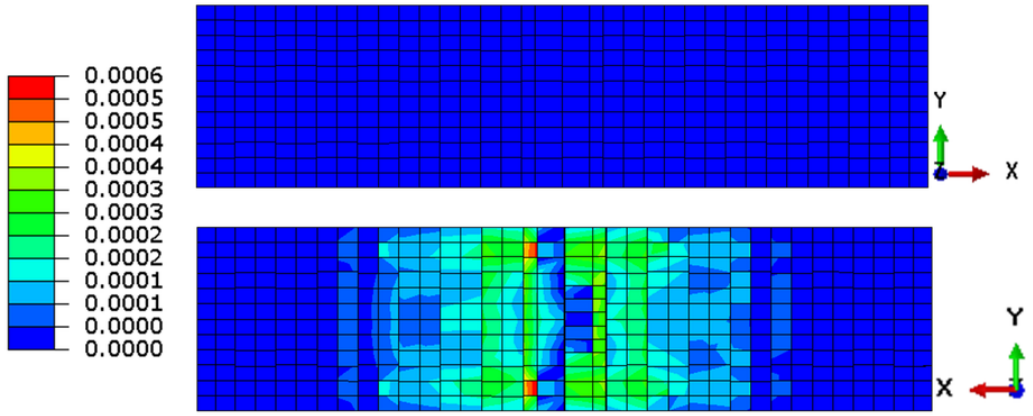


(c)

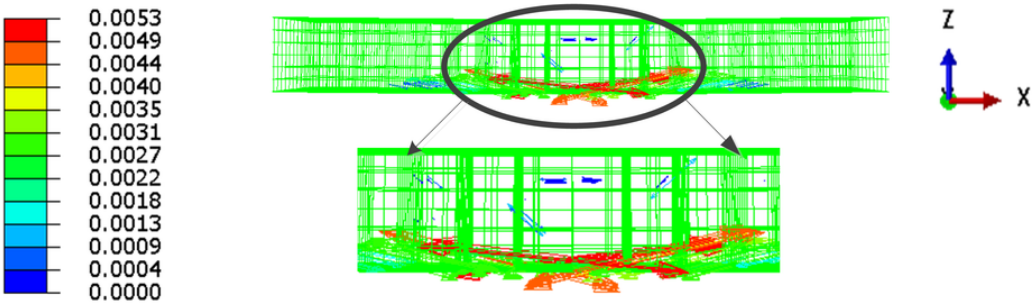


(d)

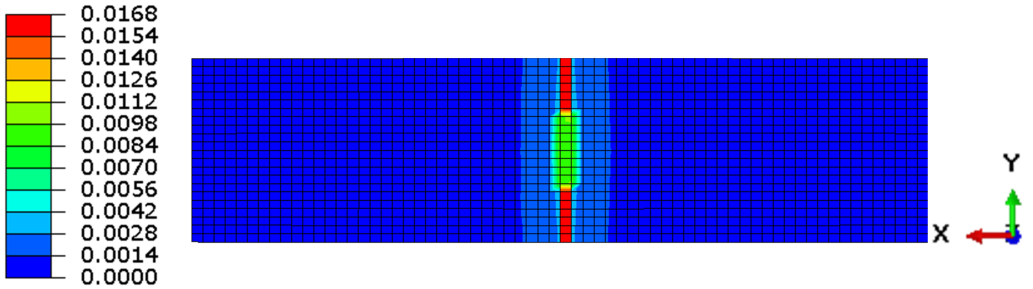
FIGURE 8.29: Strain Contours of FEM_D_C1_(Co) including (a) equivalent plastic strain on the top and bottom of the wall, (b) maximum principal plastic strain and (c) longitudinal plastic strain in the x-axis, (d) Failure mode of D_C1_(Co) specimen



(a)



(b)

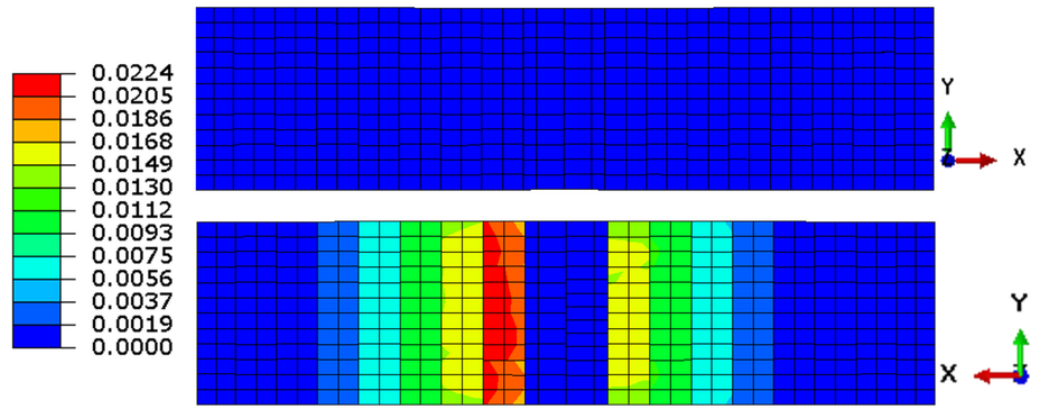


(c)

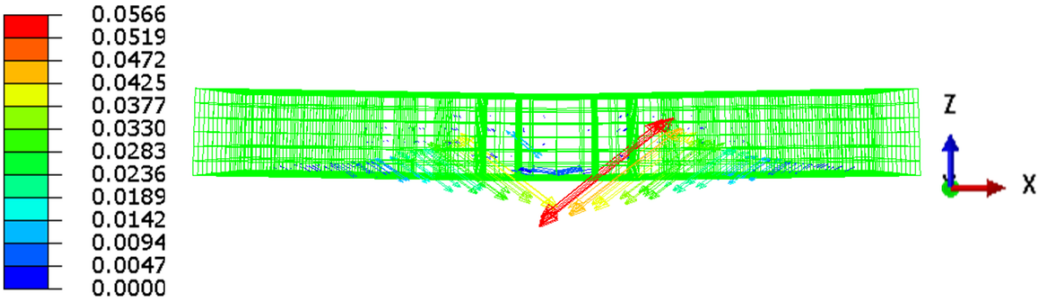


(d)

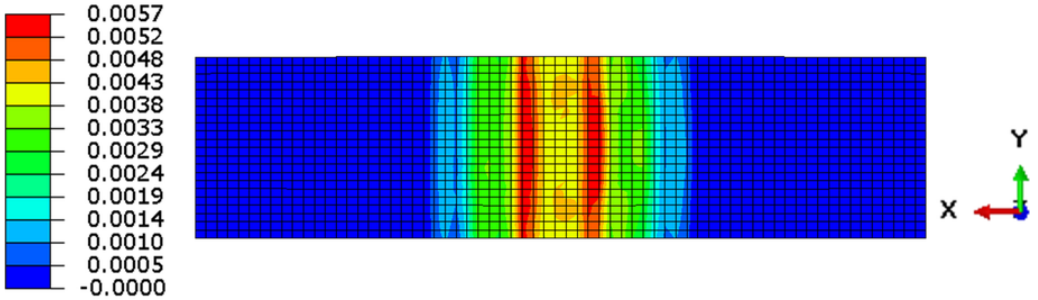
FIGURE 8.30: Strain contours of FEM_D_G3 including (a) equivalent plastic strain on the top and bottom of the wall, (b) maximum principal plastic strain and (c) longitudinal plastic strain in the x-axis, (d) Failure mode of D_G3 specimen



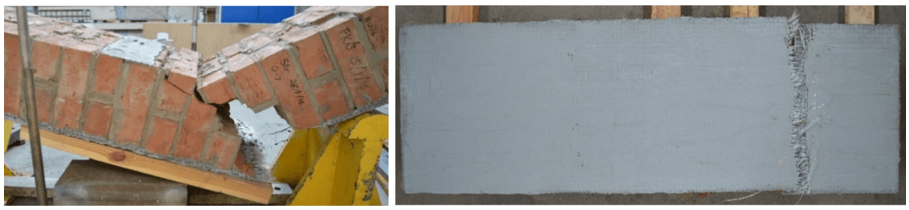
(a)



(b)

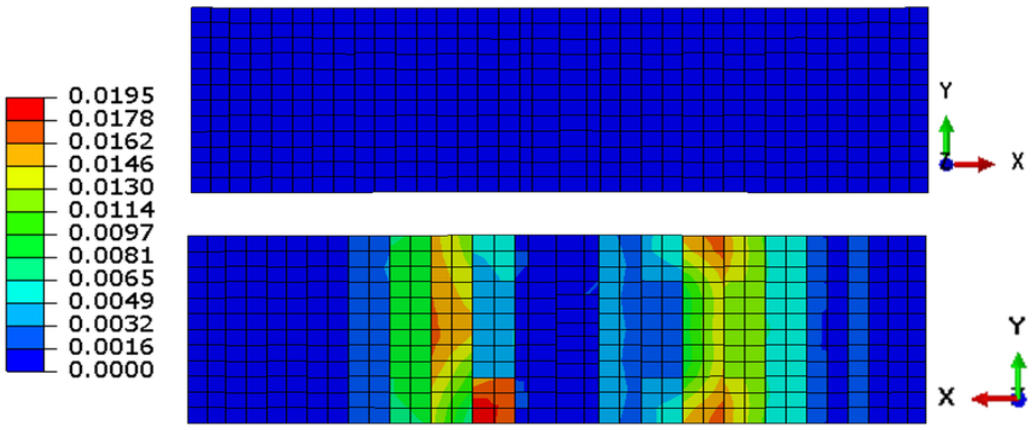


(c)

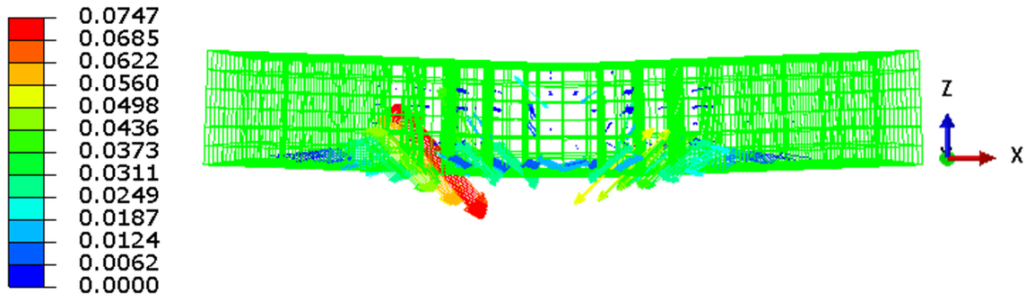


(d)

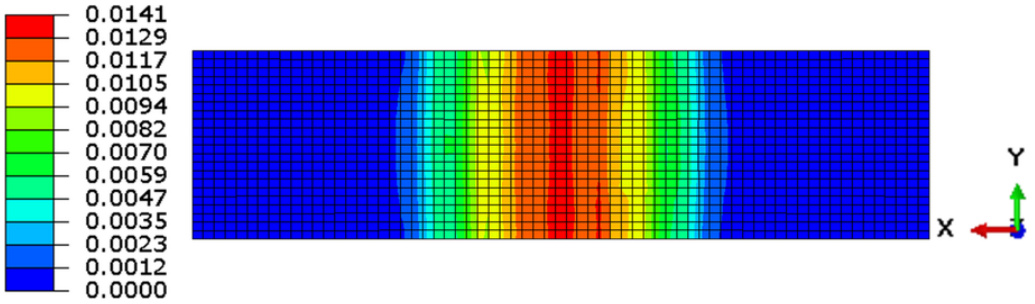
FIGURE 8.31: Strain contours of FEM_D_G7 including (a) equivalent plastic strain on the top and bottom of the wall, (b) maximum principal plastic strain and (c) longitudinal plastic strain in the x-axis, (d) Failure mode of D_G7 specimen



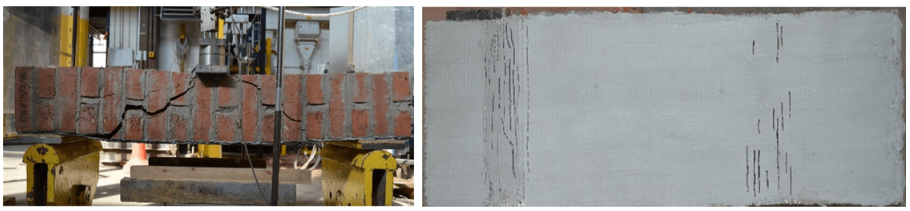
(a)



(b)

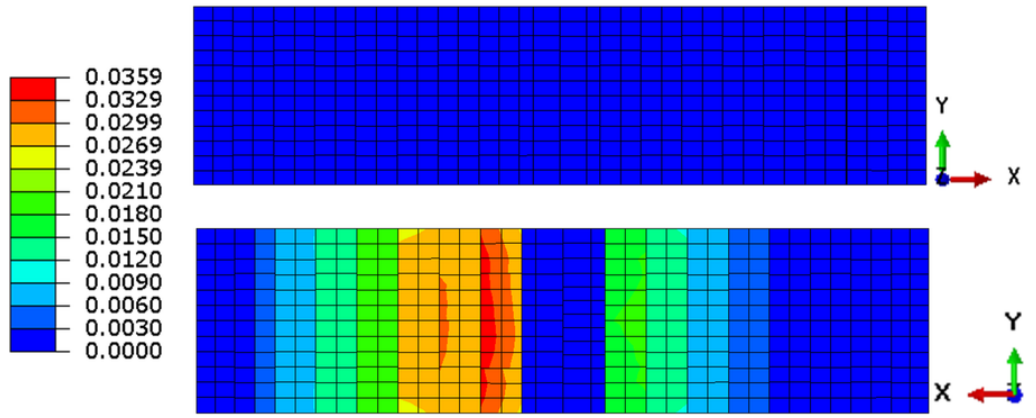


(c)

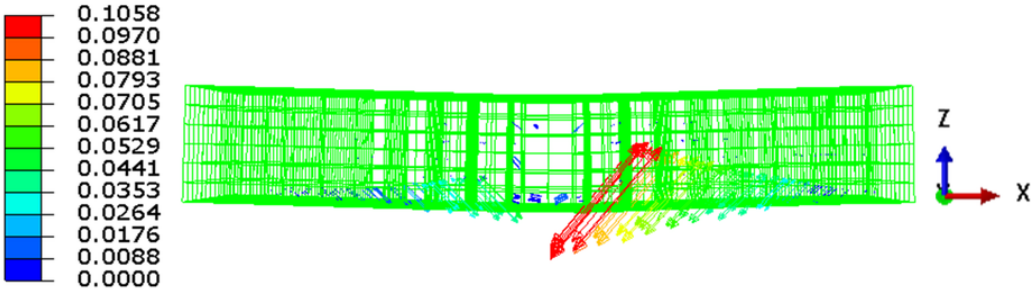


(d)

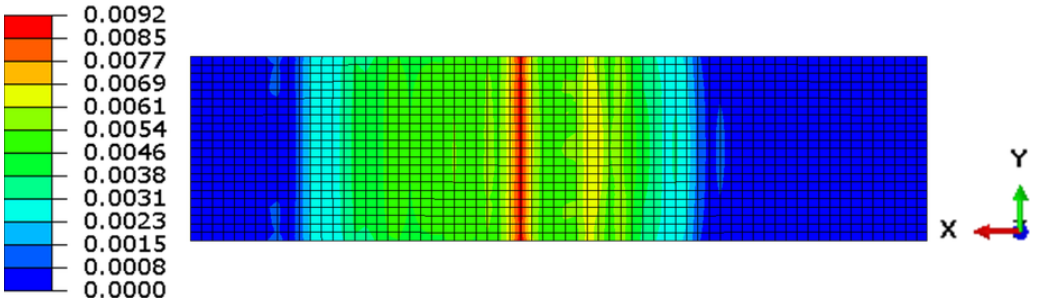
FIGURE 8.32: Strain contours of FEM_D_G3_(Co) including (a) equivalent plastic strain on the top and bottom of the wall, (b) maximum principal plastic strain and (c) longitudinal plastic strain in the x-axis, (d) Failure mode of D_G3_(Co) specimen



(a)



(b)

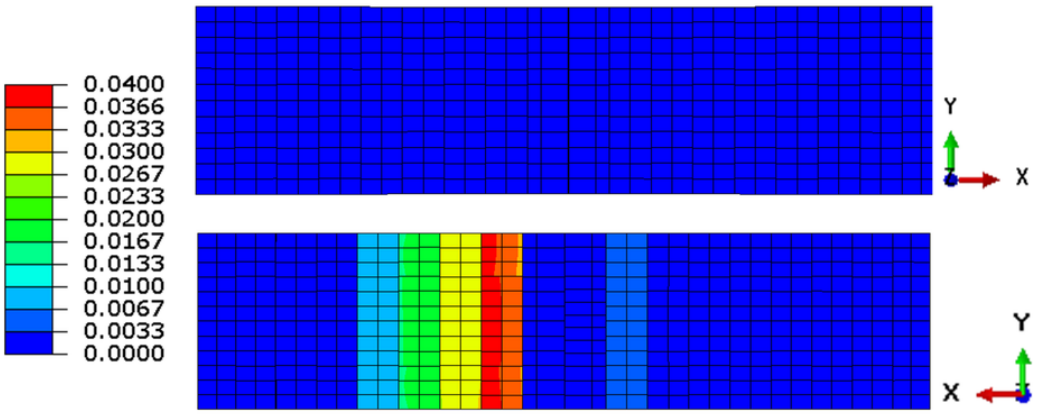


(c)

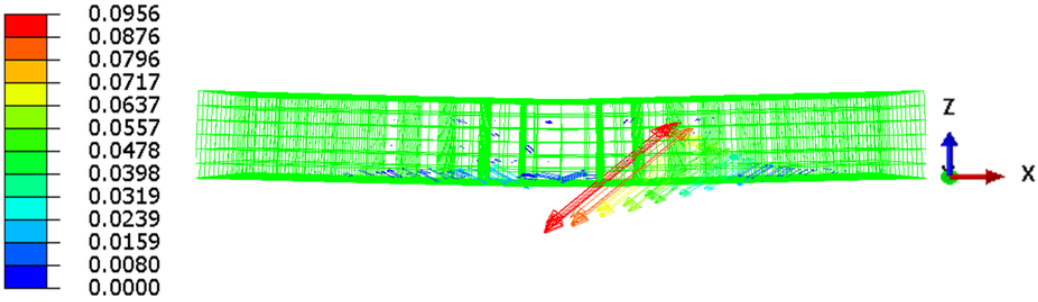


(d)

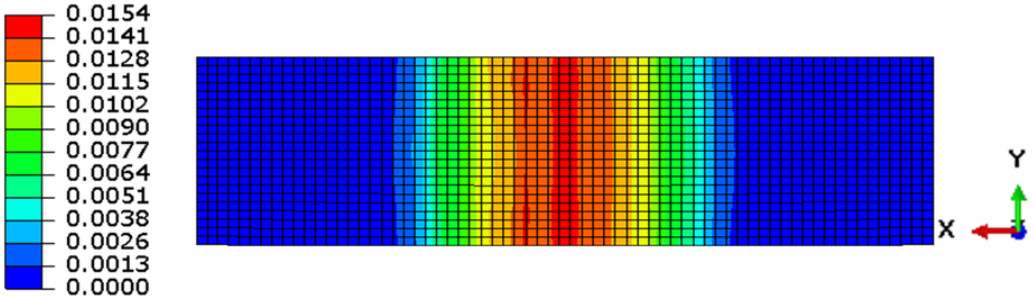
FIGURE 8.33: Strain contours of FEM15_D_G7_(Co) including (a) equivalent plastic strain on the top and bottom of the wall, (b) maximum principal plastic strain and (c) longitudinal plastic strain in the x-axis, (d) Failure mode of D_G7_(Co) specimen



(a)



(b)

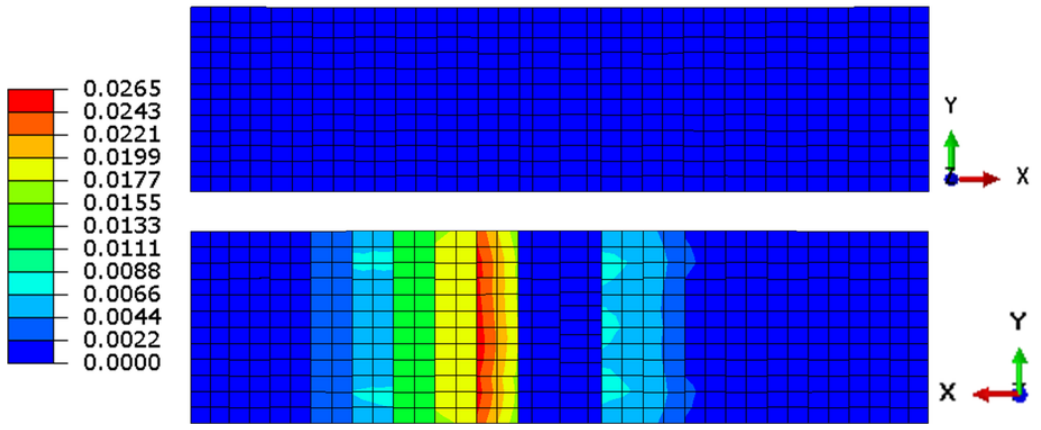


(c)

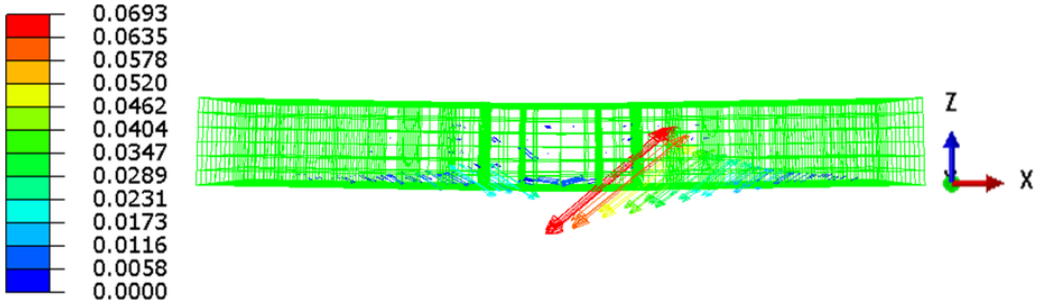


(d)

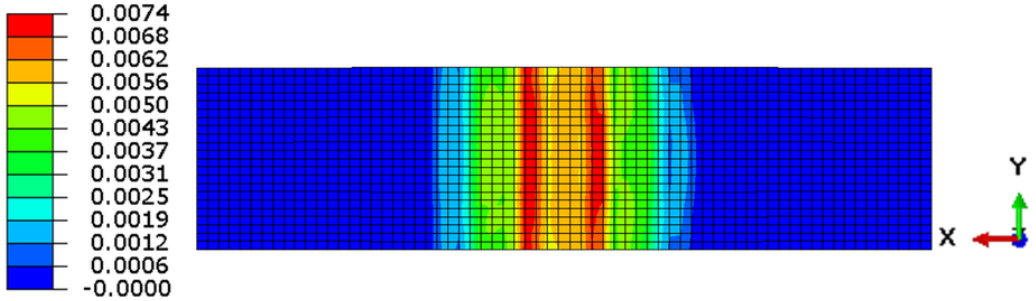
FIGURE 8.34: Strain contours of FEM_D_B3 including (a) equivalent plastic strain on the top and bottom of the wall, (b) maximum principal plastic strain and (c) longitudinal plastic strain in the x-axis, (d) Failure mode of D_B3 specimen



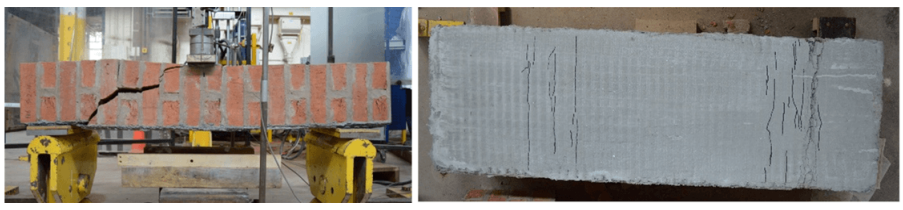
(a)



(b)



(c)



(d)

FIGURE 8.35: Strain contours of FEM_D_B7 including (a) equivalent plastic strain on the top and bottom of the wall, (b) maximum principal plastic strain and (c) longitudinal plastic strain in the x-axis, (d) Failure mode of D_B7 specimen

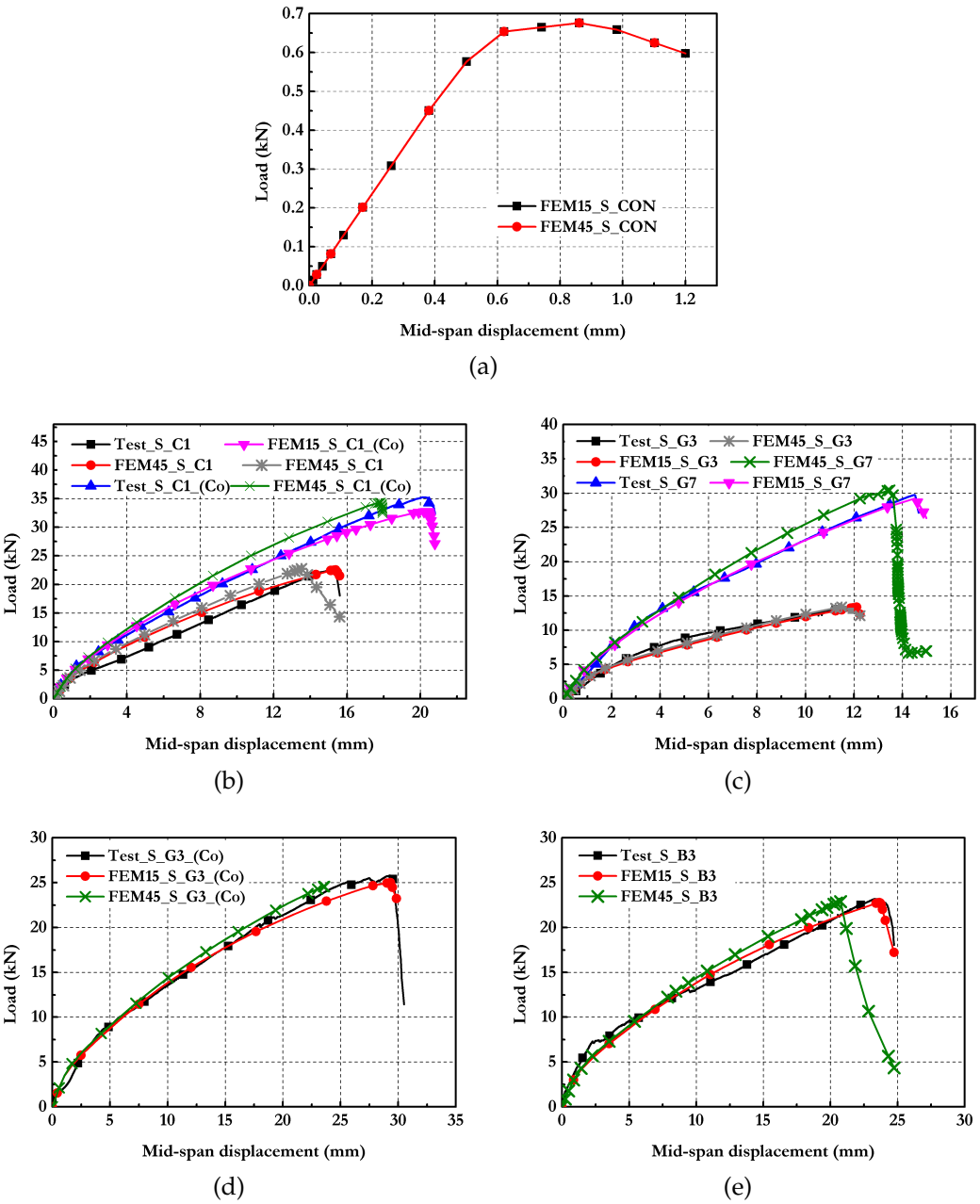


FIGURE 8.36: Load-displacement curves of single-wythe wall specimens using 15° and 45° dilation angle

and S_G7_(Co) specimens, a low value of dilation angle equal to 15° resulted in compressive damage of the brick, whereas for greater value of dilation angle equal to 45°, the brick damage in compression was prevented with a subsequent increase of the load capacity of the wall. Therefore, a greater dilation angle has a little effect on the pressure of the material, and FEM45_S_B7 and FEM45_S_G7_(Co) using 45° did not fail due to compression.

8.7.4 Effect of the textile material of the numerical models compared to experimental results

The specimens with similar textile materials, where textile rupture occurred were compared in terms of $f_{fu,out,FEM}$ and $E_{f,FEM}$ (see Table 8.7). Similar ultimate tensile stress value $f_{fu,out,FEM}$ was obtained among the corresponding single and double-wythe specimens where similar failure mode was observed namely, (S_C1/D_C1), (S_G3/D_G3) and (S_G7/D_G7). In particular, in D_C1 only 9% lower value of $f_{fu,out,FEM}$ was observed compared to S_C1. The almost identical values is an evidence that slippage of the textile occurred in D_C1 before textile rupture, as reported in Chapter 6. In D_G3 and D_G7 the $f_{fu,out,FEM}$ was increased by 24% and 17%, with respect to S_G3 and S_G7, respectively (see Table 8.7). These results show that textile rupture occurred at both pairs of numerical models.

In terms of $E_{f,FEM}$, in D_C1 40% lower value was observed compared to S_C1. In D_G3 and D_G7 the $E_{f,FEM}$ was increased by 28% and decreased by 25%, with respect to S_G3 and S_G7, respectively (see Table Table 8.7). S_G7 failed due to textile rupture, whereas in D_G7 a shear damage of the brick occurred followed by failure of the textile. Therefore, D_G7 resulted in a lower

TABLE 8.7: Textile properties of the FE models of similar failure mode

Model	$f_{fu,in}$ $_{FEM}$ [MPa]	E_f $_{FEM}$ [GPa]	$f_{fu,out}$ $_{FEM}$ [MPa]
S_C1	1270	123.50	1270
D_C1	1158	74.00	1158
S_G3	450	40.50	450
D_G3	556	52.00	556
S_G7	470	55.00	470
D_G7	550	41.00	550

value of $E_{f,FEM}$. On the other hand, in D_G3 and S_G3 failure of the textile occurred in both specimens.

8.7.5 Conclusions

- The numerically derived load vs deflection curves of the specimens failed due to textile rupture (S_C1_(Co), S_G3, S_G7, S_G3_(Co), S_B3, D_C1, D_G3, D_G7) demonstrated good agreement with respect to the experimental results, including the elastic and post-elastic stiffness up to the peak load, and the displacement at the maximum and ultimate load.

- In case that shear failure occurred in single-wythe walls (S_B7, S_G7_(Co)) or in double-wythe walls (DC1_(Co), DG3_(Co), DG7_(Co), D_B3, D_B7), a good fit was obtained among the experimental results and numerical models, including the elastic and post-elastic stiffness up to the maximum or the ultimate load; The coated TRM models (S_G7_(Co), D_C1_(Co), D_G7_(Co), D_B3, D_B7) did not capture the interlocking mechanics after shear damage of the wall occurred.

- Good agreement was observed between the simulated and experimental failure modes in all the single and double-wythe walls.

- Comparable values of ultimate tensile stress were obtained among the corresponding single and double-wythe specimens, where similar failure mode (textile rupture/ slippage) was observed, namely (S_C1/D_C1), (S_G3/D_G3) and (S_G7/ D_G7).

- In single and double-wythe walls higher distribution of plastic strains was observed in the coated TRM FE models compared to the localised plastic strains developed in the un-coated TRM models. The distribution of the plastic strains in the experiment was visualised by the transversal cracks formed at the TRM surface. S_B3 and S_G3_(Co) demonstrated similar distribution of the longitudinal plastic strains at the mid-span of the wall.

Chapter 9

Conclusions and Future Outlook

Structural strengthening increases the robustness and resilience of existing structures. It hence provides the means of preserving and extending the life span of structures that have not been designed to withstand increased environmental and operational loads, e.g., historic masonry structures. In this, work, the performance of the TRM was investigated to upgrade these structures and protect human lives. The TRM has small footprint, high stiffness, corrosion resistance, high strength-to-weight ratio, is easy to be applied and is compatible with the masonry substrate.

In this project three main experimental campaigns have been conducted to investigate the effectiveness of the TRM strengthening system. Initially, uniaxial tensile tests were conducted on the fibre-textiles used to determine their mechanical properties. Following that, bond tests were performed to investigate the bond behaviour between the TRM composite and the masonry substrate. The investigated parameters were the bond length, the textile-fibre material and the epoxy-resin coating.

Next, the out-of-plane performance of the TRM strengthened masonry walls. The objective of this study was to examine the effect of the textile fibres coating, the number of TRM layers and the type of the textile fibre material utilised.

The third experimental study investigated the effect of the TRM composite on masonry arches. The objective of this experimental campaign was to study the effect of the strengthening configuration and the amount of TRM reinforcement.

To further investigate the underlying mechanics of the TRM strengthened specimens, a finite element analysis on the strengthened masonry wall specimens was performed using the Abaqus commercial code (SIMULIA, 2016).

9.1 Conclusions on the experimental work conducted

The conclusions derived from all the experimental campaigns are summarised as follows:

- The highest ultimate tensile stress and modulus of elasticity was observed in the coated carbon fibre-textile, and the lowest mechanical properties in glass fibre textile. Coated glass and coated basalt fibre textiles performed similarly, where a slightly higher ultimate stress and strain was observed in the coated basalt fibre-textile.

- The beneficial effect of epoxy-resin coating compared to the uncoated specimens was demonstrated by (i) the uniaxial tensile tests, (ii) the bond test results between the TRM and masonry substrate and (iii) the out-of-plane tests on masonry walls.

- In the uniaxial tensile tests the coating application on the carbon and glass textile resulted in increased tensile strength and modulus of elasticity.

- In the experimental study of bond tests, coating modified the slippage between the carbon textile-fibres and mortar to the debonding failure mode

(at textile-matrix interface) in the coated carbon textile. It also modified the weak dry glass textile to a rigid textile, where rupture of the textile occurred close to the bond length area. A significant increase of the bond stress was achieved due to the epoxy-resin coating.

- In the out-of-plane tests of single and double-wythe walls the epoxy-resin coating resulted in increased maximum load capacity with respect to the uncoated counterparts. This occurred due to (i) the enhanced bonding between the textile fibre and the mortar matrix and the increased stiffness of the rovings, and (ii) the improved friction among the fibres within a roving resulting in higher tensile strength.

- The effect of coating was not pronounced in double-wythe walls when 7 TRM layers were applied (D_G7 and D_G7_(Co)), due to that shear capacity of the masonry walls controlled the corresponding failure modes.

- By increasing the TRM layers from 3 to 7, which is equal to 2.3 times, the maximum load was increased significantly in both masonry walls and masonry arches specimens.

- Using 7 layers of a coated textile fibre TRM resulted in over-reinforced masonry wall specimens, where shear failure of the wall controls their failure and not the TRM composite. Hence, the application of multiple number of layers has a similar effect to the application of coating, which improves interlocking conditions between the fibre textile and the matrix.

- Similarly, in masonry arches, the shear sliding along the mortar joints failure mode, demonstrated that after a certain amount of strengthening material, further increase of the load capacity cannot be attained, unless shearing along the mortar joints is avoided.

- The uniaxial tensile tests on bare textiles demonstrated similar performance of coated glass and coated basalt, where slightly higher values of ultimate tensile stress and ultimate strain were observed in coated basalt fibre-textile.

- The coated basalt demonstrated 20%-26% higher bond axial stress with respect to coated glass which shows its superior behaviour due to the actual roving surface of each fibre textile. Textile rupture occurred in both materials close to the bonded region of the specimens.

- In single and double-wythe masonry walls tests, coated glass and coated basalt performed similarly, in terms of maximum load. The similar performance of coated glass and coated basalt results in a strengthening configuration that can be implemented on site and is equivalent to an industrially manufactured textile composite material.

- The deformability of coated glass was significantly improved compared to coated basalt among S_G7_(Co)/S_B7 specimens. Both TRM composites have similar axial stiffness and strength, however coated glass textile fibre reinforcement seems to be providing an advantage that should be further investigated in the future.

- In masonry arches specimens, coated basalt outer-performed coated glass among B3_I/G3_I specimens in terms of load capacity. The brick masonry crushing occurred in B3_I under the point load proved beneficial as it increased the development length of the sagging zones resulting in enhanced utilisation of the TRM strengthening.

- Higher deformation capacity was observed in coated basalt masonry arches compared to their coated glass counterparts. The coarser basalt mesh

size allowed larger slippage within the mortar. This is also in agreement with the coupon test results, where higher ultimate strain was observed in coated basalt, with respect to the coated glass fibre textile.

- The coated glass extrados strengthening configuration of masonry arches outerperformed the corresponding intrados strengthened specimens. The strengthening at the extrados resulted in larger development length of the TRM which improved the bonding conditions and led to a better utilisation of the composite stiffness and strength.

- Specimens strengthened at the extrados with basalt textile fibre material resulted in identical maximum load capacity, with respect to the corresponding intrados specimens. Given that the coated glass and basalt material parameters are similar, the large mesh size of coated basalt fibre-textile is indicative of reduced bonding conditions.

- A significantly higher deformation capacity was observed at all the extrados strengthened specimens with respect to the corresponding intrados specimens as manifested by the DIR values. The well-developed sagging lengths when the failure mechanism was developed, allowed larger TRM length to be activated.

- The effective bond length of carbon, coated glass and coated basalt was greater than or equal to 200 mm, and for coated carbon was between 150 mm-200 mm. Only the glass fibre textile demonstrated similar values among the different bond lengths, which shows that with this experimental setup an effective bond length could not be derived.

- The (P_{max}) to (P_{con}) ratio indicated that the TRM effectiveness was more pronounced in single-wythe walls with respect to the stiffer double-wythe

walls, due to that maximum load of the double-wythe strengthened specimens was bounded by the shear capacity of the wall.

9.2 Conclusions on the finite element analysis results

The conclusions derived between the experimental work and the numerical analysis on masonry walls are summarised as follows:

- Good agreement was observed between the simulated and experimental failure modes in all the single and double-wythe walls.
- The numerically derived load vs deflection curves of the single and double-wythe specimens failed due to textile rupture or shear failure demonstrated good agreement with respect to the experimental results, including the elastic and post-elastic stiffness up to the peak load, and the displacement at the maximum and ultimate load.
- In case that shear failure occurred in single- and double-wythe strengthened walls, the coated TRM FE models (S_G7_(Co), D_C1_(Co), D_G7_(Co), D_B7) did not capture the interlocking mechanics after shear damage of the wall occurred.
- In specimens where similar failure mode was observed among the corresponding single and double-wythe specimens namely (S_C1/ D_C1), (S_G3/ D_G3) and (S_G7/ D_G7), similar ultimate tensile stress was developed among the specimens.

- The coated TRM models demonstrated a high distribution of plastic strains, which is in agreement with the experimental transversal cracks developed at the TRM surface of the specimens. A similar distribution of plastic strains was observed between coated glass and coated basalt, which shows the similar ductility among the two materials.

9.3 Future work

The TRM strengthening on masonry walls improved significantly their response in the out-of-plane loading, in terms of both load and deformation capacity. Similarly, the load and deformation capacity of unreinforced masonry arches increased substantially after the TRM strengthening application. Future research can be focused in the following aspects:

- The in-house epoxy-resin coating applied in both experimental campaigns of masonry walls and arches has been shown to increase significantly the effectiveness of the TRM. Therefore further research can be done to investigate the TRM effectiveness using different amount and different types of coating.

- Additional bond tests can be performed using a double-lap test setup with double-wall prisms to include multiple layers of TRM and compare the results against the current experimental study.

- The TRM performance can be investigated using different types of mortar, including fire-resistance high-strength mortars to improve the effectiveness of the TRM at high temperature or fire.

- A further investigation on the TRM mortar can be performed using cement-based mortars of different mechanical properties, cement-free natural hydraulic lime mortars and earthen mortars. Alternative of the cement constituent can be proposed as reversible, suitable with physical and chemical compatibility of the masonry substrate with the aim to preserve the cultural heritage of masonry structures.

- The influence of different TRM mortars (cement, lime, earthen) can also highlight which mortar is more compatible with each different fibre-textile utilised in this project.

- The numerical models developed to capture the behaviour of strengthened masonry walls with the TRM composite resulted in good agreement with the experimental results. Thus, similar modelling approach can be applied in masonry arches specimens to verify the experimental results but also investigate further parameters such as different loading conditions (e.g. fatigue loading) and strengthening configurations including different amount of strengthening material (e.g., 7 layers of TRM basalt at the intrados) which was not feasible to apply during the experimental work of this study. Different fibre-textile materials can also be investigated, by conducting tests on the materials utilised, which can reduce the time and cost of an entire experimental campaign.

- Future research can develop an analytical approach on the TRM strengthened masonry arch. A further research can be performed to introduce the distribution of axial, shear and flexural stresses along the arch.

- Design guidelines should be established considering the experimental and numerical analysis results obtained and the investigated parameters of this project.

Bibliography

Abaqus manual, Abaqus User (2014). "Abaqus Theory Guide Version 6.14". In: *USA: Dassault Systemes Simulia Corp*.

Abrams, DP and JM Lynch (2001). "Flexural behavior of retrofitted masonry piers". In: *KEERC-MAE joint seminar on risk mitigation for regions of moderate seismicity*, pp. 234–243.

Agnihotri, Pawan, Vaibhav Singhal, and Durgesh C Rai (2013). "Effect of in-plane damage on out-of-plane strength of unreinforced masonry walls". In: *Engineering Structures* 57, pp. 1–11.

Al-Salloum, Yousef A et al. (2011). "Experimental and numerical study for the shear strengthening of reinforced concrete beams using textile-reinforced mortar". In: *Journal of Composites for Construction* 16.1, pp. 74–90.

Albert, Michael L, Alaa E Elwi, and JJ Roger Cheng (2001). "Strengthening of unreinforced masonry walls using FRPs". In: *Journal of Composites for Construction* 5.2, pp. 76–84.

Alecci, Valerio et al. (2015). "Experimental investigation on bond behavior of cement-matrix based composites for strengthening of masonry structures". In: *Journal of Composites for Construction* 20.1, p. 04015041.

Alecci, Valerio et al. (2016). "Extrados strengthening of brick masonry arches with PBO–FRCM composites: Experimental and analytical investigations". In: *Composite Structures* 149, pp. 184–196.

Alecci, Valerio et al. (2017a). "Intrados strengthening of brick masonry arches with different FRCM composites: experimental and analytical investigations". In: *Composite Structures* 176, pp. 898–909.

Alecci, Valerio et al. (2017b). "Strengthening masonry arches with lime-based mortar composite". In: *Buildings* 7.2, p. 49.

Alejano, Leandro R and Antonio Bobet (2012). "Drucker–Prager Criterion". In: *The ISRM Suggested Methods for Rock Characterization, Testing and Monitoring: 2007-2014*. Springer, pp. 247–252.

Almeida, João APP, Eduardo B Pereira, and Joaquim AO Barros (2015). "Assessment of overlay masonry strengthening system under in-plane monotonic and cyclic loading using the diagonal tensile test". In: *Construction and Building Materials* 94, pp. 851–865.

Apreutesei, Vlad A, Daniel V Oliveira, and Paulo B Lourenco (2006). "Repair and strengthening techniques for masonry arch bridges". In: *INTERSECTII/INTERSECTIONS* 3.1.

Ascione, Luigi, Gianmarco de Felice, and Stefano De Santis (2015). "A qualification method for externally bonded Fibre Reinforced Cementitious Matrix (FRCM) strengthening systems". In: *Composites Part B: Engineering* 78, pp. 497–506.

Askouni, Paraskevi D and Catherine Corina G Papanicolaou (2019). "Textile Reinforced Mortar to masonry bond: Experimental investigation of bond critical parameters". In: *Construction and Building Materials* 207, pp. 535–547.

Askouni, Paraskevi D and Catherine G Papanicolaou (2017). "Experimental investigation of bond between glass textile reinforced mortar overlays and masonry: the effect of bond length". In: *Materials and Structures* 50.2, p. 164.

Augenti, N et al. (2010). "In-plane lateral response of a full-scale masonry subassemblage with and without an inorganic matrix-grid strengthening system". In: *Journal of Composites for Construction* 15.4, pp. 578–590.

Babaeidarabad, Saman, Francisco De Caso, and Antonio Nanni (2013). "Out of plane behavior of URM walls strengthened with fabric reinforced cementitious matrix composite". In: *Journal of Composites for Construction* 18.4, p. 04013057.

Bati, Silvia Briccoli and Luisa Rovero (2008). "Towards a methodology for estimating strength and collapse mechanism in masonry arches strengthened with fibre reinforced polymer applied on external surfaces". In: *Materials and Structures* 41.7, pp. 1291–1306.

Bernat, Ernest et al. (2013). "Experimental and analytical study of TRM strengthened brickwork walls under eccentric compressive loading". In: *Construction and Building Materials* 44, pp. 35–47.

Berto, Luisa et al. (2002). "An orthotropic damage model for masonry structures". In: *International Journal for Numerical Methods in Engineering* 55.2, pp. 127–157.

— (2004). "Shear behaviour of masonry panel: parametric FE analyses". In: *International journal of solids and structures* 41.16-17, pp. 4383–4405.

Beuerman, Thomas E (2009). "Inventory of repairing and strengtheing techniques for masonry arch bridges". MA thesis. Universitat Politecnica de Catalunya.

Bolhassani, Mohammad et al. (2015). "Simplified micro modeling of partially grouted masonry assemblages". In: *Construction and Building Materials* 83, pp. 159–173.

Borri, Antonio et al. (2009). "Strengthening of brick masonry arches with externally bonded steel reinforced composites". In: *Journal of composites for construction* 13.6, pp. 468–475.

Borri, Antonio, Giulio Castori, and Marco Corradi (2011). "Intrados strengthening of brick masonry arches with composite materials". In: *Composites Part B: Engineering* 42.5, pp. 1164–1172.

Bournas, Dionysios A et al. (2007). "Textile-reinforced mortar (TRM) versus FRP confinement in reinforced concrete columns". In: *ACI Structural Journal* 104.6, pp. 740–748.

Brookes, Carl L and Graham P Tilly (1999). "Novel method of strengthening masonry arch bridges". In: *Proc. 8th Structural faults and repairs–July*, pp. 13–15.

BS EN, 772-1 (2011). "Methods of tests for masonry units-Part 1: Determination of compressive strength". In: *British Standards Institution, London*.

Caggegi, Carmelo et al. (2017). "Experimental analysis on tensile and bond properties of PBO and aramid fabric reinforced cementitious matrix for strengthening masonry structures". In: *Composites Part B: Engineering* 127, pp. 175–195.

Calvi, G Michele and Guido Magenes (1994). "Experimental results on unreinforced masonry shear walls damaged and repaired". In: *Proceedings of the 10th International brick masonry conference*. Vol. 2, pp. 509–518.

Cancelli, AN, MA Aiello, and P Casadei (2007). "Experimental investigation on bond properties of SRP/SRG masonry systems". In: *Proceedings of the 8th international symposium on fiber reinforced polymer reinforcement for concrete structures FRPRCS 8, Patras, Greece*.

Cancelliere, Ilaria, Maura Imbimbo, and Elio Sacco (2010). "Experimental tests and numerical modeling of reinforced masonry arches". In: *Engineering Structures* 32.3, pp. 776–792.

Carloni, Christian et al. (2016). "Fiber reinforced composites with cementitious (inorganic) matrix". In: *Design Procedures for the Use of Composites in Strengthening of Reinforced Concrete Structures*. Springer, pp. 349–392.

Carozzi, Francesca Giulia and Carlo Poggi (2015). "Mechanical properties and debonding strength of Fabric Reinforced Cementitious Matrix (FRCM) systems for masonry strengthening". In: *Composites Part B: Engineering* 70, pp. 215–230.

Carozzi, Francesca Giulia, Gabriele Milani, and Carlo Poggi (2014). "Mechanical properties and numerical modeling of Fabric Reinforced Cementitious Matrix (FRCM) systems for strengthening of masonry structures". In: *Composite Structures* 107, pp. 711–725.

Carozzi, Francesca Giulia et al. (2017a). "Ancient masonry arches and vaults strengthened with TRM, SRG and FRP composites: Experimental evaluation". In: *Composite Structures*.

Carozzi, Francesca Giulia et al. (2017b). "Experimental investigation of tensile and bond properties of Carbon-FRCM composites for strengthening masonry elements". In: *Composites Part B: Engineering* 128, pp. 100–119.

Casadei, Paolo et al. (2005). "Performance of double-T prestressed concrete beams strengthened with steel reinforcement polymer". In: *Advances in Structural Engineering* 8.4, pp. 427–442.

Casolo, Siro and Gabriele Milani (2010). "A simplified homogenization-discrete element model for the non-linear static analysis of masonry walls out-of-plane loaded". In: *Engineering Structures* 32.8, pp. 2352–2366.

Cevallos, OA et al. (2015). "Flax and polyparaphenylene benzobisoxazole cementitious composites for the strengthening of masonry elements subjected to eccentric loading". In: *Composites Part B: Engineering* 71, pp. 82–95.

Chaimoon, Krit and Mario M Attard (2007). "Modeling of unreinforced masonry walls under shear and compression". In: *Engineering structures* 29.9, pp. 2056–2068.

Chuxian, Shi and Zhou Haibing (1997). "Research on Seismic Behavior of Reinforced Masonry Shear Walls [J]". In: *Journal of Building Structures* 6, p. 004.

CNR-DT200, CNR (2006). "Guide for the Design and Construction of externally bonded FRP Systems for Strengthening Existing Structures, Materials, RC and PC structures, Masonry Structures". In: *National Research Council, Rome-CNR, Roma, Italy*.

Coburn, Andrew W, Robin JS Spence, and Antonios Pomonis (1992). "Factors determining human casualty levels in earthquakes: mortality prediction in building collapse". In: *Proceedings of the First International Forum on Earthquake related Casualties. Madrid, Spain, July 1992*.

Corradi, Marco, Antonio Borri, and Andrea Vignoli (2008). "Experimental evaluation of in-plane shear behaviour of masonry walls retrofitted using conventional and innovative methods". In: *Masonry International* 21.1, p. 29.

Correia, João R (2008). "GFRP pultruded profiles in civil engineering: hybrid solutions, bonded connections and fire behaviour". In: *Lisboa: Tese de Doutoramento em Engenharia Civil, Instituto Superior Técnico-Universidade Técnica de Lisboa*.

Dambra, Claudio et al. (2018). "Experimental performance of FRCM retrofit on out of plane behaviour of clay brick walls". In: *Composites Part B Engineering* 148, pp. 198–206.

DAmbrisi, Angelo, Luciano Feo, and Francesco Focacci (2013). "Experimental and analytical investigation on bond between Carbon FRCM materials and masonry". In: *Composites Part B: Engineering* 46, pp. 15–20.

DAntino, Tommaso et al. (2015). "Experimental analysis of the bond behavior of glass, carbon, and steel FRCM composites". In: *Key engineering materials*. Vol. 624. Trans Tech Publ, pp. 371–378.

DAntino, Tommaso et al. (2016). "Effect of the inherent eccentricity in single lap direct shear tests of PBO FRCM concrete joints". In: *Composite Structures* 142, pp. 117–129.

De Felice, Gianmarco et al. (2014). "Mortar-based systems for externally bonded strengthening of masonry". In: *Materials and structures* 47.12, pp. 2021–2037.

De Felice, Gianmarco et al. (2018). "Recommendation of RILEM Technical Committee 250-CSM: Test method for Textile Reinforced Mortar to substrate bond characterization". In: *Materials and Structures* 51.4, p. 95.

De Santis, Stefano and Gianmarco de Felice (2015). "Steel reinforced grout systems for the strengthening of masonry structures". In: *Composite Structures* 134, pp. 533–548.

De Santis, Stefano et al. (2017). "Test methods for textile reinforced mortar systems". In: *Composites Part B: Engineering* 127, pp. 121–132.

De Santis, Stefano et al. (2018a). "Acceptance Criteria for Tensile Characterization of Fabric-Reinforced Cementitious Matrix Systems for Concrete and Masonry Repair". In: *Journal of Composites for Construction* 22.6, p. 04018048.

De Santis, Stefano, Francesca Roscini, and Gianmarco De Felice (2018b). "Full scale tests on masonry vaults strengthened with Steel Reinforced Grout". In: *Composites Part B: Engineering* 141, pp. 20–36.

De Santis, Stefano, Gianmarco de Felice, and Francesca Roscini (2019). "Retrofitting of Masonry Vaults by Basalt Textile-Reinforced Mortar Overlays". In: *International Journal of Architectural Heritage*, pp. 1–18.

Dhanasekar, M, AW Page, and PW Kleeman (1985). "The failure of brick masonry under biaxial stresses." In: *Proceedings of the Institution of Civil Engineers* 79.2, pp. 295–313.

Dizhur, Dmytro et al. (2011). "Performance of masonry buildings and churches in the 22 February 2011 Christchurch earthquake". In: *Bulletin of the New Zealand Society for Earthquake Engineering* 44.4, pp. 279–296.

Donnini, Jacopo, Valeria Corinaldesi, and Antonio Nanni (2016). "Mechanical properties of FRCM using carbon fabrics with different coating treatments". In: *Composites Part B: Engineering* 88, pp. 220–228.

Drucker, Daniel Charles and William Prager (1952). "Soil mechanics and plastic analysis or limit design". In: *Quarterly of applied mathematics* 10.2, pp. 157–165.

EEFIT (2009). "The L'Aquila, Italy Earthquake of 6 of April 2009-A prelimintary field report by EEFIT". In: *The Institution of Structural Engineers*.

Ehsani, MR et al. (1993). "Flexural behavior of masonry walls strengthened with composite fabrics". In: *Special Publication* 138, pp. 497–508.

Ehsani, MR, H Saadatmanesh, and JI Velazquez-Dimas (1999). "Behavior of retrofitted URM walls under simulated earthquake loading". In: *Journal of Composites for Construction* 3.3, pp. 134–142.

ElGawady, M, P Lestuzzi, and M Badoux (2004). "A review of conventional seismic retrofitting techniques for URM". In: *13th international brick and block masonry conference*, pp. 1–10.

EN, 1015-11 (1993). "Methods of test for mortar for masonry-Part 11: Determination of flexural and compressive strength of hardened mortar". In: *European Committee for Standardization, Brussels*.

EN, 1052-11 (1998a). "Methods of test for masonry-Part 1: Determination of compressive strength". In: *European Committee for Standardization, Brussels*.

EN, BS (1996). "Eurocode 6-Design of masonry structures-Part 1-1: General rules for reinforced and unreinforced masonry structures". In: *British Standards Institution, London*.

EN, CEN (1998b). "1.(2004) EuroCode 8: design of structures for earthquake resistance: Part 1: general rules, seismic actions and rules for buildings". In: *European Committee for Standardization, Brussels*.

Faella, C et al. (2009). "Composite materials for masonry structures: the adhesion issue". In: *Proceedings of the 3rd conference on mechanics of masonry structures strengthened with composite materials: modeling, testing, design, control-MuRiCo3, Venice (Italy)*, pp. 266–273.

Faella, Ciro et al. (2004). "Tuff masonry walls strengthened with a new kind of C-FRP sheet: experimental tests and analysis". In: *Proceedings of the 13th world conference on earthquake engineering, Paper*. 923.

Fedele, Roberto and Gabriele Milani (2010). "A numerical insight into the response of masonry reinforced by FRP strips. The case of perfect adhesion". In: *Composite structures* 92.10, pp. 2345–2357.

Fib Bulletin, TG (2001). *Externally bonded FRP reinforcement for RC structures*.

Firmo, Joao P, Joao R Correia, and Luke A Bisby (2015). "Fire behaviour of FRP-strengthened reinforced concrete structural elements: a state-of-the-art review". In: *Composites Part B: Engineering* 80, pp. 198–216.

Foraboschi, Paolo (2004). "Strengthening of masonry arches with fiber-reinforced polymer strips". In: *Journal of composites for construction* 8.3, pp. 191–202.

Fuggini, Clemente, E Chatzi, and Donato Zangani (2013). "Combining Genetic Algorithms with a Meso-Scale Approach for System Identification of a Smart

Polymeric Textile". In: *Computer-Aided Civil and Infrastructure Engineering* 28.3, pp. 227–245.

Galati, Nestore, Gustavo Tumialan, and Antonio Nanni (2006). "Strengthening with FRP bars of URM walls subject to out-of-plane loads". In: *Construction and Building Materials* 20.1-2, pp. 101–110.

Galvis, Francisco et al. (2017). "Preliminary Statistics of Collapsed Buildings in Mexico City in the September 19, 2017 Puebla-Morelos Earthquake". In: *John A. Blume Earthq. Engrg. Ctr., Stanford University*.

Garmendia, L et al. (2011). "Rehabilitation of masonry arches with compatible advanced composite material". In: *Construction and Building Materials* 25.12, pp. 4374–4385.

Garmendia, Leire et al. (2015). "Strengthening masonry vaults with organic and inorganic composites: an experimental approach". In: *Materials and Design* 85, pp. 102–114.

Garrity, Stephen W (2001). "Near-surface reinforcement of masonry arch highway bridges". In: *Proceedings of the 9th Canadian masonry symposium*.

Gattesco, Natalino and Ingrid Boem (2017). "Out-of-plane behavior of reinforced masonry walls: Experimental and numerical study". In: *Composites Part B: Engineering* 128, pp. 39–52.

Gattesco, Natalino et al. (2017). "Experimental behavior of masonry vaults strengthened with thin extradoxal or intradoxal layer of fiber reinforced lime mortar". In: *Key Engineering Materials*. Vol. 747. Trans Tech Publ, pp. 274–281.

Genikomsou, Aikaterini S and Maria Anna Polak (2015). "Finite element analysis of punching shear of concrete slabs using damaged plasticity model in ABAQUS". In: *Engineering Structures* 98, pp. 38–48.

Ghiassi, Bahman et al. (2013). "Numerical study of the role of mortar joints in the bond behavior of FRP-strengthened masonry". In: *Composites Part B: Engineering* 46, pp. 21–30.

Giaretton, Marta et al. (2016). "Seismic assessment and improvement of unreinforced stone masonry buildings: literature review and application to New Zealand". In: *Bulletin of the New Zealand Society for Earthquake Engineering* 49, pp. 148–174.

Hamed, Ehab and Oded Rabinovitch (2010). "Lateral out-of-plane strengthening of masonry walls with composite materials". In: *Journal of Composites for Construction* 14.4, pp. 376–387.

Hamoush, Sameer A et al. (2001). "Out-of-plane strengthening of masonry walls with reinforced composites". In: *Journal of Composites for Construction* 5.3, pp. 139–145.

Hansen, Bent (1958). "Line ruptures regarded as narrow rupture zones basic equations based on kinematic considerations". In: *Proc., Conf. on Earth Pressure Problems*. Vol. 1, pp. 39–48.

Harajli, M, H ElKhatib, and J Tomas San-Jose (2010). "Static and cyclic out-of-plane response of masonry walls strengthened using textile-mortar system". In: *Journal of materials in civil engineering* 22.11, pp. 1171–1180.

Heritage, Maintain our (2004). "Putting it off: how lack of maintenance fails our heritage: a report on the research programme on the maintenance of historic buildings led by Maintain our Heritage". In:

Hillerborg, Arne, Mats Modéer, and P-E Petersson (1976). "Analysis of crack formation and crack growth in concrete by means of fracture mechanics and finite elements". In: *Cement and concrete research* 6.6, pp. 773–781.

Huang, X et al. (2005). "Properties and potential for application of steel reinforced polymer and steel reinforced grout composites". In: *Composites Part B: Engineering* 36.1, pp. 73–82.

Indirli, Maurizio et al. (2013). "Seismic damage assessment of unreinforced masonry structures after the abruzzo 2009 earthquake: The case study of the historical centers of L'Aquila and Castelvecchio Subequo". In: *International Journal of Architectural Heritage* 7.5, pp. 536–578.

Kahn, L (1984). "Shotcrete retrofit for unreinforced brick masonry". In: *8th WCEE*. Vol. 583, p. 590.

Kalali, A and MZ Kabir (2012). "Cyclic behavior of perforated masonry walls strengthened with glass fiber reinforced polymers". In: *Scientia Iranica* 19.2, pp. 151–165.

Karantoni, Fillitsa V and Michael N Fardis (1992). "Effectiveness of seismic strengthening techniques for masonry buildings". In: *Journal of Structural Engineering* 118.7, pp. 1884–1902.

Kaushik, Hemant B, Durgesh C Rai, and Sudhir K Jain (2007). "Stress-strain characteristics of clay brick masonry under uniaxial compression". In: *Journal of materials in Civil Engineering* 19.9, pp. 728–739.

Kolsch, Holger (1998). "Carbon fiber cement matrix (CFCM) overlay system for masonry strengthening". In: *Journal of Composites for Construction* 2.2, pp. 105–109.

Koutas, L, TC Triantafillou, and SN Bousias (2014). "Analytical modeling of masonry-infilled RC frames retrofitted with textile-reinforced mortar". In: *Journal of Composites for Construction* 19.5, p. 04014082.

Kuzik, Marc D, Alaa E Elwi, and JJ Roger Cheng (2003). "Cyclic flexure tests of masonry walls reinforced with glass fiber reinforced polymer sheets". In: *Journal of Composites for Construction* 7.1, pp. 20–30.

La Mendola, Lidia et al. (2014). "Nonlinear FE analysis of out-of-plane behaviour of masonry walls with and without CFRP reinforcement". In: *Construction and Building Materials* 54, pp. 190–196.

Lee, Jeeho and Gregory L Fenves (1998). "Plastic-damage model for cyclic loading of concrete structures". In: *Journal of engineering mechanics* 124.8, pp. 892–900.

Leone, Marianovella et al. (2017). "Glass fabric reinforced cementitious matrix: Tensile properties and bond performance on masonry substrate". In: *Composites Part B: Engineering* 127, pp. 196–214.

Lignola, Gian Piero et al. (2017). "Performance assessment of basalt FRCM for retrofit applications on masonry". In: *Composites Part B: Engineering* 128, pp. 1–18.

Lotfi, Hamid R and P Benson Shing (1994). "Interface model applied to fracture of masonry structures". In: *Journal of structural engineering* 120.1, pp. 63–80.

Lourenco, Paulo B and Jan G Rots (1997). "Multisurface interface model for analysis of masonry structures". In: *Journal of engineering mechanics* 123.7, pp. 660–668.

Lourenço, Paulo B, Jan G Rots, and Johan Blaauwendraad (1998). "Continuum model for masonry: parameter estimation and validation". In: *Journal of structural engineering* 124.6, pp. 642–652.

Lubliner, J et al. (1989). "A plastic-damage model for concrete". In: *International Journal of solids and structures* 25.3, pp. 299–326.

Ma, Renle et al. (2012). "Experimental investigations on masonry structures using external prestressing techniques for improving seismic performance". In: *Engineering structures* 42, pp. 297–307.

Macorini, L and BA Izzuddin (2011). "A non-linear interface element for 3D mesoscale analysis of brick-masonry structures". In: *International Journal for numerical methods in Engineering* 85.12, pp. 1584–1608.

Maier, G, A Nappi, and E Papa (1991). "On damage and failure of brick masonry". In: *Experimental and numerical methods in earthquake engineering*, pp. 223–245.

Malena, Marialaura and Gianmarco de Felice (2014). "Debonding of composites on a curved masonry substrate: Experimental results and analytical formulation". In: *Composite Structures* 112, pp. 194–206.

Malena, Marialaura et al. (2019). "Collapse mechanism analysis of historic masonry structures subjected to lateral loads A comparison between continuous and discrete models". In: *Computers and Structures* 220, pp. 14–31.

Maroudas, Spyros R and Catherine Corina G Papanicolaou (2017). "Effect of High Temperatures on the TRM-to-Masonry Bond". In: *Key Engineering Materials*. Vol. 747. Trans Tech Publ, pp. 533–541.

Martins, A et al. (2015). "Experimental assessment of an innovative strengthening material for brick masonry infills". In: *Composites Part B: Engineering* 80, pp. 328–342.

Matthys, Stijn (2000). "Structural behaviour and design of concrete members strengthened with externally bonded FRP reinforcement". PhD thesis. Ghent University.

Meireles, H and R Bento (2013). "Rehabilitation and strengthening of old masonry buildings". In: *ICIST, Lisbon*.

Melbourne, Clive, Adrienn K Tomor, and Jinyan Wang (2004). "Cyclic load capacity and endurance limit of multi-ring masonry arches". In: *Arch bridges IV conference proceedings*, pp. 375–384.

Meriggi, Pietro et al. (2019). "Distinct Element Modelling of Masonry Walls under Out Of Plane Seismic Loading". In: *International Journal of Architectural Heritage*, pp. 1–14.

Miha, Tomazevic (1999). *Earthquake-resistant Design Of Masonry Buildings*. Vol. 1. World Scientific.

Milani, G, Paulo B Lourenço, and A Tralli (2006a). "Homogenised limit analysis of masonry walls, Part I: Failure surfaces". In: *Computers & structures* 84.3-4, pp. 166–180.

— (2006b). "Homogenised limit analysis of masonry walls, Part II: Structural examples". In: *Computers & structures* 84.3-4, pp. 181–195.

Milani, Gabriele (2008). "3D upper bound limit analysis of multi-leaf masonry walls". In: *International Journal of Mechanical Sciences* 50.4, pp. 817–836.

Montes, P and A Fernandez (2001). "Behaviour of a hemispherical dome subjected to wind loading". In: *Journal of Wind Engineering and Industrial Aerodynamics* 89.10, pp. 911–924.

Mosallam, Ayman S (2007). "Out-of-plane flexural behavior of unreinforced red brick walls strengthened with FRP composites". In: *Composites Part B: Engineering* 38.5-6, pp. 559–574.

MSJC (2002). "Building code requirements for masonry structures". In: *ACI530-02/ASCE 5-02/TMS 402-02. USA: Masonry Standards Joint Committee*.

Nazir, Shahid and Manicka Dhanasekar (2013). "Modelling the failure of thin layered mortar joints in masonry". In: *Engineering Structures* 49, pp. 615–627.

Noor-E-Khuda, Sarkar, Manicka Dhanasekar, and David P Thambiratnam (2016). "Out of plane deformation and failure of masonry walls with various forms of reinforcement". In: *Composite Structures* 140, pp. 262–277.

Oliveira, Daniel V and Paulo B Lourenco (2004). "Repair of stone masonry arch bridges". In:

Oliveira, Daniel V, Ismael Basilio, and Paulo B Lourenço (2010). "Experimental behavior of FRP strengthened masonry arches". In: *Journal of Composites for Construction* 14.3, pp. 312–322.

Olivito, Renato S, Rosamaria Codispoti, and Oscar A Cevallos (2016). "Bond behavior of Flax-FRCM and PBO-FRCM composites applied on clay bricks: Experimental and theoretical study". In: *Composite Structures* 146, pp. 221–231.

Ombres, Luciano et al. (2018). "Bond between Carbon Fabric Reinforced Cementitious Matrix and Masonry Substrate". In: *Journal of Materials in Civil Engineering* 31.1, p. 04018356.

Padalu, PKVR, Y Singh, and S Das (2018). "Efficacy of basalt fibre reinforced cement mortar composite for out of plane strengthening of unreinforced masonry". In: *Construction and Building Materials* 191, pp. 1172–1190.

Page, Adrian W (1978). "Finite element model for masonry". In: *Journal of the Structural Division* 104.8, pp. 1267–1285.

Page, John (1996). "A guide to repair and strengthening of masonry arch highway bridges". In:

Pande, GN, JX Liang, and J Middleton (1989). "Equivalent elastic moduli for brick masonry". In: *Computers and Geotechnics* 8.3, pp. 243–265.

Papanicolaou, Catherine, Thanasis Triantafillou, and Maria Lekka (2011). "Externally bonded grids as strengthening and seismic retrofitting materials of masonry panels". In: *Construction and Building Materials* 25.2, pp. 504–514.

Papanicolaou, Catherine G et al. (2007). "Textile-reinforced mortar (TRM) versus FRP as strengthening material of URM walls: in-plane cyclic loading". In: *Materials and structures* 40.10, pp. 1081–1097.

Papanicolaou, Catherine G et al. (2008). "Textile reinforced mortar (TRM) versus FRP as strengthening material of URM walls: out-of-plane cyclic loading". In: *Materials and Structures* 41.1, pp. 143–157.

Parisi, Fulvio et al. (2013). "In-plane behaviour of tuff masonry strengthened with inorganic matrix–grid composites". In: *Composites Part B: Engineering* 45.1, pp. 1657–1666.

Plecnik, Joseph, Thomas Cousins, and Edward O'Conner (1986). "Strengthening of unreinforced masonry buildings". In: *Journal of structural engineering* 112.5, pp. 1070–1087.

Portioli, Francesco et al. (2013). "Limit analysis by linear programming of 3D masonry structures with associative friction laws and torsion interaction effects". In: *Archive of Applied Mechanics* 83.10, pp. 1415–1438.

Prota, A et al. (2006). "Experimental in-plane behavior of tuff masonry strengthened with cementitious matrix-grid composites". In: *Journal of Composites for Construction* 10.3, pp. 223–233.

Rai, Durgesh C and Subhash C Goel (1996). "Seismic strengthening of unreinforced masonry piers with steel elements". In: *Earthquake spectra* 12.4, pp. 845–862.

RAIB (2010). "Failure of Bridge RDG1 48 (River Crane) between Whitton and Feltham". In: *Department of Transport UK*.

Raoof, Saad M and Dionysios A Bournas (2017a). "Bond between TRM versus FRP composites and concrete at high temperatures". In: *Composites Part B: Engineering* 127, pp. 150–165.

— (2017b). "TRM versus FRP in flexural strengthening of RC beams: behaviour at high temperatures". In: *Construction and Building Materials* 154, pp. 424–437.

Raoof, Saad M, Lampros N Koutas, and Dionysios A Bournas (2016). "Bond between textile-reinforced mortar (TRM) and concrete substrates: Experimental investigation". In: *Composites Part B: Engineering* 98, pp. 350–361.

— (2017). "Textile reinforced mortar (TRM) versus fibre reinforced polymers (FRP) in flexural strengthening of RC beams". In: *Construction and Building Materials* 151, pp. 279–291.

Rots, Jan G (1991). "Smeared and discrete representations of localized fracture". In: *Current Trends in Concrete Fracture Research*. Springer, pp. 45–59.

Rovero, Luisa, Francesco Focacci, and Gianfranco Stipo (2012). "Structural behavior of arch models strengthened using fiber-reinforced polymer strips of different lengths". In: *Journal of Composites for Construction* 17.2, pp. 249–258.

Royles, R and AW Hendry (1991). "Model tests on masonry arches". In: *Proceedings of the Institution of Civil Engineers, Part 2*. Vol. 89.

Saenz, Luis P (1964). "Equation for the stress-strain curve of concrete". In: *ACI-Jour.* 61.9, pp. 1229–235.

Santos, SP (2003). "Structural Rehabilitation of Historic Buildings". In: *40th Meeting of Commission CIB W*. Vol. 23.

Sassun, Kathy et al. (2016). "Characterising the in-plane seismic performance of infill masonry". In: *Bulletin of the New Zealand Society for Earthquake Engineering* 49.1, pp. 100–117.

Schuller, MP, Richard H Atkinson, and JT Borgsmiller (1994). "Injection grouting for repair and retrofit of unreinforced masonry". In: *Proceedings of the 10th International Brick and Block Masonry Conference*.

Schwegler, G (1994). "Masonry construction strengthened with fiber composites in seismically endangered zones". In: *The 10th European Conference on Earthquake Engineering, Vienna, Austria*.

Sheppard, P and S Tercelj (1980). *The effect of repair and strengthening methods for masonry walls, 7WCEE Istanbul*.

Shing, PB, M Schuller, and VS Hoskere (1990). "In-plane resistance of reinforced masonry shear walls". In: *Journal of structural Engineering* 116.3, pp. 619–640.

Shing, PB et al. (1992). "Finite element analysis of shear resistance of masonry wall panels with and without confining frames". In: *Proc., 10th World Conf. On Earthquake Engrg., AA Balkema, The Netherlands*, pp. 2581–6.

Silva, Vitor Cias e (2007). "Reabilitacao estrutural de edificios antigos-alvenaria, madeira. Tecnicas pouco intrusivas". In: *Argumentum, Gecorpa, 2ºa edicao*.

SIMULIA (2016). *ABAQUS version 6.16 analysis users manuals*.

Sneed, LH et al. (2015). "A comparison of the bond behavior of PBO-FRCM composites determined by double-lap and single-lap shear tests". In: *Cement and Concrete Composites* 64, pp. 37–48.

Stavridis, Andreas and PB Shing (2010). "Finite-element modeling of nonlinear behavior of masonry-infilled RC frames". In: *Journal of structural engineering* 136.3, pp. 285–296.

Sumon, SK (2005). "Innovative retrofitted reinforcement techniques for masonry arch bridges". In: *Proceedings of the Institution of Civil Engineers-Bridge Engineering*. Vol. 158. 3. Thomas Telford Ltd, pp. 91–99.

Sweidan, Raed Ibrahim (1992). "The application of fiber reinforced plastics to the strengthening of masonry structures". PhD thesis. Massachusetts Institute of Technology.

Taghdi, Mustafa, Michel Bruneau, and Murat Saatcioglu (2000). "Seismic retrofitting of low-rise masonry and concrete walls using steel strips". In: *Journal of Structural Engineering* 126.9, pp. 1017–1025.

Tao, Y, TJ Stratford, and JF Chen (2011). "Behaviour of a masonry arch bridge repaired using fibre-reinforced polymer composites". In: *Engineering Structures* 33.5, pp. 1594–1606.

Tao, Yi et al. (2012). "Numerical modelling of a large scale model masonry arch bridge". In: *Proc. of the 14th International Conference on Structural Faults+ Repair*.

Tetta, Zoi C and Dionysios A Bournas (2016). "TRM vs FRP jacketing in shear strengthening of concrete members subjected to high temperatures". In: *Composites Part B: Engineering* 106, pp. 190–205.

Tetta, Zoi C, Lampros N Koutas, and Dionysios A Bournas (2016). "Shear strengthening of full-scale RC T-beams using textile-reinforced mortar and textile-based anchors". In: *Composites Part B: Engineering* 95, pp. 225–239.

— (2018). "Shear strengthening of concrete members with TRM jackets: Effect of shear span-to-depth ratio, material and amount of external reinforcement". In: *Composites Part B: Engineering* 137, pp. 184–201.

Tiberti, Simone et al. (2017). "Masonry structures built with fictile tubules: Experimental and numerical analyses". In: *AIP Conference Proceedings*. Vol. 1906. 1. AIP Publishing, p. 090010.

Triantafillou, Thanasis C (1998a). "Shear strengthening of reinforced concrete beams using epoxy-bonded FRP composites". In: *ACI structural journal* 95, pp. 107–115.

— (1998b). "Strengthening of masonry structures using epoxy-bonded FRP laminates". In: *Journal of composites for construction* 2.2, pp. 96–104.

Triantafillou, Thanasis C and Michael N Fardis (1997). "Strengthening of historic masonry structures with composite materials". In: *Materials and Structures* 30.8, pp. 486–496.

Triantafillou, Thanasis C et al. (2006). "Concrete confinement with textile-reinforced mortar jackets". In: *ACI Materials Journal* 103.1, p. 28.

Turco, Valentina et al. (2006). "Flexural and shear strengthening of unreinforced masonry with FRP bars". In: *Composites Science and Technology* 66.2, pp. 289–296.

Valluzzi, Maria Rosa, Maurizio Valdemarca, and Claudio Modena (2001). "Behavior of brick masonry vaults strengthened by FRP laminates". In: *Journal of Composites for Construction* 5.3, pp. 163–169.

Valluzzi, Maria Rosa, Luigia Binda, and Claudio Modena (2005). "Mechanical behaviour of historic masonry structures strengthened by bed joints structural repointing". In: *Construction and Building Materials* 19.1, pp. 63–73.

Valluzzi, Maria Rosa et al. (2014). "Out-of-plane behaviour of infill masonry panels strengthened with composite materials". In: *Materials and structures* 47.12, pp. 2131–2145.

Valluzzi, MR, D Tinazzi, and C Modena (2003). "Strengthening of masonry structures under compressive loads by using FRP strips". In: *Fibre-Reinforced Polymer Reinforcement for Concrete Structures: (In 2 Volumes)*. World Scientific, pp. 1249–1258.

Vermeer, Pieter A and R De Borst (1984). "Non-associated plasticity for soils, concrete and rock". In: *HERON, 29 (3), 1984*.

Verstrynge, Els et al. (2009). "Monitoring and predicting masonry's creep failure with the acoustic emission technique". In: *NDT & E International* 42.6, pp. 518–523.

Vintzeleou, E and TP Tassios (1989). "Seismic behaviour and design of infilled RC frames". In: *European Earthquake Engineering* 3.2, pp. 22–28.

Wang, X et al. (2017). "Modelling the nonlinear behaviour of masonry walls strengthened with textile reinforced mortars". In: *Engineering Structures* 134, pp. 11–24.

Zampieri, Paolo et al. (2018). "A review of methods for strengthening of masonry arches with composite materials". In: *Engineering Structures* 171, pp. 154–169.

Zucchini, A and PB Lourenco (2002). "A micro-mechanical model for the homogenisation of masonry". In: *International Journal of Solids and Structures* 39.12, pp. 3233–3255.

Zucchini, Alberto and Paulo B Lourenco (2004). "A coupled homogenisation–damage model for masonry cracking". In: *Computers and structures* 82.11-12, pp. 917–929.

Appendix A

Out-of-plane strength of single and double-wythe walls based on EC6

The single-wythe S_CON wallete flexural strength parallel to the bed-joints f_{xk1} can be derived based on the D_CON experimental result and using Eq. A.1 for the moment resistance of the wallete M_{Rd}, where Z is the elastic section modulus. This is based on the observation that f_{xk1} depends on the mortar to brick bonding strength which, especially in the out-of-plane case was not expected to significantly vary between specimens.

$$M_{Rd} = f_{xk1}.Z \tag{A.1}$$

Thus, for the double-wythe control specimen D_CON, is determined through Eq. A.1 equal to 0.26 MPa. This value agrees well with the range provided in Table NA.6 (NA to BS EN 1996-1-1:2005 (EN, 1996)) for clay masonry units of groups 1 and 2 and M2 standardized mortars; the range provided is between 0.25 and 0.35 for units having water absorption larger than 7%.

Next, by using Eq. A.1 for the case of S_CON and considering the value of f_{xk1} derived from D_CON the value of the moment capacity and corresponding maximum load for S_CON are derived as 0.2 kNm and 0.7 kN, respectively. The

weight of the single wall was approximately 1.2 kN.